Development of advanced optical systems for spatially and temporally precise brain interrogation

Clément Molinier

To cite this version:

Clément Molinier. Development of advanced optical systems for spatially and temporally precise brain interrogation. Optics [physics.optics]. Sorbonne Université, 2021. English. NNT : 2021SORUS424 . tel-03696690

HAL Id: tel-03696690
https://theses.hal.science/tel-03696690v1

Submitted on 16 Jun 2022

Sorbonne Université

Ecole doctorale 564 :

IVISION, UMR7210, Institut de la Vision / Wavefront engineering microscopy group

Development of advanced optical systems for spatially and temporally precise brain interrogation

Développement de systèmes optiques avancés pour la manipulation des neurones avec une haute résolution spatiale et temporelle

Par Clément Molinier

Thèse de doctorat de Physique

Dirigée par Valentina Emiliani

Présentée et soutenue publiquement le 09/12/2021

Devant un jury composé de :

Dr. Emiliani Valentina (Directeur de thèse)

Dr. Fragola Alexandra (Examinateur)

Dr. Rigneault Herve (Rapporteur)

Dr. Fellin Tommaso (Rapporteur)

Acknowledgments

J'aimerais commencer par remercier chacun des membres de mon jury de thèse pour avoir accepté de prendre le temps de lire mon manuscrit et de participer à ma soutenance. Merci au Dr. Rigneault Herve, Dr. Fellin Tommaso et Dr. Fragola Alexandra, je vous souhaite une bonne lecture.

C'est avec beaucoup d'émotions que j'écris ces lignes car elle représente la touche finale d'un travail qui aura duré 4 ans. Quatre années toutes plus incroyables et inattendues les unes que les autres. Je peux dire avec certitude aujourd'hui que jamais je ne les oublierais. Mais si elles ont pu être aussi exceptionnelles, c'est avant tout grâce à toutes les personnes que je veux remercier aujourd'hui à travers les lignes qui vont suivre.

Je voudrais commencer par remercier Valentina Emiliani, ma directrice de thèse. Tu as su faire preuve de compréhension dans des moments compliqués. La confiance et la liberté d'action que tu m'as accordé au cours de ma thèse m'ont permis de pleinement réaliser mon travail.

J'ai une pensée toute particulière pour mes co-encadrants Nicolo Accanto et Emiliano Ronzetti. Nicolo, je ne pourrais pas tout résumer en quelques mots. Tu as été là comme un ami et un guide, toujours présent, et tu as su rester honnête face à mon travail. Tu auras su croire en moi quand je n'y croyais plus, merci. Emiliano, je suis fier d'avoir pu travailler avec toi et de ce que nous avons pu réaliser ensemble. Avec toi, je n'étais plus un étudiant de thèse mais un véritable chercheur. Je n'aurais pas pu imaginer meilleurs encadrants, merci à vous Nicolo et Emiliano.

J'aimerais aussi remercier mon comité de suivi de thèse Dimitris Papadopoulos et Pascal Berto. Dimitris, j'ai une énorme pensée pour toi car je ne serais tout simplement pas là où je suis aujourd'hui sans ton aide. Toi qui en 2016 as su me faire confiance et m'a pris en stage au laboratoire Luli. Un stage qui m'a permis de découvrir ma voie : l'optique.

Pascal, en écrivant ces lignes je souris déjà ! Ton humeur est contagieuse, mais heureusement elle est plutôt bonne ! J'ai eu la chance de t'avoir comme parrain de thèse, toi qui as su me pousser dans des directions inattendues et à sortir de ma zone de confort. Je ne saurais oublier tes conseils et ton attention (et surtout ton humour).

Qui dit optogénétique, dit biologistes et physiciens. Giulia Faini, tu auras été mon binôme biologie durant cette thèse et j'en suis heureux ! Je repense à ces week-ends passés ensemble autour d'une bonne table optique à patcher des cellules et déguster de délicieux *haribo* offerts par Thorlabs. Je te remercie pour l'humour et la complicité de ces moments qui m'auront permis de tenir ces longues semaines.

Dimitrii Tanese, merci à toi qui fut le premier à me faire découvrir le laboratoire, toi le préposé aux visites du gang des LUMIs et sélectionneur officielle en Masters leagues. Je pense aussi aux longues soirées d'hiver au Saint-Pères ou rester tard pour des manips les dernières lumières allumées était la diode rouge de la sécurité laser de ton setup et la lampe de ton bureau, on se sentait alors un peu moins seul.

Je voudrais aussi remercier Eirini Papagiakoumou. Eirini, tu es officiellement la 2e personne avec qui j'ai discuté dans le laboratoire. Je m'en souviens encore, c'était dans ton bureau aux St-Pères. Tu m'expliquais le Temporal Focusing, et tout d'un coup, tu m'as posé cette question : « tu n'aurais pas fait un stage à Apollon au Luli… ? » Je tairais la suite car elle n'est pas à mon avantage mais j'en ris encore aujourd'hui.

Je me dois aussi de remercier Christophe Tourain. Christophe c'est simple, sans ton aide je serais très probablement toujours en train de chercher comment brancher des miroirs galvanométriques. Tu as été une présence rassurante tout au long de cette thèse. Une personne avec qui j'ai pu discuter et échanger. Même si nos horaires de cantine coïncidaient rarement, j'ai été ravie de discuter impression 3D avec toi au détour d'un café. Merci encore pour ton aide.

Je ne pourrais pas continuer ces remerciements sans parler de Vincent De Sars. Nos echanges autour de l'informatique et du langage QT ont été pour moi une véritable bulle d'air frais durant ma thèse. C'était le sujet dans lequel j'aimais me plonger quand rien d'autres ne fonctionnait. Merci énormément pour ton écoute et tous ces conseils qui m'ont permis d'avancer 100 fois plus vite. C'est promis, je penserais au texte de présentation pour le site de l'IDV.

Je remercie aussi Imane Bendifallah, toi qui as supporté mes effroyables talents de chanteur durant les journées de manip en 2-ème année. Toi qui as été une oreille attentive. A tous ces fous rires qui m'ont changé les idées, merci pour ton amitié.

Ruth Sims, je te remercie pour ta joie de vivre et ton usage intensif de Python, je me sentais enfin moins seul ! Et je te serais à jamais reconnaissant de m'avoir fait découvrir votre sirop violet de Mark&Spencer. Est-ce un jus, est-ce un sirop ? Telle est la question... Si britannique !

Valeria Zampini, je te remercie encore pour la délicieuse mascarpone que tu nous as faites, sans toi les repas de Noël mais surtout le panettone n'aurait pas eu la même saveur.

Je voudrais aussi remercier I-Wen Chen pour tes conseils en Biologie et les moments d'échanges que nous avons au cours de ces années.

SI on me demandait ce qui m'a fait tenir, je répondrais très probablement le café. Aussi je voudrais remercier ceux grâce à qui j'ai toujours pu en profiter, j'ai nommé Gilles Tessier, Robert Kuszelewicz et Benoît Forget.

Cécile Telliez, je suis ravie d'avoir pu te transmettre le plaisir de l'alignement, fais-en bon usage.

Un petit clin d'œil au gang des LUMI : Cécile, Antonio Lorca, Massilia Hamdani. Je vous souhaite bon courage pour le début et la fin de vos thèses. J'aimerais aussi remercier tous les autres doctorants que j'ai croisé pendant ma thèse : Chang Liu, Marco Pascucci, Minh-Chau Nguyen, Joe Chan. Joe, si un jour, tu as des problèmes de retopologie, n'hésites pas à m'appeler.

Alexis Picot, mon prédécesseur, je te remercie pour ton amitié, ton soutien et ton organisation débordante ! Une fois diplômé, je t'inviterais à une thé-rasse.

Je voudrais également remercier mes amis et ma famille.

Bruno, merci à toi qui a été là à toute heure et à tous les moments importants, toi qui m'as aidé à déménager 2 fois en 4 ans et qui a toujours cru en moi ! Thibault, conseillé gastronomique durant le confinement, merci d'avoir répondu à mes insomnies de programmation. Nicolas, grâce à toi, je craignais moins de faire brûler des choses, au moins, je savais qu'il y avait un pompier compétent dans les parages ! Cédric, attends que je finisse la thèse, promis je viens grimper. Térence, je serais bientôt assez crédible pour reprendre tes cours de maths. William, je vais bientôt te rejoindre de l'autre côté ! Aurélien, merci d'avoir cru à mes projets les plus fous !

J'ai une pensée pour tous les membres de ma famille qui ont pris de mes nouvelles et m'ont aidé durant la période compliquée du Covid. A vous : Catherine, Bernard, Jean-Yves, Pauline, Camille, Ezra, Guillaume, Nadège. Mais aussi Marie-Christine, Pierre, Jeremy, Jonathan, Solène et Claude mon parrain.

Je voudrais remercier ma grand-mère, qui s'est occupé de moi et m'a hébergé pendant plus d'un an et demi, sans toi, je serais probablement mort de faim.

A mon père et à ma mère, qui eux, n'ont pas eu le choix que de me soutenir depuis bien plus longtemps que ces 4 dernières années. Papa, Maman, j'ai enfin la date de ma soutenance ! Je vous suis énormément reconnaissant de tout ce que vous avez fait pour moi et je me sens véritablement chanceux de vous avoir comme parent.

Florence, rien n'aura su nous résister et ensemble, nous avons pu surmonter toutes les épreuves. Grâce à toi, j'ai pu grandir et découvrir des ressources insoupçonnées, tu es la première à croire en moi.

Abstract

With the discovery of optogenetics, using light becomes essential to study and control neural activity and connectivity. However, the complexity of the brain circuits demands advanced optical methods for detailed investigation. One of the most significant optical challenges is to address multiple targets with cellular resolution and high temporal precision in deep brain regions. During this thesis, I worked on three new optical systems to provide a possible answer to some of these technical challenges.

First, we developed a new system to multiplex temporally focused light shapes (MTF-LS) for precise 3D photostimulation of neurons. Thanks to the flexibility of this new approach, different light-shaping methods can be applied: either computer-generated holography (CGH) or speckle-free generalized phase contrast. With these two approaches, the system was limited to multiplex only one shape at the time. To solve this issue, we demonstrate an innovative amplitude/phase modulation technique, to multiplex different shapes in 3D.

Due to the absorption and scattering, it is difficult to stimulate cells beyond ~ 600 µm of brain tissue with two-photon (2P) stimulation technique. Facing similar limitations in imaging, other laboratories used gradient index (GRIN) lenses implanted in the brain to access deep regions. Thus we develop a new in-depth photostimulation method, by coupling a GRIN lens with the MTF-LS previously demonstrated. This system represented the first microendoscope capable of generating tens of axially confined 2P excitation patterns matching target neuronal soma in a 3D volume for in-depth experiments.

Third, to manipulate neuronal activity at sub-millisecond temporal scales and large cell populations, we built a new system using ultra-fast sequential light targeting (FLiT). We managed to control the spike delay among two cells with µs temporal resolution. We also demonstrate a new stimulation protocol where the illumination time optimization allows to stimulate five times more cells than conventional static illumination for the same laser power.

Résumé

Avec la découverte de l'optogénétique, l'utilisation de la lumière est devenue essentielle pour étudier et contrôler l'activité et la connectivité neuronales. Cependant, la complexité des circuits cérébraux exige d'employer des méthodes optiques avancées pour toute investigation approfondie de son fonctionement. C'est pourquoi, l'un des plus grands défis optiques est d'atteindre des cibles multiples avec une résolution cellulaire et une bonne précision temporelle dans les régions les plus profondes du cerveau. Au cours de cette thèse, j'ai travaillé sur trois nouveaux systèmes optiques afin d'apporter une réponse possible à certains de ces défis techniques.

Premièrement, nous avons développé un nouveau système de génération de formes lumineuses focalisées dans le temps (MTF-LS) pour la photostimulation précise en 3D des neurones. Grâce à la flexibilité de cette nouvelle approche, différentes méthodes de modelage de la lumière ont put être utilisées: l'holographie générée par ordinateur (CGH) ou le contraste de phase généralisé. Avec ces deux approches, le système était limité à la multiplication en 3D d'une seule forme à la fois. Pour résoudre ce problème, nous avons proposé une technique innovante de modulation amplitude/phase, pour générer différentes formes en 3D.

En raison de l'absorption et de la diffusion, il est difficile de stimuler des cellules au-delà de ~ 600 µm de tissu cérébral avec une methode de stimulation à deux photons (2P). Face à des limitations similaires en matière d'imagerie, d'autres laboratoires ont utilisé des lentilles à gradient d'indice (GRIN) implantées dans le cerveau pour accéder à des régions profondes. Nous avons donc développé une nouvelle méthode de photostimulation en profondeur, en couplant une lentille GRIN avec le MTF-LS précédemment démontré. Ce système représente le premier microendoscope capable de générer des dizaines de sites d'excitation 2P, confinés axialement et correspondant aux dimensions du soma d'un neurone cible dans un volume 3D .

Troisièmement, pour manipuler l'activité neuronale à des échelles temporelles inférieures à la milliseconde et/ou de grandes populations de cellules, nous avons construit un nouveau système utilisant le ciblage lumineux séquentiel ultra-rapide (FLiT). Nous sommes parvenus à contrôler le retard d'activation entre deux cellules avec une résolution temporelle de l'ordre de la microseconde. Nous avons également démontré un nouveau protocole de stimulation où l'optimisation du temps d'illumination permet de stimuler cinq fois plus de cellules que l'illumination statique conventionnelle pour la même puissance laser.

Contents

Chapter 1: Introduction 1
1.1 Optical control of neuronal firing by optogenetics and wave front shaping 2
Chapter 2: Two-photon excitation and single-cell precision 8
2.1 One and Two photon Microscopy 8
2.2 Advanced two-photon optical configuration for stimulation 10
Chapter 3: Beam Shaping 14
3.1 Holography 14
3.2 Computer Generated Holography 15
3.2.1 Liquid Crystal on Silicon Spatial Light Modulators 16
3.2.2 Holographic set-up and performance 17
3.2.3 Phase-hologram calculation algorithms 25
3.3 Generalized phase contrast methods 28
3.4 Axial resolution 31
Chapter 4: Temporal focusing Beam Shaping 35
4.1 Concepts 35
4.2 Realization 36
4.3 2D setup configuration: 40
4.3.1 TF-effect 41
4.4 3D configuration 42
Chapter 5: Holography in dept 71
5.1 light-matter interaction in nervous tissue 71
5.1.1 Absorption : 71
5.1.2 Scattering: 72
5.1.3 Multi-photon stimulation in brain medium 74
5.2 The Micro-endoscope solution 77
5.2.1 Micro-endoscope GRIN lens: 77
Chapter 6: Fast Stimulation .... Erreur ! Signet non défini.
Chapter 7: Software Development .... Erreur ! Signet non défini.
7.1 Fast Scan Interface .... Erreur ! Signet non défini.
7.2 SLM Control .... Erreur ! Signet non défini.
7.3 Protocol Generator .... Erreur ! Signet non défini.
7.3.1 Protocol 1 .... Erreur ! Signet non défini.
7.3.2 Protocol 2 .... Erreur ! Signet non défini.
Chapter 8: Conclusions 164

List of figures

Figure 1: Schematic representation of the principles governing an action potential. 4
Figure 2: Current trace from voltage clamp recording of a cell with ChR2 expression 5
Figure 3: Schematic representation of performance criteria for photo stimulation technique 7
Figure 4: 1P vs 2P fluorescence microscopy. 9
Figure 5: 2P light stimulation approaches targeting opsin-expressing cell 11
Figure 6: Multi-cell targeting strategy 12
Figure 7: Schematic representation of Gabor holography 14
Figure 8: Spatial Light Modulator composition and mechanism. 16
Figure 9: Schematic representation of the SLM parameters and objective aperture. 18
Figure 10: Schematic representation of the most straightforward optical system for CGH 18
Figure 11: Representation of the two possible configurations for SLM illumination and projection at the BA 19
Figure 12: Mathematical expression for the Spatial digitalization of the desired phase signal 20
Figure 13: The link between a conventional blazed grating and a stepped phase function. 20
Figure 14: Schematic diagram showing the effect of the SLM digitalization 22
Figure 15: The diffraction efficiency for stepped grating phase function.. 23
Figure 16: Graphical representation of the diffraction efficiency obtained with equation (3.17) 23
Figure 17: Zero-order correction 24
Figure 18: Diagram of the Gerchberg & Saxton 27
Figure 19: Schematic representation of the method proposed by Zernike 29
Figure 20: Schematic representation of a GPC set-up. 29
Figure 21: Schematic representation the filter and the spatial profile of a Fourier filter. 30
Figure 22: Plot the spatial variation of the normalized SRW amplitude 31
Figure 23: Comparison of different beam types. 32
Figure 24: Evolution of the axial resolution as a function of the diameter of the generated spot 33
Figure 25: Axial propagation of spatially and temporally focused beams 35
Figure 26: Illustration of a laser pulse decomposition in spectral domain by Fourier transform 36
Figure 27: Broadening of a Laser pulse propagating in a dispersive medium. 37
Figure 28: Representation of the angular dispersion of colors. 38
Figure 29: Geometrical description of the pulse deformation by a grating reflection. 38
Figure 30: Grating compressor and scanning effect. 40
Figure 31 Representation of 2D TF: GB, CGH, GPC system and confinement performance. 41
Figure 32: Comparison of the axial resolution as a function of the diameter of the generated spot 42
Figure 33: Schematic representation of 2D TF-CGH system. 43
Figure 34: Simulation of beam shaping with a single SLM illuminated by a TF Gaussian beam 44
Figure 35: Grating illumination configuration 45
Figure 36: Light absorption coefficient evolution over the 0.1-12-µm spectrum for water, oxygenated 72
Figure 37: Scattering coefficients evolution over the 400-1700 nm spectrum for brain 73
Figure 38: Schematics representation of laser pulse propagating in a scattering media 74
Figure 39: Attenuation spectrum of a tissue model based on Mie scattering and water absorption 74
Figure 40: Schematic representation of a high-NA objective focusing light in a different sample. 75
Figure 41: Description of the temporal focusing resilience to scattering. 76
Figure 42: Illustration of temporal performance in photostimulation: 93
Figure 43: Photostimulation protocol to stimulate two patched-cells with holography or FLiT 95
Figure 44: Use of two SLMs to improve the temporal resolution (from Marshel et al.) 97
Figure 45: Multiplexed Temporally Focused Multi-Shape system (MTF-MS) 98
Figure 46: The fast sequential light patterning system (FLiT): 99
Figure 47: Degree of focusing of the illumination beam on the SLM (FLiT): 100

Figure 48: Evaluation of the impact of tiled Holograms and line illumination on the performance 101
Figure 49: Evaluation of the impact of the line laser displacement on the optical performance........................ 102
Figure 50: Evaluation of the switching speed of the system FLiT 104
Figure 51: Software homepage divided in four sections. 105
Figure 52: Navigation and display (section 1) divided in three parts. 106
Figure 53: Management of General Parameters (Section 2) divided in 4 parts 107
Figure 54: Management of General Parameters (Section 2) part 5 109
Figure 55: Diffraction efficiency Weights map 110
Figure 56: z displacement Weights map 111
Figure 57: Management of lines created on the SLM (section 3) divided in two parts 111
Figure 58: Phase generation and access to the protocol programming page (Section 4) divided in two 112
Figure 59: Protocol 1 fast scan control window divided in 3 sections. 113
Figure 60: : Protocol 1 section 2. 113
Figure 61: Protocol 2 mimicking control window divided in 3 zones.. 115
Figure 62: Protocol 2 zone 2 115

List of abbreviations

1P: *single-photon*

2P*: Tow photons*

AP*: Action potential*

BA: *Back aperture,*

BFP: *Back focal plane*

CGH: *Computer-generated holography*

ChR2: *Channelrhodopsin-2*

CW: *Continuous wave*

EPSP: *Excitatory postsynaptic potential*

FFP: *Front focal plane, Fresnel flat phase*

FliT: *Fast sequential light patterning*

FOE: Field of excitation

FOV: *Field of view*

FWHM: *Full width at half maximum*

FZP: Fresnel zone plate

GECIs*: genetically encoded calcium indicators*

GEVIs*: genetically encoded voltage indicators*

GFP: *Green fluorescent protein*

GL: Gratings and lenses

GM: *Galvanometric mirrors*

GPC: *Generalized phase contrast*

GS: *Gerchberg-Saxton*

LC: *Liquid crystals*

LC-SLMs: *Liquid crystals SLMs*

NA: *Numerical aperture*

PCF: Phase contrast filter

ROI: *Region of interest*

SFO: *Step function opsins*

SRW: *Synthesized reference wave*

STED*: stimulated-emission-depletion*

TPE: Two-photon excitation

Chapter 1: Introduction

Today, the brain is considered the site of our thoughts, but it has not always been so. In ancient times, the Greek Aristotle described it as a radiator (Aristotle, 1955). A radiator to cool the blood heated by the heart's passion. It takes centuries of questioning and significant scientific developments in various fields to establish our current vision of the brain: a dense and complex network of interconnected neuronal cells communicating through electrical impulses. This nerve impulse governs our body, senses, memory, dreams, and fears. Thus, even if it is not the only vital organ in our body, it has a unique and almost sacred character. However, our understanding of the brain is still very fragmented as two fundamental aspects need to be studied. First, the anatomy: at the brain and cell scale with the mapping of neuronal connections and the description of the structures and mechanisms of the neurons. Second, physiology involves investigating how information is encoded and flowed across the neuronal networks in space and time.

Although still incomplete, morphological knowledge of the brain has benefited from significant advances in microscopy in the last 100 years, such as electronic microscopy, confocal microscopy, two-photon (2P) microscopy, and super-resolution microscopy. The electron microscopy offers a magnification of up to 2 million times. Thanks to this method, a synaptic connectivity map (connectome) of the whole nervous system of the Caenorhabditis elegans (C. elegans) has been realized (John Graham White et al., 1976). Confocal imaging enables *in vitro* observations of very small structures of the neurons (few µm range). Two-photon techniques allow imaging fluorescent tissue with a sufficient resolution to distinguish soma, dendritic spines, and axons (few µm range) in depth. The stimulated-emission-depletion (STED) development offered a resolution beyond the conventional light-based microscopes, enabling, for example, high-resolution imaging *in vitro* and *in vivo* of synapses, the most basic functional units of the brain, 500 times smaller than a neuron (Bommel et al., 2019; Nägerl & Bonhoeffer, 2010).

Investigating signal propagation in the brain and how specific activity patterns are linked to behavior requires going beyond the morphological study, which technically requires recording and manipulating functional signals.

Traditionally this was done using electrophysiology to allow direct recording and stimulation of the nerve signals. Among the different configurations, the patch-clamp is the gold-standard technique. Developed in 1976 by Neher and Sakmann (E Neher & B Sakmann, 1992), it is still widely used today because of its unique performance in terms of signal-to-noise ratio, allowing measurements of small electric signals at the picoampere (pA) scale with microsecond (µs) temporal resolution over a patched cell. Over the years, new techniques have been developed to target a more significant number of neurons while reducing invasiveness (G Buzsáki, 2004). For instance, the multi-electrode arrays contain multiple thousands of microelectrodes through which it is possible to record the electrical signal from a few hundred cells simultaneously. Other approaches much used in the medical field, such as Electroencephalography, allow reading neuronal activity from large brain regions with minimal invasiveness.

All these techniques reach a balance between 3 factors: invasiveness, spatial precision, and scalability. Low invasiveness reduces the impact on the tissues and thus, avoids possible modification of the studied structure. Spatial accuracy is required to resolve the signal from a single cell or cellular process.

Scalability enables multiple target recordings. Unfortunately, the reduction of invasiveness and the increase of recorded targets is made at the expense of spatial accuracy.

Back in the 1990s, the co-discoverer of DNA structure, Francis Crick (Crick Francis, 1979; Crick Francis and Frs OM, 1999), as a well-known frontrunner scientist, point out this lack in the available techniques. He speculated on a future optical method for investigating cells: "the ideal signal would be light, probably at an infrared wavelength to allow the light to penetrate far enough. This seems rather farfetched, but it is conceivable that molecular biologists could engineer a particular cell type to be sensitive to light in this way". If Francis Crick proposed the light as a means of investigation, it is not by coincidence. The advantages of using light are clear: it is noninvasive; it has the resolution for single cell illumination but can also, through multiplexed approaches, reach multiple targets on large brain regions.

The challenges of the past 30 -50 years have been then to replace electrodes with light (M Scanziani & M Häusser, 2009), for neuronal signal recording (reading), and neuronal signal manipulation (writing).

Reading: the first step consisted in finding optical probes capable of converting an electrical signal into a fluorescent signal 1) activity indicators (Ca^{+} and voltage dyes) 2) genetically encoded calcium and voltage indicators (GECIs, GEVIs). Secondly: develop optical approaches capable of recording a functional signal with cellular resolution from neuronal cells embedded in scattering tissue. This was first realized with the evolution of 2P microscopy. All in all, these discoveries put so the way for precise reading of neuronal signal from thousands of cells in mm^{3} volumes with single cell.

Writing: the first step consisted in making neurons sensitive to light and was solved with the apparition of optogenetic. By expressing suitable opsins, i.e., light-gated ion channels or pumps, in genetically identified neuronal populations, it is possible to switch on or off the neural activity of the illuminated neurons (Karl Deisseroth, 2011). Optogenetics, elected method of the year in 2010 by the prestigious journal Nature Methods, has revolutionized the field of neuroscience. In its most widely used approach, optogenetics makes use of a single optical fiber to illuminate with visible light the entire brain region in which suitable opsins were previously expressed, thereby activating the whole brain area. This established method has allowed mapping of neuronal function with cell-type specificity (Jennings et al., 2013, 2015; Lin et al., 2011; RD Proville et al., 2014). However, to really decrypt the neural code, we need to understand how individual neurons collaborate to build up a local brain circuit and how neural activity's spatial and temporal organization at the single cell level influences brain computation. The realization of these objectives requires a transition from whole region optogenetics to more sophisticated illumination approaches capable of controlling single and multiple neurons independently in space and time.

In this chapter, we will describe the mechanisms behind the firing properties of neurons. Then, we will introduce the opsin structure and processes responsible for the neuronal control, discussing the constraints it imposes on optical development.

1.1 Optical control of neuronal firing by optogenetics and wavefront shaping

This section will shortly describe the mechanism behind the essential electrical signal used by neurons to control neuronal circuits, namely the action potential (AP). Then we will see how these APs are controlled using optogenetics and which are the main requirements for developing an illumination method to generate physiological activity patterns.

Neurons are the fundamental unit of the nervous system. Ramon Y Cajal highlighted the essential function of the neurons in 1899 with the first drawing of the neuron structure that controls the entire body function. The neuron's anatomy comprises three main parts: the cell body or soma-, from which two types of extensions emerge: the axon which transmits the signal to other neurons, and dendrites for the integration of signal input through the ”button” (synapse), which connects and transmits chemical or electrical signals between neurons. In the human brain, the soma diameter can vary from few micrometers to several tens of micrometers according to its type: sensory, motor or interneurons. The axon proportion also changes, with a length ranging from less than a millimeter to a meter or more. Finally, dendrites' diameter varies between few micrometers, and their lengths can reach the millimeter.

The neuronal membrane is submitted to a voltage difference (called the membrane potential) between the intra- and extra-cellular compartments (usually ranging from -60 mV to -90 mV at rest). This is due to the difference in charge distribution across the membrane generated and maintained by ion channels and pumps in which ions can travel, leading to changes in Na+, K+, Ca2+ and Cl- concentrations.

Action potentials are highly stereotypical electrical signals encoding and transmitting the information from cells to cells (via synapses) as electrical impulses propagating along the nervous system.

The AP, characterized by a localized change in the permeability of the neuron membrane, typically last 1 to 2 ms and can be described in three stages (Figure 1). This starts with the excitatory postsynaptic potential (EPSP): if the membrane potential of the neuron reaches a threshold (typically ~ -55 mV), the voltage-gated Na+ channels will open and let Na+ ions enter the cell, resulting in a depolarization from the resting potential to a positive value (> +30 mV). This is followed by the repolarization and hyperpolarization steps: voltage-gated sodium channels close, and voltage-gated potassium channels open. K+ ions exit the cell, and the membrane potential reaches a value lower than the resting potential. Finally, the action of sodium-potassium ion pumps allows the return to the resting potential of the cell membrane. In many neurons, the depolarization also induces the opening of voltage-gated Ca2+ channels leading to a Ca2+ concentration increase within the cell cytoplasm.

The stimulus given to a resting neuron must depolarize the membrane above a threshold value to induce a spike. Once the threshold surpasses, an AP is induced regardless of the final stimulus intensity. However, the strength of the stimulus does impact the temporal frequency of the AP potentials generated. In theory, the maximum achievable frequency for a neuron is limited by the absolute refractory period. Although the frequency increases with the stimulus intensity, there is a limit to the rate at which a neuron can generate AP. When an action potential is initiated, the next one can occur only after a delay of $\sim 1-2\,ms$ called the absolute refractory period. This led to a maximum frequency response of around $\sim 500-1000\,Hz$. In addition, the absolute refractory period is followed by the relative refractory period (several milliseconds), during which the stimulus to elicit an AP is higher than under normal conditions.

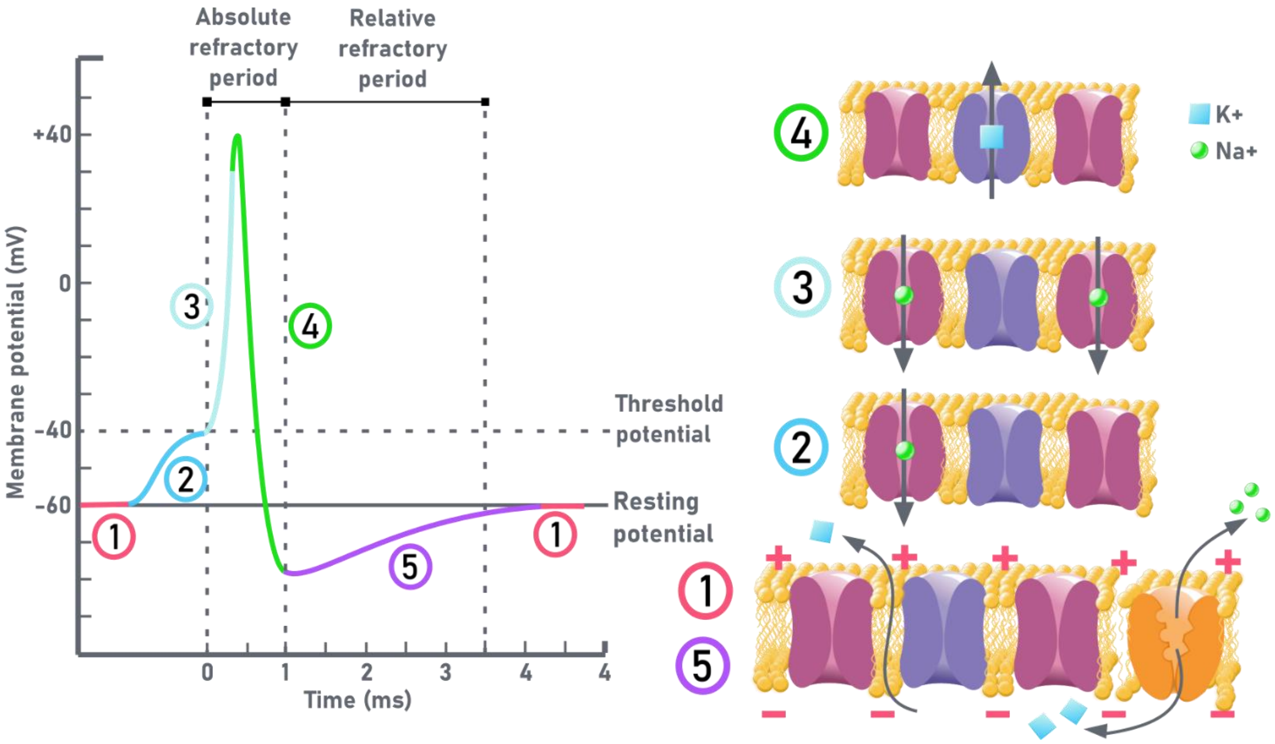

Figure 1: Schematic representation of the principles governing an action potential. (a) Typical voltage trace generated by an AP separated in 5 states. (b) depict the mechanisms behind the 5 states at the membrane level. Step 1 or resting state: all the ion gates are closed and the membrane resting potential is maintain by the Na^+/K^+ *pump (in orange) which counterbalances ion* K^+ *leakage through the membrane. Step 2 or depolarization: Under external stimulation part of the* Na^+ *channels (purple) open, starting to depolarize the membrane. If the potential exceeds the threshold the next step is triggered. Step 3 or rising phase: the membrane potential drastically increases under the massive opening of* Na^+ *channels. Step 4 or falling phase: Moste of the* Na^+ *channels are now closed, leaving the room to the* K^+ *one to opens and rebalance the gradient. During this step the potential often exceeds its original value, it is called the Hyperpolarizing state. Step 5 or undershoot: Both type off gates are now closed. The membrane progressively return at is initial value with the help of the* Na^+/K^+ *pump.*

Thus, any technique intended to control neuron must be able to evoke one or multiple AP at variable firing frequencies. Ideally, this should be done on numerous targets with tunable spiking delay and single cell precision to control neuronal circuits.

In 1971 Oesterhelt and Stoeckenius identified the first opsin in a microbial organism, named bacteriorhodopsin (D Oesterhelt & W Stoeckenius, 1971). The Opsins are constituted of an ion pump or channel coupled with a light-sensitive retinal group (J Duebel et al., 2015). Once exposed to light, the opsin undergoes a conformational change that opens the pump or channel, enabling the selective entrance of positive or negative ions through the cell membrane. This discovery was particularly important since it highlighted the existence of microbial opsins (type I) more efficient in transduction light into current than their homolog of animal origin (type II). (BR Rost et al., 2017; EG Govorunova et al., 2015; J Duebel et al., 2015; Karl Deisseroth, 2015). In the following years, investigative efforts in the field have revealed two new subclasses of microbial opsins: halorhodopsins (A Matsuno-Yagi & Y Mukohata, 1977) and channelrhodopsins (G Nagel et al., 2002, 2003). In 2005 Boyden (Boyden et al., 2005) trigger reliable APs using light, on a population of mammalian neurons genetically modified to express channelrhodopsins-2 (CHR2). This experience signs the birth of what Karl Deisseroth later called optogenetics (Karl Deisseroth, 2011). This exploit was quickly followed by Zhang (F. Zhang et al., 2007) using this time halorhodopsin to inhibit the cells. Since then, numerous study have ben conduct to better understand these proteins an find new, natural or artificial variant.

One of the hallmarks of optogenetic is the capability for targeting genetically identified cells. Transduction of the opsin genes can be done via three main approaches: transgenesis, viral transduction, and electroporation (SC Barnett et al., 2018). The selection of the method depends on the tissue and design of the experiment. Currently, viral transduction is the most widespread approach using lentivirus, adenovirus, or herpes virus (Karl Deisseroth, 2015; SC Barnett et al., 2018). With this method, the researchers can target a type of cell in the body (e.g., brain, lung, retina) and focus on specific subpopulations as in the case of neurons: excitatory only or inhibitory only. It is even possible to target the opsin expression on a particular structure, such as the cell body of the neuron (soma) and not the surrounding elements (dendrite or axons)(Shemesh et al., 2017).

The capacity of opsin to provide efficient and reliable AP depends on the balance of several key properties. First, the photocurrent amplitude is related to two criteria:

- The single channel conductance or the ion flow allowed by the opening of a channel or pump.
- The expression level which determines the density of channels expressed per membrane unit.

These properties define the opsin ability to induce a sufficient current to reach the expected cell threshold. Regarding the illumination approach (Chapter 2) It also impacts the temporal precision of the activation i.e., the degree of reproducibility of the occurrence timing of a photo-evoked AP (also indicated as photo-evoked spike jitter). A high conductivity will have a higher probability of eliciting AP with low jitter.

Second, the opsin kinetics (Figure 2). At the beginning of the stimulation, the inward current increase thanks to the opsin opening, reaching a peak value. Then the opsin progressively enters an intermediary state, reducing the generated current until reaching a steady-state value. Finally, when the illumination stops, the current returns to its initial level as the opsin progressively close. The time durations off this different phase represent the opsin kinetics and are respectively called τ_{ON}, τ_{DES} , and τ_{OFF}. These parameters vary from one opsin to the over and directly impact the time performance in photostimulation.

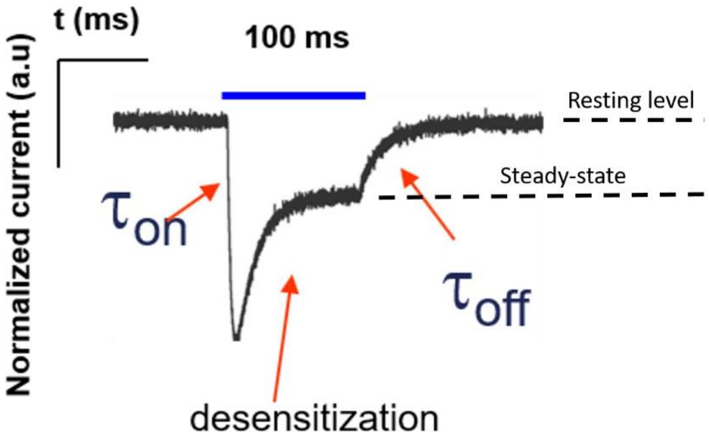

Figure 2: Current trace from voltage clamp recording of a cell with ChR2 expression during 100ms steady illuminations using 1P blue shifted light. Three distinct stages: activation, desensitization and inactivation. τ_{ON} *time rise to peak current,* τ_{DES} *from peak to steady state,* τ_{OFF} *time to resting level after ending the photostimulation. [adapted from E.Chaigneau]*

τ_{ON} represents the time needed to reach the maximal photocurrent. It is related to the opsin photocycle, the excitation power, and the single or two-photon cross-section. A fasten increasing photocurrent will lead to a fast depolarization.

τ_{DES} during this period, the photocurrent goes from its maximum value to a lower one. This second opsin kinetic should be considered for long-term illumination protocols, especially with step-function opsins (SFO) introduced later.

τ_{OFF} is the decay time of the photocurrent after the end of the stimulation. Therefore, it represents the minimum waiting time to re-excite the opsin and governs the minimum effective inter-AP interval (a low “tau off” and short illumination time allows the control of high spiking rates).

The Channelrhodopsin-2 (ChR2) was the first opsin to show sufficient kinetic parameters to induce action potential (AP). Today dozens of variants exist, and the vast majority are artificial. Each of them offers different balances between these parameters for different applications. Chronos mutants, for example, have fast activation and deactivation kinetics that allows high spiking rates up to 100Hz (E Ronzitti et al., 2017). Conversely, step-function opsins (SFO) mutants have opening times of up to half an hour. Typically, these mutants produce low amplitude depolarizations and cannot sustain an AP by simple illumination. However, they can generate persistent activity by sustainably increasing the excitability of neuron populations (A Berndt et al., 2014; O Yizhar et al., 2011).

In a mouse brain, the typical diameter of a neuron, regardless of its type, will be around 10 to $20\ \mu m$. In terms of density, the mouse cortex region reaches 100 thousand neurons/mm3 (Keller et al., 2018). With this very high density of cells, it should be clear that illuminating a brain region with wide-field light, would synchronously activate hundreds of neurons, which in most cases is far from reproducing a physiological activity pattern. As mentioned in the introduction, this has required a transition from whole region optogenetics to more sophisticated illumination approaches capable of controlling on large volume single and multiple neurons independently in space and time with cellular resolution on large brain volumes. The rate and time at which a neuron would fire are crucial for encoding the brain function and transmit information within neuronal circuits. This also requires optimizing the temporal precision (or jitter), which characterizes the reproducibility of the spike time among successive stimulations and the temporal resolution, that is, the minimum time delay between two consecutive APs and two sequential illumination patterns. Finally, the need to access deep brain regions also requires finding solutions to compensate for light scattering.

In summary, the ideal approach for precise optical brain manipulation would require cellular resolution, large (mm^3) excitation volumes, mm or more penetration depth, millisecond temporal resolution, and precision. In this thesis, I have worked on innovative photostimulation approaches for 2P optogenetics to solve these 4 requirements.

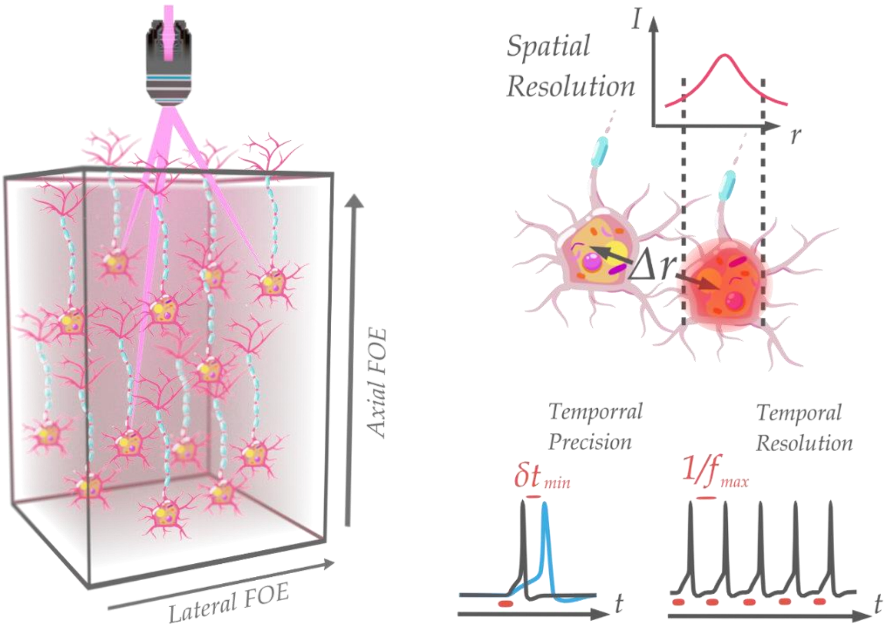

Figure 3: Schematic representation of performance criteria for photo stimulation technique: (a) demonstrate the importance of possessing precise 3D stimulation capabilities to interrogate neurons populations. It also represents the system field of excitation (FOE) or the volume accessible for light delivery. (b) Δr is the minimum distance between two targets at which we can guarantee independent cell activation. (c) representation of two action potential traces obtains ender the same stimulation condition. Despite similar protocols, a time delay δ *t is observed between the spikes. The repeated measurement of this delay among successive stimulations quantifies the spike time's reproducibility or temporal precision (jitter). (d) The temporal resolution represents the minimal achievable time delay between successive APs.* f_{max} *is the maximum firing rate achieved with photostimulation protocol [Adapted from (Ronzitti et al., 2018).]*

Precisely, I have developed three optical schemes: (1) MTF-LS for multi-targets excitation with single cell resolution in three-dimension volume. (2) MTF-Endoscopy for patterned photostimulation of deep brain regions. (3) FliT for fast sequential light patterning.

The thesis is organized into five chapters. (Chapter 2) will introduce the two-photon effect and consider its application for neuronal stimulation in optogenetics. Then we will see in (Chapter 3) the different beam shaping methods used during my Ph.D. (Chapter 4) will describe the temporal focusing effect and how we implement it in optical systems for 3D stimulation. For (Chapter 5) we will discuss the problems related to in-depth stimulation and the solution we develop using microendoscopy. In Chapter 6 the research was focused on the development of a fast simulation method able to write the neuronal activity with short time delays. We also optimize the illumination during the stimulation protocols to significantly increase the number of targets activable with the same power compared to the methods presented in (Chapter 4). Before concluding, we will detail in (Chapter 7) the control software that I have developed during my thesis to control the system shown in (Chapter 6).

Chapter 2: Two-photon excitation and single cell precision

The first challenge in the development of optical methods for brain stimulation was to achieve single cell resolution. In other words, the ability to target a cell precisely without inducing minimal effect on its neighbors. To this end, the transition from a one-photon to a two-photon stimulation method represented a significant evolution. This section will describe the phenomena involved in one and two-photon absorption and its advantages. In the last part, we will present the different approaches using two-photon for photostimulation.

2.1 One and Two photon Microscopy

Fluorescence is a phenomenon of absorption and radiative relaxation of a molecule (or an atom). This phenomenon may be reduced to two steps: first, an electron goes from a ground equilibrium energy level (S0) to an excited one (S1) by absorbing a photon which equivalent energy corresponds to the energy gap between the two states. Secondly, the electron is de-excited by emitting a photon returning to its ground state. Before de-exciting, the atom (or molecules) usually undergoes a vibrational relaxation, losing some of the absorbed energy in the form of vibration. Then the emitted photon is less energetic (a greater wavelength) than the absorbed one. This difference is called the Stokes shift. Typically, the generated fluorescence intensity will be linearly related to the absorbed light intensity ($F \propto I$). If one can find written traces reporting the effect of fluorescence 500 years ago, it is only in 1850 that Ange Gabriel Stokes gave it its name. Thanks to the discovery and study of fluorescent proteins such as Green fluorescent protein (GFP) by Osamu Shimomura, Martin Chalfie, and Roger Tsien, Nobel Prize in Chemistry 2008, a new branch of microscopy emerged, namely fluorescence microscopy.

To fully exploit the potential of fluorescent microscopy for biological study, multiple optical methods have been developed. First, the epi-fluorescence approach, where the whole sample is excited using wide-field illumination. Then the fluorescence light emitted by the sample is collected while blocking the light used for stimulation. However, this approach lacks axial sectioning, meaning that fluorescence is produced all along the stimulation path.

To address this issue, a new method emerged: confocal microscopy. With this approach, a focused excitation spot is scanned over the sample. The generated fluorescence is collected after passing through a micrometer-sized pinhole to reject out of focus light, thus achieving axial confinement.

In 1930, the existence of a two-photon absorption process was theorized by Maria Göppert-Mayer, the second woman to receive the Nobel Prize in Physics in 1963. According to her theory, an atom could reach an excited state by quasi simultaneous absorption of two photons. These two photons may have two different wavelengths, but the sum of their equivalent energies should be equal to the energy gap between the ground and excited state of the molecule. However, to observe such a phenomenon, the two photons must be absorbed in a short time interval of around 10^{-16} seconds (Papagiakoumou et al., 2020). This time corresponds to the lifetime τ_i of a transient state called virtual state reached after the absorption of the first photon. Thus, the probability of observing a 2P absorption may be expressed as: $I^2\delta_{2P}$. Where I is the light intensity and δ_{2P} the 2P cross-section. Since molecular δ_{2P} are typically very small of the order of $10^{-58}\ m^4 s$ (Papagiakoumou et al., 2020; Xu Chris, 2002), two-photon events have a low probability of occurrence. This can be compensated by using large excitation intensities. To reach a sufficient intensity while avoiding the use of continuous laser sources with excessive power, researchers used pulsed laser. In a pulsed laser source, photons are distributed into discrete pulses generated at a given frequency. The peak power of the pulse is magnified compared to the average power over time. The shorter the laser pulse, the greater the concentration of photons in time and thus the higher the peak power relative to the average power. Therefore, using such a laser source allows maintaining low incident power while improving the generation of the two-photon effect (Denk et al., 1990). In addition, the high numerical aperture (NA) objective used in microscopy facilitates the generation of important intensities by playing on the spatial concentration of photon flux. For example, as expressed in (Papagiakoumou et al., 2020), to stimulate GFP molecules optimally, the intensity to deliver would be around $I_0(t) \approx 10^{30} photons/m^2 s$. The power to reach such intensity with a pulsed laser at $900\ nm$, (pulse $\tau\ =\ 100\ fs$, repetition rate of $80\ MHz$), focused to a surface $(A = \lambda 2/\pi\ 2NA)$ with a $0.8\ NA$ objective, corresponds to $\sim 80\ mW$, while using a continuous wave (CW) laser would require a power that is around $\sim 25\ W$.

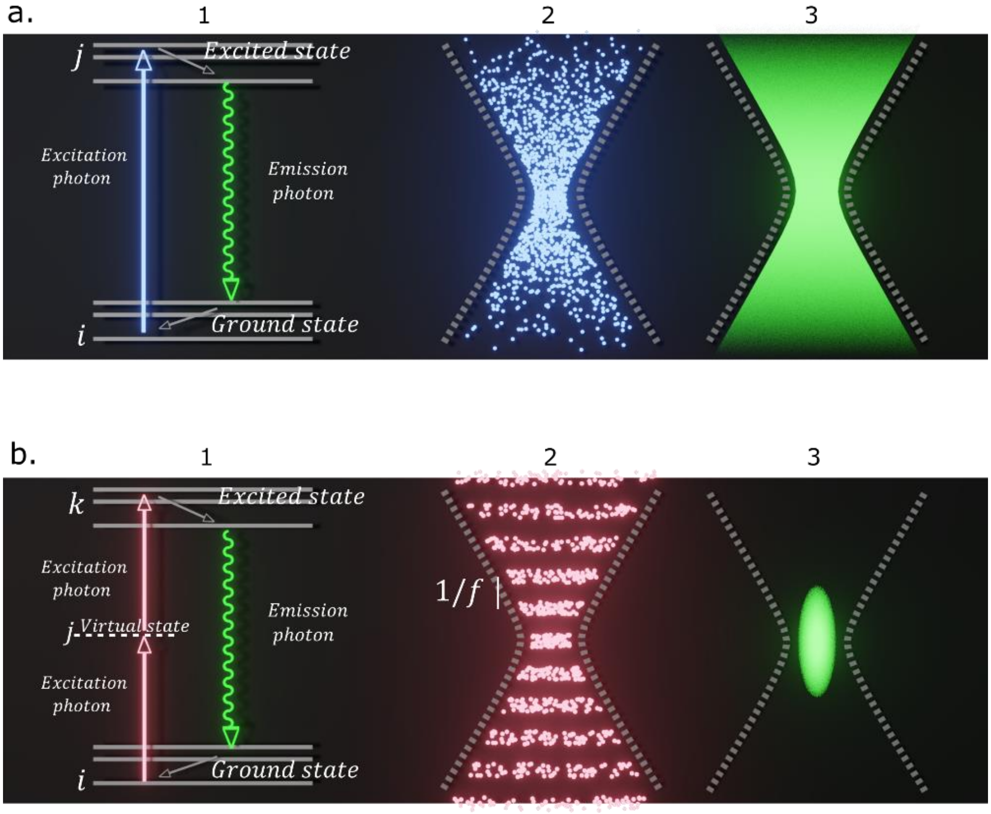

*Figure 4: 1P vs 2P fluorescence microscopy (a1,b1) Jablonski diagrams for 1P and 2P process. (**a2-b2**) are schematic representations of the photon distribution in a focused laser beam for a continuous laser and an impulse laser, respectively (**a3-b3**) Schematic representation of the fluorescence signal confinement or excitation volume obtain with 1P and 2P.*

Using a pulsed laser source with a high-NA objective, the illumination converges to a diffraction-limited spot at the focal plane. As we get closer to the focal point, the photon density increases, with the chance of two photons' absorption. Due to the nonlinear dependence between 2PE and light intensity, the probability of inducing out-of-focus fluorescence decrease quadratically. Thus 2P excitation occurs only close to the center of the focus. This optical sectioning was first introduced by (Denk et al., 1990; Helmchen & Denk, 2005). It is possible to express the 2P fluorescence signals, obtained by an intensity profile varying spatially (focusing) and temporally (laser pulse) $I_0(r, z, t)$by (Papagiakoumou et al., 2020a):

$$\mathrm{s_e(r, z, t)} \propto \frac{1}{\tau\,\mathrm{f}} \mathrm{I_0(r, z, t)^2} \qquad (2.1)$$

Where $r = \sqrt{x^2 + y^2}$, τ is the pulse duration and f the pulse repetition rate. For a Gaussian beam, with beam waists smaller than the objective aperture, the axial resolution obtained at the focal plane of the objective and defined as the full width at half maximum (FWHM) of the fluorescence observed along the optical axis can be written: $\Delta z = 2z_R$ where $z_R = \frac{\pi w_0^2}{\lambda}$ and $\mathrm{w_0} \approx \lambda/2\mathrm{NA}$ is the beam waist at the focal plane ($z = 0$) and z_r is the Rayleigh range of the focused beam.

Besides improving the axial resolution, TPE also reduces photobleaching or degradation of fluorescent proteins because of the reduced out-of-focus excitation. It also improves the penetration into the tissue for the exciting beam as it requires two photons of lower energy and, therefore, of longer excitation wavelength. For the wavelengths typically used for two-photon microscopy in biology, in the infrared range, this enables imaging in vivo animal up to 1.6 mm in-depth with optimized systems (Kobat et al., 2011), compared to the $< 100\ \mu m$ in single-photon excitation (Theer & Denk, 2006), (Chapter 4).

The considerations made here to describe the 1P and 2P absorption by fluorescent molecules also apply to the excitation of photosensitive ion channels and pumps, as we will see in the rest of the thesis.

2.2 Advanced two-photon optical configuration for stimulation

The use of two-photon excitation for optogenetic neuronal stimulation is particularly important to reach single cell resolution in depth. However, reaching efficient 2P optogenetics has required the development of *ad hoc* photostimulation methods for two main reasons.

First, the low single-channel conductance of microbial opsins ($40\ f$s)(Feldbauer et al., 2009). Secondly, the low number of channels recruited under the small illumination volume conventionally used in 2P microscopy. Consequently, in most cases, using a standard 2P excitation volume of few cubic micrometers failed to induce sufficient depolarization to drive APs.

To overcome these difficulties, two complementary strategies have been proposed (Figure 6):

Scanning: It is performed by rapidly scan a 2P diffraction-limited spot over the entire region of interest (ROI), e.g., the cell soma. This approach was first demonstrated in cell cultures then further extend to brain slices and in vivo experiments by (Rickgauer & Tank, 2009) and (Prakash et al., 2012), respectively. With this approach way more opsins are illuminated than in the case of static illumination, but their recruitment is spread over the entire duration of the scan (T_s). To potentially elicited an AP, Ts is chosen lower than the characteristic time τ_{off} of the opsin. Doing so all the opsin recruited during the scan remains open and participle to the depolarization. However, inducing reliable AP with this approach depend on a subtle balance between the stimulation and ospin parameters (Rickgauer and Tank, 2009). Among the scan parameters, we can mention the T_s time which will influence the speed of opsin recruitment and the intensity and scan speed which determines the number of opsins recruited within a given volume of excitation at one point of the scan. For the ospin the parameters like τ_{On} and τ_{OFF} are of primary importance as well as the single channel conductance. In 2012 the use of a new opsin C1V1 with a slow τ_{OFF} $(\sim 60\ ms\ (\text{Mattis et al.}, 2011))$ and a higher current compared to ChR2, allowed efficient photostimulation (AM Packer et al., 2012; Prakash et al., 2012; Yang et al., 2018). Using this opsin (Prakash et al., 2012) demonstrate 10-15 ms temporal resolution (i.e. illumination time to generate an AP) with 20 mW laser intensity from a Ti-Sapphire laser source at 1040 nm. With a low repetition rate laser at 1040 nm (Yang et al., 2018) demonstrates similar temporal resolution (10 to 20 ms)with a diminution of the laser stimulation power(4,5 and 2,25 mW). By drastically increasing the power to 20 mW they could achieve a time resolution of 1ms (Marshel et al., 2019). This represents a clear improvement for scanning methods as long stimulation protocols (tens of milliseconds) are usually subject to low temporal accuracy (jitter = 4.9±3.8 and 1.3±0.9 ms for 20 and 10 ms temporal resolution (Yang et al., 2018)).

Parallel: The illumination spot is designed to cover the ROIs, recruiting in parallel a maximum number of opsins. With this method, the achievable temporal resolution is no longer related to the opsin photocycle and only depends on the stimulation parameters (spot size, intensity, and illumination time). Using an extended light pattern of 10 µm in diameter with a power between 23-40 mW (Papagiakoumou et al., 2010) demonstrate the possibility to trigger action potential with a temporal resolution of 10 ms using light source at 880 nm on ChR2-expressing cells. In the same year (Andrasfalvy et al., 2010) used an over light shaping approach to stimulate ChR2-expressing cells at 880nm with a 4-14 µm spot and demonstrate a temporal resolution of 1-3 ms. Several methods exist to modify the illumination pattern using either an enlarged Gaussian spot (Andrasfalvy et al., 2010; JP Rickgauer et al., 2014) obtained by under-filling the objective back numerical aperture (NA) or more sophisticate methods such as computer-generated holography (CGH)(Bègue, Leshem, et al., 2013; Forli et al., 2018; Papagiakoumou, de Sars, et al., 2008), generalized phase contrast (GPC)(Papagiakoumou et al., 2010). These approaches represent the foundation of this thesis and will be detailed in the next chapter.

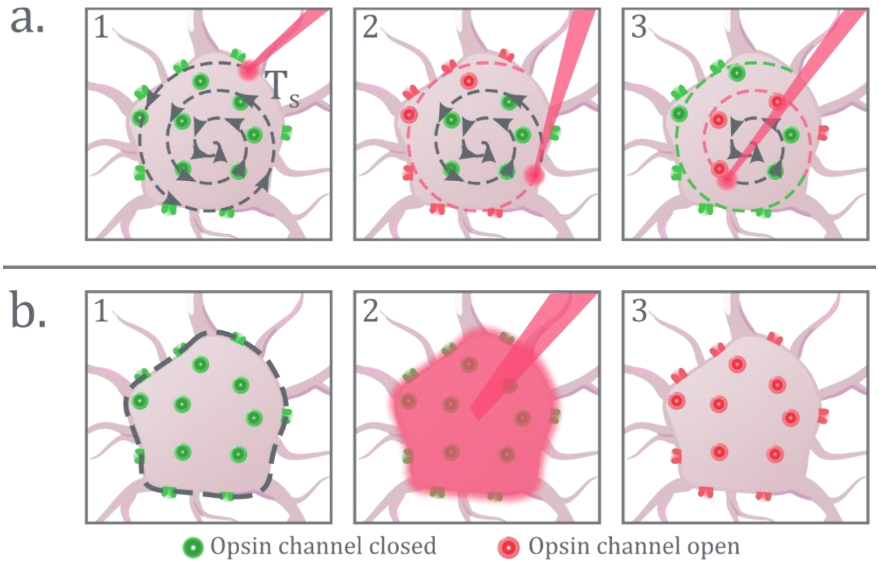

Figure 5: 2P light stimulation approaches targeting opsin-expressing cell. (a) Scanning approach with a total scan time of T_s. (a.2) Represent an intermediary state where part off the cell have already been scanned and opsin recruited. (a.3) In this configuration the time T_s is not inferior to the opsin τ_{OFF}. Therefor some opsin activated at the beginning of the protocol gets closed before the end of the scan. (b) Parallel approach. (b.1) A pattern is designed to match the cell shape. (b.2) the illumination pattern is projected over the target.

For a multi-cell targeting strategy, there are two possible approaches (Figure 6).

Sequential: which passes from one ROI to another using GM. Then, we can stimulate only one cell at a time, but this allows concentrating all the laser power on one target. This solution should be preferred when the laser power is of concern.

Simultaneous: where all ROIs are addressed at the same time. In contrast to the sequential system, the laser power is distributed to each of the targets

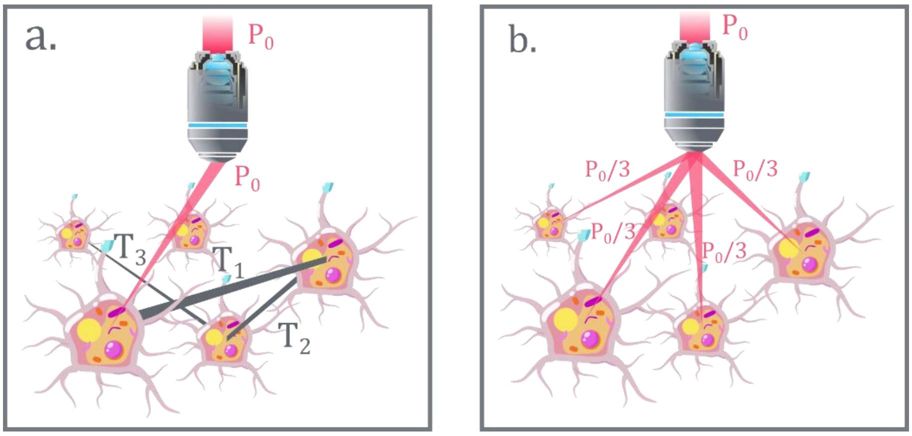

Figure 6: Multi-cell targeting strategy (a) Schematic representation of the sequential photostimulation of a series of neurons. Tn *is the inter-location time necessary to redirect the beam from the* nth *to the* mth *neuron. (b) Simultaneous multi-cell targeting in patterned approaches enabled by simultaneously redistributing an illumination beam of power P0 on three different neurons (P0/3 power per neuron)*

The combination of these different elements gave rise to 4 methods for which we will present the respective total temporal resolution. In over word the total protocol duration to stimulate N targets :

Scanning-Sequential: This approach uses the scanning technique to elicit action potential, with the sequential strategy to target multiple cells. The main advantage of this method is its simple implementation using galvanometric mirrors to perform the membrane scan and move the laser beam from one target to an over as presented in (JP Rickgauer & DW Tank, 2009). In this configuration the total temporal resolution can be express as a function of N the number of targets, l_s the length of the scanning trajectory over the cell, v_s the scan speed and T_{move} the time to switch from one target to the other, thus we obtain $T = \frac{l_s}{v_s} \times N + T_{move} \times (N-1)$ as presented in (Ronzitti et al., 2017).

Parallel-Sequential: Extended illumination pattern is used to illuminate the entire cell soma (JP Rickgauer et al., 2014). Like the precedent technique, the multiple targets are accessed sequentially by moving the pattern from one target to another. The total temporal precision is: $T = T_{dwell} \times N + T_{move} \times (N-1)$. Where T_{dwell} is the illumination time to trigger the response of one cell.

Scanning-Simultaneous: In this approach, diffraction-limited spots are generated over the N cell using an SLM device and simultaneously scanned with galvanometric mirrors to stimulate at once the N cells. (AM Packer et al., 2012; Packer et al., 2014). This approach benefits from a good total temporal resolution compared to the two precedent approaches as all the cells are simultaneously stimulated: $T = \frac{l_s}{v_s}$

Parallel-Simultaneous: These methods take full advantage of SLMs capacity by generating light patterns covering the entire ROIs of the different targets at the same time. (Bègue, Papagiakoumou, et al., 2013; Papagiakoumou et al., 2010, 2013) Thus the total temporal precision is: $T = T_{dwell}$

In the next part of this manuscript, we will focus on Parallel-Simultaneous methods by describing the different beam shaping techniques used and developed during this project.

Chapter 3: Beam Shaping

3.1 Holography

Seeking to improve the resolution in electronic microscopy, Denis Gabor, in 1948, developed holography. This revolutionary imaging technique used a plate medium to reconstruct the image in 3 dimensions of an object (Gabor, 1948). Two stages procedures are required:

First step: A monochromatic and coherent light source is divided into two beams, one called reference wave and a second called illumination wave used to illuminate the object of interest. Therefore, that object diffuses the light (object beam), which interferes with the reference beam. The resulting interference patterns is printed on the photographic plate. The image obtained after developing the plate is called the hologram. It contains both the information on the phase and amplitude distortion produced by the object on the reference wave. Indeed, the intensity at each point of the interference pattern depends on the phase difference between the reference and the object waves and its amplitude.

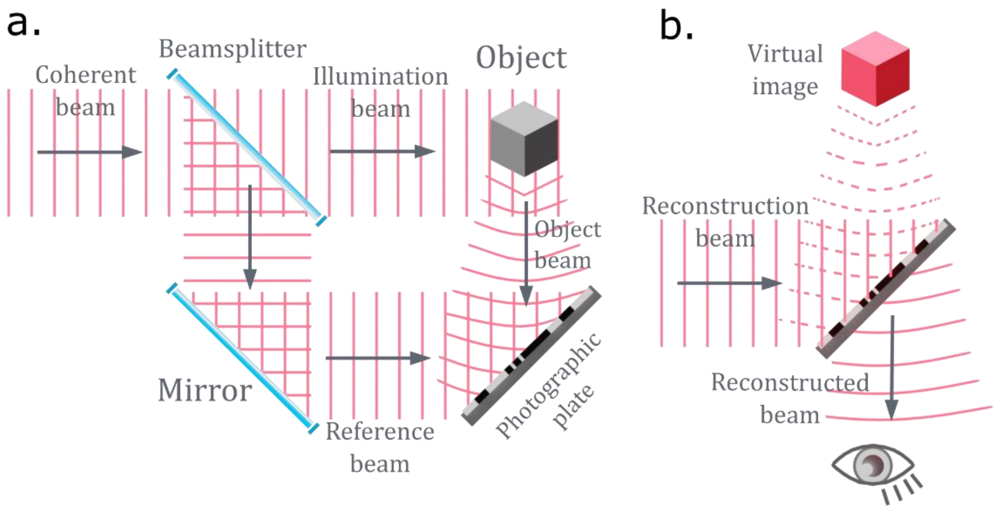

Figure 7: Schematic representation of Gabor holography (a) hologram generation process by recording the interference pattern between the coherent reference beam and object beam diffuse by the object on a photographic plate. (b) Holographic image reconstruction: Once illuminated by a coherent light source the plate diffracts part of the light in a correct order (reconstructed beam), generating the illusion of an object for the observer.

Second step: Secondly, the hologram is illuminated with the reference wave, diffracting the light in different orders. One order corresponds to the non-diffracted light. The main order to consider, the reconstructed beam (Figure 7) allows in the far-field or after a lens to obtain a virtual 3D image of the object.

To date, holography is a very rich field that encounters a broad range of disciplines from physique to chemistry and even art. But the technique first remained relatively unnoticed from the necessity to use a monochromatic and coherent light source. Therefore, the real breakthrough for the technology came with the invention of the laser in 1960, which provided a suitable light source to exploit the potential of holography fully. After the emergence of lasers, the development of computer science and microelectronics greatly broadened the possible applications of holography. High-resolution CCD and CMOS cameras allowed the digitization of holograms to replace the photographic plate. The exponential increase in computing power allowed the direct reconstruction of phase and intensity of the complex wavefront (Lohmann & Paris, 1967). Finally, the development of spatial light modulators (SLM) enabled the dynamic generation of holograms digitally stored or computer generated (Osten, 2006). This new domain is called computed generated holography CGH.

3.2 Computer Generated Holography

CGH is a sophisticated method to shape the laser light dynamically into arbitrary 3D patterns in the imaging volume. This new approach empowers the use of holography, broadening its application from video projection (Georgiou et al., 2008) to generate holographic optical tweezers (Curtis et al., 2002). It later became an essential tool in neuroscience thanks to its capability of precisely target different cells, used to image, and especially photo stimulate opsin expressing neurons, either in 1P (Lutz et al., 2008a) or 2P (Papagiakoumou, de Sars, et al., 2008; v Nikolenko et al., 2008).

In CGH, the hologram is calculated and displayed on a spatial light modulator to modulate the beam at the lens's back focal plane (BFP) (i.e., the Fourier plane). Once propagated through the lens to the front focal plane (FFP) (i.e., at the sample plane), the light interferes accordingly to the modulation introduced by the SLM and forms the desired pattern. In theory, the amplitude and phase need to be modulated to get an image similar to the one performed by conventional holography. Although independent control over these two parameters may be achieved with SLMs, it is rarely used, as amplitude modulation masks the undesired light to obtain the shape, causing substantial power loss. With respect to amplitude modulation approaches, phase holography based on liquid crystals SLMs (LC-SLMs), enables better light efficiency by redirecting light at the sample plane.

Experimentally, CGH uses an iterative algorithm, the Gerchberg-Saxton (GS) (Gerchberg & Saxton, 1972) to compute, given an illumination profile (often Gaussian) and a target pattern, the corresponding phase hologram. The latter is addressed to a LC-SLM to impose the phase modulation onto the input beam's wavefront and obtain the target pattern in the far-field or after a lens.

However, the limitation to phase modulation directly impacts the image restitution, leading to light distribution fluctuation called intensity speckles. They arise principally from the approximation in the iterative algorithm (since the problem of obtaining a desired intensity pattern in the Fourier plane by using only phase modulation does not have an exact solution, the output intensity is optimized by leaving a random phase distribution at the focal plane) and from the crosstalk of adjacent pixels of the LC-SLM (E Ronzitti et al., 2012a).

Regarding the algorithms and optical setup used, several types of light patterns can be created in the imaging space, ranging from 2D or 3D diffraction limited spots, or more complex patterns that selectively match the samples' spatial features.

In the rest of this section, we will study the two essential components that govern the achievable performance of this method: the LC-SLM and algorithms used.

3.2.1 Liquid Crystal on Silicon Spatial Light Modulators

The term SLM refers to all devices capable of dynamically modulating the amplitude and/or phase of light. Among them, we can find Magneto-Optic Spatial Light Modulators, Digital Micromirror Devices (Martial & Hartell, 2012; Zheng et al., 2009), Deformable Mirrors, Acousto-optic Bragg cells (Gupta & Ballato, 2007; Saleh & Teich, 2019).

We will focus our attention on the Liquid Crystal on Silicon (LCoS) Spatial Light Modulators used during this work to display phase-only holograms.

Liquid Crystal:

The liquid crystals (LC) that constitute the pixels in LC-SLM are rod-like molecules. Thanks to two essential characteristics, these molecules can dynamically modulate the amplitude, phase and polarization of light. The name liquid crystal well depicts the first main property of this molecule, their mesophase state. This state reflects their ambivalence between the isotropic liquid and crystalline solid-state, offering the possibility to influence the molecule's spatial orientation. From their crystalline ascendancy, LC inherits birefringent properties. In other words, their refractive index is different for the long and short axes. The light propagation speed through the LC crystals changes according to polarization and crystals orientation. By fixing the illumination beam polarization (LC-SLM work for a precise polarization) and controlling the orientation of the LC, we can modulate the light propagation speed and, therefore its output phase. As the dielectric constant of the LC molecules is usually larger along the long axis this leads to a permanent electric dipole. Consequently, it is electrically possible to control the direction of the LCs and thus the phase shift introduced.

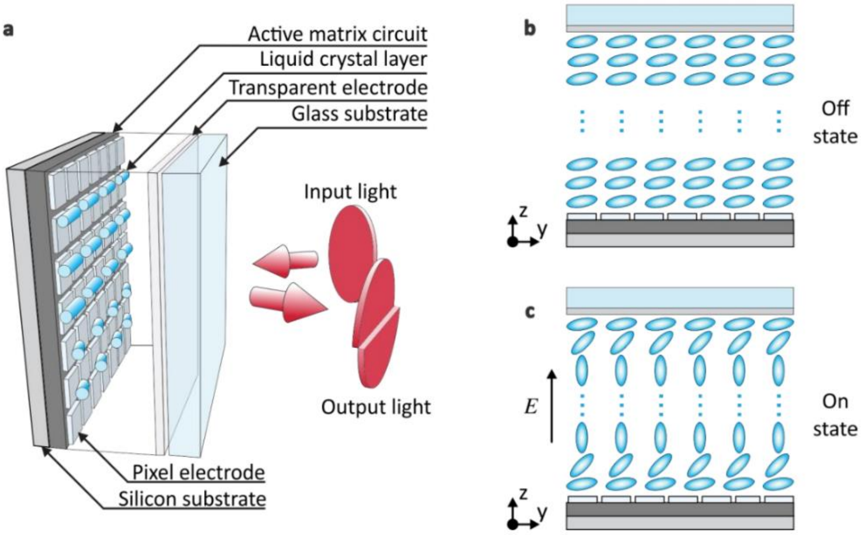

Figure 8: Spatial Light Modulator composition and mechanism. (a) phase modulation of incoming light by the liquid crystal on silicon SLM [adapted from Hamamatsu Photonics K.K., "Opto-semiconductor Handbook" Editorial Committee] (b) Off-state: no current is applied to the electrodes, inducing parallel alignment of the rod-like liquid crystal molecules (c) On-state: the current changes the rod orientations, inducing perpendicular alignment of the liquid crystal molecules to the electrodes [adapted from Z.Zhang et al. 2014]

Design and parameters:

LC-SLM comprises a first layer of electronic circuit printed on a silicon substrate, in contact with an electrode array. Each element of the array is independently controlled with a specific electrical potential. Depending on the desired reflection, the matrix is covered with either an aluminum-coated or a dielectric mirror whose reflection efficiency determines the maximum intensity reflected by the SLM screen. Afterward, the LC are capped with a second transparent electrode layer to close the electric circuit. Finally, a glass substrate protects the display. With this configuration, the electric field across the liquid crystal layer can be controlled pixel by pixel to impose a precise phase shift. It is possible to express the phase shift as a function of an equivalent optical index n(x) reflecting the LC orientation for a given electrical courant :

$$\delta\phi = \frac{\lambda n(x) l}{2\pi} \qquad (3.1)$$

In this way, LC-SLM can modulate the incoming wavefront and act like a diffractive optical element. The generated phase profiles are often created to induce interference patterns in the far-field or, in practice, at the focal plane of a lens. We can mathematically link the FFP (output pattern) and the BFP (SLM screen) plan based on diffractive optics laws by a Fourier transformation.

$$E_{pattern}(u,v) \ = F\,\{E_{hologram}\,(x,y)\} \quad (3.2)$$

As a dynamic hologram display, the LC-SLM characteristics play an essential role in the achievable holographic performances, such as pattern restitution quality and reconfiguration speed (the speed at which two successive holograms can be displayed on the SLM) and the light shaping efficiency. In the next part, we will discuss the influence of the different LC-SLM parameters when used in microscopy.

3.2.2 Holographic set-up and performance

SLM Aperture filling and resolution:

Usually, LCOS-SLM are rectangular in shape with a surface of roughly one centimeter square. These dimensions can be expressed as the product of pixel pitch d_{slm} (similar for x and y direction as the pixels are squares) and pixel numbers N_{slm} (different for x or y direction in case of rectangular screen):

$$\mathrm{L} = N_{slm} \times d_{slm} \quad (3.3)$$

In contrast, the laser illumination beam has circular symmetry and therefore cannot be perfectly matched to the SLM screen leading to an evident issue for SLM illumination. Two possible solutions exist: One consists in enlarging the laser beam to cover the entire SLM at the expense of illumination efficiency as part of the beam will extend outside the surface of the SLM. The other is to limit the size of the beam to the smallest dimension of the screen. This will have the opposite effect, optimization of the intensity but a loss of usable pixels.

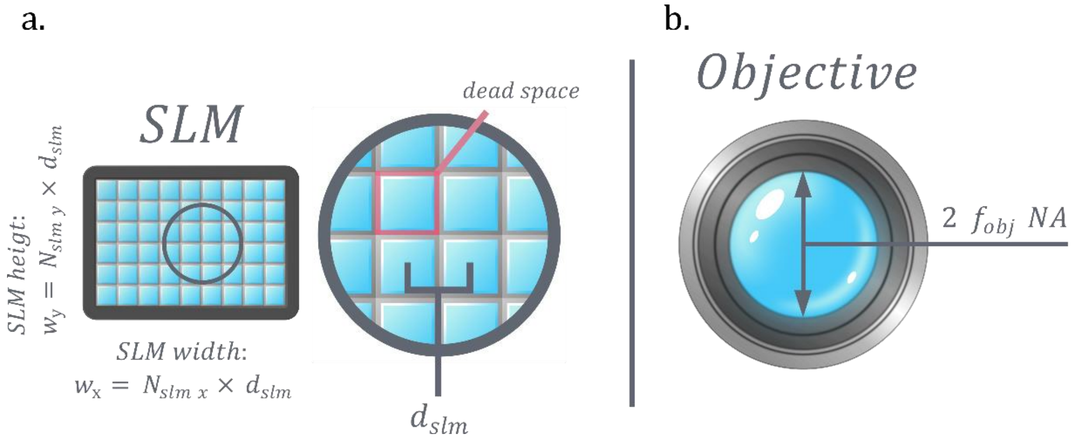

Figure 9: Schematic representation of the SLM parameters and objective aperture. (a)SLM screen representation traducing is discretized nature. d_{slm} is the distance separating the center of two adjacent pixels. We can express the width and height of the SLM as a function of their respective pixel number and d_{slm}. The dead space corresponds to a gap between two pixels where the light is not modulated. (b) represents the objective back aperture and the expression of its diameter as a function of the parameters of the objective.

Theoretically, the easiest way to implement a LC-SLM in microscopy would be to place it at the objective BFP. Unfortunately, this conformation is impossible as most LC-SLMs work in reflection and are too bulky to be placed at the objective BFP. The simplest solution is to add a telescope (L1, L2) in a 4f configuration to image the plane of the SLM on the objective BFP. Typically, the focal lengths of lenses L1 and L2 are chosen, so the minor axis of the SLM, (L) corresponds to the pupil diameter (D) of the microscope objective. We can express this condition as in the paper of (Golan et al., 2009):

$$m_{tel}L = D = 2\ f_{obj}\ NA \qquad (3.4)$$

$$\text{Where: } m_{tel} = \frac{f_{L2}}{f_{L1}}$$

Where f_o is the objective focal length and NA the objective numerical aperture.

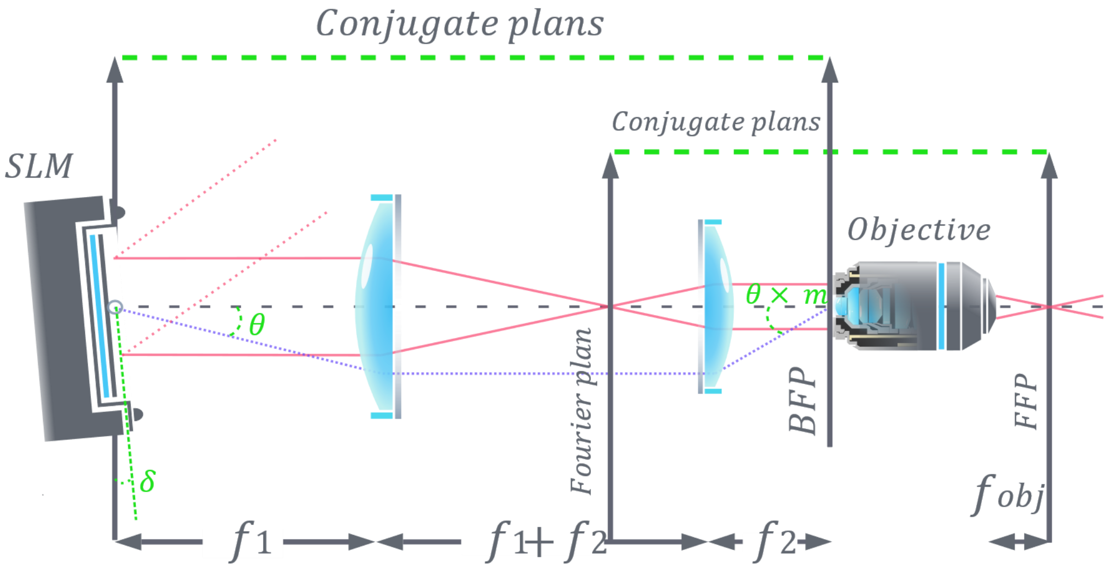

Figure 10: Schematic representation of the most straightforward optical system for CGH application in microscopy using LCOS-SLM. The two lenses F1 and F2 are place in a 4f configuration to image and demagnify the SLM screen at the objective BFP. The blue dotted line represents a θ deflection realized by the SLM for potential displacement at the objective image plane. We can see the effect of the 4f demagnification on the angle obtained at the BFP and therefore on the final displacement after the objective.

In this way, one makes the best use of the NA of the objective and obtains optimal resolution. Precisely, the lateral resolution is given by the diffraction limit and expressed by Abbe equation:

$$PSF_{x,y} = \frac{\lambda}{2NA} \quad (3.5)$$

And the axial resolution is expressed as:

$$PSF_z = \frac{2n\lambda}{NA^2} \quad (3.6)$$

Where λ is the wavelength used and n the immersion medium refractive index after the objective.

In this configuration, the image of the SLM screen is cropped by the objective pupil leading to unused SLM pixels (Figure 11.(a)).

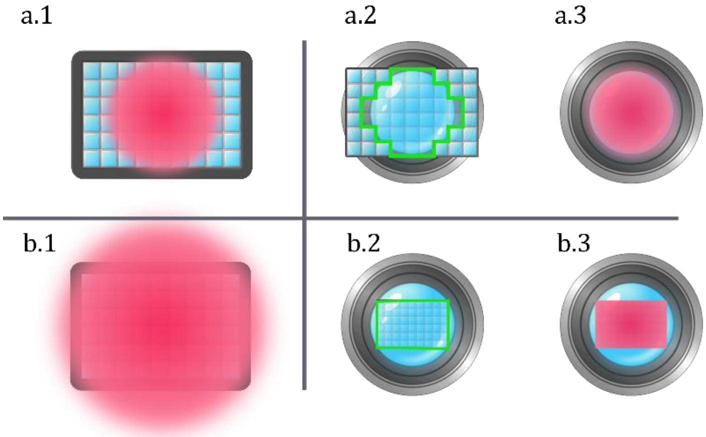

Figure 11: Representation of the two possible configurations for SLM illumination and projection at the BA. (a.1, b.1) Corresponds to the illumination of the SLM. (a.2, b.2) Show the demagnified image of the SLM screen at the BA. The green line delimits the usable pixels after the projection. (a.3, b.3) The illumination at the objective BA.

SLM pixels and Field-of-view:

The field of view represents the volume of the sample in which the light can be patterned. It is characterized by the maximal lateral and axial displacement achievable and is directly related to the SLM screen and objective specification. The maximum deflection angle θ, that the SLM can achieve is related to the maximum spatial period of the grating according to the following equation:

$$m\lambda = \Lambda\, sin(\theta) \quad (3.7)$$

Where m is the diffraction order, λ the wavelength, Λ the spatial period of the grating, and θ the angle of deflection (Figure 13). Reproducing the theoretical phase ramp profile of a blazed grating would require a continuous phase profile which is not compatible with the pixelated structure of the LC-SLM. This effect can be mathematically described thanks to the Dirac and boxcar function as presented in (Figure 12)

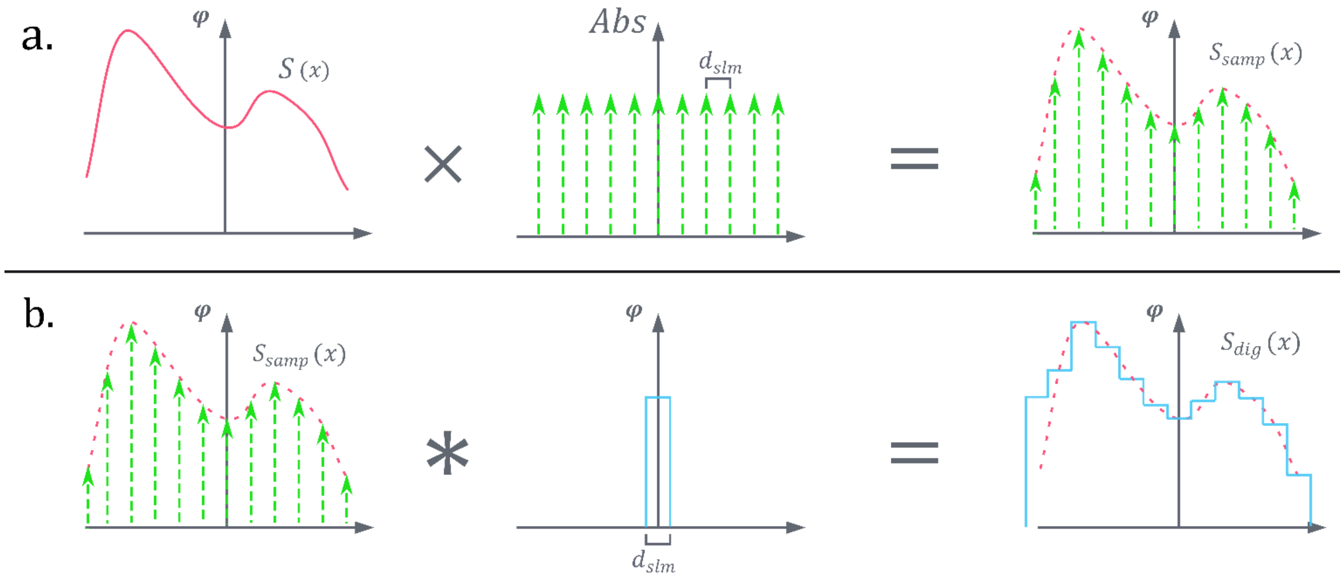

Figure 12: Mathematical expression for the Spatial digitalization of the desired phase signal due to the finite size and number of the SLM pixels. (a) We use a Dirac distribution to represent the spatial repartition of the pixel. The distance between two pikes corresponds to the SLM pixel pitch (d_{slm}). By multiplying the desired phase profile S(x) with the Dirac distribution, we obtain a sampled signal traducing the finite nature of the SLM screen. (b)We can represent the finite pixel dimension with a gate function of height equal to 1 and width equal to d_{slm} and translate its effect over the signal $S_{samp}(x)$ with a convolution.

Given these constraints, the best approximation of a blazed grating is a multi-level or stepped phase function (Figure 13). Therefore, the spatial period Λ of the grating becomes: $\Lambda = \mathrm{N_{pixel}} d_{slm}$ where $\mathrm{N_{pixel}}$ represent the number of pixels used to approximate one grating period. In this condition, a two-pixel $\Lambda = 2\ d_{slm}$ represent the minimal accessible period for an SLM (Nyquist limit).

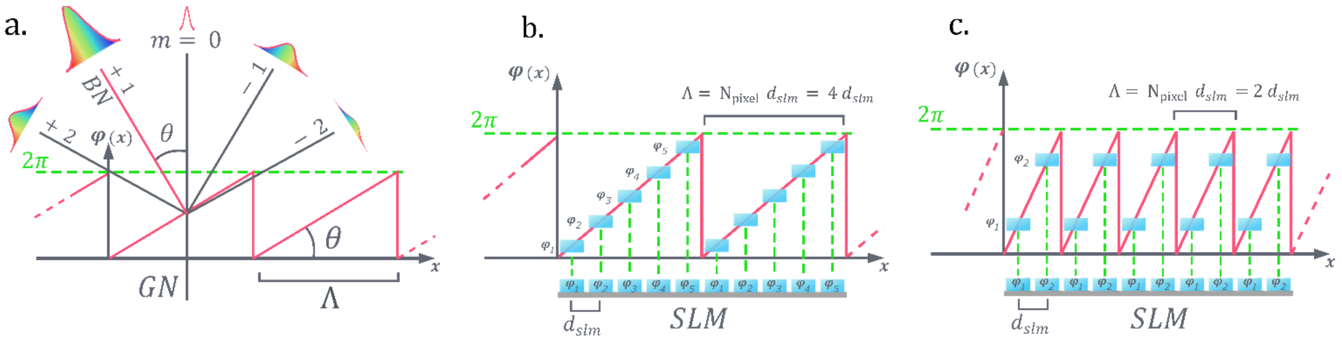

Figure 13: The link between a conventional blazed grating and a stepped phase function. (a) show the reflection of an incident monochromatic beam arriving perpendicular to the grating (parallel to the normal grating GN). Most of the light intensity is redirected to the +1 order while the remaining power is spread over different orders. For itches order, the spectrum is dispersed around the central wavelength of the light source. θ is the blaze angle and Λ the grating period. (b,c) Show the effect of fitting the phase profile of a blazer grating using a discretize SLM screen. The phase profile obtained with the SLM is a stepped phase function where each phase step corresponds to a pixel. The number of pixels used to fit a grating phase period (the number of levels of the stepped phase) depends on the grating period and SLM pixel size. For a constant d_{slm} the number of pixels used for to fit the signal decreases with the period. (c) Correspond to the minimal achievable period for a stepped grating phase function with only two pixels per period also called the Nyquist limit.

If we consider the first order m = 1 and apply the small-angle approximation $sin(\theta) \sim \theta$ to the equation (3.7), we can link the maximum deflection angle to the pixel size of the SLM:

$$\theta_{max} = \frac{\lambda}{2d_{slm}} \qquad (3.8)$$

This maximum angle is expressed in a lateral shift at the sample plane by considering the first L_1 focal and the(L_2, objective lens) telescope magnification. We obtain:

$$\Delta x_{max} = \frac{\lambda}{2d_{slm}} \times \frac{f_{obj}}{m_{tel}} \quad (3.9)$$

Wich defines the field of view (FOV) size at the objective focal plane as:

$$FOE = 2 \times \Delta x_{max} = 2 \times \Delta y_{max} \quad (3.10)$$

Therefore, the maximum displacement at the sample plane depends on the imaged pixel size at the objective back aperture (BA).

It is possible to increase the size of FOV by using SLMs with small pixels and/or by acting on the telescope's magnification (L1, L2). Nevertheless, if we look more closely, any decrease in pixels size for an SLM while keeping the same number of pixels will correspond to a smaller SLM matrix. Therefore, to respect the BA filling condition, the telescope's magnification, m_{tel}, must be changed to have the imaged SLM matrix matching the BA. Consequently, we obtain no gain in FOV. Otherwise, one can keep the same m_{tel} thus the imaged pixel size at BA is smaller, leading to a larger FOV. However, this corresponds to a loss of axial resolution due to the underfilling of the BA.

To traduce this tradeoff between FOV and resolution, we need to consider the condition mentioned above: fill the objective BA. As already said, respecting this condition is essential to achieve the best resolution ($PSF_{x,y}$). In fact, by applying the equation (3.3) and (3.4), we can translate this condition over the equation (3.9). First we can replace L in equation (3.4) describing the BA filling condition using (3.3) we obtain :

$$m_{tel} N_{slm} d_{slm} = 2 f_{obj} NA$$

Then we can define :

$$d_{slm} = \frac{2 f_{obj} NA}{m_{tel} N_{slm}}$$

By inserting this expression in equation (3.9)

$$\Delta x_{max} = \frac{\lambda \, \mathrm{N_{slm}}}{4\, NA} = \frac{1}{2}\, PSF_x \, N_{slm} \quad (3.11)$$

A similar relationship can be established for axial displacement. The desired effect is obtained with a lens effect of equivalent focal length f. In this case, the equal diffractive element is called a Fresnel flat phase (FFP) and/or Kinoform. This phase profile reproduces the so-called Fresnel lens, a famous optical component used in lighthouses. They consist of concentric annulus (zone), each with equivalent area and address with variable period grating (Figure 13).

As expressed for the lateral FOV size, the two-pixel period is the minimal achievable one for a SLM. In other words, the feasible boundary lens is the one whose border zone respects $\Lambda = 2\, d_{slm}$ and radius r_p exploits the whole SLM. Then we have $r_p = d_{slm} \frac{N_{slm}}{2}$ where N_{slm} is the number of pixels in the direction of the smallest SLM there for it is possible to write:

$$f_{max} = d_{slm}^2 \frac{N_{slm}}{\lambda} \qquad (3.12)$$

By translating f_{max} in axial displacement regarding the optical system, we obtain:

$$\Delta z_{max} \simeq \frac{n\lambda\, f_{obj}}{2\, d_{slm}\, m_{tel}\, NA} \quad (3.13)$$

As for lateral displacement, we can apply the BA filling condition and obtain:

$$\Delta z_{max} \simeq \frac{1}{8}\, PSF_z\, N_{slm} \qquad (3.14)$$

Thus, a relationship like the lateral FOV between resolution, number of pixels, and maximal displacement is set.

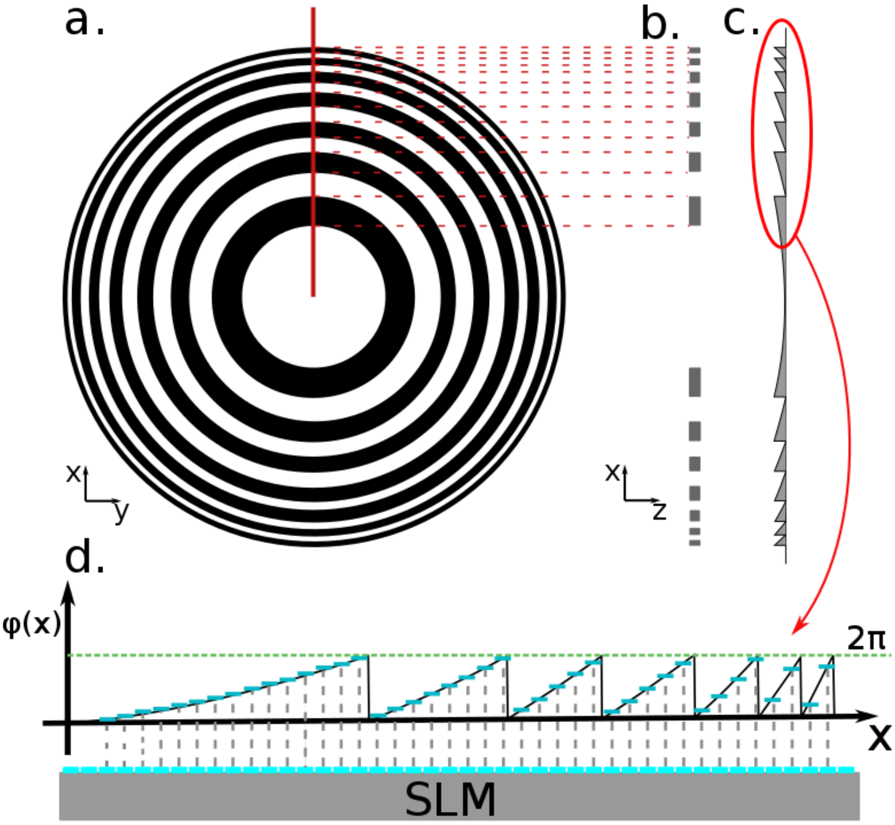

Figure 14: Schematic diagram showing the effect of the SLM digitalization. (a) Schematic representation of a Fresnel zone plate (FZP) seen from the front. (b) Projection and lateral section of an FZP. (c) Application of the analogy between an FZP and a variable pitch circular diffraction grating (d) Application of a variable pitch circular diffraction grating phase profile on an LC-SLM, highlighting the effect of the digitization.

Diffraction efficiency:

As introduced previously, the displacement in a plane is governed by the grating equation. We have studied the extreme case of the strongest displacement obtained for the smallest feasible period of two pixels. For intermediate displacements, the necessary period is thus larger and uses more pixels to fit the phase ramp. It is possible to link the number of used pixels N to the displacement x by:

$$N = \frac{\lambda}{d_{slm}} \times \frac{f_{obj}}{m_{tel}} \times x \qquad (3.15)$$

As any element based on diffraction, this grating generates different diffraction orders. If we define the diffraction efficiency as the light intensity diffracted in an order m, in the case of a discretized grating, we can express it in function of the number of pixels used per period N as follows:

$$\eta_m = \left(\frac{\sin\left(\pi\left(\frac{m}{N}\right)\right)}{\pi\left(\frac{m}{N}\right)}\right)^2 \qquad (3.16)$$

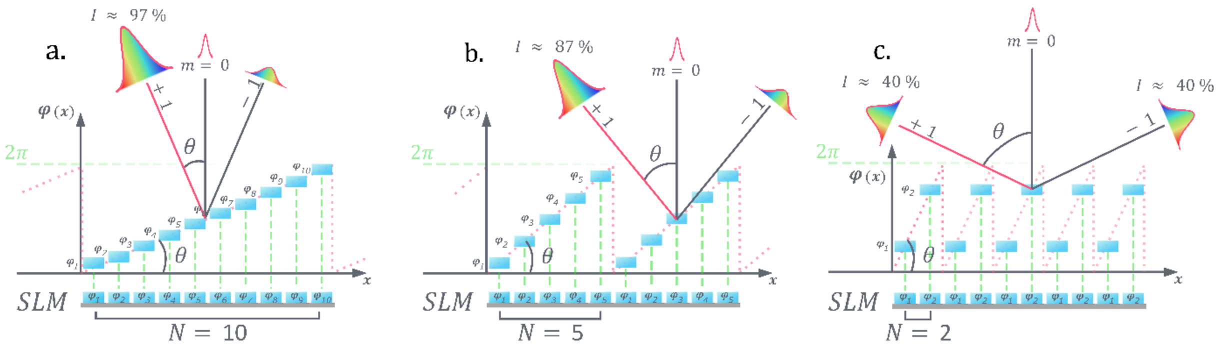

Figure 15: The diffraction efficiency for stepped grating phase function. From (a) to (c), the period is reduced, increasing the first-order diffraction angle (θ), in return the number of steps (pixel) by period drops, reducing the diffraction efficiency of the grating function.

By combining the last equation with the (3.14) and considering the m=1 order, it is possible to link the axial displacement and the diffraction efficiency in one equation:

$$\delta(x,y) = \mathrm{sinc}^2\left(\frac{\mathrm{d_{slm}}\, m_{tel}}{\lambda\, \mathrm{f_{obj}}} x\right) \mathrm{sinc}^2\left(\frac{\mathrm{d_{slm}}\, m_{tel}}{\lambda\, \mathrm{f_{obj}}} y\right) \quad (3.17)$$

Which can also be stated as:

$$\delta(x,y) = \mathrm{sinc}^2\left(\frac{x}{\mathrm{PSF_x}\, N_{slm}}\right) \mathrm{sinc}^2\left(\frac{y}{\mathrm{PSF_y}\, N_{slm}}\right) \quad (3.18)$$

A similar relationship may be determined for the Z-axis as found in Golan et al. 2009.

This equation links a spot displacement from the center of the FOV to the energy loss due to the diffraction efficiency. Indeed, a higher spot deflection requires a grating with a smaller period; consequently, the number of pixels recruited to fit the period phase ramp (N) is reduced (Figure 15). This N reduction impacts the diffraction efficiency resulting in higher energy loss at the sample. In the end, this mechanism leads to a non-uniform optical power density over the FOV.

To generate uniform illumination patterns in the entire FOV, it is essential to counterbalance this effect. Thereby, it is necessary to compensate the position dependence of the diffraction efficiency and guarantee a constant light illumination in the entire excitation volume.

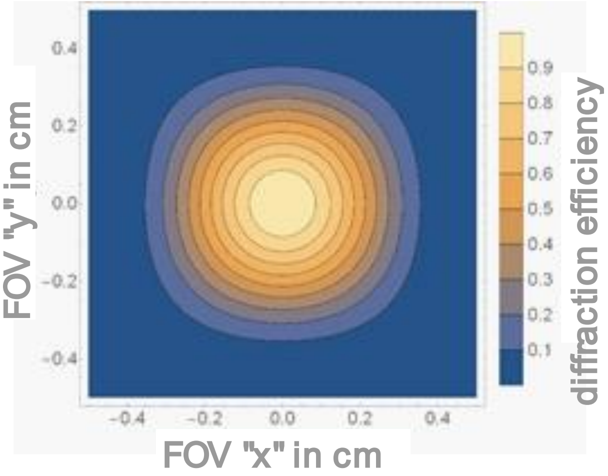

Figure 16: Graphical representation of the diffraction efficiency obtained with equation (3.17). The parameters of the system used are $f_{obj} = 4.5\,mm$ (correspond to an Olympus 40X) $f_1 = 1000\,mm, f_2 = 500\,mm, \lambda = 1040\,nm$ and $d_{slm} = 12.5\,\mu m$

For this, the illumination distribution is controlled with the algorithm used to generate the hologram. To this end, each position in the FOV is associated with a value of diffraction efficiency, based on the equation (3.17). To obtain a homogeneous illumination, we need to distribute the initial laser intensity according to the point's coordinates and their corresponding light loss. Let us take the simple case of two points with respectively δ_1 and δ_2 efficiency. Without instruction, the initial intensity will be distributed equitably between the two points: $\frac{I_{tot}}{2} = I_1 = I_2$. Then at the sample, the intensity for each point is:

$$I_{end1} = I_1\delta_1 \;\; et \;\; I_{end2} = I_2\delta_2 \quad (3.19)$$

To obtain a homogeneous illumination, it must be verified:

$$I_1\delta_1 = I_2\delta_2 \quad (3.20)$$

So $I_1 \neq I_2$. Then we can write the correction:

$$I_1 = I_2\frac{\delta_2}{\delta_1} \quad (3.21)$$

An example of this correction has been shown using diffraction-limited spots (Golan et al., 2009) or arbitrary holographic patterns (Golan et al., 2009; Hernandez et al., 2016).

Zero-Order

The use of LC-SLM generates a "zero-order ", corresponding to non-modulated light by the LC. It appears as an undesired intensity pattern at the centre of the image plane (Figure 177). It may have several origins linked to the LC-SLMs properties.

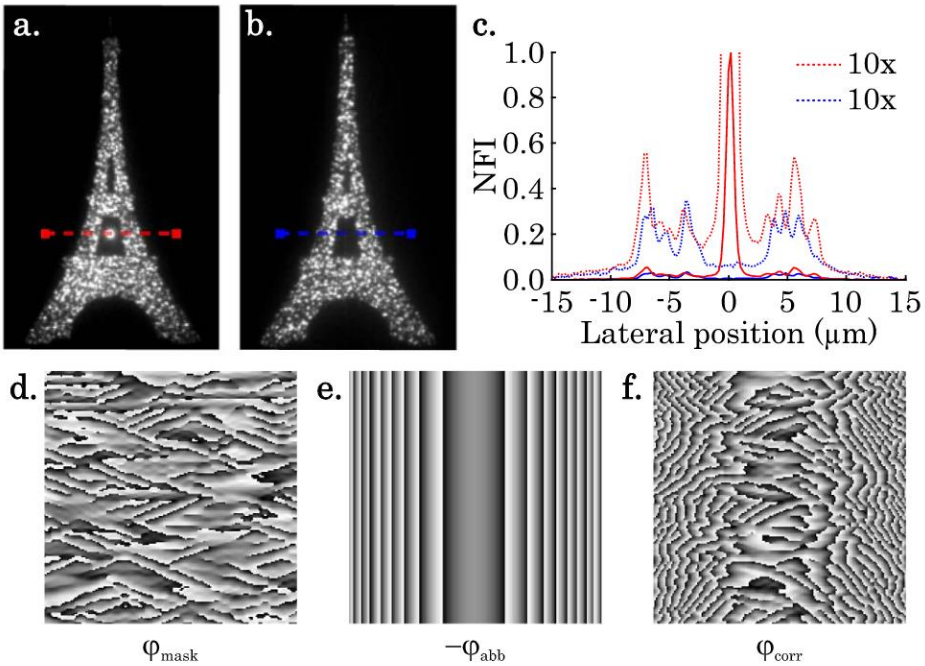

Figure 17: Zero-order correction (a-b) 2P fluorescence image (a) we can observe a bright spot in the middle of the Eiffel tower corresponding to the zero-order (b) a 1 m cylindrical lens is placed in front of the SLM. The Eiffel tower pattern is preserved by counterbalancing the aberrations of the lens with the SLM (c) is the normalized Axial profile for the red and blue lines in (a) and (b). Dotted curves correspond to the same signal

multiplied by 10 for better visualization (d) phase mask projected by the SLM to generate the Eiffel tower pattern observed in (a). (e) cylindrical lens phase hologram for aberration compensation. (f) Phase combining (d) and (e). Once addressed to the SLM, we obtain the image of the Eiffel tower without the zero-order. [image adapted from (Hernandez et al., 2014)]

First, the filling factor of the SLM , which is related to the empty space between the pixels, reflecting non-modulated light. However, modern SLM, have a large filling factor with only 10 to 5 % dead space.

Second, the liquid crystal display's protective glass is usually made to operate with a broad wavelength spectrum, requiring an average reflectivity of 80%.

Third, the complexity of the phase profile. It may contain important phase variations (hight frequency) the SLM cannot resolve (above the Nyquist limit). This low sampling of the phase profile leads to the generation of low frequency or aliasing effect, reducing the overall diffraction efficiency of the phase pattern, increasing the light lost in the zero-order. (E Ronzitti et al., 2012b; Persson et al., 2012)

The most straightforward method to get rid of the zero-order is to block it physically. This is performed by placing a beam blocker in an intermediate image plane where the zero-order is observed. However, it also block any over light resulting in a dead zone where it is impossible to generate spots.

Another suitable solution for 2PE experiments consists in spreading the zero-order spot over a large area to take advantage of the non-linearity of the 2P effect as presented in (Figure 17). During this work, we used the approach proposed by (Hernandez et al., 2014). Placing a cylindrical lens in front of the SLM screen generates optical aberrations in the excitation beam. Then, we can introduce a cylindrical lens hologram in the SLM phase with a suitable focal to compensate for the aberrations previously introduced. Doing saw all the light modulated by the SLM will correctly generate the desired pattern at the sample thanks to the correction. The zero-order corresponds to non-modulated light, is not affected by the SLM correction phase and remains subject to aberration.

3.2.3 Phase-hologram calculation algorithms

This paragraph will review the algorithms used in this thesis to generate a distribution of discrete spot or a continuous shape using CGH: the grating and lenses and the Gerchberg and Saxton algorithms, respectively.

Gratings and lenses (GL):

Taking a single holographic spot, a constant phase at the SLM will leave the spot unchanged at the focal point of the objective. On the other hand, a grating phase at the SLM will induce a lateral displacement of the spot and a parabolic phase (lens) an axial displacement, as introduced in the previous section. By discretizing the desired pattern, we can express it as 3D distribution of points, each associated with corresponding prism and lens phases. The electric field for each focal spot at a specific position (x_0, y_0, z_0) will then be expressed at the SLM as:

$$E_{slm}(x,y) = exp\left(i\phi_{grating}(u,v) + i\phi_{lens}(z)\right) \quad (3.22)$$

For the superposition of N focal points in 3D, the total phase at the SLM plane is expressed as:

$$\phi_{slm}(x,y) = arg\left[\sum_{n=1}^{N} exp\left(i\phi_{grating}(u_n,v_n) + i\phi_{lens}(z_n)\right)\right] \quad (3.23)$$

This type of algorithm necessitates few operations steps compared to the iterative algorithm like the Gerchberg Saxton, offering reduced calculation time. For applications requiring fast sequential patterning, a compromise must be found between calculation time and pattern's quality. Which is given by the generated intensity distribution homogeneity (even more important in the case of 2P stimulation where the effect is related to the square of the intensity) and diffraction efficiency (loss of light intensity for the obtained pattern).

If the GL achieves a good intensity distribution and diffraction efficiency whenever asymmetric patterns are required, it is not the case for high symmetry one (Curtis et al., 2005b). In this last condition, the degradation comes from the prevalence of the ghost spots (undesired replicas of the target spots due to imperfect modulation of the SLM, especially the higher diffraction orders of the phase profiles) (Bowman et al., 2011; Hermerschmidt et al., 2011). In comparison, iterative algorithms can better perform in high symmetry conditions.

Solution has been studied to remove ghost spots and obtain good uniformity over the desired patterns by applying the random mask-encoding algorithm (di Leonardo et al., 2007). It extends the gratings and lenses approach by adding an arbitrary phase shift for each point (Curtis et al., 2005a). Then, it is possible to optimize the initially randomly introduced value iteratively. As a counterpart, the efficiency is reduced, and the calculation time is extended.

The Gerchber and Saxton algorithm:

The Gerchberg and Saxton algorithm was initially presented in 1972. Knowing both the Fourier and image plane's intensity distribution, the idea was to compute the phase distribution of the electric field at the Fourier plane to generate the desired light distribution at the image plane.

The algorithm runs through 6 main steps.

(1) We first initiated the algorithm by generating a complex amplitude $g(x0,y0) = |U(x0,y0)|expi\varphi(x0,y0)$, where $|U(x_0,y_0)|^2$ corresponded to the desired amplitude pattern at the sample and $\varphi(x0,y0)$ a random phase distribution.

(2) Then we calculate the electric field $G(x1,y1) = |G(x1,y1)|expi\varphi(x1,y1)$ obtained at the SLM plain using an inverse Fourier transform.

(3) At this stage the phase parameter $\varphi(x1,y1)$ of $G(x1,y1)$ is preserved. However, the amplitude $|G(x1,y1)|$ do not correspond to the laser illumination at the SLM. Thus $|G(x1,y1)|$ is replaced by $|U(x1,y1)|$ the correct illumination amplitude. This led to: $Gj(x1,y1) = |U(x1,y1)|expi\varphi(x1,y1)$.

(4) Using a Fourier transform $Gj(x1,y1)$ is backpropagated to the sample, giving rise to a complex amplitude $gj(x0,y0) = |Uj(x0,y0)|expi\varphi(x1,y1)$.

(5) At this step we evaluate the quality of the hologram by comparing the calculated and desired light distribution using the expression $E'^2 = \sum_{x1,y1}[|g'(x_0,y_0)| - |U(x_0,y_0)|]^2$. If the value of E obtained is lower than the error criterion introduced by the user, then the quality of the hologram is considered sufficient, and the iterative process stops. On the other hand, if the criterion is not respected, the iteration process continues.

(6) if the algorithm does not stop at the previous step the complex amplitude obtained at stage (4) is modified. Regarding step (3) the phase $\varphi(x1,y1)$ is conserved and $|Uj(x0,y0)|$ replaced by the desired amplitude pattern at the sample: $|U(x_0,y_0)|^2$. Thus, we obtain $g1(x0,y0) = |U(x0,y0)|expi\varphi(x1,y1)$ and repeat the all process starting at step (2).

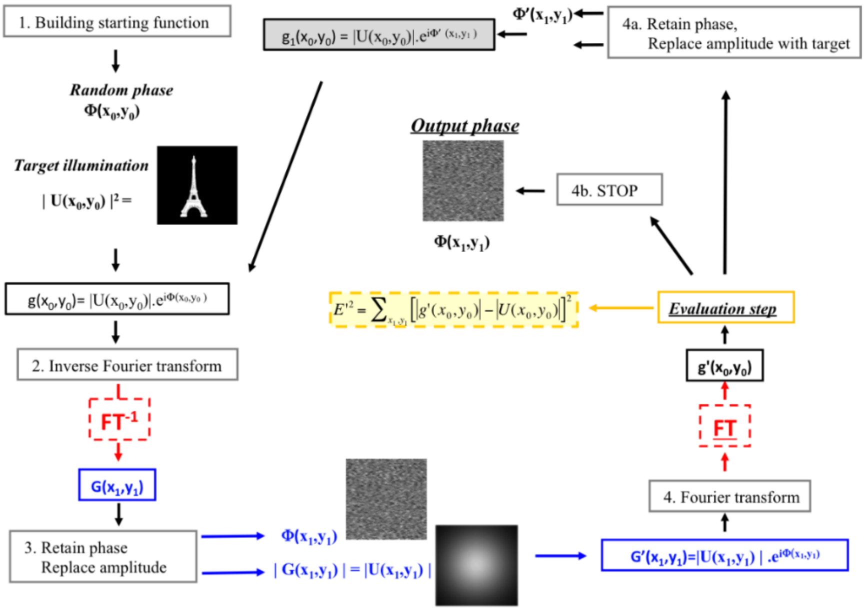

Figure 18: Diagram of the Gerchberg & Saxton algorithm for the calculation of the phase profile sent to the SLM

If the algorithm stops at the evaluation step, the output value $\varphi(x1,y1)$ is kept as the final phase to generate the desired light distribution $|U(x0,y0)|$.

As we already presented in the CGH introduction, using this type of approach where only the phase is modulated leads to the generation of interference patterns or speckle patterns within the intensity distribution of the spot.

This intensity variation inside the generated pattern is amplified in the case of 2PE by the non-linearity of the process as presented in (Lutz et al., 2008b; Papagiakoumou, Oron, et al., 2008) (the magnitude of this variation in 1PE is around 20% for 50% in 2PE). Different approaches have emerged to reduce these variations like using rotating diffusers or rapidly switching between various holograms to average the effect of the speckle over time. Another solution that does not require a loss of temporal resolution like the two previous proposals is the speckle-free phase modulation technique, such as the generalized phase-contrast method, introduced in the next paragraph.

With the development of computers and calculation tools, the use of GS has been greatly simplified, promoting the development of variants improving its performance. (better: convergence speed, uniformity of the patterns)(Chang et al., 2015; Gaunt & Hadzibabic, 2012; Z Zalevsky et al., 1996).

In this work we calculated the phase with two different algorithms depending on the different setup configurations. For complex shape generation we used a derivative form of the GS (Haist et al., 1997).

The second algorithm employed was the one proposed by (di Leonardo et al., 2007) to optimize the generation of 3D diffraction-limited points.

3.3 Generalized phase contrast methods

The generalized phase contrast method (GPC) finds its origin in the so-called phase-contrast microscopy. The latter was developed by the physicist Frederik Zernike in the 1930s. This method's primary goal was to increase the contrast for imaging transparent samples by converting slight phase differences into detectable intensity modulations. As explained below, the GPC method is a generalization of this approach for phase objects imposing more significant phase shifts.

Phase-contrast method:

For instance, with a transparent object as a sample and a monochromatic plane wave as the light source (Figure 19). When the light wave passes through the sample, its phase is modified according to media properties (refractive index and object thickness). Then we can express the transmitted light as: $exp[i\varphi(x,y)]$, with an intensity: $exp[i\varphi(x,y)]^2$. Under the assumption of small phase shifts, one can use a first-order Taylor development to express the wave:

$$t(x,y) = exp[i\phi(x,y)] \approx 1 + i\Delta\phi(x,y) \quad (3.24)$$

Where (1) correspond to the undiffracted light and $(\, i\Delta\varphi(x,y))$ to the diffracted component, carrying in the information of the phase object.

Given for the intensity:

$$I \approx \left(1 + i\Delta\phi(x,y)\right)^2 \approx 1, \qquad \Delta\phi^2 \approx 0 \qquad (3.25)$$

Which corresponds to an almost uniform light distribution and therefore to a weakly contrasted image.

The idea of phase contrast microscopy is to increase the contrast by making the diffracted and un diffracted component interfering by introducing an extra phase shift of $\pi/2$ among the two components. This can be achieved by first placing a focalizing element after the sample, which will focalize the diffracted component at the center of the focal plane, while distributing the high spatial frequencies and diffracted component around it.

This will generate at the lens focal plane, a light distribution given by:

$$TF[t(x,y)] = \tilde{T}(u,v) \approx \delta(u,v) + j\widetilde{\Phi}(u,v) \qquad (3.26)$$

Once the two components are spatially separated a phase filter, imposing a central phase difference of $\pi/2$, is placed at the lens focal plane. This is equivalent to multiplying $\delta(u,v)$ by $j = exp(j\pi)$. Neglecting $\varphi 2$, the intensity transmitted, becomes:

$$\mathrm{I(x,y)} \approx (\exp(\mathrm{i}(\pi/2)) + \mathrm{i}\phi(\mathrm{x,y})))\text{^}2 = (\mathrm{i}(1+\phi)\text{^}2) \approx 1 + 2\,\phi \qquad (3.27)$$

Then the final intensity will depend on the phase introduced by the object.

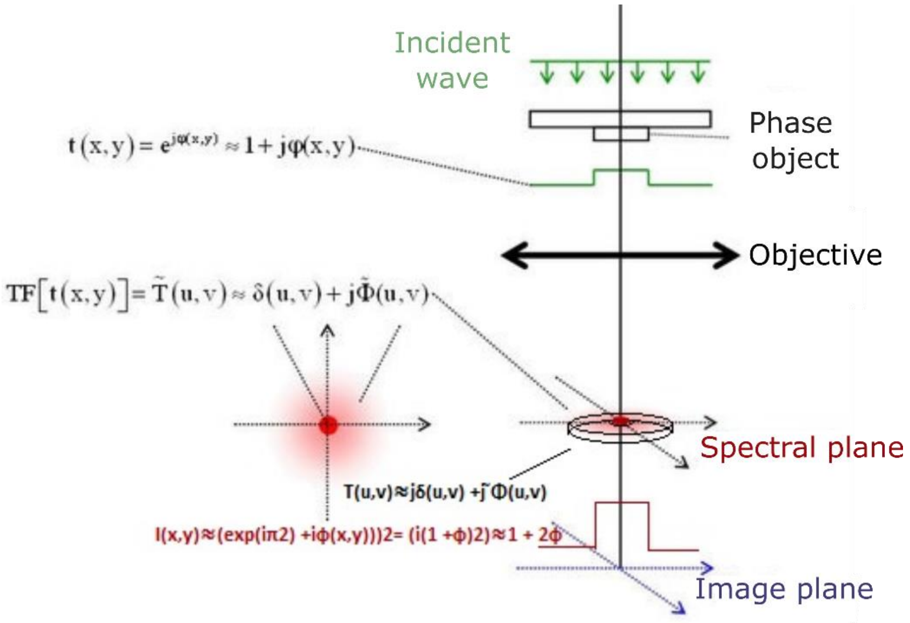

Figure 19: Schematic representation of the method proposed by Zernike.[adapted from (optique-ingenieur)]

The generalized phase contrast method (GPC):

The generalized phase contrast method, introduced by Jesper Glückstad in 2002, was first developed to extend the phase-contrast microscopy principle to objects generating larger phase shifts. It was then proposed to use in a configuration where the phase object is replaced with an LC-SLM. In this way the GPC enables to traduce an arbitrary binary phase modulation (0 and π phase shift) addressed on the LC-SLM into an equivalent intensity distribution at the output plane (Glückstad, 1996; Glückstad & Mogensen, 2001).

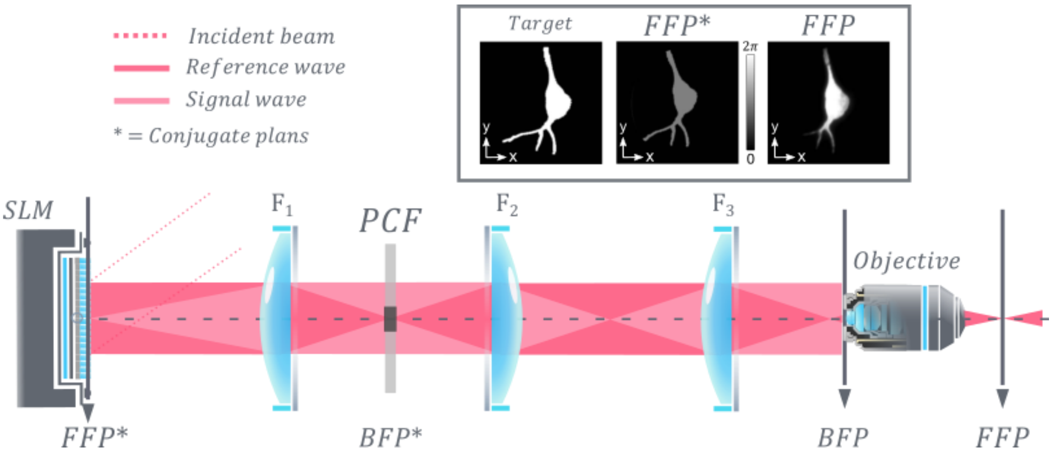

*Figure 20: Schematic representation of a GPC set-up. Illumination intensity patterns in the FFP are obtained by modulating the phase of the illumination beam by means of an LC-SLM placed in an FFP*and a PCF placed in a BFP* plane. Low spatial frequency content, 'reference wave', and higher spatial frequency content 'signal wave' are highlighted in dark and light red, respectively. Inset: GPC pattern generation process: a binary image is designated as the target illumination (left); a binary image matching the target image but encoding for $0/\pi$ phase shifts is addressed on the SLM (middle); a uniform intensity distribution corresponding exactly to the phase pattern on the SLM is generated in FFP [text and image Adapted from (Ronzitti et al., 2017)].*

Briefly, the LC- SLM will generate a $p(x,y) = a(x,y)exp[i\phi(x,y)]$ Input field. With $a(x,y)$ given as $circ(r/\Delta r)exp[i\phi(x,y)]$ where $circ$ is a function equal to 1 for $r = \sqrt{x^2+y^2}\Delta r$ and zero elsewhere. The phase contrast filter (PCF) is a small phase-shifting disc placed at the common focal plane between the two Fourier lenses. It will phase shift the reference wave zero-order (the light undiffracted by the SLM). The phase pattern encoded by the SLM is converted into intensity variations when the image of the input field interferes with the synthesized reference wave (SRW) with the PCF at the output plane. We can describe the effect of the PCF modifying the diffraction-limited zero-order with a θ phase shift as:

$$H(f_x, f_y) = 1 + [exp(i\theta) - 1]circ\left(\frac{f_r}{\Delta f_r}\right) \quad (3.28)$$

where the spatial frequency coordinates f_x and f_y are related to f_r by $f_r = \sqrt{f_x^2 + f_y^2}$.

The terms are grouped together and show the double action of this filter: the first term transmits the signal, and the second creates a reference wave out of phase. Then we can mathematically translate the effect of the optical elements on our initial field by a first Fourier transform, followed by the multiplication with the parameters of our PCF, before ending with an inverse Fourier transform, inverting the coordinates. Then we obtain an expression of the intensity describing the interferogram at the output plane:

$$I(x',y') \approx \left(a(x',y')exp(i\phi(x',y')) + \overline{\alpha}(exp(i\theta) - 1)g(r')\right)^2 \quad (3.29)$$

The intensity is thus formed by the interference of the input image field, $a(x',y')exp(i\phi(x',y')$ with the SRW: $\overline{\alpha}(exp(i\theta) - 1)g(x',y')$. $\overline{\alpha}$ represents the amplitude of the focused light and is expressed:

$$\overline{\alpha} = |\overline{\alpha}exp(i\phi_{\overline{\alpha}})| = \frac{\int a(x,y)exp(i\phi(x,y))dxdy}{\int a(x,y)dxdy} \quad (3.30)$$

The spatial profile of SRW, $g(r')$ support of information on our filter parameters is governed by diffraction effects due to the finite size of the PCF (Figure 18). However, it is the interference between:

$$g(r') = \mathcal{F}^{-1}\left(circ\left(\frac{f_r}{\Delta f_r}\right)\mathcal{F}\big(a(x,y)\big)\right) \quad (3.31)$$

and the phase image that allows us to generate our interferogram.

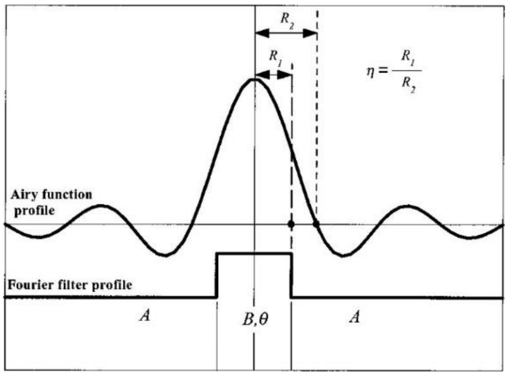

Figure 21: Schematic representation of the relationship between the profile of the incident wave on the filter and the spatial profile of a Fourier filter. [Adapted from (Glückstad, 1996)]

Where $g(r')$ could be expressed as a function of:

$$\eta = R_1/R_2 = (0.61)_{-1}\Delta r \Delta f_r \quad (3.32)$$

R1 is the radius of the PCF and R2 the radius of the main lobe of an Airy function representing the wave incident on the PCF (Figure 18) and Δf_r the radius of the PCF in the spatial frequency domain. This led to the following results (Figure 22) from (Glückstad, 1996).

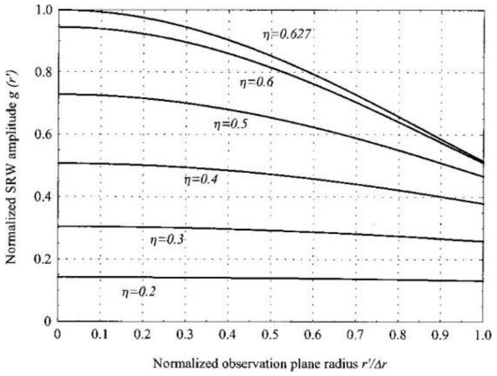

Figure 22: Plot the spatial variation of the normalized SRW amplitude along the radius of the observation plane. [Adapted from (Glückstad, 1996)]

(Figure 22) Allow visualizing the evolution of the SWR amplitude along the radius of the observation plane for different values of η. For high values of η , the amplitude of SRW does not remain constant along r' but will tend to decrease. Thus, when interfering with the input image wave, the result will be distorted. On the other hand, the smaller η is, the more homogeneous the intensity will be, but the amplitude of the SRW is low, which will induce a lower contrast at the output. Therefore, it is important to correctly choose your filter as well as the dimensions of your input and output phase image. Another important criterion to optimize this method was obtained in (Glü & Mogensen, 2001) by setting the following condition: the intensity outside our light source must be as low as possible $I = 0$ giving as operating criterion:

$$\overline{|\alpha|} = \frac{1}{2|sin(\theta/2)|} \Longrightarrow 1/2 \leq |\overline{\alpha}| < 1 \quad (3.33)$$

This other condition was translated as the need to monitor specific proportions between signal and reference wave.
In the end, this method has many advantages with respect to CGH: it requires little or no computation time, has no zero order and uniform light distribution in the generated patterns (no speckles). But it also presents few limitations: it is not possible to generate 3D pattern as in CGH and it is not suitable for experimental strategies requiring large variation of the excitation spot size, as the diffraction efficiency is optimized only when the area of the shape is ¼ of the illuminated area.
We will see that all these limitations can be solved in a hybrid combination CGH-GPC (Chapter 4).

3.4 Axial resolution

We will now study the optical confinement offered by GPC, CGH, and Gaussian methods for the generation of excitation patterns. As we can see in (Figure 23), the CGH system allows obtaining a much better axial confinement ($\sim 20\ \mu m$) than the GPC and Gaussian illumination ($\sim 1\ mm$). This comes from the difference in phase profile at the objective BA. In CGH the wavefront at the BFP is the image of the phase profile projected on the SLM. The profile being highly inhomogeneous it generates in the wavefront high spatial frequency. These frequencies act as rays with a high angle of incidence at the pupil entrance, taking advantage of the whole objective NA. On the other hand, the GPC and Gaussian methods have a quasi-uniform phase profile, leading to a drastic loss of axial resolution (Vaziri & Emiliani, 2012).

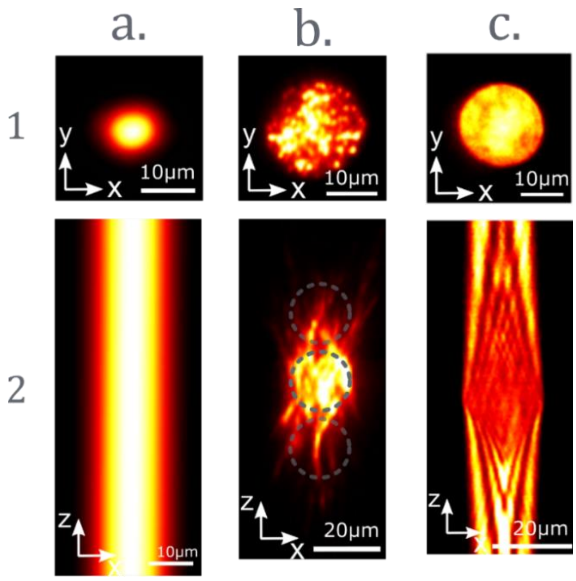

Figure 23: Comparison of different beam types. Lateral profile and maximum orthogonal projection along the z-axis of two-photon excitation fluorescence simulated for laterally extended light patterns using different techniques: Low-NA Gaussian beams (GB) (spot: 10 μm), CGH (spot: 20 μm) and GPC (spot: 20 μm).

For the Gaussian illumination it is possible to determine an analytical expression of the two photons intensity signal obtained in a z plane as (Óscar R. Hernández Cubero, 2016):

$$I_{TPE}(z) = \frac{z_R^2}{z_R^2+z^2} \quad (3.34)$$

Where:

$$z_R = k\frac{s^2}{4\ln(2)} = kW^2$$

With $\sqrt{2}W = \frac{s}{\sqrt{2\ln(2)}}$ the beam radius and s the spot diameter at FWHM of the TPE fluorescence. By solving this equation, we obtain as an expression of the axial confinement for the FWHM:

$$\Delta z(W) = 2z_R = 2\,kW^2 \quad (3.35)$$

It is also possible to determine an analytical expression for Holographic circular spot as demonstrate in (Leshem et al., 2014; Óscar R. Hernández Cubero, 2016). One can then express the two-photon signal obtained as:

$$I_{TPE}(z) = \frac{z_R^2}{z_R^2+z^2(1+\frac{2W^2}{\sigma})} \quad (3.36)$$

With for expression of the axial containment:

$$\Delta z(W) = \frac{2z_R\sigma}{\sqrt{2W^2+\sigma^2}} = \frac{2kW^2\sigma}{\sqrt{2W^2+\sigma^2}} \quad (3.37)$$

In this approach, a speckle pattern is introduced to model the complex amplitude of holographic pattern and : $\sigma \approx \frac{\lambda}{NA\sqrt{8\ln(2)}}$ is the term used to describe the speckles size.

As stated at the beginning of the chapter, the phase profile at the objective BA for the GPC method is free of high-frequency fluctuation. On the other hand, it is closer to the uniform profile obtained with a Gaussian system. Then we can consider the evolution of the axial resolution for the GPC proportional to Gaussian performance.

Based on equations (3.35) and (3.37), we obtain the (Figure 244):

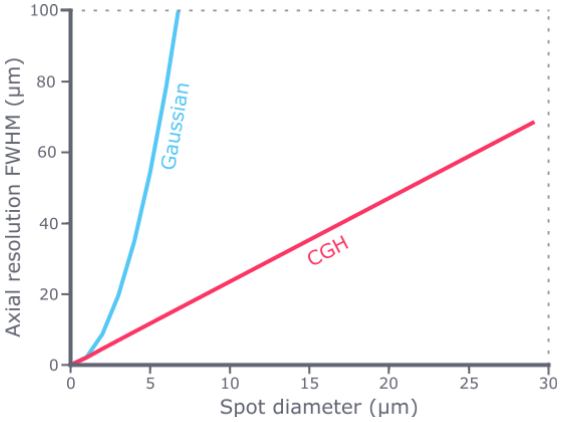

Figure 24: Evolution of the axial resolution as a function of the diameter of the generated spot for the Gaussian and CGH methods in the case of 2P excitation with $\lambda = 1040\ nm,\ Numerical\ aperture = 1,$

Despite the clear improvement of resolution brought by holography, it is not sufficient to guarantee single-cell confinement. A neuron target may be approximate as a sphere of diameter ranging from 12 to 20 µm. The resolution achievable with a holographic spot of the same diameter appears to be around 28-47 µm (based on equation (3.37)). Considering the extremely dense nature of the brain (Intro), the performance offered by holography at neuronal scale cannot guarantee the absence of adjacent elements stimulation. With this concern in mind, we will now move on to the next chapter.

Chapter 4: Temporal focusing Beam Shaping

In this part, we will see the underlying principles of the TF method. Then we will discuss its simplest integration within the different CGH GPC or Gaussian optical systems. Next, we will study the performances obtained in terms of axial confinement. Finally, we will see the problems related to the integration of the TF in a CGH system and the solution brought during my thesis.

4.1 Concepts

As we have seen in (Chapter 2) the 2P effect is a nonlinear effect of order two ($S \propto I^2$). Based on this dependence it is possible to realize an optical sectioning by confining the photon to the desired point. This confinement can be of two different natures: Spatial (objective focusing) and temporal (pulsed laser) (Figure 25).

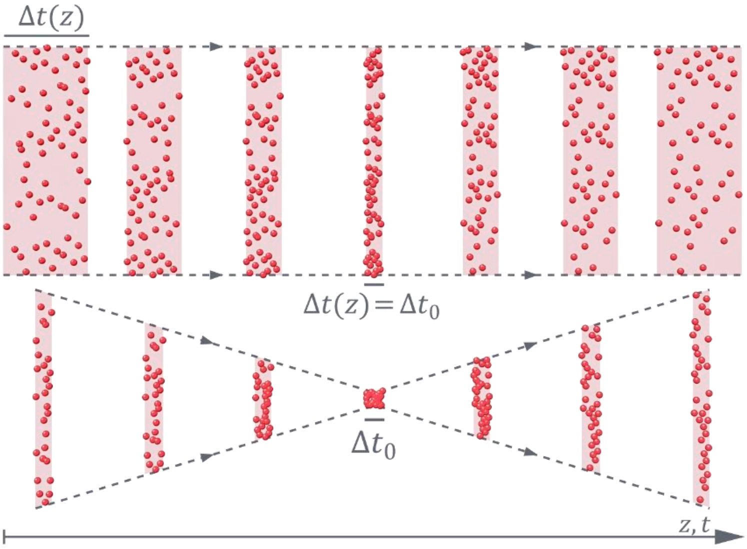

Figure 25: Axial propagation of spatially and temporally focused beams. Representation of the spatiotemporal evolution along the Z axis (spatial coordinate) and time (t) of the photon's distribution (red dots) and laser pulses duration (pink bands) for: (a) Temporal focusing the photon density increases at the focal plane because of the temporal confinement of photons: that is, the width of illumination pulses gradually shortens as they get closer to the focal plane. (b) Spatial focusing photon density increases at the focal plane because of spatial confinement of photons [adapted from (Papagiakoumou et al., 2020b).]

In the case of spatial focusing the concept is well known, spatial photon density increases as the beam size decreases, reaching a maximum at the focal plane. For temporal focusing we can rewrite this sentence this time with the duration of the pulse: " In temporal focusing the photon density increases as the pulse duration decrease, reaching a maximum at the focal plane." This concept was introduced in 2005 by two groups (Oron et al., 2005a; Zhu et al., 2005).

To perform temporal focusing, the pulse duration needs to be stretched before the objective. Once passing through it, the stretched pulse should gradually reach back its original duration at the FFP. In the following section we will explain how this can be done using a dispersive element.

4.2 Realization

Before dealing specifically with the set up to generate a temporal focusing effect, let's have a look at the more straightforward case of short pulse propagation in a medium of index n. First, a laser pulse in the time domain is linked by a Fourier transform to its spectral domain (Figure 26). Thus, a Gaussian laser pulse in the time domain transforms to a Gaussian spectrum in the spectral domain, whose bandwidth is inversely proportional to the pulse duration.

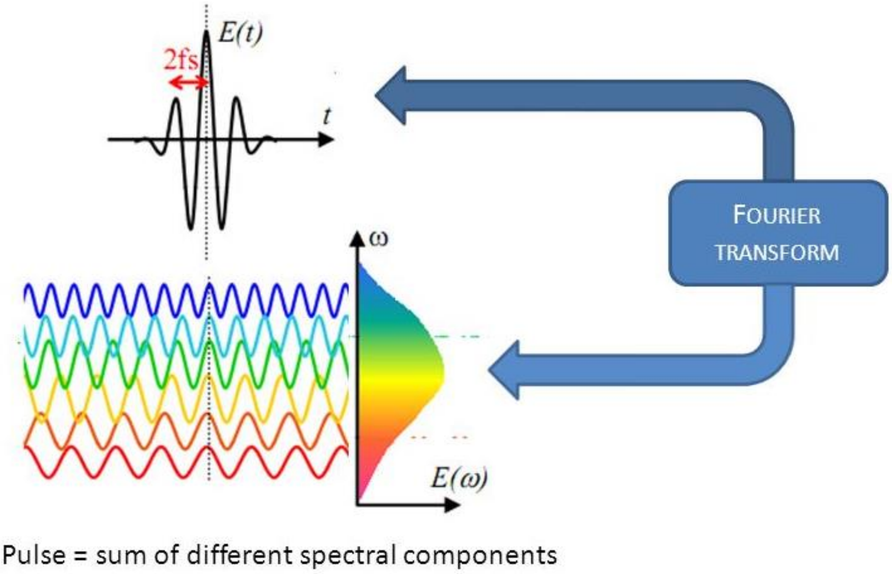

Figure 26: Illustration of a laser pulse decomposition in spectral domain by Fourier transform

Based on this notion, it is possible to understand the propagation effect of a pulse in a medium of index n. The optical index of a medium seen by light is wavelength dependent. As a pulse is composed multiple wavelengths, each of them will propagate at a different speed in the medium, introducing a delay between them and thus a phase shift. The expression of the propagation, in the simple case of a plane wave propagating along *z* leads to:

$$E(z,t) = \int_0^{+\infty} \tilde{E}\,(\omega)\exp[i(k(\omega)z-\omega t)]\frac{d\omega}{2\pi}$$

With $k(\omega) = n(\omega)\frac{\omega}{c}$ where $n(\omega)$is the refractive index of the material.

We can simplify the expression introducing the spectral phase: $\varphi(z,\omega) = \ \omega \cdot n(\omega) \cdot \frac{z}{c}$

We obtain:

$$E(z,t) = \int_0^{+\infty} \tilde{E}\,(\omega)\exp\left(\mathrm{i}\varphi(z,\omega)\right)\ \exp(-\,i\omega t)\frac{d\omega}{2\pi}$$

Where the dependence on z is confined only in $\varphi(z,\omega)$.

In other words, all the variations of our pulse are linked to the spectral phase variation introduced by the medium. We can decompose in a Taylor series the spectral phase (Borzsonyi et al., 2013) and for simplicity approximate the expression to the second order:

$$\varphi(z,\omega) = \varphi(z,\omega_0) + \frac{d\varphi(z,\omega)}{d\omega} \cdot (\omega - \omega_0) + \frac{1}{2}\frac{d^2\varphi(z,\omega)}{d^2\omega} \dots$$

These different values are called respectively:

$$GD \equiv \varphi^1 = \frac{d\varphi(z,\omega)}{d\omega}$$

$$GDD \equiv \varphi^2 = \frac{d^2\varphi(z,\omega)}{d^2\omega}$$

The terms above represent: 1) the group delay (GD), which can be considered as the speed at which the overall pulse envelope propagates; 2) the group-delay dispersion (GDD), which accounts for possible changes of the pulse instant frequency.

It could be shown that the GDD determines the pulse duration. when a laser pulse travels through a dispersive medium of index $n(\omega)$, a delay between the spectral components is observed introducing GDD. There for the pulse duration after the dispersive medium is changed accordingly.

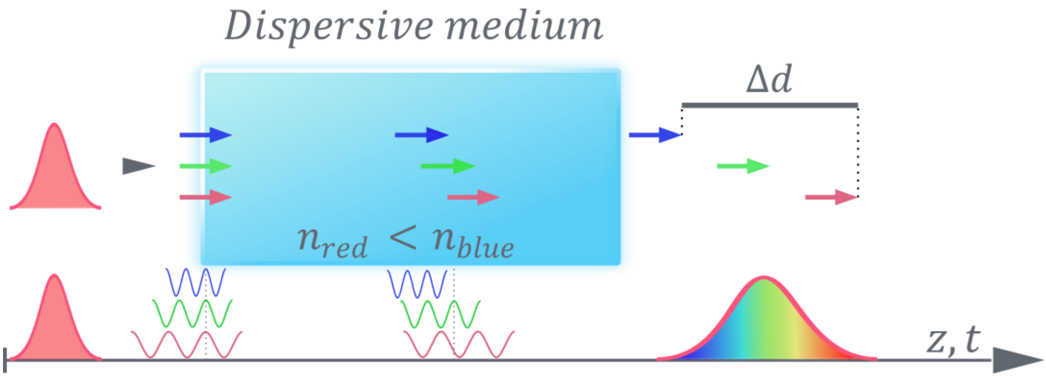

Figure 27: Broadening of a Laser pulse propagating in a dispersive medium. The spectral component here represented by the blue, green and red arrows sees different indexes and propagates at a different speed in the medium, introducing a delay between components corresponding to Δd *. This example represents a positive chirp (the short components are delayed compared to the long ones).*

Temporal focusing make use of this effect. Precisely In Ref. (Oron et al., 2005b; Zhu et al., 2005) it was proposed to use a diffraction grating to induce GDD and thus pulse broadening. Indeed, as we have seen in (Chapter 3), a grating induces angular dispersion of the colors according to the grating law. Thus, each wavelength will see a different optical path, introducing a phase delay compared to the central wavelength as shown in (Figure 28). This will lead to GDD generation and thus to a longer pulse in time as the beam propagates away from the grating. At larger distances from the grating, different colors will no longer overlap in space, an effect called spectral lateral walk-off, which increases further the pulse duration. A complete study of the grating effect on the pulse duration and the amplitude has been done in the papers of (O. E. Martinez, 1986).

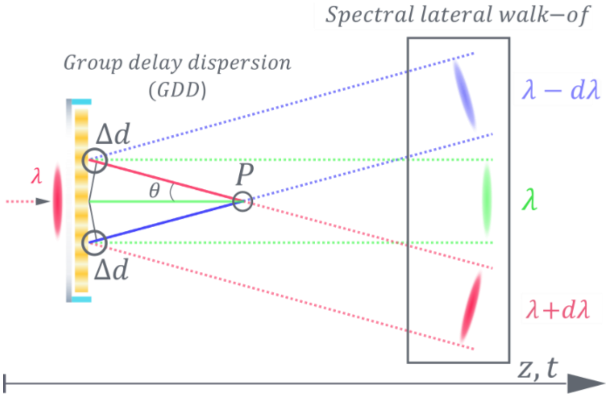

Figure 28: Representation of the angular dispersion of colors. We can observe two different regimes contributing to the pulse broadening. First, all the colors contribute to the pulse generation but are delayed at any point P, introducing GDD effect. Second, the spectral components move away from each other and start no longer overlapping and thus no longer contribute to the pulse generation inducing a broadening effect (Spectral lateral walk-of).

However, dispersion is not the only effect introduce by the grating. We can cite two others:

- Pulse front tilt: At each point in time the intersection between the laser beam and the diffraction grating is a line parallel to the grating grooves (Figure 29). As the beam propagates, the line is scanned over the grating. Because light incident at a given angle over a grating is reflected at an unconventional angle compared to the one obtains with a mirror, a delay is introduced between each line, resulting in a tilted wavefront.

- Deformation of the beam. It is an elongation of the beam for a fixed wavelength in the direction of dispersion. Indeed, as already said the reflection by a grating for a given incidence angle is different to the one obtained with mirror. Therefore, the output beam is stretched (Figure 29). We can express this stretching as a function of the angle as: $S = \frac{1}{\cos(\theta_i)}$ where S is the stretch factor $\frac{D_F}{D_i}$ relating the initial beam diameter and the final one. This effect needs to be counterbalanced when TF is combined with beam shaping to avoid that the generated spot will be elongated in the grating dispersive direction

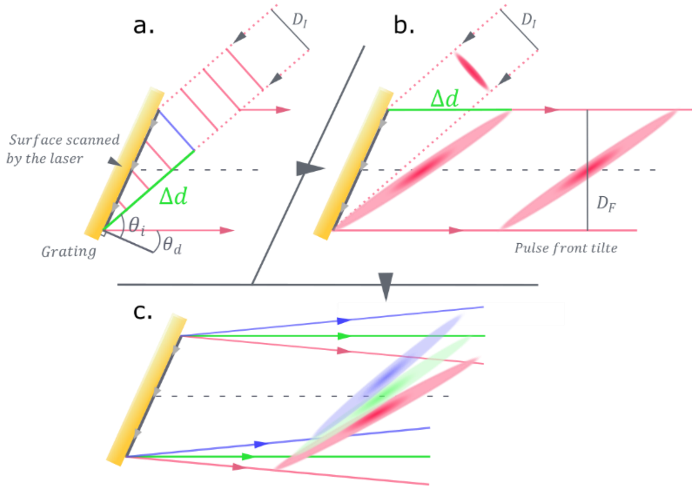

Figure 29: Geometrical description of the pulse deformation by a grating reflection. (a) Illustrate the intersection of a laser impulse with the grating surface during its propagation. The blue line corresponds to the first point intersection between the pulse and the grating. The gray line is the surface scan by the impulse during the propagation. in green represent the distance the pulse needs to travel to reach the final point scan over the grating. (b) Due to the particular reflection angle of the grating, the path difference Δd results in a pulse front tilted, and the beam's diameter is enlarged. (c) Each color undergoes the same deformation

We have seen that, by using a diffraction grating, a short pulse is broadened in time as it propagates away from the grating plane, as a consequence of the angular dispersion of the different colors. To perform TF however, we need a broadened pulse that is recompressed to its shortest value at the focus of a microscope objective and that broadens again when propagating away from it. To obtain this, it is sufficient to add two lenses in a 4f configuration after the diffraction grating (Figure 30). As the 4f configuration makes a perfect image of the BFP of the first lens (F_1) in the FFP of the second one (F_2), all the colors, spatially separated after the grating, will be recombined in the FFP of the second lens. This effect can be also seen as the broadened pulse being recompressed in time after the second lens of the 4f system. The shortest pulse duration will then be achieved in a plane that corresponds to the FFP image of the diffraction grating. Similarly, as the incoming beam scanned in time the diffraction grating, the recombined beam also scans in time the FFP image of the diffraction grating. By propagating away from this image plane, different colors will again propagate in different directions, thus broadening the pulse in time. The conjugated image of the diffraction grating represents the temporal focusing plane. Two photon effects will be optimal on such a plane and will be minimized in all the planes before and after it.

If we now want to apply this concept to optical microscopy, it is sufficient to replace the second lens with a microscope objective, making sure that the grating dispersion and the focal length of the first lens are chosen such to fill, in the grating dispersion direction, the objective pupil, as described later.

To note, a diffraction grating and a 4f lens system is reminiscent of a grating compressor in a Martinez configuration (O. Martinez, 1987), as sketched in (Figure 30). In such a system, by placing a second diffraction grating in the FFP image of the first, all the colors, recombined by the second lens, are then also put back on the same axis by the second grating, thus completely restoring the initial propagation condition. By walking away one of the two gratings from the ideal 4f configuration, it is possible to finely change the amount of GDD without separating the different colors in space.

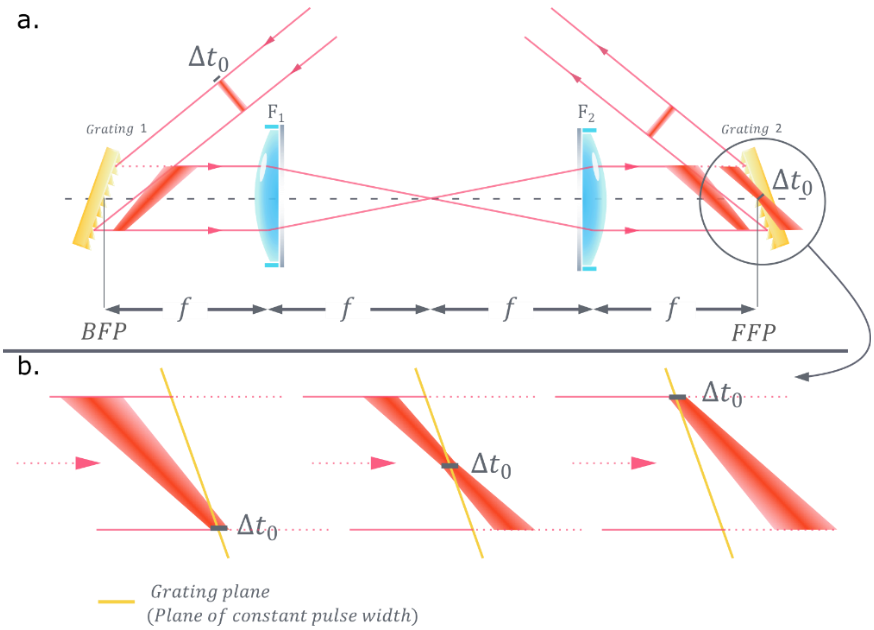

Figure 30: Grating compressor and scanning effect. (a). The laser pulse is broadened after its reflection over the first grating and propagates through the 4f telescope. The output pulse of a 4f configuration is considered all most identical to the input pulse. Thus, a broadened pulse exits the second lens and is gradually recompressed during its propagation to the second grating. In a compressor system, a second grating is placed at the image plane of the first grating to recouple the different colors. (b) represents a zoom over the region of the second grating at different times. The yellow line represents the second grating surface (or the image of the first grating by the 4f system). As the pulse propagates, it returns to its initial duration at the position it crosses the grating plane.

4.3 2D setup configuration:

The grating illumination initiate the TF. Thus, the simplest way to couple a beam shaping setup (holographic, Gaussian or GPC pattern) to TF is to project the desired patterns on the diffraction grating. With CGH or GPC systems, a grating is added after the SLM in a plane conjugated with the sample plane (Papagiakoumou et al., 2008, 2010). For CGH this requires placing the grating in the focal plane of the first lens after the SLM. In GPC instead, the grating is placed in the focal plane of the lens after the phase contrast filter (Figure 31). In this configuration, the designed pattern is projected onto the grating, inducing the temporal focusing effect.

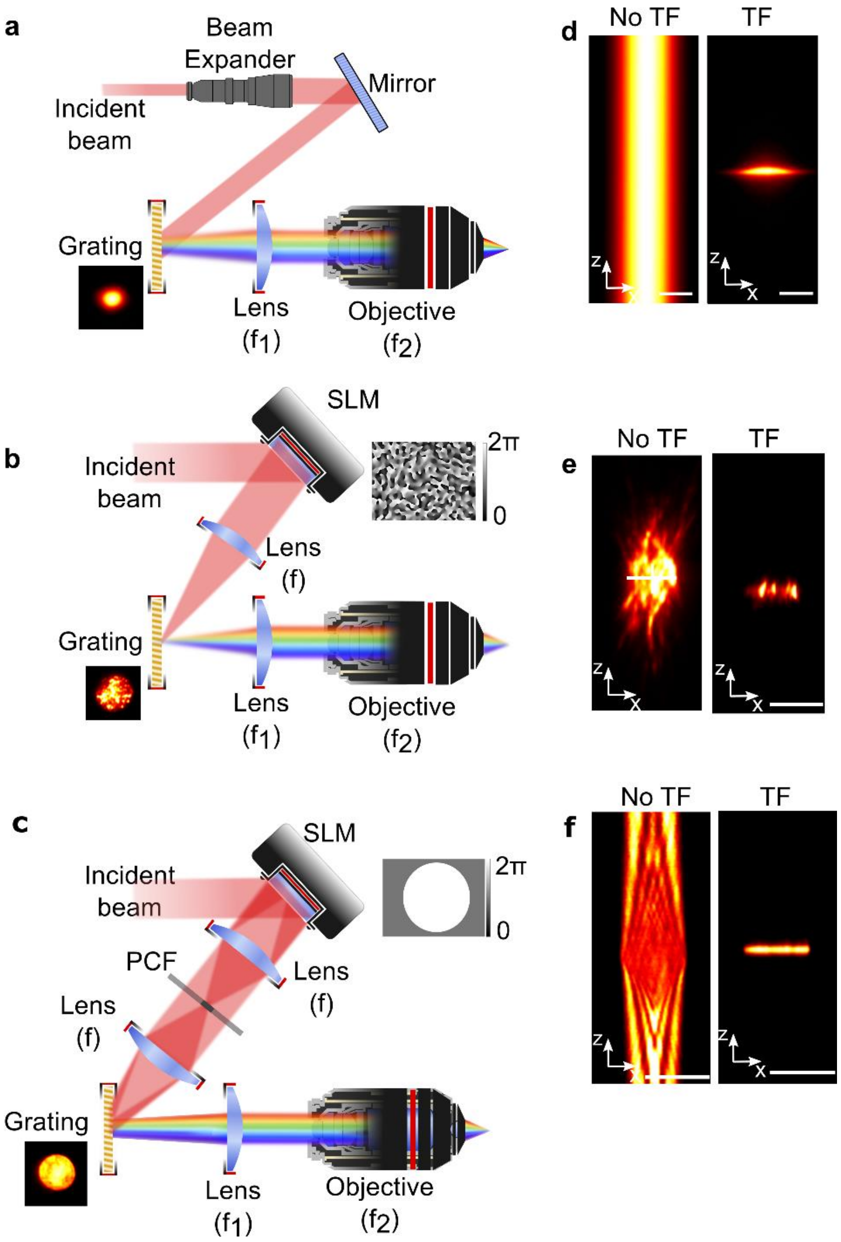

Figure 31 Representation of 2D TF: GB, CGH, GPC system and confinement performance. (a,b,c) are respectively the Gaussian , CGH and GPC systems. (d,e,f) Correspond to the lateral profile and maximum orthogonal projection along the z-axis of two-photon excitation fluorescence simulated for laterally extended light patterns with TF/No TF: Low-NA GB (spot: 10 µm), CGH (spot: 20 µm) and GPC (spot: 20 µm) [Adapted from (Papagiakoumou et al., 2020a)].

4.3.1 TF-effect

In (Figure 31), we can see the concrete effect of temporal focusing on spot axial resolution compared to non-TF spots. The resolution changing from tens of micrometer to $\sim 5\mu m$ with TF effect. It's possible to find an analytic expression of the axial resolution obtained by two-photon effect ender TF – Gaussian beam (GB) or holographic illumination. Based on expressions proposed in (Óscar R. Hernández Cubero, 2016) to model the axial resolution offered by the TF approach apply to GB and CGH we drive the expected axial resolution (Figure 32).

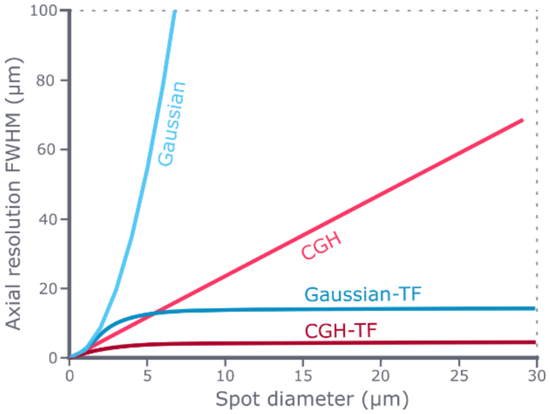

Figure 32: Comparison of the axial resolution as a function of the diameter of the generated spot for TF and NoTF Gaussian and CGH methods. 2P excitation confinement with $\lambda = 800\,nm,\ Numerical\ aperture = 1, \tau = 160\,fs,\ g = 800\,Lines/mm\,(grating\ groove\ density)$ *[adapted from (Óscar R. Hernández Cubero, 2016)]*

On the plot linking spot diameter to axial resolution, we can observe that the axial confinement for temporally focused spots is almost constant regardless of the spot diameter. This represents a significant advantage, especially for the holography and GPC method, generating deferent patterns to cover a single or multiple cells. For example, a simple circular spot of $10\ \mu m$ or a distribution of multiple spots will all maintain a good axial resolution.

4.4 3D configuration

If the use of TF for 2D patterns is relatively straight forward it requires further development when used for the generation of 3D patterns. The reason is simple: as we have seen, to correctly induce the TF effect to a 2D pattern, the SLM needs to generate that pattern precisely at the grating surface. As we can see in (Figure 33), this condition corresponds to an overlap between the spatial focusing plane (the plane at which the SLM generates the pattern) and the temporal focusing plane (the grating surface). Using the SLM we can introduce a lens effect to displace the generated pattern in z. Doing so the spot is also displaced at the image plane of the SLM where the grating is placed. In this circumstance, the spot is no longer generated over the grating and the TF is not correctly induced (Figure 33). We then say that the temporal and spatial focusing plane are separated. Therefore, it is not possible to generate 3D illumination patterns with this kind of system.

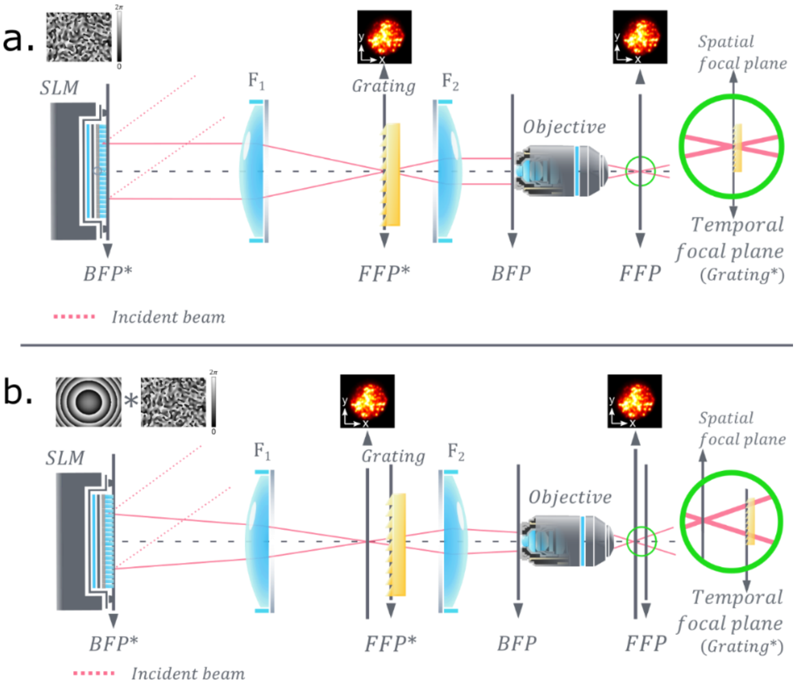

Figure 33: Schematic representation of 2D TF-CGH system. (a) The SLM generate a circular pattern. (b) a lens hologram is added to the pattern's phase to operate a z displacement. Thuse these cercle is no longer generated at the grating plan, the spatial focusing and temporal focusing are separated.

A possible solution is to place the grating before the SLM allowing it to displace the temporal and spatial focusing plane simultaneously (Pégard et al., n.d.; Sun et al., 2017). Unfortunately, this configuration does not allow to modify the spot shape or size. This can be intuitively thought in these terms: what is temporally focused is what one sees at the diffraction grating plane. If a SLM changes the shape after the grating by using CGH, then the recombined spectral frequencies at the sample plane are not anymore the same as when they were separated at the grating plane. Thus, one no longer gets at the sample plane what was projected on the grating, and therefore loses the effect of TF.

To confirm this intuitive picture, in (Figure 34) below we show the result of a simulation comparing a simple temporally focused Gaussian beam to a Gaussian beam that, after being temporally focused, illuminates an SLM placed at the Fourier plane of the grating. (Figure 34) shows the results for simple Gaussian beams, in the case of a small and a big Gaussian beam (5 µm and 50 µm respectively at the sample plane). In both cases the TF effect works well, giving an axial resolution of about 6 µm. In (Figure 34.4b) instead, we simulate the propagation for a small Gaussian beam on which we apply with the SLM (after the grating) the phase modulation for projecting a big shape (round spot of ~50 µm) at the sample plane. As we can see from the axial propagation of the shape, this is not at all temporally focused.

At this stage we have seen two possible implementations of TF and CGH, each of them with advantages and limitations. Either we place the grating after the SLM and can generates different patterns but only in 2D (2D configuration), or we can place the grating before the SLM to gain the capacity to displace in 3D a gaussian spot, but we lose the possibility to change the shape of the beam at the sample plane (3D configuration).

Losing the capacity to generate different patterns is not the only counterpart of the latter configuration. If we look closely at the setup (Figure 35) we can observe a line illumination over the SLM screen, we will also find this illumination at the objective BA as it is conjugated with the SLM. This line illumination represents a limitation for the generation of CGH pattern as it limits the total illumination power we can use before damaging the SLM or overheating the component.

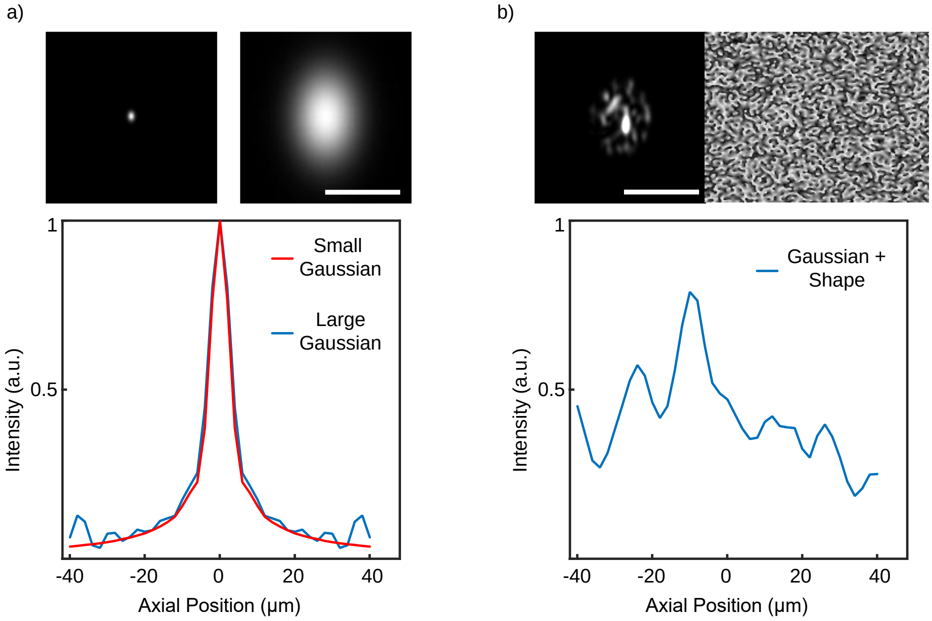

Figure 34: Simulation of beam shaping with a single SLM illuminated by a TF Gaussian beam. (a) Properties of the TF Gaussian beam. We simulated two different sizes of a Gaussian beam a small one of $5\ \mu m$ and a big one of $50\ \mu m$ FWHM. Top: Intensity of the Gaussian beams. Common Scale bar: $50\ \mu m$. Bottom: Axial fluorescence intensity profile for the two beams. The FWHM axial resolution is $\sim 6\ \mu m$, as expected for a TF beam. (b) Generation of a holographic spot of $50\ \mu m$ in diameter, with the SLM placed at the Fourier plane of the grating. Top left: Intensity of the spot. Scale bar: $50\ \mu m$. Topright: Phase profile addressed to the SLM for generating the spot. Bottom: Axial fluorescence intensity profile of the spot. It is obvious that the axial confinement of the Gaussian beam is lost.

The first step to find a solution to the line illumination is to simply describe in a geometrical way its origin (Figure 35). First, we need to separate the propagation in x and y , each of them being impacted differently by the grating. We will define the x-direction as the one responsible for dispersion or temporal focusing (direction in which the grating disperses the colors). On the contrary, the direction y will be the direction for which the grating does not apply any specific effect. In other words, these two axes differ by the separation of the colors during the propagation.

When the grating is placed before the SLM, it is illuminated by a collimated gaussian beam. If we continue to study its propagation, in the direction y the beam remains collimated until the first lens, which then focuses the beam at its focal plane. In the x direction, the same behavior is observed but, because of dispersion, each color is focused on a different point. We obtain at the Fourier plane a series of diffraction limited focused points for each color. As the laser spectrum is continuous the illumination at the SLM screen resembles a gaussian line illumination.

To find a solution enabling at the same time to change the illumination shapes in 3D without losing the advantages of TF and maintaining a extended illumination of the SLM, we combined the two setups previously described in a double SLM configuration. Thus, the system will be composed of a first part “SLM-grating” to modulate the shape and a second part “grating-SLM” to displace the pattern in 3D. This configuration solves the shape modulation limitation but also the line illumination over the second SLM placed after the grating. Indeed the grating is no longer illuminated by a collimated beam, but by a focused light pattern, as seen in (Figure 35). We can study the propagation we obtain after a grating illuminated by a focused laser light (Figure 35): in the direction y our beam diverges and is collimated by the first lens. Again, for the x-direction, the same behavior is observed but for each of the colors along their dispersion axis. In the Fourier plane of our grating were the second SLM is placed, we thus obtain a wide illumination represented by a superposition of parallel Gaussian beams, each describing a different color. Its size will depend on the lens magnification and grating dispersive power.

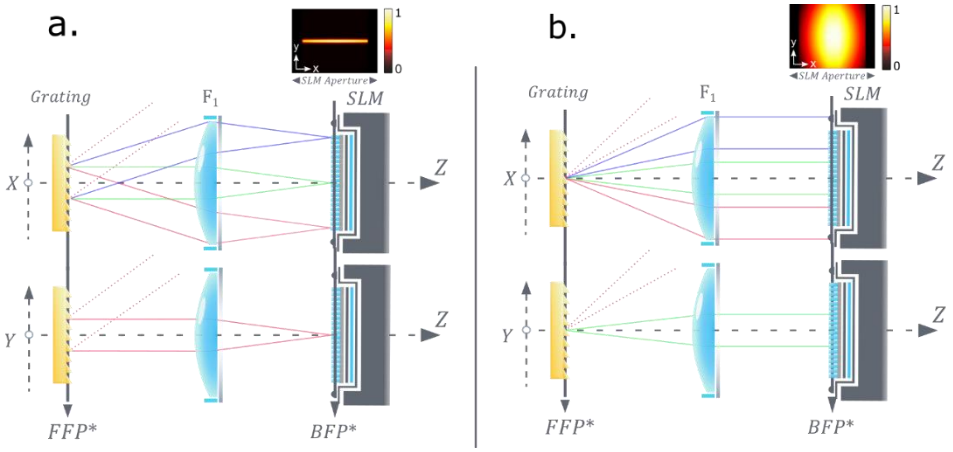

Figure 35: Grating illumination configuration The grating is illuminated by; (a) a collimated laser beam (b) a focalizing laser

This new configuration was first introduced by (Hernandez et al., 2016). The setup was composed of a 2D system to generates different patterns on the grating plane and a second SLM to displace this different TF-pattern in z using a lens effect. Each pattern generated over the grating was addressed on another region of the second SLM. Thus, each area could generate an independent equivalent focal lens to reach a different z plane. However, the number of simultaneously accessible plane in z is limited by the number of distinct regions addressable on the second SLM (around 6 regions/planes). Despite this limitation, the concept of separating the 2D generation and 3D displacement was validated. Therefore, in the following section, we present the development of a new configuration based on the same concept but without limitation on the number of accessible planes. This approach is particularly flexible, working with different methods for pattern generation (CGH,GPC).

Publication

For this paper Nicolò Accanto and I conjointly work on the development of several methods to perform 3D-TF-patterning. I have been particularly involved in the development of the different optical systems and there characterization, with a particular attention to the multiplexed temporally focused - GPC and Multi Shapes approaches.

Multiplexed temporally focused light shaping for high-resolution multi-cell targeting

NICOLÒ ACCANTO[1†], CLÉMENT MOLINIER[1,2†], DIMITRII TANESE[1], EMILIANO RONZITTI[1,2], ZACHARY L. NEWMAN[3], CLAIRE WYART[4], EHUD ISACOFF[3,5,6], EIRINI PAPAGIAKOUMOU[1,7] AND VALENTINA EMILIANI[1]*

[1] *Wavefront-Engineering Microscopy group, Neurophotonics Laboratory, CNRS UMR8250, Paris Descartes University, 45 rue des Saints-Pères, Paris, France.*
[2] *Sorbonne Université, CNRS, INSERM, Institut de la Vision, 17 Rue Moreau, 75011, Paris, France.*
[3] *Department of Molecular and Cell Biology, University of California, Berkeley, Berkeley, California, USA.*
[4] *Institut du Cerveau et de la Moelle épinière (ICM), Sorbonne Universités, UPMC Univ. Paris 06, Inserm, CNRS, AP-HP, Hôpital Pitié-Salpêtrière, Boulevard de l'hôpital, F-75013, Paris, France.*
[5] *Helen Wills Neuroscience Institute, University of California, Berkeley, California, USA.*
[6] *Physical Bioscience Division, Lawrence Berkeley National Laboratory, Berkeley, California, USA.*
[7] *Institut national de la santé et de la recherche médicale (Inserm), Paris, France.*
[†] *Equally contributing authors.*
**Corresponding author :valentina.emiliani@parisdescartes.fr*

Optical wavefront shaping is a powerful technique to control the distribution of light in the focus of a microscope. This ability, combined with optogenetics, holds great promise for a precise manipulation of neuronal activity with light. However, a deeper understanding of complex brain circuits requires pushing light shaping methods into a new regime: the simultaneous excitation of hundreds of targets, arbitrarily distributed in the three dimensions, with single-cell resolution. To this end we developed a new optical scheme, based on the spatio-temporal shaping of a pulsed laser beam, to project several tens of spatially confined 2-photon excitation patterns in a large volume. The compatibility with several different phase shaping strategies allows the system to be optimized towards flexibility, simplicity or multiple independent light manipulations, thus providing new routes for precise three-dimensional optogenetics. To validate the method we performed multi-cell volumetric excitation of photoactivatable GCaMP in the central nervous system of Drosophila larvae, a challenging structure with densely arrayed neurons, and photoconversion of the fluorescent protein Kaede in zebrafish larvae.

1. INTRODUCTION

Optical wavefront shaping through computer-generated holography (CGH) [1] enables precise 2D and 3D light manipulation and has become a widely used approach in different fields of optics. In its original version, CGH used the "prism and lenses" [2] or a weighted Gerchberg and Saxton algorithm (GSA) [3,4] and a spatial light modulator (SLM) to generate a distribution of diffraction-limited spots. This configuration was first adopted for multi-trap optical tweezers [1] and for the optical stimulation of neurons both in the one-photon (1P) [5,6] and in two-photon (2P) regime [7,8].

CGH can analogously be used to generate extended illumination patterns, which for instance can be tailored to excite the entire body of a cell [9]. This ability, especially when combined with 2P excitation (2PE), turned out to be of key importance in the field of optogenetics [10,11], in which suitable light-sensitive proteins are genetically expressed in a population of neurons. On the one hand, 2P excitation increases the optical penetration depth, while on the other hand, illuminating the whole cell body ensures the simultaneous excitation of a sufficient number of light-gated channels on the targeted neuron [12–14]. As a downside, an increased spot size results in a loss of axial confinement, which may prevent the excitation of neurons with single-cell resolution. To overcome this limitation, 2P-CGH was combined with the temporal focusing (TF) technique [15–17], in which the beam dispersion from a diffraction grating temporally smears the pulse away from the focal plane, which remains the only region irradiated at sufficient peak powers to induce 2PE. By using TF, it is possible to maintain high optical sectioning for non spatially focused beams, such as large holographic spots, low numerical aperture Gaussian beams (LNAG) or optical beams generated by the generalized phase contrast (GPC) method [18]. The use of TF in all these configurations successfully resulted in the efficient optogenetic stimulation of single [14,19,20] or multiple cells [21,22] with high spatial and temporal resolution, while helping at the same time to preserve the desired excitation pattern through scattering tissues [14,23,24].

The next logical step, which at the same time represents a great optical challenge, is to extend these methods to the simultaneous illumination of hundreds of targets in mm3 volumes with single-cell resolution. This could lead to the precise optogenetic control of large neural circuits in a time frame compatible with physiological transmission of brain signals (milliseconds).

A first solution for 3D multi-target illumination used CGH to generate multiple diffraction-limited spots at the positions of the targeted cells and scanned all of them simultaneously over the cell membranes using a galvanometric system [25–27]. Yet, the need of scanning over the cell body limited the achievable temporal resolution (>20 ms for single AP generation) and precision (temporal jitter > 6 ms) [25,28]. A better resolution (1-3 ms) could be obtained using 2 to 5 times higher illumination power [27], with the downside of risking higher nonlinear photo-damage [29]. Additionally, using focused light at saturation power to compensate for the small spot surface generated important out-of-focus excitation [30–32].

Simultaneous illumination of multiple targets was achieved by generating extended holographic shapes in 3D [33]. However, as previously discussed, CGH alone is not sufficient to ensure single-cell axial resolution, especially when targeting multiple spatially close cells at the same time [34,35]. On the other hand, the combination of 3D-CGH with TF is much more challenging than its 2D counterpart, as TF requires the holographic patterns to be focused at the diffraction grating. We recently overcame this issue by using two SLMs, the second one placed after the TF grating [34], and by tiling the SLMs to encode multiple holograms, which independently controlled the lateral shape and position (SLM1) and the axial position (SLM2) of each pattern. This strategy enabled the remote axial displacement of a temporally focused shape, as well as projecting different temporally focused patterns at axially distinct planes. Yet, the need of tiling the SLMs physically limited the number of planes that could be addressed. Moreover, this approach was hardly compatible with other beam-shaping techniques such as GPC or LNAG.

3D multiplexing of GPC or LNAG was recently demonstrated by combining a GPC scheme or a LNAG beam with a SLM generating multiple diffraction-limited spots through CGH. With this configuration it was possible to replicate 1P GPC patterns [36,37], or temporally focused 2P LNAG beams [38,39]. While in the former case, 1P excitation limited the achievable axial resolution, in the latter [38,39], the use of a single beam-shaping unit, i.e. the multiplexing SLM, restricted the method to the generation of a static and single-sized Gaussian spot. Additionally, all the mentioned works [36,38,39] suffered from a spatially reduced illumination of the multiplexing SLM, which could limit the performances of the system in terms of maximum usable power and quality of the holograms. The solution proposed by Pégard et al. [38] of introducing a spherical lens before the TF diffraction grating, increased the size of the illuminated area at the SLM by simply defocusing the beam, but created two different foci for every spot at the sample plane, thus deteriorating the overall axial resolution.

In this work, we demonstrate a versatile configuration for multiplexed temporally focused light shaping (MTF-LS) that combines the advantages of the past approaches and removes their limitations. The main concept behind it is, as proposed by [34,38,39], to decouple the light shaping into two independent steps: a first beam-shaping unit that generates and focuses the desired 2D shape(s) on the TF grating and a second step where a second SLM, placed after the grating, laterally and/or axially multiplexes the 2D shape(s) in the sample volume. We demonstrate that this configuration can be used in combination with different light shaping approaches such as CGH, GPC or amplitude/phase modulation.

Precisely, we first show and characterize a multiplexed temporally focused computer-generated holography (MTF-CGH) scheme, which demonstrates the potential of the system. We then extend the work of Ref. [36] to the use of TF, thereby demonstrating multiplexed temporally focused generalized phase contrast (MTF-GPC). Subsequently, we present an amplitude/phase modulation approach, which allows us to create excitation spots with uniform intensity distribution and different shapes independently multiplexed at the sample plane. We call this method multiplexed temporally focused multi-shapes (MTF-MS). We finally validate the performances of MTF-LS by performing in vivo multi-cell volumetric excitation of photoactivatable GCaMP (sPA-GCaMP) [40] in fruit flies, and Kaede photoconversion [41] in zebrafish larvae. In both scenarios, we show the specific targeting of individual neurons selected out of dense arrays and distributed over multiple planes.

2. METHODS

A. General Optical System

The optical system for multiplexed temporally focused light shaping, schematically represented in Fig. 1, consisted of three main parts: (i) the beam-shaping unit, which generated a 2D illumination pattern, described at the objective focal plane by the function $F(X,Y,Z)$; (ii) the temporal focusing unit comprising the grating and the appropriate lenses, which temporally focused the 2D pattern at the objective focal plane; (iii) the multiplexing unit, constituted of a liquid-crystal SLM (SLM2), which created, using CGH, the desired 3D distribution of diffraction-limited spots $G(X,Y,Z)$ at the sample positions Xi, Yi and Zi, thereby replicating the original 2D pattern $F(X,Y,Z)$ at such positions (Fig. 1).

For the beam-shaping unit, we demonstrated four different configurations: 1) CGH based on the use of a liquid-crystal SLM (SLM1) (Fig. 1a); 2) CGH using a static holographic phase mask (Fig. 1a, inset); 3) GPC interferometry (Fig. 1b); 4) an amplitude/phase modulation scheme for the simultaneous generation of multiple shapes, in which SLM1 both defined the 2D illumination patterns and shaped the illumination of SLM2 (Fig. 1c).

B. The beam shaping units

We briefly describe here all the configurations we used for the beam-shaping units. In all the experiments the laser source was a femtosecond fiber laser (Fidelity 18 or Fidelity 10, Coherent), emitting at 1040 nm, delivering 140 fs pulses at a pulse repetition rate of 80 MHz, with an average power of 18 W or 10 W.

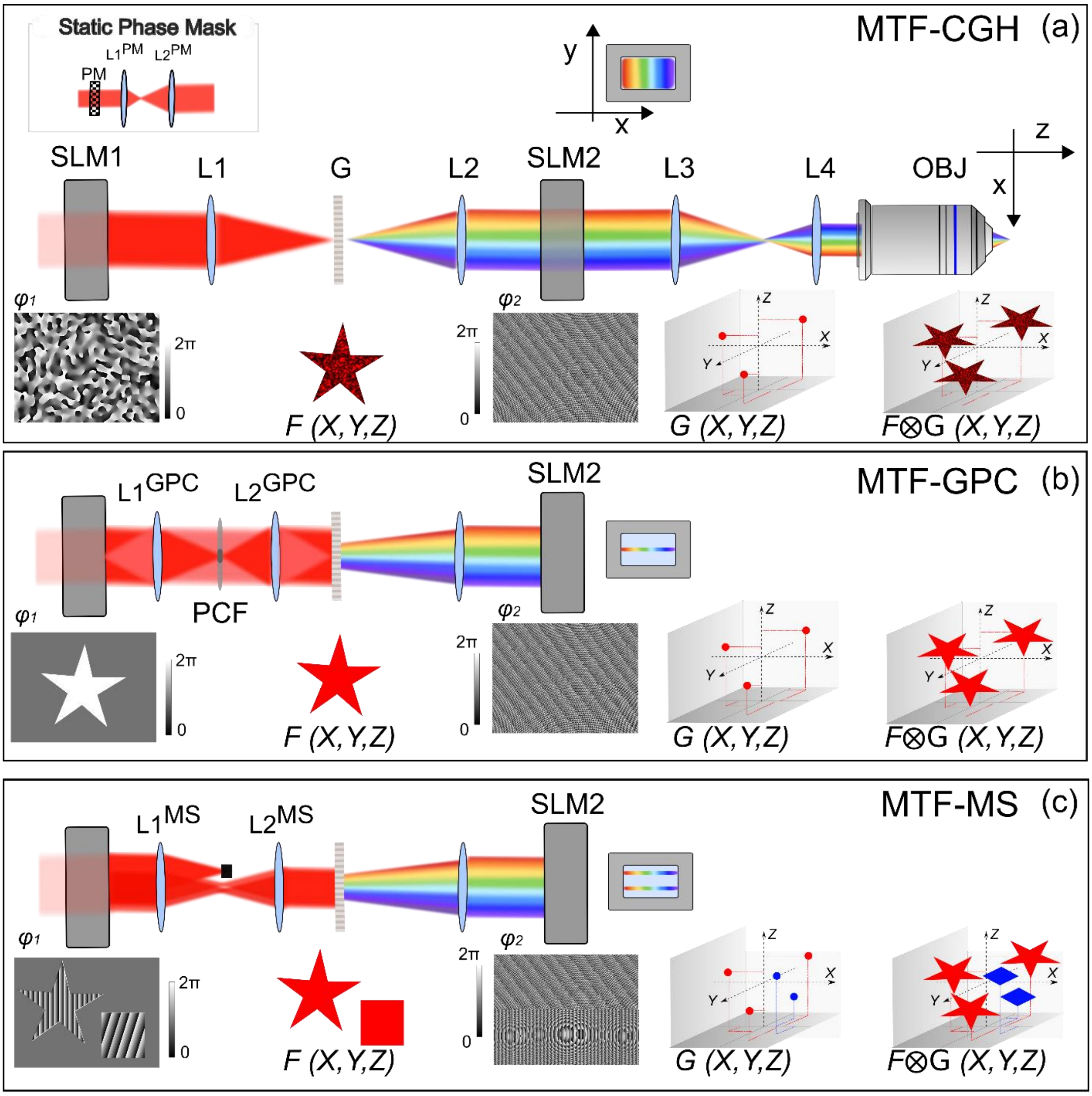

Fig. 1. Experimental setup and principle of MTF-LS. (a) In a first realization, the beam-shaping unit consisted of a dynamic CGH system, composed of a beam expander (BE) to match the active area of a SLM (SLM1), which performed the appropriate phase modulation for generating the desired 2D pattern. The 2D speckled illumination pattern was then focused on the grating (G) for TF through lens L1. The first diffraction order was collimated by lens L2 and directed to the second SLM (SLM2), which created the predefined 3D distribution of diffraction-limited spots at the sample positions thereby replicating the 2D pattern generated by SLM1. Lenses L3 and L4 conjugated the SLM2-plane at the objective (OBJ) back focal plane and scaled the beam at the objective back aperture. Close to SLM2 is shown the x-y illumination of SLM2. In the case of MTF-CGH the full active area of SLM2 was illuminated. Inset: the second realization of the beam-shaping unit was obtained by replacing SLM1 with a static phase mask producing a circular 20-μm diameter holographic spot. The telescope constituted by lenses L1PM and L2PM magnified the size of the static phase mask, to match the size of SLM2. (b) In a third realization, the beam shaper was a GPC-interferometer. Binary phase modulation for a circular spot of 12-μm diameter was imposed on SLM1, and lens L1GPC focused the beam on the phase contrast filter (PCF), which introduced a λ/2 phase delay to the low-spatial-frequency components over the high-spatial frequencies. Finally, the lens L2GPC recombined high and low-spatial frequencies to form the interference pattern at the output plane of the GPC-shaper, which coincided with the grating plane. In the case of MTF-GPC, the x-y light distribution on SLM2 resulted in a single focused line of dispersed colors, covering all the SLM active area in the x direction but greatly underfilling SLM2 in the y direction. (c) The forth configuration, MTF-MS, was obtained from the MTF-GPC one by removing the PCF and using SLM1 perform both amplitude shaping to create the desired shapes and phase shaping to optimize the illumination of SLM2. In the example SLM1 is used to create two different shapes. A holographic prism effect is imposed on the desired shapes to separate them from the unwanted light in the x direction, such as to create two spots aligned in the y direction after L1GPC. A beam stop blocks the undesired non-diffracted light (zero order), leaving only the desired shapes at the grating. The two shapes result in two parallel lines at SLM2, which is addressed with two different multiplexing holograms. (a-c) bottom: schematic principle of MTF-LS showing the phases applied on both SLMs, the 2D shape(s) at the diffraction grating position and the distribution of the targets at the sample position.

1. Dynamic CGH

In a first configuration (Fig.1a), the laser beam was expanded (10×) to fit the active area of SLM1 (LCOS-SLM X10468-07, Hamamatsu Photonics, resolution 800x600 pixels, 20 µm pixel size), which modulated the phase of the incoming beam with CGH, by using a standard GSA to create the desired 2D intensity pattern. The first image of the pattern was formed through the lens L1 (f_1=500 mm) on a blazed reflective diffraction grating (1200 l/mm, 53004ZD02-035R, Richardson Gratings; G) for TF. The grating was aligned such as the first diffraction-order was diffracted along the optical axis of the microscope, perpendicular to the grating plane. The beam was subsequently collimated by lens L2 (f_2=500 mm) and impinged on SLM2 (LCOS-SLM, X13138-07, Hamamatsu Photonics, 1280x1024 pixels, 12.5 µm pixel size). A beam stop physically blocked the SLM's zero order, i.e. the part of light not modulated by SLM1.

2. CGH with a static phase mask

In a second experiment we replaced SLM1 with a static phase mask (Fig.1a, inset) fabricated by etching of fused silica (Double Helix Optics, LLC) on the base of an 8-grey-level phase profile calculated with the GSA to produce a 20-µm diameter circular holographic spot. The laser beam was expanded (5×) to fit the 5×5 mm^2 of the encoded area of the mask. A subsequent 2:1 telescope (f_1^{PM}=200 mm, f_2^{PM}=400 mm) was then used to magnify the mask approximately to the size of SLM2.

3. GPC

In a third approach, we changed the beam-shaping unit to a GPC-interferometer (Fig.1b). Similarly to the setup previously described [21,24], the 10× expanded laser beam illuminated SLM1 on which we applied the desired binary phase profile. A first achromatic lens ($L1^{GPC}$, f_1^{GPC}=300 mm) focused the reflected beam from the SLM on the phase contrast filter (PCF), of a diameter ranging from 80 to 100 µm. The PCF phase-shifted by ~ $\lambda/2$ the low-spatial-frequency components [42]. A second achromatic lens ($L2^{GPC}$, f_2^{GPC}=60 mm) recombined the high (signal wave) and low (synthetic reference wave) spatial frequency components [43], thereby converting the SLM1 phase profile into a 2D illumination pattern at the diffraction grating. Importantly, in contrast to the two holographic cases described above, and as Fig.1b illustrates, in this configuration the lens after the diffraction grating (L2) focused the beam at SLM2 in the direction perpendicular to TF (*y*-direction, vertical to the optical table). The dispersion in the TF direction resulted in a focused line (approximately 16 mm in *x* and 1.5 mm in *y*) of different colors at SLM2.

4. Amplitude/phase modulation for multi shapes

The last configuration was obtained from the previous one by removing the PCF (Fig.1c). The plane of SLM1 was therefore conjugated to the diffraction grating and coincided with the Fourier plane of SLM2. In this configuration, SLM1 was used at the same time to perform 1) an amplitude shaping of the beam, which produced the desired 2D pattern(s) at the grating (and hence at the sample), and 2) a phase shaping to optimize the illumination of SLM2.

More precisely, we defined multiple, identical or different 2D shapes on SLM1, such that they would transform, after all the lenses and the objective, in the desired shape(s) at the sample position. As

Fig.1c shows, the inner parts of such shapes were patterned with precise holographic ‘prism’ phase profiles, encoding displacements in the *x-y* directions. As a result, we obtained multiple diffraction-limited spots after L1^{MS} (f=300 mm) aligned in the *y* direction and all displaced by the same quantity in the *x* direction from the center of the optical axis. Light falling out of the patterned regions on SLM1 propagated unaltered, therefore focusing into a central diffraction limited spot after L1^{MS}. Using a beam stop to block this part of the beam left only the desired shapes at the position of the diffraction grating, after collimation by L2^{MS} (f=60 mm). The introduced displacement in the *x* direction allowed us to better separate the desired spots from the unshaped light.

The multiple diffraction-limited spots transformed, after the dispersion of the diffraction grating, into multiple parallel horizontal lines at SLM2. In this way each line, which we could finely displace using CGH to hit the desired area on SLM2, encoded a different shape and could be independently multiplexed by dividing SLM2 in different regions.

C. The multiplexing unit

In all the described configurations, SLM2 was in the Fourier plane of the diffraction grating, and was conjugated to the back focal plane of the excitation microscope objective via lenses L3, f_3=1000 mm and L4, f_4=500 mm. The phase modulation applied on SLM2 produced a set of 3D diffraction-limited spots, which multiplexed the 2D pattern(s) created on the grating by the beam shaping unit. For precise axial displacement, the phase profile applied on SLM2 was calculated with a weighted Gerchberg-Saxton algorithm [3], modified to include the non-parabolic terms in the description of the microscope objective [5]. Also for SLM2, we blocked the SLM’s zero order using a beam stop. This created a small (~20 µm) inaccessible region in the central part of the FOE. To make use of the entire FOE, other solutions for suppressing the excitation effect of the zero order could be considered, as for example adding one or a pair of cylindrical lenses in front of the SLMs [44], or adding a destructively interfering spot to the phase hologram design [45,46].

In the MTF-MS approach SLM2 was tiled vertically into different holograms, as illustrated in Fig.1c, one for each shape defined by SLM1, and independently multiplexed them at the sample position.

A custom-designed software, Wavefront-Designer IV [9], written in C++ and using the open graphic library Qt 4.8.7, controlled both SLMs for the dynamic CGH configuration, using Gerchberg-Saxton-based algorithms. The software also included the phase corrections for the first orders Zernike aberrations.

D. Two-photon excitation of rhodamine layers

After the two-step phase manipulation, the beam was focused by a microscope objective at the sample position. The excitation microscope objective was an Olympus LUMPLFL 40xW/IR2, NA 0.8 for all the experiments except for those involving the static phase mask, which was designed to make a 20 µm spot at the sample position when using the objective Olympus LUMPLFL 60xW/IR2, NA 0.9. For characterizing the performances of the system, 2PE fluorescence from a thin (~1 µm) spin-coated fluorescent layer of rhodamine-6G in polymethyl methacrylate 2% w/v in chloroform was collected by a second microscope objective (Olympus XLUMPlanFL N 20XW, NA 1) in transmission geometry and detected with a CCD camera (CoolSNAP HQ2, Roper Scientific), using a dichroic mirror and a short pass filter for rejecting laser light (Chroma Technology 640DCSPXR; Semrock, Brightline Multiphoton Filter 750/SP). For 3D reconstruction of illumination volumes, the ‘imaging’ objective imaged the rhodamine-layer plane throughout all the experiment, while the excitation objective was scanned over the desired *z* range with a piezoelectric scanner (PI N-725.2A PIFOC).

We performed the analysis of the recorded stacks with Matlab, ImageJ and the Imaris software (Bitplane, Oxford Instruments). The 2PE fluorescence values for each spot were obtained by integrating the intensity of all the pixels in a circular area containing the spot, in the plane where the intensity was at its maximum value (i.e. the TF plane). Axial intensity distributions were obtained by integrating the intensity of the pixels in the same area for each plane of the recorded stack. Reported values for the axial confinement were the fit of the axial profile of the spots with a Lorentzian model and referred to the FWHM of the curves. Statistical data in axial resolution measurements were reported as mean±standard deviation.

E. Optical system used in biological experiments

The biological experiments were performed in a microscope using MTF-CGH with two SLMs for photostimulation and a commercial 2P-scanning microscope with galvanometric mirrors (VIVO, 2-PHOTON, 3i-Intelligent Imaging Innovations). The setup was built around a commercial upright microscope (Zeiss, Axio Examiner.Z1). The laser used in this case was a Ti:Sapphire oscillator (pulse width ~100 fs, repetition rate 80 MHz, tuning range 690-1040nm, Mai Tai DeepSee, Spectra-Physics). The photostimulation path consisted of a lens system (f_{BE1}=19 mm and f_{BE2}=150 mm) which expanded the laser beam (~8×) before SLM1 (LCOS-SLM X10468-07, Hamamatsu Photonics, resolution 800x600 pixels, 20 µm pixel size). The intermediate holographic images were then focused by a f_1=500 mm lens on the diffraction grating (830 lines/mm, Item No. 55262, Edmund Optics), followed by a second lens, f_2=500 mm, the SLM2 (LCOS-SLM X13138-07, Hamamatsu Photonics, 1280x1024 pixels, 12.5 µm pixel size) a 4-f telescope (f_4= f_5 =500 mm), and the last telescope before the objective with f_6=300 mm, f_7=250 mm. The objective used for the experiments was a water immersion 40x-NA 0.8 objective LUM PLAN FI/IR, Olympus.

The holographic path was then coupled with the commercial 2P-scanning module, made of 2P galvo-scanner and a detection based on two spectrally resolved GaAsP photomultipliers. Acquisition was controlled by SlideBook6 software (3i). The two illumination paths were recombined on a polarizer cube and shared the f_4=250 mm lens before entering the microscope. The switch between the optical path for scanning imaging and holographic illumination was performed with a movable mirror driven by a servomotor. The ower and pulses were controlled by a Pockels cell (350-80, Conoptics).

G. Kaede photoconversion

1. Zebrafish housing and handling

All procedures were approved by the Institut du Cerveau et de la Moelle épinière (ICM) and the National Ethics Committee (Comité National de Réflexion Ethique sur l'Expérimentation Animale Ce5/2011/056) based on E.U. legislation. Embryos were raised in an incubator at 28.5°C under a 14/10 light/dark cycle until the start of experimentation. Experiments were performed at room temperature (23-26°C) on 2-6 days post fertilization (dpf) larvae. All experiments were performed on Danio rerio embryos of AB and TL background and mitfa -/- animals were used to remove pigments above the hindbrain. For photoconversion experiments, we used double transgenic *Tg(HuC:gal4; UAS:kaede)* larvae where the HuC promoter drives pan-neuronal expression of Kaede at the larval stage. Embryos were dechorionated and screened for green fluorescence at 1 dpf. Larvae screened for Kaede fluorescence were later embedded laterally in 1.5% agarose. Larvae were anaesthetized in 0.02% tricaine (MS-222, Sigma-Aldrich, USA).

2. Photoconversion and imaging

A first 2P *z*-stack of green fluorescence was recorded with the scanning laser at 920 nm to map the location of neurons. We then selected a subset of neurons for photoconversion using MTF-CGH (wavelength 800 nm). The relative intensity between the spots was adjusted in order to compensate for both diffraction efficiency and tissue scattering (low diffraction efficiency or deeper regions) [3,34,47]. To minimize thermal damage during photoconversion, we delivered trains of 10-ms pulses at 50 Hz with total laser power around 130 mW (average illumination density of ~0.4 mW/µm^2), for periods of time that ranged from few tens of seconds to four minutes. After photoconversion, we acquired a second *z*-stack in the green and red channels with the scanning laser tuned to 780 nm to efficiently excite red-photoconverted fluorescence. The increase in red fluorescence in target cells was estimated by comparing their red emission after photoconversion with the average red emission from five non-targeted coplanar neighboring cells that were randomly selected.

H. sPA-GCaMP photoactivation

1. Drosophila preparation

We used female wandering third instar *Drosophila* larvae, expressing sPA-GCaMP6f and mCherry-nls in all motor neurons under the control of OK6-Gal4 [48] with the genotype *w*^{1118};OK6-Gal4/UAS-mCherry-nls;UAS-sPA-GCaMP6f/UAS-sPA-GCaMP6f. Larvae were dissected in HL3 saline containing, in mM: 70 NaCl, 5 KCl, 0.45 $CaCl_2 \cdot 2H_2O$, 20 $MgCl_2 \cdot 6H_2O$, 10 $NaHCO_3$, 5 trehalose, 115 sucrose, 5 HEPES (pH adjusted to 7.2). The CNS and peripheral motor neurons were exposed by making a longitudinal dorsal incision, removing all organs, and pinning the cuticle flat.

2.Photoactivation and imaging:

The initial reference ventral nerve cord 2P stack was performed at 920 nm, to record nuclear mCherry fluorescence. Photoactivation was performed with a 760 nm patterned. We used trains of 100-ms pulses at 5 Hz with total laser power around 130 mW (corresponding to an average illumination density of ~1 mW/um^2) and for periods of time that ranged from 1 up to 4 minutes. After activation, a 2P *z*-stack with the scanning laser at 920 nm was acquired to reconstruct both mCherry and activated sPA-GCaMP6f fluorescence. As a reference for total motor neuron density and sPA-GCaMP6f expression, large field 1P photoactivation was achieved separately (Zeiss LSM780 confocal microscope) by scanning the whole ventral nerve cord with a 405 nm diffraction limited spot and imaging with 488 nm and 561 nm excitation.

3. RESULTS

A. Multiplexed Temporally Focused Computer-Generated Holography (MTF-CGH)

We first tested the capabilities of our system by creating 50 replicas of a circular 15-µm-diameter shape using a conventional scheme for CGH based on a liquid-crystal SLM (SLM1; Fig. 1a). The 50 spots were visualized by measuring the 2PE fluorescence from a thin (sub-µm) rhodamine layer in a two-photon microscope equipped with a 40x, 0.8 NA objective (Fig. 2a and Visualization 1). Fig. 2b shows three replicas of the excitation spot at three different axial planes (-250, 0, 240 µm from the focal plane). One can notice the speckled intensity profile, typical of holographic spots [49], as well as the similarity of the speckle distribution for spots lying on different planes, confirming that each spot was indeed a replica of the original 2D shape. As previously described [3,34,47], by calculating the phase that we sent to SLM2 with a weighted Gerchberg-Saxton algorithm we could compensate for diffraction efficiency-induced intensity variations. In this way the 2PE fluorescence from the 50 spots varied less than 40% around the mean value, corresponding to less than 25% variation in the illumination intensity (Fig. 2c).

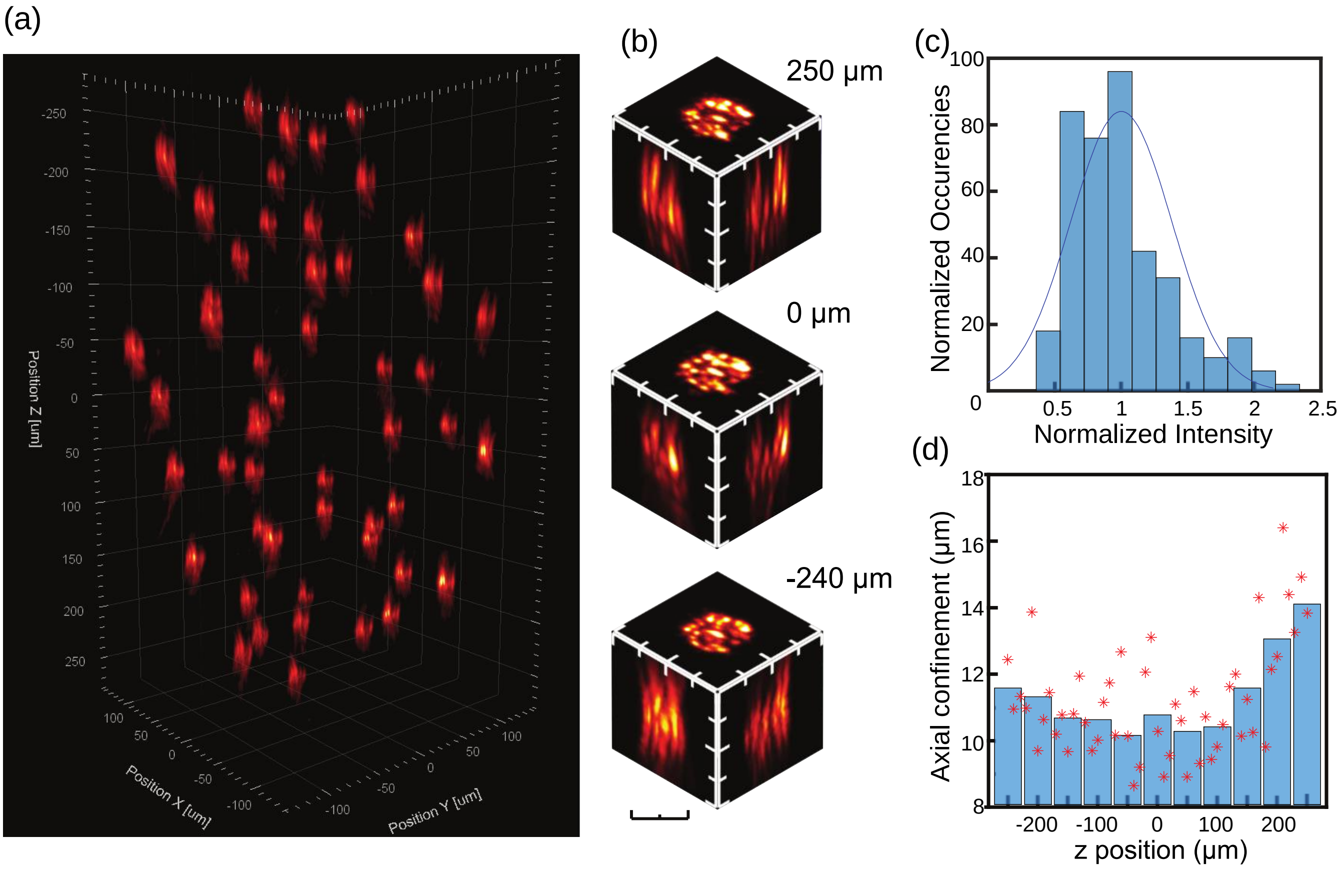

Fig. 2. MTF-CGH with two SLMs. (a) 2PE fluorescence volume representation of 50 holographic circular spots of 15-µm diameter, each of them lying on a different plane, in a volume of 300x300x500 µm^3. Average laser power at the sample position = 450 mW. (b) x-y, x-z and y-z projections of three spots, located at z=-250, 0, 240 µm from the focal plane. Scale bar: 15 µm. (c) Histogram of the maximal 2PE fluorescence intensity for each spot, normalized to the average intensity of all spots, after diffraction efficiency correction. The results represent an average for each plane from 4 different realizations of 50-spots light configuration. (d) Axial confinement, calculated as the FWHM of the axial intensity profile of each spot, as a function of the z position. Red stars represent the individual measurements for each spot (average on 4 different realizations of 50 spots) and blue bars show the mean values in a range of 50 µm around the designated z position. The mean value across the whole FOE was 11.1±1.8 µm FWHM.

In Fig. 2d we plot the full-width at half maximum (FWHM) of the axial intensity distribution for the 50 spots, which was found to vary between 8 and 16 µm, with a mean value across the whole investigated field of excitation (FOE ≈300×300×500 µm^3) of 11.1±1.8 µm and only few spots, at the very edge of the FOE in the z direction, reaching a FWHM >15 µm. As shown in detail in Figs. S1-S3 in Supplement 1, the FWHM was as small as 7 µm at the center of the FOE and increased both in the x-y plane (~0.4% and 0.5% per µm for the x and y direction, respectively) and in the z-direction (~0.4% per µm) as we moved away from the center of the FOE. Two main effects could cause such axial resolution broadening. First, large axial shifts required beams highly converging or diverging at the back aperture of the objective, whereas large lateral shifts corresponded to strongly tilted beams after SLM2. Therefore, in both cases, the optical elements that the beam propagated through after SLM2 introduced strong aberrations [50] and a possible cropping of the beam with consequent loss of spectral frequencies. A second possible contribution to the axial broadening may come from spatiotemporal coupling effects related to the spatial separation of the spectral frequencies at the position of SLM2 (Figs. S1-S3 in Supplement 1). This latter effect could also induce the few-micrometer axial shift of the spatiotemporal focal plane when shifting the illumination spots in the direction of TF (Fig. S2 in Supplement 1) not observed in the non-TF direction (Fig. S3 in Supplement 1).

Overall, these results demonstrate that our method can produce multiple spatiotemporally focused spots with a <15 µm axial resolution and uniform (within 40% from the average) light distribution across at least 300×300×500 µm^3. For comparison we show in Fig. S4 in Supplement 1 the same spot distribution without TF revealing a 3 times larger axial resolution.

B. MTF-CGH with a static phase mask

Next, we replaced SLM1 with a static custom-made 8-grey level phase-mask, which was fabricated to create a 20-µm diameter circular holographic spot (See Methods, Fig.3a) when coupled to a 60× objective (NA=0.9). Fig. 3b shows the 3D reconstruction of the 2PE fluorescence generated by 21 excitation spots arranged in a FOE of 130×130×400 µm^3. Fig. 3c illustrates the details of three replicas for three different z planes (-200, 0, 200 µm), demonstrating the preservation of the spot quality in a z range of 400 µm. Fig. 3d shows the dependence of the axial confinement for 21 spots in z-direction. The mean axial resolution was 11.0±4.0 µm, reaching a minimum value of ~5 µm at the center of the FOE. Using a larger NA and higher magnification objective improved the axial resolution at the center of the FOE but also induced a stronger dependence on the axial position (with the 40× objective the FWHM increased by ~0.4% per µm; with the 60× objective it increased by ~1% per µm), since in this case one needs a more divergent beam at the back aperture to obtain the same axial shift, resulting in larger aberrations. Overall, Fig. 3b demonstrates that the generation of multiple spatiotemporally focused spots can be achieved by replacing a dynamic SLM with a fixed phase. This limits the generation of patterns to pre-defined 2D shapes but enables to considerably reduce complexity and cost of the optical system.

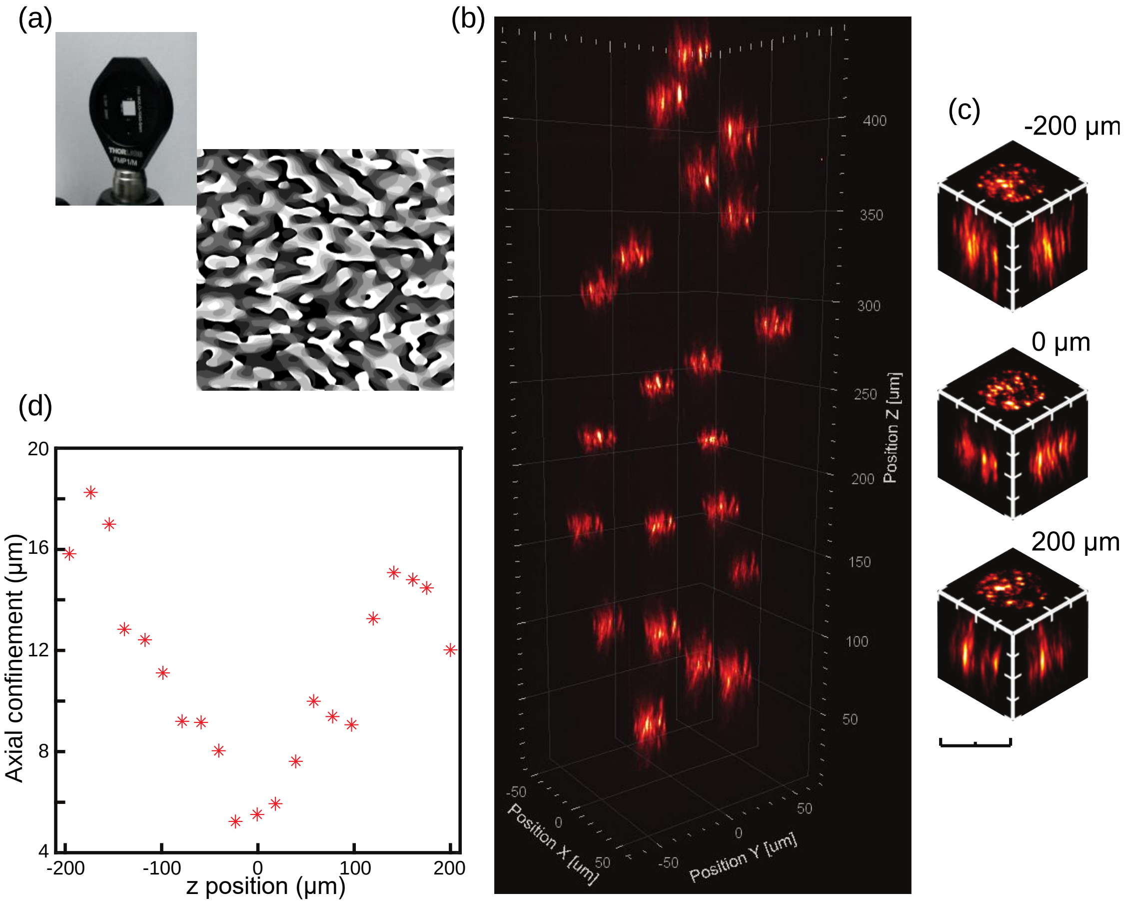

Fig. 3. MTF-CGH with a static phase-mask. (a) Left: Picture of the holographic static phase mask mounted on a 1-inch circular holder. Right: 8-level computer-generated hologram used to fabricate the static phase mask. (b) 2PE fluorescence volume representation of 20 holographic circular spots of 20-µm diameter, each of them lying on a different plane, in a volume of 130x130x400 µm3. Average laser power at the sample position = 200 mW. (c) x-y, x-z and y-z projections of three spots, located at z=-200, 0, 200 µm from the focal plane. Scale bar: 20 µm. (d) Axial confinement, calculated as the FWHM of the axial intensity profile of each spot, as a function of the z position. The mean value across the whole FOE was 11.0±4.0 µm FWHM.

C. Multiplexed Temporally Focused Generalized phase contrast (MTF-GPC)

In a third approach, we changed the beam-shaping unit to a GPC-interferometer (Fig. 1b, inset), whose image plane coincided with the grating for TF [21,24]. As Fig. 4 demonstrates, by coupling such a system with the holographic multiplexing of SLM2, we generated multiplexed temporally focused generalized phase contrast (MTF-GPC) patterns on a FOE of 200×200×200 µm^3. Fig. 4b shows the excitation spots at three different planes (-95, 0 and 100 µm) from which one can clearly recognize the uniform speckle-free intensity distribution typical of GPC. In agreement with previous findings [21], the flat optical wavefront of GPC enabled achieving a higher axial resolution (6.0±1.5 µm FWHM, ~5 µm at the centre of the FOE (Fig. 4c)) than the one achievable with CGH using the same objective (Fig. 2c). It has to be noted that in this configuration, as the scheme of Fig.1b illustrates, the dispersed beam after the diffraction grating was focused on SLM2, resulting in the illumination of only a small portion of it in the direction perpendicular to TF (y-direction, vertical in the optical table). In the TF direction instead, dispersion of spectral frequencies enabled illumination of the full SLM2 chip. With the optical components used in our case, a spot size of 12-µm diameter at the sample plane determined a vertical beam size at SLM2 of ~1.5 mm. This imposed a limit to the total laser power that could be used for avoiding damage of the SLM. In the described experiment, we limited the average laser power on SLM2 to ~ 0.2 W, which in turns limited the total number of spots that we could project. However, Fig.4 also interestingly demonstrates that, even when illuminating only a small portion of SLM2, the phase modulation that the laser beam underwent, was sufficient to create several replicas of the original shape. The next method that we present is based on this property.

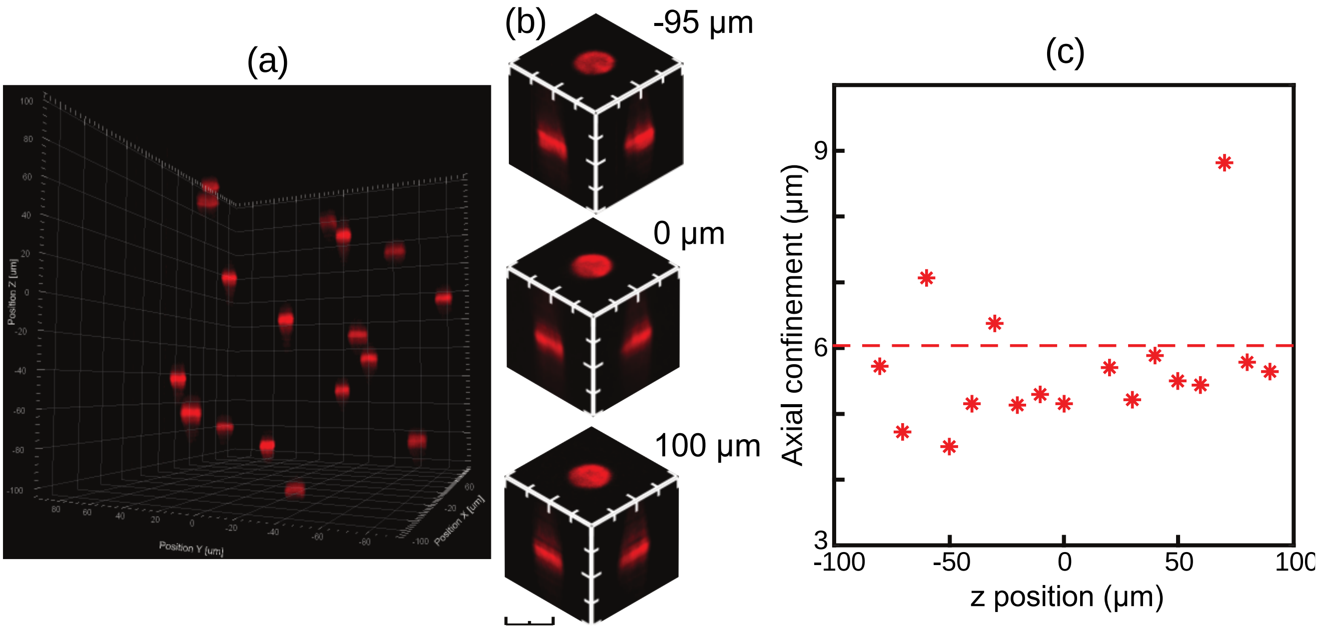

Fig. 4. MTF-GPC. (a) 2PE fluorescence volume representation of 17 GPC circular spots of 12-µm diameter, each of them lying on a different plane, in a volume of 200x200x200 µm3. Average laser power at the sample position = 150 mW. (b) x-y, x-z and y-z projections of three spots, located at z=-95, 0, 100 µm from the focal plane. Scale bar: 12 µm. (c) Axial confinement, calculated as the FWHM of the axial intensity profile of each spot, as a function of the z position. The mean value across the whole FOE was 6.0±1.5 µm FWHM.

D. Multiplexed Temporally Focused Multi Shapes (MTF-MS)

As a last configuration, we tested MTF-MS, which combined the advantages of previously described configurations, such as the uniform illumination (typical of GPC or LNAG), the multi-scale capability (as in MTF-GPC and MTF-CGH), and the possibility to independently generate different shapes simultaneously, as in [34]. The idea behind MTF-MS is based on the results we obtained in the MTF-GPC experiments (Fig.4) and particularly on the experimental evidence that illuminating SLM2 with a single line is sufficient for generating at least ~20 excitation spots. We therefore exploited this property to create multiple lines at SLM2, each of them aligned with an independent 3D hologram.

In Fig.5 we present the results obtained when making 4 different shapes (round, square, star, hexagon) with SLM1 and multiplexing them separately with SLM2 to make 40 spots at the sample plane (10 for each shape). Fig.5a shows the phase applied on SLM1. Similar to the example in Fig.1c, the 4 shapes were encoded with a holographic prism phase to displace them laterally at the same x- but different y- positions. This resulted in 4 vertically aligned diffraction-limited spots after the lens L1MS, plus a single spot displaced in the x direction corresponding to the unshaped light, blocked with the beam stop. This procedure resulted in a power loss of a factor of ~ 3 after the beam stop.

Fig. 5b,c show the 40 spots from a top and side view respectively. From the former image one can distinguish the different shapes, whereas the latter one illustrates the good axial resolution and homogeneity across the full FOE. From Fig.5d one can more closely see the 4 different shapes as they appeared at the sample plane. The quality of the spots was comparable to that obtained for MTF-GPC. Finally, in Fig. 5e we plot the FWHM of the axial intensity distribution for the 40 spots, which was found to vary between 6 and 13 µm, with a mean value across the whole investigated FOE (≈300×300×400 µm^3) of 9.5±1.5 µm.

These results confirm that MTF-MS removed some of the limitations inherent to other methods. In particular, by making several lines at SLM2 we could illuminate a much wider area compared to the case of MTF-GPC, use higher power and generate a larger amount of spots at the sample plane. At the same time, as SLM2 was divided in several 3D multiplexing holograms, MTF-MS was not limited in the achievable number of different planes, as in the case of [34].

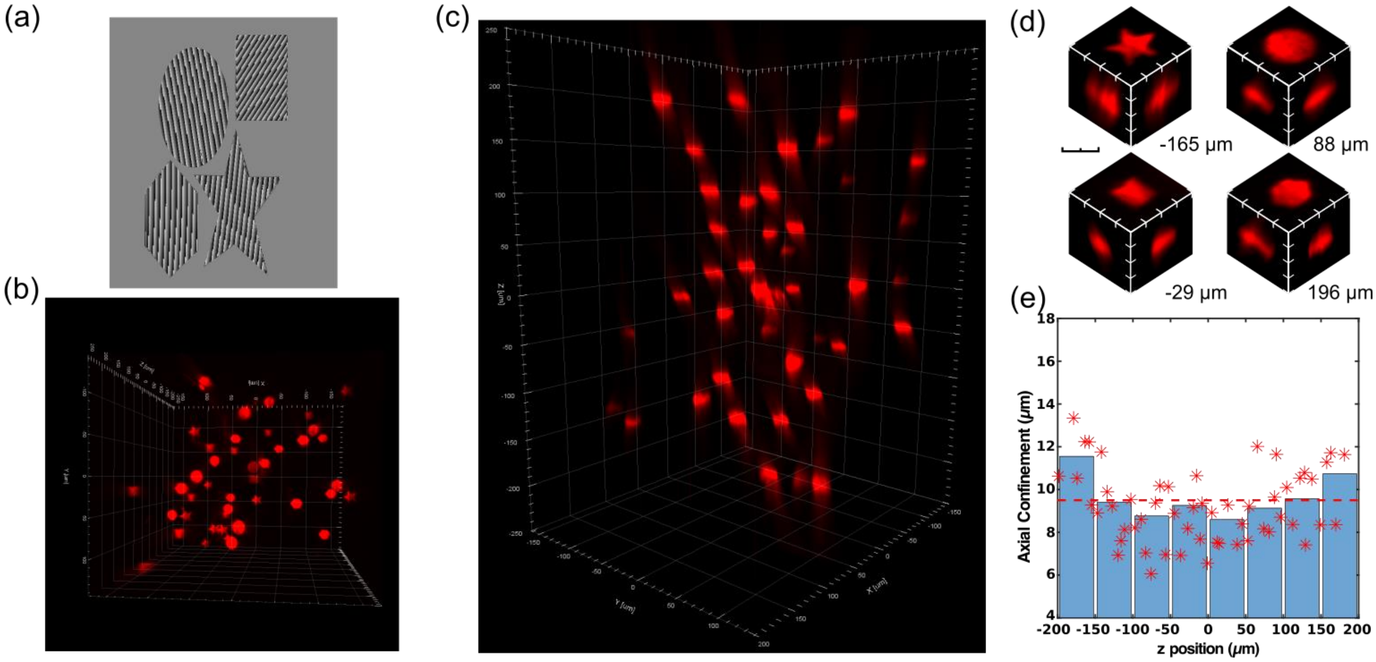

Fig. 5. MTF-MS. (a) Phase applied on SLM1 made up of 4 different shapes encoded with different prism holographic phases. The unshaped light was blocked using a beam stop. The shapes are elongated on SLM1 to compensate for the tilted illumination of the diffraction grating. After the diffraction grating the 4 shapes converted into 4 parallel lines at SLM2, which independently multiplexed them. (b-c) Top and side views of a 2PE fluorescence image of 40 spots, 10 for each shape, in a volume of 300×300×400 µm^3. Average laser power at the sample position = 400 mW. (d) x-y, x-z and y-z projections of the 4 different shapes at different planes. Scale bar = 15 µm. (e) Axial confinement, calculated as the FWHM of the axial intensity profile of each spot, as a function of the z position. The mean value across the whole FOE was 9.5±1.5 µm FWHM. Red stars represent the FWHM measurements at each z position (average on 4 different

E. In-vivo high resolution multi-cell targeting

We finally applied our reference technique for the 3D generation of multiple temporally focused spots, namely MTF-CGH, to two different biological paradigms: the 2P-photoconversion of Kaede protein [51] in zebrafish larvae (Fig. 6 and S5 in Supplement 1) and the 2P photoactivation of superfolder GCaMP (PA-GCaMP) in drosophila larvae [40] (Fig. 7).

1. Kaede photoconversion in the hindbrain of zebrafish larvae

We prepared samples of zebrafish larvae expressing the Kaede protein in a very dense population of neurons of the hindbrain using Tg(HuC:gal4;UAS:Kaede) transgenic larvae (Fig. 6a). Kaede is a photoconvertible protein that emits initially green fluorescence and red-shifts its emission under UV [51] or near-infrared 2P illumination [52]. We first acquired a 2P scanning z-stack of the green fluorescence from a ~200×200×300 μm^3 volume in the larva hindbrain (Fig. 6b), from which we selected 11 individual neurons, distributed at 11 different depths, for photoconversion. We then precisely tailored the 3D patterned illumination to simultaneously photoconvert these neurons using 2P excitation (λ=800 nm). For this experiment SLM1 generated a circular spot of 6 µm in diameter to excite individual neurons, while SLM2 multiplied such a shape, temporally focused by the diffraction grating, at 11 distinct positions. SLM2 was also used to adjust the relative intensity of each spot to compensate for both diffraction efficiency and losses due to scattering through different depth of the tissue (see Methods).

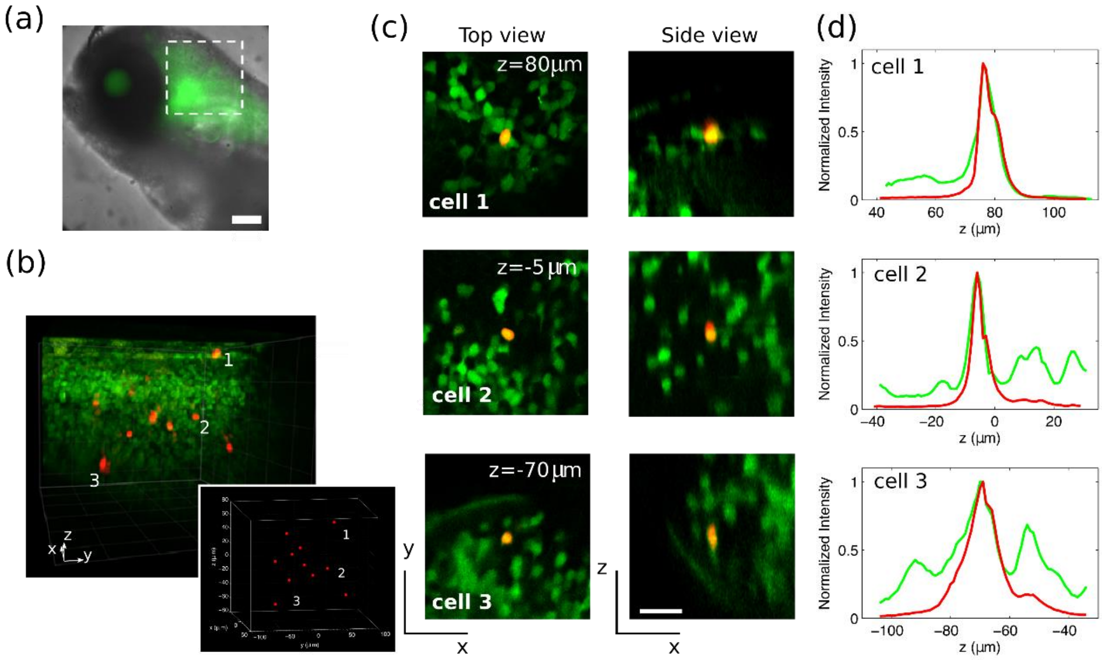

Fig. 6. Simultaneous photoconversion of Kaede expressing neurons in zebrafish. (a) Superposed brightfield and widefield fluorescence images of the head of a double transgenic Tg(HuC:gal4; UAS:kaede) zebrafish larvae. The dashed square represents the approximate area where we performed photoconversion. Scale bar: 100 μm. (b) 3D view of a 2P stack (λimaging=780 nm) merging green and red fluorescence after targeted simultaneous 2P photoconversion (λconversion=800 nm) of a set of 11 neurons. Represented volume: 178x178x251 μm3. The inset represents the 3D MTF-CGH illumination pattern composed of multiple 6-μm diameter spots used for photoconversion. (c) Top and side single frame view extracted from the 2P stack reported in b, zooming on 3 representative photoconverted cells (labelled 1-3 in panel b). Scale bar: 20 μm. (d) Normalized axial intensity profiles of green and red fluorescence integrated over z for the 3 cells reported in c.

Finally, we acquired a second 2P scanning *z*-stack to measure both the green and red fluorescence. Photoconversion increased the red fluorescence in the target cells by more than a factor of 15 (19±10 fold; n=11 targeted cells) with respect to neighbouring cells (Fig. 6b-d). Top and lateral views from 3 photoconverted cells are reported in Fig. 6c (more cells are shown in S5 in Supplement 1). The corresponding normalized fluorescence axial profiles (Fig. 6d) show red fluorescence induced solely in the targeted neurons. This confirms the precise targeting and single-cell resolution (FWHM of red fluorescence axial profiles = 7.7 ± 3.3; n=11 cells) of the patterned illumination, down to ~200 μm deep in the brain tissue with minimal photoconversion induced in neighboring cells, despite the highly packed neuron ensemble.

2. Targeted Simultaneous 3D Photoactivation of sPA-GCaMP6f in Drosophilae larvae

We subsequently tested the potential of our system in the central nervous system of *Drosophila* larvae, whose cells expressed a recently developed photoactivable genetically encoded calcium indicator, sPA-GCaMP6f. Such indicator switches from an original dark state to a bright state via UV or 2P infrared illumination [40].

Larvae were dissected to expose the ventral nerve cord where sPA-GCaMP6f was expressed in all motor neurons (*OK6-Gal4*). These neurons co-expressed a nuclear mCherry (Fig.7 a,b). A 2P image of the mCherry fluorescence allowed us to reconstruct the 3D distribution of the sPA-GCaMP6f expressing motorneurons (Fig. 7a).

We then selected for 2P photoactivation at 760 nm with our MTF-CGH system a subset of 6 individual motorneurons, belonging to a stereotyped group that all projected to a common hemisegment in the larval body (Fig. 7c).

We generated 6 different 5 μm holographic spots aimed at the cell nuclei. Subsequent imaging of the green fluorescence from sPA-GCaMP6f monitored the photoactivation of sPA-GCaMP6f molecules. As Fig. 7c-d show, green fluorescence increased >15 times only in the targeted neurons. Photoactivation of untargeted neighboring cells was minimal, despite the very dense distribution of sPA-GCaMP6f expressing neurons and the even denser neuropil containing the processes of the expressing neurons (see Fig. 7b, where photoactivation was done by wide-field 1P illumination). Within minutes after

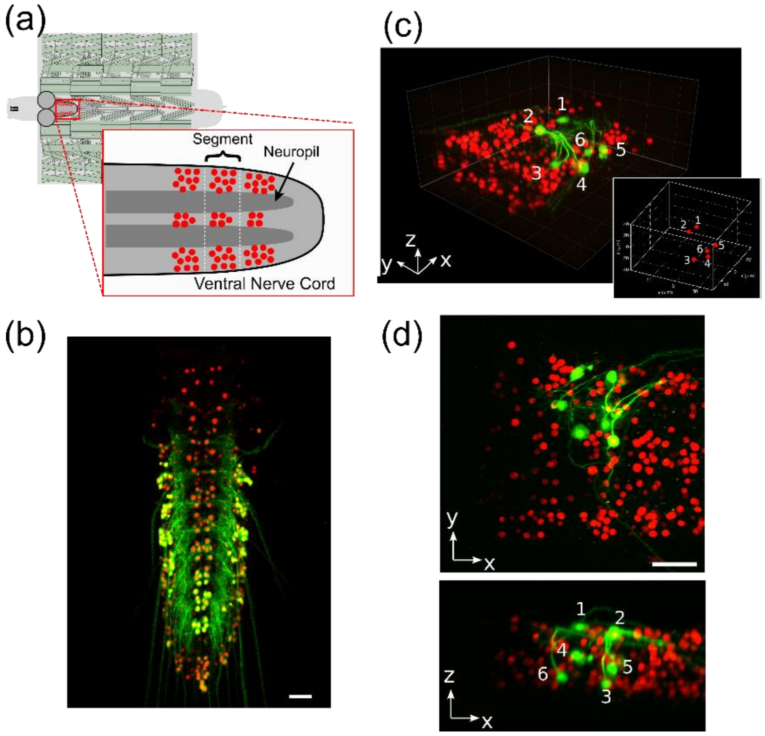

Fig. 7. ***Photoactivation of sPA-GCaMP in drosophila larvae.*** *(a) Schematic representation of a dissected drosophila larva. The dissection exposes the ventral cord (red rectangle) in which motor neurons co-express nuclear mCherry (red dots) and photoactivable sPA-GCaMP6f. (b) Max projection of a z-stack of green (sPA-GCaMP6f) and red (mCherry) fluorescence performed after wide 1P (405 nm) photoactivation of motorneurons of the ventral central cord (see Methods). Image acquired on a confocal microscope. Scale bar: 30 μm. (c) 3D view of a 2P stack ($\lambda_{imaging}$=920 nm) merging green and red fluorescence after 2P ($\lambda_{activation}$=760 nm) targeted simultaneous photoactivation of a set of 6 motor neurons (labeled with numbers). Represented volume: 178x178x140 μm^3. The inset represents the 3D MTF-CGH illumination pattern composed of multiple 5-μm diameter spots used for photoactivation. (d) Top (up) and side (down) max projection of green and red fluorescent after photoconversion, corresponding to panel c. Numbers label targeted photoactivated neurons. Scale bar: 30 μm.*

photoactivation, neuronal processes of the targeted cells could be clearly distinguished from background (Fig. 7c-d), making it possible to track neuronal morphology precisely.

3. DISCUSSION

We have demonstrated a versatile optical system enabling the generation of multiple temporally focused patterns in 3D in a large volume. The system is based on two independent beam-shaping steps: the first one defines the lateral shape of the illumination spot(s) and projects it on the TF grating; the second performs a lateral and axial multiplexing of the original shape(s) in the sample volume.

In this configuration, the total number of excitation spots, as well as the size of the achievable FOE at the target volume and the number of achievable planes are mostly dependent on the performances of SLM2 (total number of illuminated pixels, pixel size, number of grey levels). This feature makes our system compatible with several different beam-shaping approaches such as dynamic CGH, CGH with a static phase mask, GPC interferometry and amplitude/phase shaping approaches, each of them with advantages and limitations. This is in contrast to the previous approach [34], in which, because the lateral and axial displacement of the 3D spots was performed by different SLMs, the performances of the system were determined by the properties of both SLMs.

Among the approaches that we tested, dynamic CGH, which uses a reconfigurable liquid crystal SLM, allows for high flexibility and quick lateral shaping capability. Replacing the bulky SLM with a smaller static phase mask reduces the flexibility of the system but leads to a simpler, more compact and cost-effective optical design. A phase mask made on a single substrate with different holograms imprinted on it could offer the flexibility to choose among different spot sizes and shapes and hence to cover more applications.

Similar to dynamic CGH, GPC is capable of quickly adjusting the spot size and shape. Moreover, it generates illumination patterns with superior axial resolution and higher uniformity (speckle-free). In the past, the main limitations of GPC were the reduced FOE imposed by the constrain of keeping the ratio of the illuminated over the non-illuminated area in the FOE to 0.25 [21], as well as the lack of 3D light shaping capability. As previously shown in [36,37], using SLM2 for axial and lateral multiplexing removes both these constrains. Our MTF-GPC approach generalizes the scheme of [36] to the use of TF, making the approach highly suitable for in depth studies. Yet, the <2 mm vertical size of the beam at SLM2 limits the power that can be used and therefore the maximum number of achievable targets.

To overcome this limitation, we have demonstrated a new configuration (MTF-MS) where SLM1 is used both as an amplitude shaper to define multiple spots even of different shapes, and as a phase shaper to optimize the illumination of SLM2. This scheme has two major advantages: 1) it generates uniform (speckle-free) illumination patterns, as with MTF-GPC, but, because of the improved illumination of

SLM2, it allows one to use more power and therefore to create more spots than the GPC counterpart. 2) Similarly to [34], it can be used to generate multiple shapes at the same time, but with no limitation in the maximum number of achievable planes, or a degradation in the spot quality for large number of planes, which constituted the main issues of the approach of [34].

The main disadvantage of MTF-MS is the unavoidable power loss, which is inherent in amplitude shapers. As the undesired part of the light impinging on SLM1 is physically blocked (see Fig.1c), this method leads to a power loss of a factor of ~3, when making 4 different shapes (see Fig.5). Replacing SLM1 with a GPC interferometer to create the desired shapes, followed by a static holographic phase mask encoding different displacements in the *y* direction to optimize the illumination of SLM2 could completely solve this problem.

For all the MTF-LS techniques described in this paper, the total FOE at the sample position depends mainly on the SLM2 pixel size and the telescope used to conjugate the SLM2 plane with the objective back aperture. When using the 40×, 0.8 NA objective our system had a theoretical FOE [34] of 750×750×990 μm^3. Experimentally we could demonstrate an axial resolution as small as 5-7 µm at the center of the FOE, and <15 µm throughout the whole FOE, with an average intensity per spot varying less then 40% within a FOE of 300×300×500 μm^3, limited by the size of the optics (mirrors and lenses) placed after SLM2. An optical design using larger optical elements and careful aberration correction should enable to reach the theoretical FOE.

Similar to our scheme, a multiplexing SLM was recently used to project low-NA temporally focused Gaussian beams [38,39] in 3D. This approach, of easier implementation, is restricted to the generation of a static and single-sized spot, lacking also the capability of creating multiple shapes simultaneously. As an additional limitation, similar to the case of MTF-GPC, using Gaussian beams results in a vertical under-fill of SLM2. To overcome this Pégard and colleagues [38] defocused the laser beam before the diffraction grating, achieving a better illumination of SLM2. This procedure however, had the clear downside of shifting away the spatial and temporal foci with respect to each other, which appeared as separate features at the sample plane, thus spoiling the axial propagation of the temporally focused beam [53].

We applied MTF-CGH to the *in vivo* 2P conversion of Kaede protein in the brain of zebrafish larvae and to the *in vivo* 2P activation of a photoactivable version of GCaMP (sPA-GCaMP6f) in the central nervous system of fruit flies. In both applications, we demonstrated in-depth simultaneous targeting of multiple individual neurons. Temporally focused patterns, as already demonstrated in previous works [24,34], are robust against propagation through scattering media, which allowed individual neurons within a highly packed ensemble to be precisely targeted up to a depth of 200 µm, with minimal spurious fluorescence induced in neighboring cells. The primary limitation in photo-converting a higher number of targets was the total laser power available at each position. Longer exposure times combined with the introduction of real-time movement correction (as well as the use of more powerful lasers) should allow increasing the number of targeted neurons. The capability of the optical system to precisely target multiple cells can be applied to a large variety of photo-switchable proteins [54,55], and could be useful for tracking specific cellular ensembles *in vivo* and during development. In particular, targeted photoactivation of calcium indicators opens the way to the simultaneous morphological and functional investigation of specific neuronal sub-circuits where cells are either too dense for traditional analysis, or where there is a lack of cell-specific genetic driver lines [33,40].

4. CONCLUSIONS

In this work we demonstrated, thoroughly characterized and applied to biological proofs-of-principles a novel optical system enabling the generation of multiple temporally focused illumination targets at arbitrary 3D locations. The system is robust and versatile, which makes it compatible with several different beam-shaping approaches.

The demonstrated MTF-LS techniques could therefore constitute the basis of a reliable approach for 3D 'all-optical' brain circuits control on large scales, especially if combined with 3D imaging techniques [56–59]. At the same time, its use is not only limited to neuronal activation, but could as well be extended, in combination with camera detections [60,61] and multi-plane spatial demixing algorithms [62], to fast volumetric functional imaging, using calcium or voltage sensors. More generally, any application relying on light patterning methods and non-linear phenomena, such as photo-polymerization [63], optical data storage and photolithography [64], could benefit from this technique.

Acknowledgments

We thank Vincent de Sars for software developing, Leslie Kimerling (Double Helix LLC) for providing the phase mask, Coherent Inc. for the loan of the Fidelity laser, Intelligent Imaging Innovations, Inc. for providing the 2P scanning microscope, Martin Booth for useful discussions, Anna Segú-Cristina for help in the preparation of the zebrafish sample, SCM (Service Commun de Miscroscopie – Faculté des Sciences Fondamentales et Biomédicales - Paris) for providing the software Imaris (Imaris v8.4, Bitplane, software available at www.bitplane.com), Sophie Nunes-Figueiredo from the ICM zebrafish facility for animal care, Sorbonne Universités, UPMC Univ. Paris 06, Inserm, CNRS, AP-HP, Hôpital Pitié-Salpêtrière), the team of Jean-René Huynh (Institut Curie, Paris) and of Bassem Hassan (ICM, Paris) for their help with the Drosophila's transgenic lines. This research was developed with funding from the Defense Advanced Research Projects Agency (DARPA), Contract No. N66001-17-C-4015. The views, opinions and/or findings expressed are those of the author and should not be interpreted as representing the official views or policies of the Department of Defense or the U.S. Government. It received support as well from the 'Agence Nationale de la Recherche' (grant ANR-15-CE19-0001-01, 3DHoloPAc and ANR-14-CE13-0016, Holohub), the Human Frontiers Science Program (Grant RGP0015/2016), Getty Lab, the National Institute of Health (Grant NIH U01NS090501-03). N.A. received funding from the European Union's Horizon 2020 research and innovation programme under the Marie Skłodowska-Curie grant agreement no. 746173. C.W. received funding from the European Research Council (Starting grant #311673) and the New York Stem Cell Foundation as a Robertson Neuroscience Investigator

Supplementary

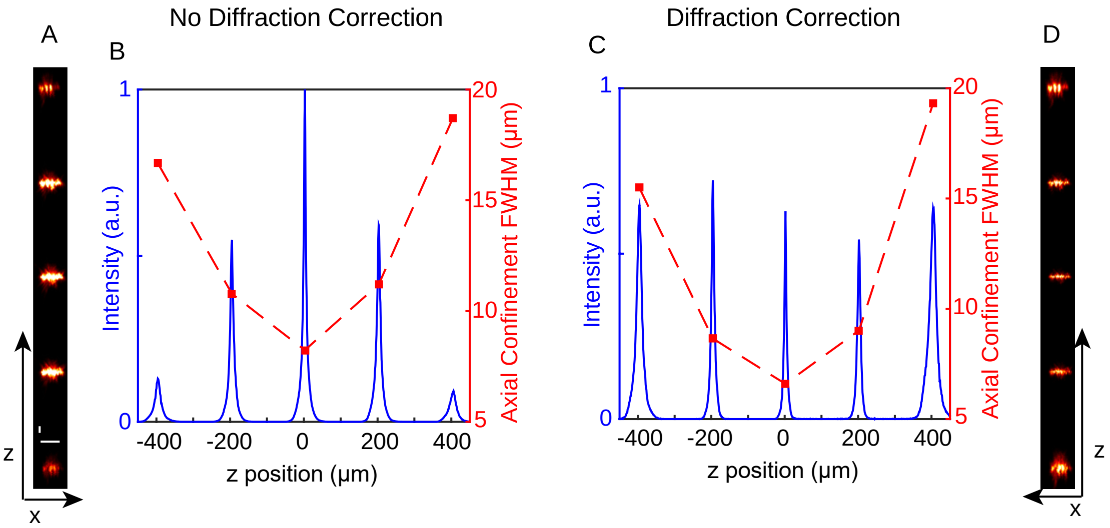

Figure S1. Characterization of holographic spots in z*. (****a****) x-z view of 7 holographic spots (15 µm in diameter) placed one on top of the other, at relative distances of 200 µm in z. No diffraction-efficiency correction was applied in the experiment. Scale bars: 15 µm. In order to properly visualize the image the pixel are not square, which is why the scale bars have different lengths in z and x for the same real length of 15 µm. Note that, as a consequence of the lower diffraction efficiency of SLM2 when making spots out of the centre of the FOE, the spots are less intense as one moves away from the central position. (****b****) Intensity profiles (blue curves) and axial confinement (red filled squares) for the 7 spots in (a). One can notice the lower signal produced by the spots far from the centre. The second notable effect is the degradation of the axial confinement as one moves away from z=0. The dashed line is a guide to the eye. (****c****) Same as (****b****) but when diffraction efficiency correction was applied. We could correct for the lower signal and produce spots with similar maximal intensity in region from (-600 to 600 µm) in z. (****d****) Same as (****a****) but when the diffraction-efficiency correction was applied. Without saturating the image one sees all the 7 spots at the same time with similar intensity.*

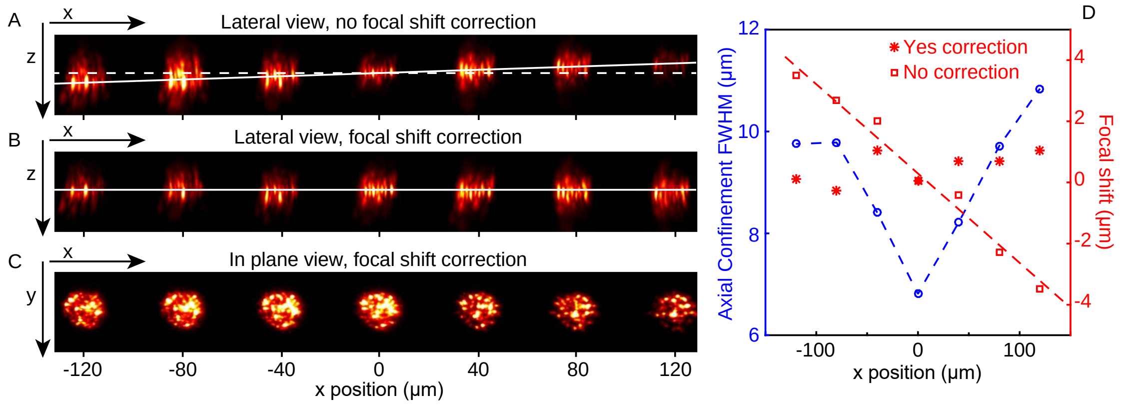

***Figure S2*. *Characterization of holographic spots in the TF direction (x axis)*.** *(**a**) x-z view of 7 holographic spots (15 μm in diameter) placed in a line along the TF direction (x axis) at relative distances of 40 μm. Two effects are visible: i) the axial confinement got worse when approaching the edges of the FOE in x; and ii) the focal position was not exactly the same for all the spots but shifted linearly, as indicated by the solid line. As the latter effect was not observed in the y direction (i.e. the direction perpendicular to TF, see **Supplementary Figure 3**), we attribute this to spectral frequencies dispersion by the diffraction grating, which in turns caused an asymmetry at the position of SLM2 (spectral frequencies were dispersed in the x but not in the y direction). This is similar to pulse-shaping setups, in which the separation of the spectral frequencies at the SLM gives the possibility to change the time profile of the laser pulse. However, contrary to what is commonly done in a pulse shaping experiment, in this case we were not correcting for the intrinsic wavelength dependence of SLMs. We can then speculate that our system likely introduced spatio-temporal coupling effects, which might be the cause of the axial shift. An improvement of the current setup will therefore consist in a systematic study of this possible spatio-temporal effects, in order to get advantage from the double regime that the SLM2 operates with, i.e the spatial and time domain. (**b**) Same as (**a**) but after correcting the focal shift holographically, i.e. by introducing an opposite focal shift with the SLM. The white solid line indicates the new focal plane of the spots. (**c**) x-y view of the 7 spots. (**d**) Behaviour of the axial confinement (blue circles) and the focal position for the 7 spots before (red squares) and after (red crosses) focal shift correction. Indeed, the focal position shifts linearly with the x coordinate when no correction is applied. The red dashed line is a guide to the eye.*

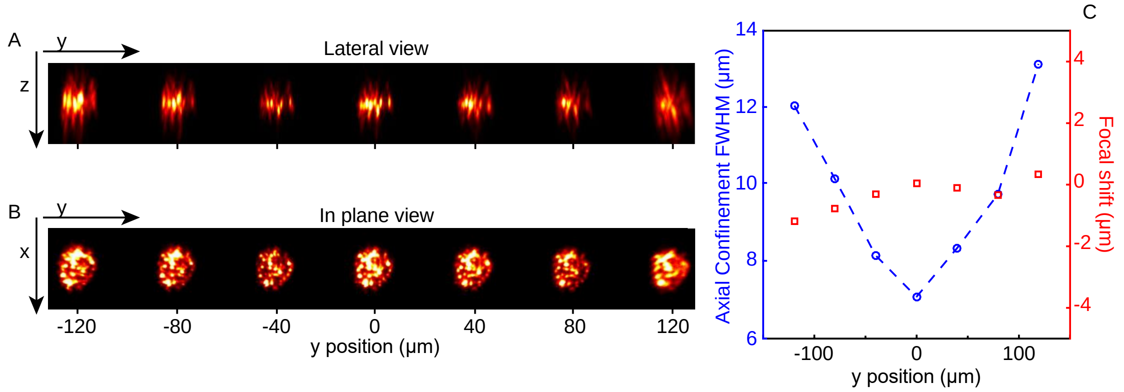

***Figure S3*. *Characterization of holographic spots in the perpendicular to TF direction (y axis)*.** *(**a**) y-z view of 7 holographic spots (15 μm in diameter) placed in a line along the direction perpendicular to TF (y axis) at relative distances of 40 μm. The axial confinement got worse close to the edges of the FOE in y. In contrast to the TF direction, in this case all the spots focused in the same z position. (**b**) x-y view of the 7 spots. (**c**) Behaviour of the axial confinement (blue circles) and the focal position (red squares) for the 7 spots. The axial confinement was worse at the edges of the FOE, while the focal position was the same for all the spots.*

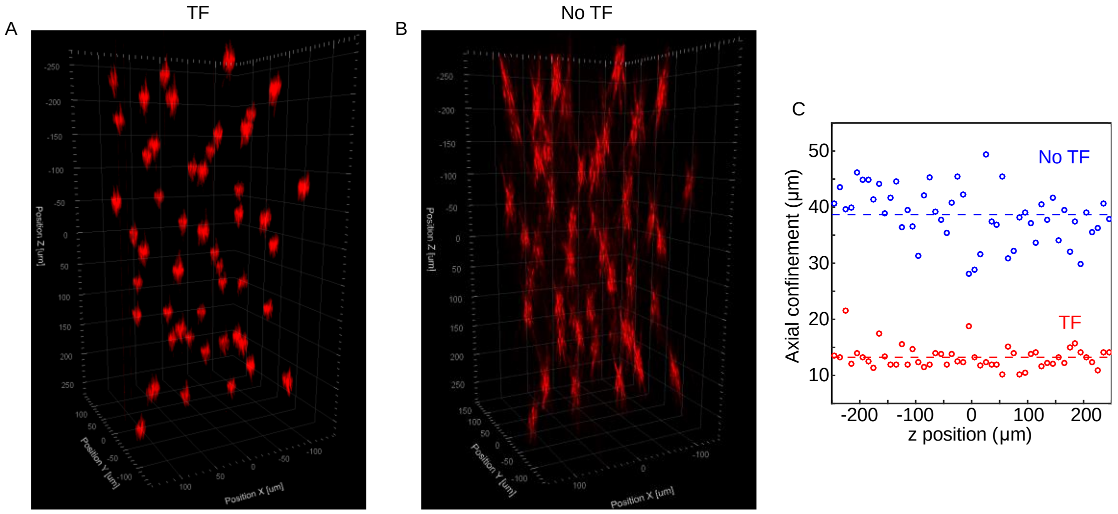

***Figure S4**. **Comparison of 3D-CGH-TF with and without TF**. (**a**) 2PE fluorescence volume representation of 50 holographic temporally-focused circular spots of 15 μm diameter, each of them lying on a different plane, in a volume of 300x300x500 μm^3. The experimental procedure was the same as the one for Fig. 2 of the main manuscript. (**b**) Same as (**a**) but without TF. In this case the diffraction grating for dispersing the spectral frequencies and performing TF was replaced by a mirror. Significant increase in axial resolution when TF was applied, allowed us to better distinguish neighbouring holographic spots in the 3 directions. (**c**) Axial confinement, calculated as the FWHM of the axial intensity profile of each spot, as a function of the z position for the TF case (red symbols) and no TF (blue symbols) case. The red and blue dashed lines represent the mean FWHM for the two cases which was ~13 μm in the TF case and ~38 μm in the no TF case.*

References

1. J. E. Curtis, B. A. Koss, and D. G. Grier, "Dynamic holographic optical tweezers.," Opt. Communi. **207**, 169 (2002).

2. J. Leach, K. Wulff, G. Sinclair, P. Jordan, J. Courtial, L. Thomson, G. Gibson, K. Karunwi, J. Cooper, Z. J. Laczik, and M. J. M. J. Padgett, "Interactive approach to optical tweezers control," Appl Opt **45**, 897 (2006).

3. R. Di Leonardo, F. Ianni, and G. Ruocco, "Computer generation of optimal holograms for optical trap arrays.," Opt. Express **15**, 1913–22 (2007).

4. R. W. Gerchberg and W. O. Saxton, "A pratical algorithm for the determination of the phase from image and diffraction pictures," Optik (Stuttg). **35**, 237–246 (1972).

5. S. Yang, E. Papagiakoumou, M. Guillon, V. de Sars, C. M. Tang, and V. Emiliani, "Three-dimensional holographic photostimulation of the dendritic arbor," J. Neural Eng. **8**, 46002 (2011).

6. F. Anselmi, C. Ventalon, A. Begue, D. Ogden, and V. Emiliani, "Three-dimensional imaging and photostimulation by remote-focusing and holographic light patterning," Proc Natl Acad Sci U S A **108**, 19504–19509 (2011).

7. V. Nikolenko, B. O. Watson, R. Araya, A. Woodruff, D. S. Peterka, and R. Yuste, "SLM Microscopy: Scanless Two-Photon Imaging and Photostimulation with Spatial Light Modulators.," Front. Neural Circuits **2**, 5 (2008).

8. V. R. Daria, C. Stricker, R. Bowman, S. Redman, and H. A. Bachor, "Arbitrary multisite two-photon excitation in four dimensions," Appl. Phys. Lett. **95**, (2009).

9. C. Lutz, T. S. Otis, V. DeSars, S. Charpak, D. A. DiGregorio, and V. Emiliani, "Holographic photolysis of caged neurotransmitters.," Nat. Methods **5**, 821–827 (2008).

10. K. Deisseroth, "Optogenetics," Nat. Methods **8**, 26–29 (2011).

11. K. Deisseroth, "Optogenetics : 10 years of microbial opsins in neuroscience," Nat. Neurosci. **18**, 1213–1225 (2015).

12. E. Ronzitti, R. Conti, V. Zampini, D. Tanese, A. J. Foust, N. Klapoetke, E. S. Boyden, E. Papagiakoumou, and V. Emiliani, "Sub-millisecond optogenetic control of neuronal firing with two-photon holographic photoactivation of Chronos," J. Neurosci. **37**, 10679–10689 (2017).

13. E. Chaigneau, E. Ronzitti, M. A. Gajowa, G. J. Soler-Llavina, D. Tanese, A. Y. B. Brureau, E. Papagiakoumou, H. Zeng, and V. Emiliani, "Two-Photon Holographic Stimulation of ReaChR," Front. Cell. Neurosci. **10**, 234 (2016).

14. A. Bègue, E. Papagiakoumou, B. Leshem, R. Conti, L. Enke, D. Oron, and V. Emiliani, "Two-photon excitation in scattering media by spatiotemporally shaped beams and their application in optogenetic stimulation," Biomed. Opt. Express **4**, 2869–2879 (2013).

15. D. Oron, E. Tal, and Y. Silberberg, "Scanningless depth-resolved microscopy," Opt. Express **13**, 1468–1476 (2005).

16. G. Zhu, J. van Howe, M. Durst, W. Zipfel, and C. Xu, "Simultaneous spatial and temporal focusing of femtosecond pulses.," Opt. Express **13**, 2153–2159 (2005).

17. E. Papagiakoumou, V. de Sars, D. Oron, and V. Emiliani, "Patterned two-photon illumination by spatiotemporal shaping of ultrashort pulses.," Opt. Express **16**, 22039–22047 (2008).

18. J. Glückstad, D. Palima, P. J. Rodrigo, and C. A. Alonzo, "Laser projection using generalized phase contrast," Opt. Lett. **32**, 3281 (2007).

19. J. P. Rickgauer, K. Deisseroth, and D. W. Tank, "Simultaneous cellular-resolution optical perturbation and imaging of place cell firing fields," Nat. Neurosci. **17**, 1816–1824 (2014).

20. B. K. Andrasfalvy, B. V Zemelman, J. Tang, and A. Vaziri, "Two-photon single-cell optogenetic control of neuronal activity by sculpted light," Proc. Natl. Acad. Sci. **107**, 11981–11986 (2010).

21. E. Papagiakoumou, F. Anselmi, A. Bègue, V. De Sars, J. Glueckstad, E. Y. Isacoff, and V. Emiliani, "Scanless two-photon excitation of channelrhodopsin-2," Nat. Methods **7**, 848-U117 (2010).

22. I.-W. Chen, E. Ronzitti, B. L. R., T. D. L., H. Zeng, E. Papagiakoumou, and V. Emiliani, "Parallel holographic illumination enables sub-millisecond two-photon optogenetic activation in mouse visual cortex in vivo," BioArxiv (2017).

23. G. Sela, H. Dana, and S. Shoham, "Ultra-deep penetration of temporally-focused two-photon excitation," Proc. SPIE 8588, Multiphot. Microsc. Biomed. Sci. XII **858824**, 10–15 (2013).

24. E. Papagiakoumou, A. Bègue, B. Leshem, O. Schwartz, B. M. Stell, J. Bradley, D. Oron, and V. Emiliani, "Functional patterned multiphoton excitation deep inside scattering tissue," Nat. Photonics **7**, 274–278 (2013).

25. A. M. Packer, L. E. Russell, H. W. P. Dalgleish, and M. Häusser, "Simultaneous all-optical manipulation and recording of neural circuit activity with cellular resolution in vivo," Nat. Methods **12**, 140–146 (2015).

26. L. Carrillo-Reid, W. Yang, Y. Bando, D. S. Peterka, and R. Yuste, "Imprinting and recalling cortical ensembles," Science (80-.). **353**, 691–694 (2016).

27. W. Yang, L. Carrillo-Reid, Y. Bando, D. S. Peterka, and R. Yuste, "Simultaneous two-photon imaging and two-photon optogenetics of cortical circuits in three dimensions," Elife **7**, e32671 (2018).

28. A. M. Packer, D. S. Peterka, J. J. Hirtz, R. Prakash, K. Deisseroth, R. Yuste, O. Yizhar, B. Grewe, C. Ramakrishnan, N. Wang, I. Goshen, A. M. Packer, D. S. Peterka, R. Yuste, M. J. Schnitzer, and K. Deisseroth, "Two-photon optogenetics of dendritic spines and neural circuits," Nat. Methods **9**, 1202–1205 (2012).

29. A. Hopt and E. Neher, "Highly Nonlinear Photodamage in Two-Photon Fluorescence Microscopy," Biophys. J. **80**, 2029–2036 (2001).

30. J. P. Rickgauer and D. W. Tank, "Two-photon excitation of channelrhodopsin-2 at saturation," Proc. Natl. Acad. Sci. U. S. A. **106**, 15025–15030 (2009).

31. R. Prakash, O. Yizhar, B. Grewe, C. Ramakrishnan, N. Wang, I. Goshen, A. M. Packer, D. S. Peterka, R. Yuste, M. J. Schnitzer, and K. Deisseroth, "Two-photon optogenetic toolbox for fast inhibition, excitation and bistable modulation," Nat. Methods **9**, 1171–1179 (2012).

32. E. Ronzitti, C. Ventalon, M. Canepari, B. C. Forget, E. Papagiakoumou, and V. Emiliani, "Recent advances in patterned photostimulation for optogenetics," J. Opt. **19**, 113001 (2017).

33. M. dal Maschio, J. C. Donovan, T. O. Helmbrecht, and H. Baier, "Linking Neurons to Network Function and Behavior by Two-Photon Holographic Optogenetics and Volumetric Imaging," Neuron **94**, 774–789.e5 (2017).

34. O. Hernandez, E. Papagiakoumou, D. Tanesee, K. Fidelin, C. Wyart, and V. Emiliani, "Three-dimensional spatiotemporal focusing of holographic patterns," Nat. Commun. **7**, 11928 (2016).

35. E. Papagiakoumou, E. Ronzitti, I. W. Chen, M. Gajowa, A. Picot, and V. Emiliani, "Two-photon optogenetics by computer-generated holography," in *Neuromethods* (2018), Vol. 133, pp. 175–197.

36. A. Bañas and J. Glückstad, "Holo-GPC: Holographic Generalized Phase Contrast," Opt. Commun. **392**, 190–195 (2017).

37. M. A. Go, P.-F. Ng, H.-A. Bachor, and V. R. Daria, "Optimal complex field holographic projection," Opt. Lett. **36**, 3073 (2011).

38. N. C. Pégard, A. R. Mardinly, I. A. Oldenburg, S. Sridharan, L. Waller, and H. Adesnik, "Three-dimensional scanless holographic optogenetics with temporal focusing (3D-SHOT)," Nat. Commun. **8**, 1228 (2017).

39. B. Sun, P. S. Salter, C. Roider, A. Jesacher, J. Strauss, J. Heberle, M. Schmidt, and M. J. Booth, "Four-dimensional light shaping: Manipulating ultrafast spatiotemporal foci in space and time," Light Sci. Appl. **7**, 1–14 (2018).

40. S. Berlin, E. C. Carroll, Z. L. Newman, H. O. Okada, C. M. Quinn, B. Kallman, N. C. Rockwell, S. S. Martin, J. C. Lagarias, and E. Y. Isacoff, "Photoactivatable genetically encoded calcium indicators for targeted neuronal imaging.," Nat. Methods **12**, 852–858 (2015).

41. M. Tomura, N. Yoshida, J. Tanaka, S. Karasawa, Y. Miwa, A. Miyawaki, and O. Kanagawa, "Monitoring cellular movement in vivo with photoconvertible fluorescence protein “Kaede” transgenic mice.," Proc. Natl. Acad. Sci. U. S. A. **105**, 10871–6 (2008).

42. A. Banas, D. Palima, M. Villangca, T. Aabo, and J. Gluckstad, "GPC light shaper for speckle-free one-and two-photon contiguous pattern excitation," Opt. Express **22**, 5299–5310 (2014).

43. J. Glückstad, "Phase contrast image synthesis," Opt. Commun. **130**, 225–230 (1996).

44. O. Hernandez, M. Guillon, E. Papagiakoumou, and V. Emiliani, "Zero-order suppression for two-photon holographic excitation," Opt. Lett. **39**, 5953–5956 (2014).

45. D. Palima and V. R. Daria, "Holographic projection of arbitrary light patterns with a suppressed zero-order beam.," Appl. Opt. **46**, 4197–201 (2007).

46. A. Jesacher and M. J. Booth, "Parallel direct laser writing in three dimensions with spatially dependent aberration correction.," Opt. Express **18**, 21090–9 (2010).

47. R. Conti, O. Assayag, V. De Sars, M. Guillon, and V. Emiliani, "Computer generated holography with intensity-graded patterns," Front. Cell. Neurosci. **10**, 236 (2016).

48. H. Aberle, A. P. Haghighi, R. D. Fetter, B. D. McCabe, T. R. Magalhães, and C. S. Goodman, "wishful thinking Encodes a BMP Type II Receptor that Regulates Synaptic Growth in Drosophila," Neuron **33**, 545–558 (2002).

49. E. Papagiakoumou, V. de Sars, D. Oron, and V. Emiliani, "Patterned two-photon illumination by spatiotemporal shaping of ultrashort pulses," Opt. Express **16**, 22039–22047 (2008).

50. B. Sun, P. S. Salter, and M. J. Booth, "Effects of aberrations in spatiotemporal focusing of ultrashort laser pulses.," J. Opt. Soc. Am. A. Opt. Image Sci. Vis. **31**, 765–72 (2014).

51. R. Ando, H. Hama, M. Yamamoto-Hino, H. Mizuno, and A. Miyawaki, "An optical marker based on the UV-induced green-to-red photoconversion of a fluorescent protein.," Proc. Natl. Acad. Sci. U. S. A. **99**, 12651–12656 (2002).

52. K. Isobe, H. Hashimoto, A. Suda, F. Kannari, H. Kawano, H. Mizuno, A. Miyawaki, and K. Midorikawa, "Measurement of two-photon excitation spectrum used to photoconvert a fluorescent protein (Kaede) by nonlinear Fourier-transform spectroscopy.," Biomed. Opt. Express **1**, 687–693 (2010).

53. I.-W. Chen, E. Papagiakoumou, and V. Emiliani, "Towards circuit optogenetics," Curr. Opin. Neurobiol. **50**, 179–189 (2018).

54. G. H. Patterson and J. Lippincott-Schwartz, "A Photoactivatable GFP for Selective Photolabeling of Proteins and Cells," Science (80-.). **297**, 1873–1877 (2002).

55. D. M. Chudakov, V. V Belousov, A. G. Zaraisky, V. V Novoselov, D. B. Staroverov, D. B. Zorov, S. Lukyanov, and K. A. Lukyanov, "Kindling fluorescent proteins for precise in vivo photolabeling," Nat Biotechnol **21**, 191–194 (2003).

56. J. N. Stirman, I. T. Smith, M. W. Kudenov, and S. L. Smith, "Wide field-of-view, multi-region, two-photon imaging of neuronal activity in the mammalian brain," Nat. Biotechnol. **34**, 857–862 (2016).

57. N. Ji, J. Freeman, and S. L. Smith, "Technologies for imaging neural activity in large volumes," Nat. Neurosci. **19**, 1154–1164 (2016).

58. R. Prevedel, A. J. Verhoef, A. J. Pernía-Andrade, S. Weisenburger, B. S. Huang, T. Nöbauer, A. Fernández, J. E. Delcour, P. Golshani, A. Baltuska, and A. Vaziri, "Fast volumetric calcium imaging across multiple cortical layers using sculpted light," Nat. Methods **13**, 1021–1028 (2016).

59. A. Song, A. S. Charles, S. A. Koay, J. L. Gauthier, S. Y. Thiberge, J. W. Pillow, and D. W. Tank, "Volumetric two-photon imaging of neurons using stereoscopy (vTwINS)," Nat. Methods **14**, 420–426 (2017).

60. S. Quirin, J. Jackson, D. S. Peterka, and R. Yuste, "Simultaneous imaging of neural activity in three dimensions.," Front. Neural Circuits **8**, 29 (2014).

61. S. J. Yang, W. E. Allen, I. Kauvar, A. S. Andalman, N. P. Young, C. K. Kim, J. H. Marshel, G. Wetzstein, and K. Deisseroth, "Extended field-of-view and increased-signal 3D holographic illumination with time-division multiplexing," Opt. Express **23**, 32573 (2015).

62. E. A. Pnevmatikakis, D. Soudry, Y. Gao, T. A. Machado, J. Merel, D. Pfau, T. Reardon, Y. Mu, C. Lacefield, W. Yang, M. Ahrens, R. Bruno, T. M. Jessell, D. S. Peterka, R. Yuste, and L. Paninski, "Simultaneous Denoising, Deconvolution, and Demixing of Calcium Imaging Data," Neuron **89**, 299 (2016).

63. L. Kelemen, P. Ormos, and G. Vizsnyiczai, "Two-photon polymerization with optimized spatial light modulator," J. Eur. Opt. Soc. **6**, 11029 (2011).

64. F. Burmeister, S. Steenhusen, R. Houbertz, U. D. Zeitner, S. Nolte, and A. Tünnermann, "Materials and technologies for fabrication of three-dimensional microstructures with sub-100 nm feature sizes by two-photon polymerization," J. Laser Appl. **24**, 42014 (2012).

Chapter 5: Holography in dept

This part will question the achievable performance of the 2P photo stimulation approaches in a biological medium by introducing the optical properties of the brain. We will also see how to overcome these limitations through more invasive techniques.

5.1 light-matter interaction in nervous tissue

Many biological tissues, like the brain, are defined as turbid media due to the structural diversity of their main components, such as the nucleus of a cell, its membrane, the blood vessels, the blood, to name a few. Each of these elements exhibits different optical properties due to their shape and composition and strongly affect the light propagation. We can describe the light propagation through a specific medium through 4 processes: reflection, refraction, absorption, and scattering.

The reflection/refraction phenomenon operates at the brain surface where the optical index between the immersion medium of the objective and the brain are different. This type of phenomenon will be predominant as soon as the difference in the index is due to macroscopic elements (organs, skull, etc.). It is possible to minimize this effect by using immersive media with indexes close to the sample.

Once the light has passed the first interface, two effects are predominant: absorption and scattering. Depending on the optical parameters of the medium and the wavelength, one of the two factors or both will be dominant. Absorption will be directly affects the light penetration depth. While the scattering will impact the light trajectory.

5.1.1 Absorption :

Photons propagating in the media can be absorbed by atoms/molecules to reach exited states. The light intensity variation due to the absorption along the propagation direction, z, can be described as:

$$I(z) = I_0 exp(-\mu_a z) \qquad (5.1)$$

Where I_0 is the initial intensity and μ_a the absorption coefficient that can be expressed as a function of the light wavelength: $\mu_a = \frac{4\pi n''}{\lambda} = \frac{1}{l_a}$. Where n'', is the imaginary index of the media, representing the energy loss link to the absorption and $l_a$is the absorption length or the distance at which the intensity has dropped to $\frac{1}{exp(1)}$.

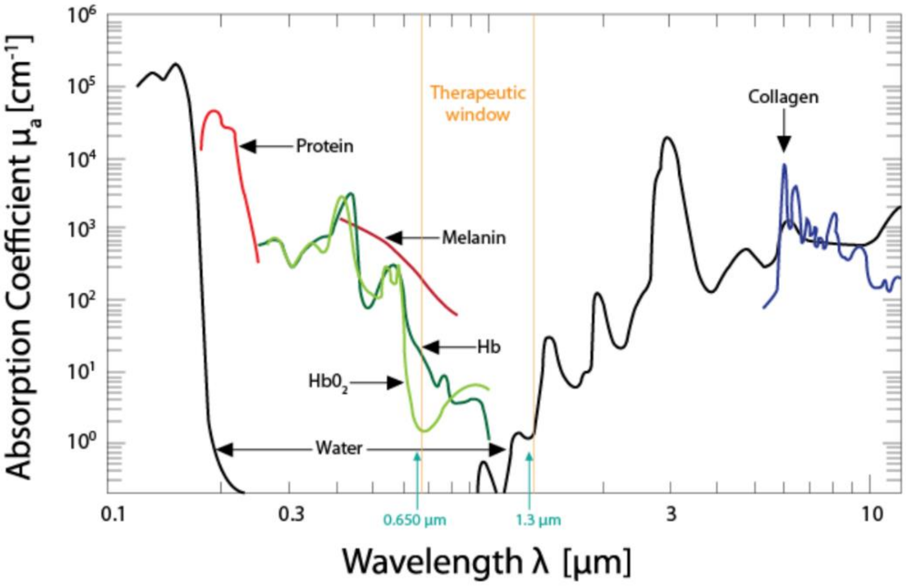

Figure 36: Light absorption coefficient evolution over the 0.1-12-µm spectrum for water, oxygenated and deoxygenated hemoglobin. [Adapted from (Vogel & Venugopalan, 2003)]

We can approximate the composition of biological tissue by two main component water and hemoglobin. They absorption coefficient depend on the illumination wavelength as shown in (Figure 36). This two-component exergue different absorbance tendency however for the intermediate range, between 600 and 1300 nm both of their absorption is minimal. This area is called the therapeutic window (Figure 36), explaining why the IR wavelength used in 2P typically around $900 - 1040\,nm$ enables to increase the penetration depth.

5.1.2 Scattering:

Three different regimes can describe the light scattering, depending on the relative size of the particles d compared to the wavelength λ of the incident light: geometrical scattering, Mie scattering, and Rayleigh scattering.

Geometrical scattering (d/λ>>1): to trace the light propagation in this regime, we can apply geometrical optics and use reflection, refraction, and deflection. Usually in this regime the scattered radiation is mainly directed forward.

Mie scattering (d/λ≈1): in this regime, the wavelength and scatterer's size are close, leading to anisotropic light distribution in the forward direction.

Rayleigh scattering $(d/\lambda \ll 1)$: in this regime, the wavelength is much bigger than the size of the scatterers. Cell membrane are typical elements respecting this constrain when illuminated with typically 2P wavelength. In this condition, the distribution of scattered light is isotropic.

Due to the diversity of the structure size encounter in biological tissue the light propagation can undergo the three forms of scattering. This is described by using average parameters such as the scattering mean free path l_s (the mean distance traveled by a photon between two successive diffusion events) and the scattering anisotropy factor g (mean cosine of the scattering angles). As an order of magnitude in biological tissues, the l_s is of the order of $50\mu m$ and g around $0.7{\sim}0.9$ traducing a diffusion preferably forward. This model allows to express the loss of intensity due to the absorption of the media during the light propagation as:

$$I(z) = I_0 exp(-\mu_s z) \quad (5.2)$$

Where I is the resulting intensity, z the propagation length, I_0 the incident light intensity and $\mu_s = \frac{1}{l_s}$ is the scattering coefficient.

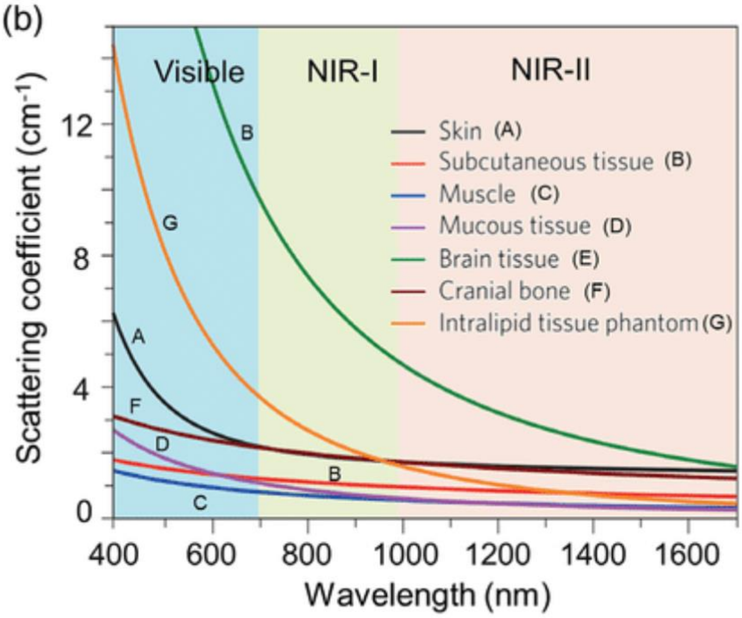

Figure 37: Scattering coefficients evolution over the 400-1700 nm spectrum for brain tissue and over biological sample [Adapted from (Upputuri & Pramanik, 2019).]

Equation (5.2) only depicts the non-scattered absorbed light that still follows the original propagation direction. To describe the propagation of the scattered (deviated light) we can use the anisotropy factor g to introduce the diffusion length l' that defines the distance at the end of which a photon has lost the memory of its initial direction as:

$$l' = \frac{l_s}{(1-g)} \quad (5.3)$$

After propagating through a turbid medium, it is possible to separate the photons in three categories according to their paths as shown in (Figure 38):

Ballistic Photons: These photons travel in a straight line, without undergoing scattering events, remaining coherent. But their number decreases exponentially with the distance.

Snake photons: Those undergoing few scattering events, remaining partially coherent. There trajectory is still close to the one of ballistic photons.

Diffuse photons: Experience multiple diffraction events resulting in a trajectory far from their initial direction.

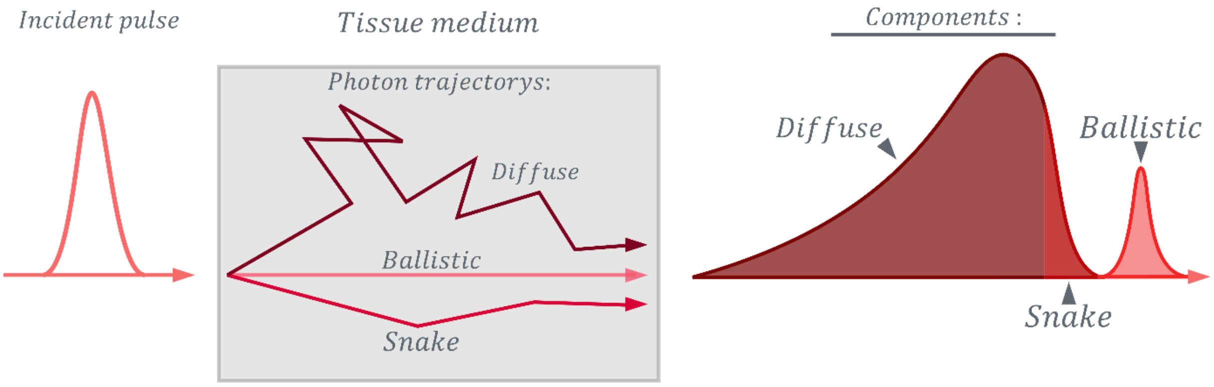

Figure 38: Schematics representation of laser pulse propagating in a scattering media with different photons trajectories. [adapted from (Das et al., 1997).*]*

In conclusion, the two phenomena governing the propagation of light in biological tissue are Water absorption and brain tissue diffusion. However their impact on the penetration depth with respect to wavelength is different. This is why Nicholas G. Horton et, al introduce the attenuation lengths that combine absorption and scattering effect $l_e = \left(\frac{1}{l_a} + \frac{1}{l_s}\right)^{-1}$ to better evaluate the suitable wavelength for tissue penetration. The (Figure 399) from (Horton et al., 2013) shows the attenuation length l_s regarding the wavelength λ when water absorption and brain tissue scattering are considered. As we can see, the usual range $900 - 1040\ nm$ used for 2P stimulation in the brain performs great. However, the wavelength offering potentially the best penetration would be around $1700\ nm$.

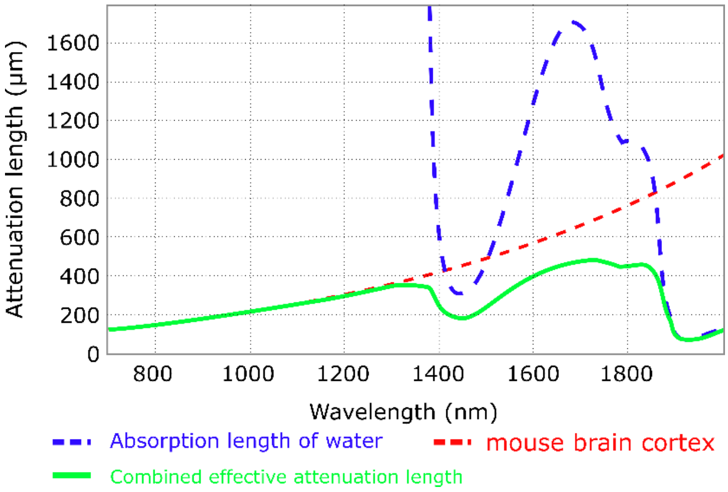

Figure 39: Attenuation spectrum of a tissue model based on Mie scattering and water absorption, showing the absorption length of water (blue dash line), the scattering length of mouse brain cortex (red dash-dot line), and the combined effective attenuation length (green solid line). [text and image adapted from (Horton et al., 2013)*]*

5.1.3 Multi-photon stimulation in brain medium

We can describe the absorption and scattering effect over the light propagation for 2P excitation with two effects: loss in power and spot quality.

Power: For the wavelengths used ($900 - 1040\ nm$), we can consider the scattering the main source of energy loss as the absorption of biological media in this range is relatively low in comparison. It is important to remember that stimulation is performed in 2P and so quadratically related to intensity.

Therefore, the expression we have previously given of the intensity as a function of the depth of propagation in the tissues (5.2) must be considered squared.

Another problem concerning the deliverable power is related to the pulse broadening due to dispersion as presented in (Papagiakoumou et al., 2020a). Fortunately, this effect is negligible for pulses around $100\,fs$ propagating through $\sim 1\,mm$ of brain tissue (Katz et al., 2011). This low deterioration of laser impulse can be explained by the high anisotropy factor g of around $0.7\sim 0.9$ traducing a diffusion, preferably forward of the tissue (M Oheim et al., 2001). Therefore, the delays generated by repetitive scattering events are very much lower than the pulse duration.

It is possible to compensate the scattering by increasing the excitation power which will increase the ballistic photons. However, too high excitation power can cause linear (heating) and non-linear photodamage effects.

Degradation of spot quality: The main factors that can distort the spot shape are the aberrations. They can be introduced by the first interaction between the light and the sample or by a refractive index mismatch, where refraction at the interface distorts the wavefronts. Or can be generated by the scattered propagation into the media.

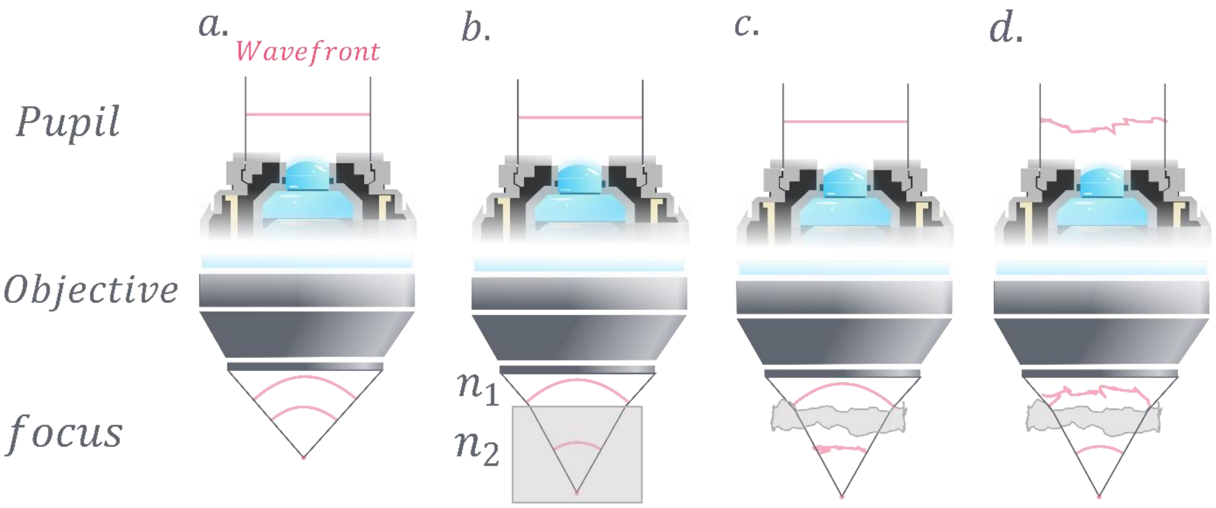

Figure 40: Schematic representation of a high-NA objective focusing light in a different sample. (a) non-aberrated focalization (b) Effect of the aberration introduced by the refractive index difference between the objective immersive media and the sample. (c) Warfront distortion introduced by the propagation in turbid media (with nonuniform refraction index) (d) the laser wave front modulated to compensate for the deformation introduced by the sample. [Adapted from (Booth, 2007)*]*

The aberrations lead to the spreading of the spot confinement both in the lateral plane and, more importantly, an elongation along the optic axis in addition to a reduction in the focal intensity. The spot distortion reduces the resolution of the system. For large excitation spot the scattering can induce a speckle light distribution (Figure 41). But (Dana & Shoham, 2011, 2012) and (Papagiakoumou et al., 2013b) demonstrate using temporally focused large Gaussian beams and GPC/CGH, respectively, the resilience of TF shape to scattering. They generated patterns through several hundred micrometers of diffusing tissue (Figure 41) and observed the conservation of the shape and axial resolution compared to non-TF beams. Papagiakoumou et al., 2013 attribute this performance to the TF "spectral self-healing" properties. In over word in TF configuration, all colors dispersed by the grating travel through a different path in the sample, imprinting a distinct speckle pattern. When all the colors are recombined, each speckle is sufficiently different to be considered uncorrelated, allowing their interference to smooth the intensity.

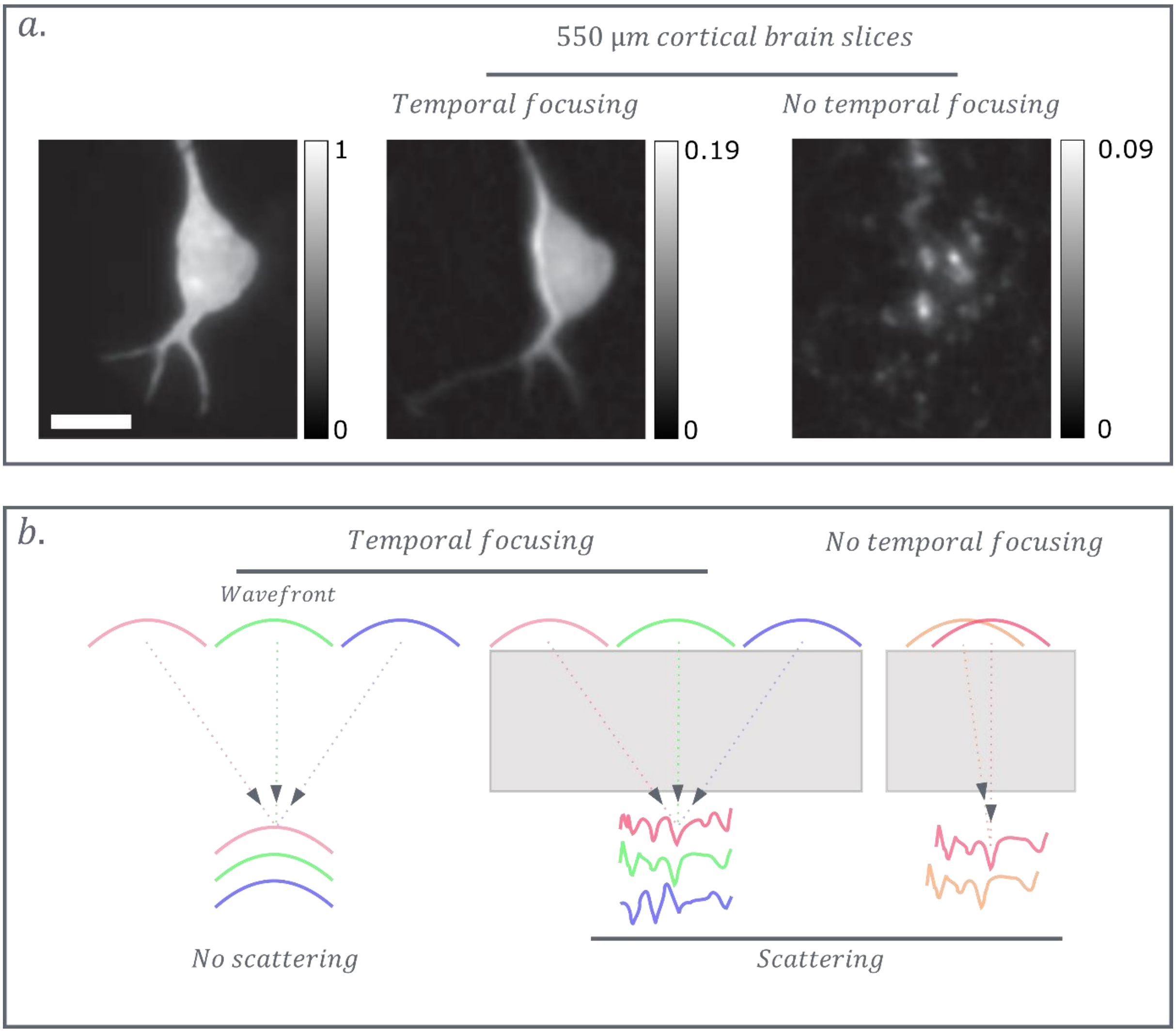

Figure 41: Description of the temporal focusing resilience to scattering. (a) Two-photon fluorescence images of the GPC pattern mimicking a neuron shape, after propagation through acute cortical brain slices of 550mm (950 nm). (b) Schematics representation of different spectral components (red, green and blue) dispersed by the TF effect and propagating through a scattering media. Once recombined at the focal plane, each color poses different speckle patterns resulting in a smoothed intensity pattern. On the over hand near spectral component obtained similar speckle patterns slightly shifted along the chromatic dispersion direction (bottom panel, right). The latter results in anisotropic smoothing along the dispersion direction. [Adapted from (Papagiakoumou et al., 2013b)*]*

5.2 The Micro-endoscope solution

5.2.1 Micro-endoscope GRIN lens:

Many mouse brain structures remain inaccessible to conventional stimulation or imaging methods: as for example the thalamus at $3\ mm$ depth from the pial surface and cerebellum $350\ mm$.

To reach these depths it is necessary to couple 1P or 2P imaging with a micro endoscope that could be inserted in the mouse brain. According to its definition in Nature, a micro endoscope is a type of endoscopy that uses optical fibers or fiber bundles in conjunction with microscopy techniques to obtain images of tissue immediately adjacent to the imaging end of the endoscope inserted into the body. In the shorter term, a small insert to implant inside the brain may be a solution. Moreover, adding fibers to it could facilitate freely moving experiments to perform in more natural behavior conditions.

GRIN (Gradient Index) lens-based micro-endoscopes represent a powerful solution to reach deeper regions. It offers us deeper access with a small size tool from 0.7 to $1.4\ mm$ diameter and $1\ mm$ length. The use of miniaturized microscopes has also been broadened to get imaging with smaller optic tools. So far, there are three categories of micro endoscopes.

First, 1P miniscope mounted on the animal's head (Aharoni & Hoogland, 2019). Second, 2P miniaturized microscope head mounted (Zong et al., 2017). Third, 1P or 2P fiber-based with or without a GRIN lens (Ozbay et al., 2018). All those systems present advantages and disadvantages for imaging, but none have shown the capacity to reading and stimulating single cells at cellular resolution.

The following manuscript demonstrates the possible combination of micro endoscopes with the MTF-LS system presented in the previous chapter. We first characterize the achievable performance for different configurations by generating 3D TF spots in volume up to $100\ \times\ 150\ \times\ 300\ \mu m3$. We then apply this approach "in vivo" in all-optical neuron control experiments. During this work, my colleagues Nicolò Accanto, I-Wen Chen and Emiliano Ronzitti worked on developing the all-optical system and its application in vivo. On my part, I worked together with Nicolò Accanto to create and characterize the different optical configurations presented in this work.

Multiplexed temporally focused light shaping through a GRIN lens for precise in-depth optogenetic photostimulation

Nicolò Accanto[1,2*], I-Wen Chen[1,2*], Emiliano Ronzitti[1,2*], Clément Molinier[1,2], Christophe Tourain[1,2], Eirini Papagiakoumou[1,2] and Valentina Emiliani[1,2]

[1] Wavefront-Engineering Microscopy group, Neurophotonics Laboratory, CNRS UMR8250, Paris Descartes University, 45 rue des Saints-Pères, 75270 Paris 06 Cedex, France

[2] Institut de la Vision, Sorbonne Université, Inserm S968, CNRS UMR7210, 17 Rue Moreau, 75012 Paris, France

* Equally contributing authors

In the past 10 years, the use of light has become irreplaceable for the optogenetic study and control of neurons and neural circuits. Optical techniques are however limited by scattering and can only see through a depth of few hundreds µm in living tissues. GRIN lens based micro-endoscopes represent a powerful solution to reach deeper regions. In this work we demonstrate that cutting edge optical methods for the precise photostimulation of multiple neurons in three dimensions can be performed through a GRIN lens. By spatio-temporally shaping a laser beam in the two-photon regime we project several tens of targets, spatially confined to the size of a single cell, in a volume of 150x150x400 µm^3. We then apply such concept to the optogenetic stimulation of multiple neurons simultaneously in vivo in mice. Our work paves the way for an all-optical investigation of neural circuits at previously unattainable depths.

Introduction

Understanding communication among neurons and how they coordinate and integrate multiple signals is essential for discovering how neural circuits determine brain function and dysfunction. With a still growing toolbox of optogenetic reporters [1,2] and actuators [3,4], and the parallel development of advanced optical techniques, it is today possible to activate and inhibit neuronal activity with light while optically recording the evoked response. Ultimately this will enable all-optical neural circuit interrogation with single-cell and single-action potential precision, even in deep brain regions [5].

One-photon (1P) wide field illumination using single optical fibers, enables the simultaneous illumination of large brain regions up to few mm deep and has already permitted to establish the links between neural activity and behaviour in different areas [6‑11]. This light-delivery approach however lacks spatial selectivity. More sophisticated multi-point photonic probes [12‑14] achieved selective excitation of single brain layers but still lacked cellular resolution and did not permit concurrent optical recording of functional activity. By using 1P-computer generated holography (CGH) for patterned illumination through a fiber bundle coupled with a small objective, our group previously demonstrated single- and multi-neuron activation together with functional calcium imaging in freely moving mice [15]. However, the large dimension of the micro-objective (< 2.5 mm diameter) limited this approach to superficial brain layers and the use of the fiber bundle did not preserve the holographic phase, thus constraining multi-spot generation to a single plane.

Two-photon (2P) excitation [16,17] combined with wave front shaping and opsin engineering allows millisecond manipulation of brain circuits with single cell resolution at multiple planes in three dimensions (3Ds). This was done either by generating multiple diffraction-limited spots that were scanned simultaneously across multiple cell somata [18‑20], or by using computer generate holography (CGH) to produce light patterns covering multiple cell somata at once [21], thus optimizing the temporal precision of the photostimulation [22]. Recently, several research groups [23‑27] have shown that using a two-step wave front shaping combined with temporal focusing (TF) [28‑31] it is possible to generate multiple high resolution extended light patterns in 3D, a technique we named multiplexed temporally focused light shaping (MTF-LS). These approaches led to the first demonstrations of neural circuit manipulation in 3D [25,26], yet the need of using conventional high numerical aperture (NA) objectives limited their use to circuits in superficial $(\leq\ 300\ \mu m)$ cortical areas or to in-vitro applications.

Micro-endoscopes (MEs), i.e. small optical probes that can be inserted into living tissues, represent a promising solution to extend optical brain manipulation to deeper brain structures.

Most MEs are based on the use of gradient index (GRIN) lenses, which are small cylinders of glass of diameter < 1 mm and length of several centimetres, characterized by a gradual variation of refractive index in the radial direction [32]. In the last 15 years, GRIN lenses were studied and optimized for the 2P imaging of living tissues, e.g. implanted till a few mm deep inside the rodent brain [33‑41]. In vivo functional calcium imaging was demonstrated through GRIN lenses both in 1P [42] and in 2P excitation [43‑46]. In Ref.[43], 2P CGH was also performed through a GRIN lens (NA=0.5, diameter 0.5 mm) and a GRIN objective (NA=0.8, diameter 1 mm). Multiple diffraction-limited spots allowed the activity from several neurons to be imaged simultaneously through the GRIN lens. Extended light patterns were also generated through the GRIN objective (10 µm spots with axial resolution of ~ 22 µm). However, CGH was limited to a single plane and extended holographic patterns with single cell axial resolution were only shown through the larger and more invasive GRIN objective. Moreover, no experiment showed so far optogenetic photostimulation through GRIN lenses.

In this work we demonstrate an optical system combining our recent MTF-LS technique [27] with the use of a GRIN lens (NA=0.5, diameter 0.5 mm), and we show that a small ME is suitable for the generation of multiple axially-confined 2P excitation spots matching target somata in 3D. Successively, using this system we demonstrate all-optical control of single or multiple neurons through the ME, by performing in vivo 2P optogenetic stimulation of target cells and reading out their induced activity with 2P calcium imaging.

Results

Optical setup

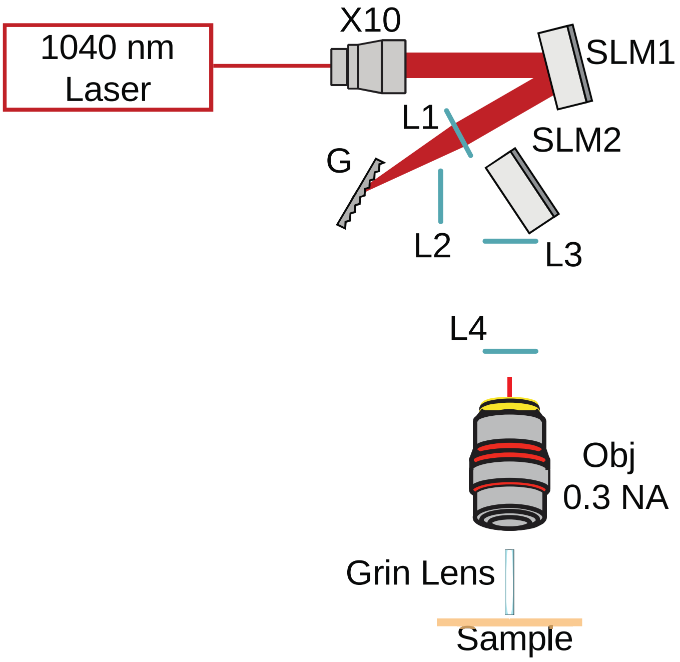

***Fig.1 Schematics of the optical setup used in the experiment**, comprising a 10 times beam expander, two SLMs, the diffraction grating (G) for TF, the appropriate lenses (L), the 10X, 0.3 NA air objective and the GRIN lens. For optical characterization the sample was a thin layer of rhodamine that was scanned in z for axial resolution measurements.*

The optical setup coupling the MTF-LS [27] to a GRIN lens ME is shown in Fig.1. In the optical characterization experiments we used a femtosecond fiber laser (Fidelity 10, Coherent), emitting at 1040 nm. The MTF-LS setup consisted of (1) a first SLM that determined the size and shape of the spot(s) to be generated at the sample plane; (2) a diffraction grating for TF; (3) a second SLM that multiplexed the axially confined spot(s) at arbitrary positions in 3D. The two SLMs were also used to correct for the aberrations of the system, in particular of the GRIN lens. To do so we maximized the 2P signal from a diffraction-limited spot made at the centre of the field of view (FOV) by introducing the appropriate first orders Zernike aberration corrections. We used an air objective (Olympus, UPLFLN 10X) with NA of 0.3 to focus into the GRIN lens, which we purchased from GRINTECH GmbH (model NEM-050-25-10-860-DM). It had a diameter of 0.5 mm and a total length of 9.86 mm, with NA of 0.19 on the objective side and of 0.5 on the sample side, resulting in a total field of view (FOV) of ~ 150 µm diameter [46]. For the optical characterization, the spots produced using MTF-LS through the GRIN lens were focused onto a thin rhodamine layer and imaged with a second objective (40x-NA 0.8 objective LUM PLAN FI/IR, Olympus) in transmission on a CCD camera (CoolSNAP HQ2, Photometrics). To characterize the axial resolutions, the rhodamine sample was vertically scanned together with the imaging objective with a piezoelectric z scanner (PI N-725.2A PIFOC). As discussed in Ref.[27], the MTF-LS technique is compatible with several different beam-shaping strategies that one can perform with the first SLM. In the following we show the results of (i) multiplexed temporally focused computer generated holography (MTF-CGH) and (ii) multiplexed temporally focused multi shapes (MTF-MS) through the GRIN lens.

MTF-CGH through the GRIN lens.

In a first experiment we used the first SLM (see Fig.1) to generate a simple holographic shape (a 15-µm diameter round spot) that was focused onto the diffraction grating for TF. The second SLM multiplexed the axially confined spot at arbitrary positions in 3D. In Fig. 2a we compare the axial resolution of a 15-µm spot generated through the GRIN lens at the centre of the FOV to the case of a non temporally focused spot of the same size (red) and to that of a spot generated through the 0.3 NA air objective alone (with no GRIN lens) with TF (blue). As the green curve clearly suggests, when TF was not used, the axial resolution, calculated as the full width at half maximum (FWHM) of the curve, was excessively large (~ 80 µm), as a consequence of the relatively small NA of the GRIN lens. When using TF, the axial resolution at the centre of the FOV improved to ~ 20 µm.

In Fig. 2b we compare how the axial resolution of the holographic spots changed as a function of the lateral displacement both in the x (direction of dispersion of the diffraction grating) and in the y (perpendicular to the dispersion) direction (Fig. 2b). From the graph one sees that the axial resolution worsened in the TF direction (i.e. the x direction) when moving away from the centre much faster than for the y direction. This asymmetry, as detailed in the discussion, was not observed in previous experiments [27], and could be due to a loss of colours through the GRIN lens when displacing the holographic spot in the TF direction. In any case, the temporally focused spots maintained an axial resolution better than 25 µm across 120 µm in the y direction and across 60 µm in the x direction, reaching the value of 35 µm at 60 µm from the centre along x.

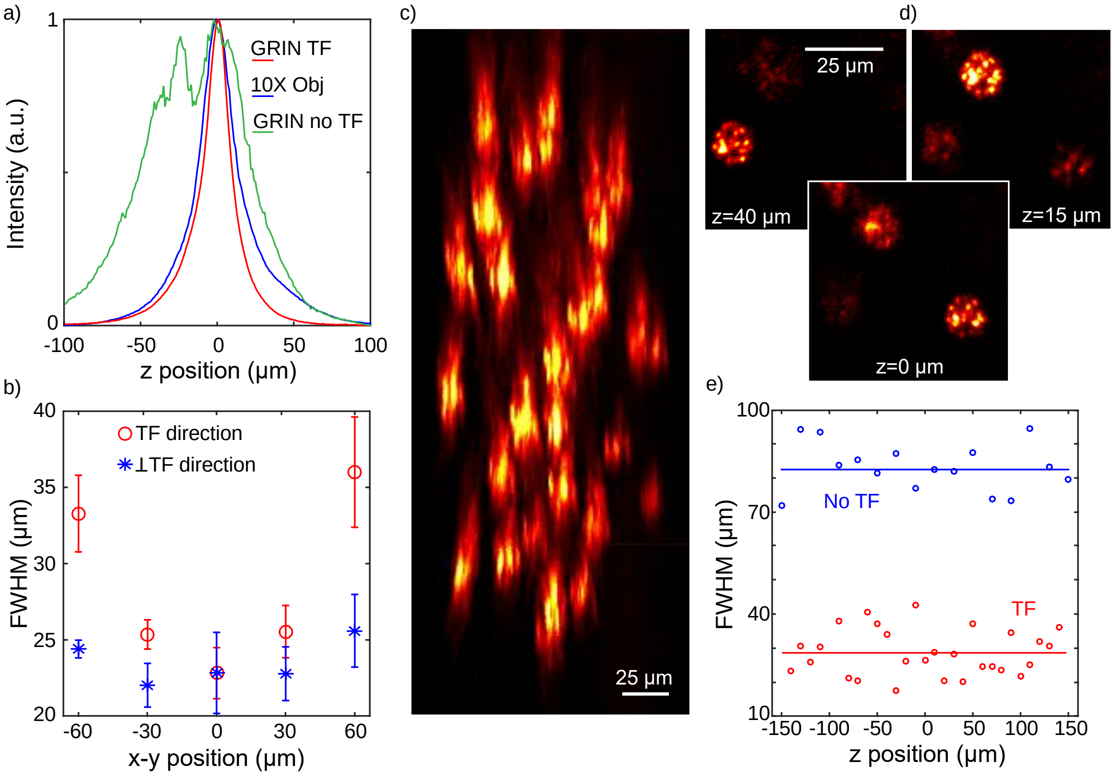

Fig. 2 ***Results obtained using the MTF-CGH technique though the GRIN lens****. a) Axial profiles for a 15 µm holographic spot at the center of the FOV when using the GRIN lens with TF, without TF and the 10X objective alone with TF. b) Behavior of the FWHM of one holographic spot displaced along the TF (x) or the perpendicular (y) direction. The data are the average over 6 different repetition of the same experiment and are given with*

an error bar calculated as the standard deviation over all the repetitions. c) Lateral view of 28 holographic spots distributed in 3D. d) In plane view of 3 holographic spots at 3 different depths. e) Comparison of the axial resolutions with TF (28 spots) and without TF (16 spots).

We next used the MTF-CGH system to produce 28 holographic spots in a FOV of 150x150x400 µm^3 through the GRIN lens. Fig. 2c,d show respectively a lateral projection (xz plane) of the spots and the xy view at three different z positions, illustrating how different spots are focused at different depths. The plot in Fig. 2e compares the axial resolutions of the 28 temporally focused spots with a similar experiment in which we generated a distribution of 16 spots without using TF. The difference between the two cases is striking; the mean axial resolution was 28±7 µm in the former and 82±7 µm in the latter case (the error was calculated as the standard deviation over all the experimental repetitions). From these results one can clearly see that advanced optical methods, here CGH and TF, can be implemented through a GRIN lens ME. Moreover, TF is essential to preserve single cell axial resolution when using low-NA GRIN lenses to create extended 2P excitation spots.

MTF-MS through the GRIN lens.

As described in Ref.[27], the MTF-MS method relies on a mixed phase/amplitude shaping approach, capable of simultaneously producing different speckle-free shapes, with an overall better axial resolution with respect to MTF-CGH, and to independently multiplex them at the sample plane. Here we used MTF-MS in two different configurations (Fig. 3): in the first one we generated a mixture of round and stars (for a total of 20 spots) (Fig. 3a,b); in the second one we generated 16 identical round spots (Fig. 3c). In Fig. 3a we show the lateral view (xz plane) corresponding to the case of two different shapes, whereas in Fig. 3b and c we show the projections along the z direction in the case of two and one shapes respectively. As expected, in both cases, we could generate a 3D distribution of shapes with improved axial resolution and intensity homogeneity with respect to Fig. 2. As summarized in Fig. 3d, the axial resolution was around 22±6 µm in the case of a single shape and 26±7 µm when using two different shapes. As discussed later, contrary to previous results through a normal objective [27], when using the GRIN lens we could not easily generate more than two shapes, probably due to the larger aberrations of the system.

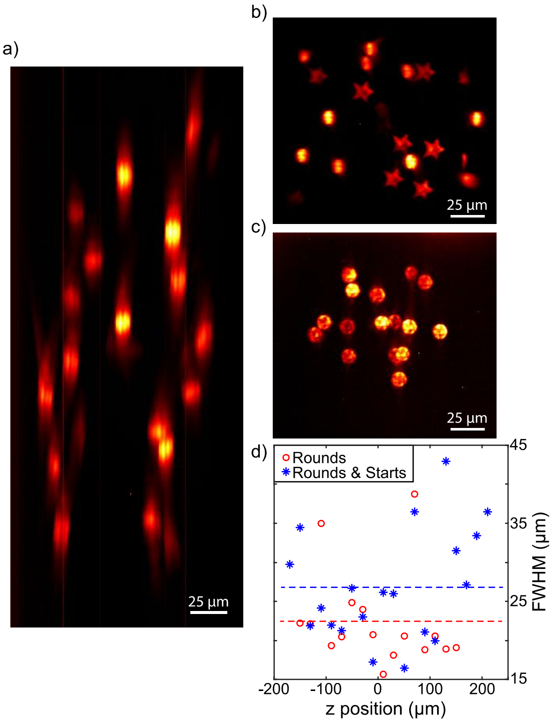

Fig. 3 ***Results obtained using the MTF-MS technique though the GRIN lens****. a) Lateral view of 20 spots distributed in 3D when using the first SLM to produce two shapes. b, c) Projections along the z direction in the case of two (rounds and stars) and one (rounds) shapes produced by the first SLM respectively. e) Comparison of the axial resolutions for the two cases.*

In vivo setup

We next used the GRIN lens based ME to perform concurrent holographic stimulation of single or multiple cells and optical readout of population activity in vivo in mice. As previously reported, a subset of neurons can be reliably co-labelled with opsins and calcium sensors by infecting cortical neurons of GCaMP6s transgenic mouse line GP4.3 [47,48] with ReaChR [49] viral vectors [50].

In the in vivo experiments, we mounted the GRIN lens ME on a microscope already equipped for 2P optogenetic stimulation and 2P scanning imaging, described in Ref.[50]. In this case, we used a more basic version of the holographic setup shown in Fig. 1, comprising only one SLM and a diffraction grating, which could therefore only generate excitation spots on a single plane. The laser sources were an amplified fiber laser (Satsuma HP, Amplitude Systemes) emitting at 1030 nm for the photostimulation and a tuneable Ti-Sapphire laser (Coherent Chameleon Vision II) for imaging. The imaging laser beam was raster scanned on the sample with xy galvanometric mirrors (6215H series, Cambridge Technology) and the emitted fluorescence was collected back through the GRIN lens and objective, separated from the excitation path with a dichroic mirror, and directed to two photomultiplier tubes.

After viral infection of ReaChR at the depths of ~250 µm and ~500 µm in the mouse primary visual cortex (V1), we performed acute craniotomy and removed the dura mater to expose the brain in anesthetized mice. All the in vivo experiments were performed in the anesthetized mouse V1 using the GRIN lens to image and photo stimulate through the craniotomy. By moving the objective and the GRIN lens together with a z motor we could change the focus of the system from the brain surface down to ~250 µm deep (when the GRIN lens was in contact with the brain surface), possibly deeper if the GRIN lens slightly penetrated the brain.

All-optical control of neuronal activity through GRIN lens in vivo

Through the GRIN lens, we were able to resolve on average 34±3 individual cortical neurons in a FOV of 150×150 μm^2 (mean±s.e.m., 9 FOVs). As Fig. 4a shows, we observed GCaMP6s fluorescence changes in single (5 FOVs) or multiple (5.2±0.7 cell, 5 FOVs) target neurons by stimulating with 10 light-pulses at a repetition rate of 11.84 Hz, through 12-µm diameter circular holographic spots at a threshold illumination intensity (defined as the intensity resulting in ≥0.5 activation probability in target cells, see Methods) of 0.39±0.09 mW/μm^2. The imaging power was kept at 90±14 mW, using a scanning speed of 5.92 or 11.84 Hz. Higher imaging powers led to an increased GCaMP6s fluorescence in cytosol, probably due to the slow channel kinetics of ReaChR47.

To examine the spatial selectivity of photostimulation, we determined the relationship between the activation probability (see methods) of non-target cells and their distance to the target cells [50]. We found the critical distance where non-target cells displayed 50% of target cells’ activation probability at the threshold stimulation intensity (see methods) to be 18 µm for single-cell activation (4 FOVs) and as 72 µm for multi-cell activation (5 FOVs) (Fig. 4b). Of note, for 2 FOVs in multi-cell activation experiments, non-target cells displayed >0.9 activation probability at the threshold stimulation intensity up to 100 μm away from a target cell, which implied neuronal network activation, thus reducing the spatial selectivity of photoactivation.

In sum, we demonstrated in vivo all-optical control of a single and multiple neurons through a GRIN lens. Out-of-target activation could result from a combination of neurite activation, smaller FOV and the relative low NA of the GRIN lens.

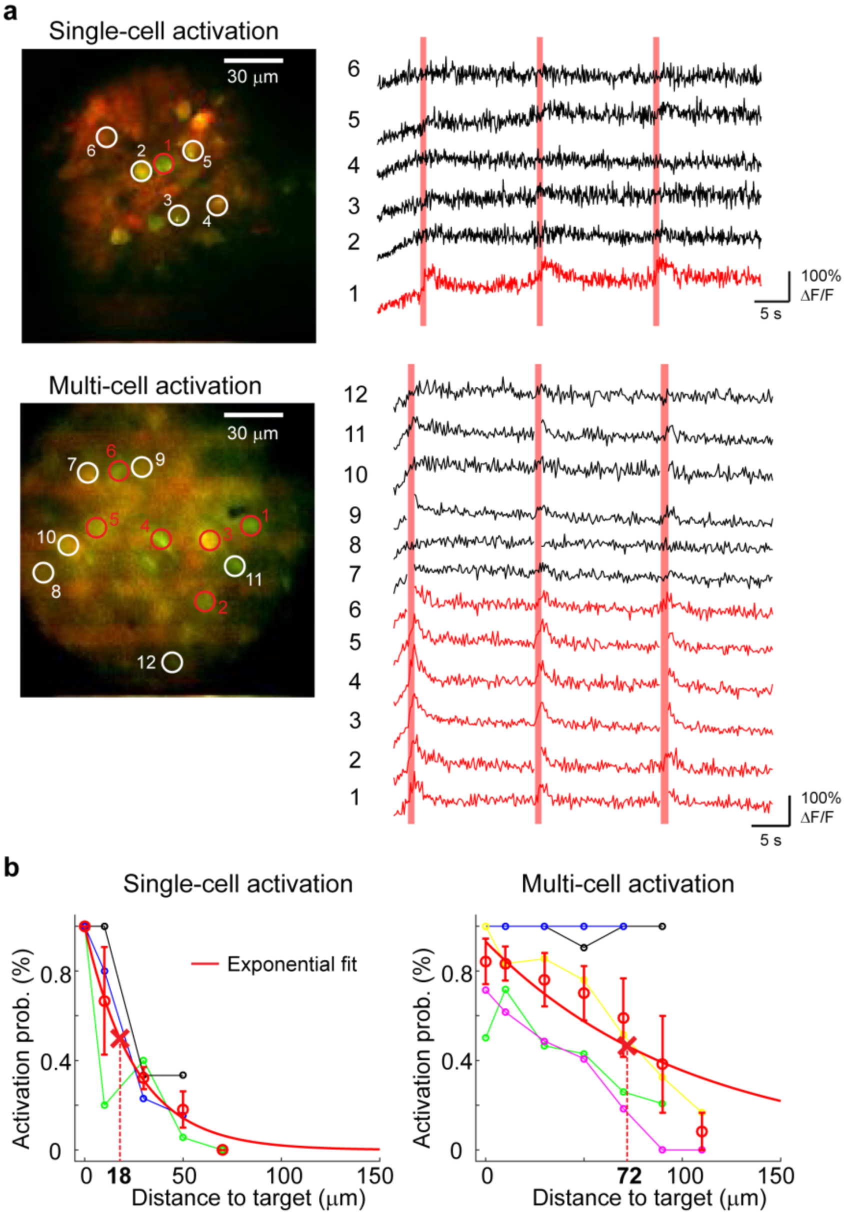

Figure 4 All-optical control through the GRIN lens in mouse V1 in vivo. (a) Upper panels show a case of single-cell activation experiment at the depth of ~110 μm below the brain surface. The red circle, in the average projection profile of 2P image intensity from 2 channels, represents the target cell and the 5 white circles are examples of non-target cells. The corresponding calcium traces are displayed at the right, with red vertical bars denoting the photostimulation epochs. Lower panels show a case of multi-cell activation experiment with 6 target cells (red circles) and 6 examples of non-target cells (with circles) at the depth of ~250 μm. Of note, the consecutive lines of bright pixels in the 2P images (upper and lower left) are photostimulation artefacts. Calcium signal in imaging frames from ROIs that were affected by stimulation artefacts is not shown. (b) Color lines (except red) indicate activation probability of target and non-target cells in relation to the distance to target cell for 5 FOV of single-cell activation (left) and 5 FOV of multi-cell activation (right). Red circles with error bars as mean ± s.e.m. Red solid lines represent the exponential fits of activation probability. Dash lines indicate the distance where non-target cells displayed 50% target cells’ activation probability at the threshold illumination intensity. The distance between non-target and target cell is distributed in 20-μm bins.

Discussion

In this work we developed a ME, based on the combination of MTF-LS with a GRIN lens, for the 2P excitation of multiple targets in 3D and we combined it with functional imaging to enable cell-targeted all-optical interrogations of deep brain regions in vivo.

Using the TF technique and holographic multiplexing we could generate 3D distributions of extended excitation spots over a total FOV of ~ 150x150x400 μm^3, keeping at the same time an axial resolution better than 30 µm. Importantly, our results demonstrate that the TF effect is maintained through the GRIN lens, despite its larger aberrations [51]. As shown in Fig. 2, this is crucial to keep a good axial confinement when generating large excitation spots, as the relatively small NA of the GRIN lens (0.5 on the sample side) would lead to a 4 times worse axial confinement if TF were not used therefore preventing targeted excitation. We showed that the GRIN lens is compatible with different MTF-LS techniques, such as MTF-MS. This latter configuration has the advantage of generating uniform speckle-free shapes with better axial resolution and gives the flexibility to separately multiplex different shapes. The increased light uniformity could be advantageous for parallel multi target imaging, while the possibility of generating distinct shapes could be used in experiments requiring activating different cellular compartments or different neuronal populations with variable cell size.

Compared to a MTF-LS conventional microscope, the use of a GRIN lens imposes few limitations (Fig. 2 and 3). First, we observed an asymmetric deterioration of the axial resolution when moving holographic spots in the x,y plane. Precisely, the axial resolution worsened more in the TF (x) than in its perpendicular direction (y) (Fig. 2b), a feature we did not observe when using a conventional high NA objective [27]. One can think at the GRIN lens as a doublet, which collimates the light it receives at the input and focuses it back at the output. There is therefore inside the GRIN lens an effective Fourier plane, namely a plane at which the wavelength components (or colours) of the laser pulse are separated in space. Shifting the spots at the entrance of the GRIN lens results in some portion of the beam (at some intermediate plane inside the GRIN lens) being closer to the edges of the GRIN lens, which are more prone to effective loss of light and aberrations. Intuitively, one can think that moving the spots in the x direction away from the centre, results in some of the wavelength components at an intermediate plane inside the GRIN lens being closer to the edge of the GRIN lens, producing a net loss of colours and hence of axial resolution. Moving the spots in the y direction instead, causes a similar loss of light for all the colours, leading to a net decrease of light, but not of axial resolution.

The second limitation was in the maximum number of different shapes we could create when using MTF-MS. While using a conventional high NA objective allowed us to simultaneously generate up to 4 different shapes [27], using the GRIN lens we could only generate 2 different shapes. MTF-LS requires illuminating different portions of the second SLM with each shape, which in turns means entering into the microscope objective at different positions of its back entrance. This results in a tilted propagation at the sample plane for those shapes entering in the objective away from the centre, as also explained in [23]. If this problem had negligible consequences in the case of a high NA objective [27], when using the GRIN lens it resulted in a loss of axial resolution and spot quality as the number of different shapes created by the first SLM increased. This was probably due to the larger aberrations of the GRIN lens compared to a normal objective [51]. A deeper study of the aberrations, including a method to use the two SLMs to correct for aberrations at multiple planes and/or lateral positions (and not only at the centre of the FOV as demonstrated here), or the future availability of optimized GRIN lenses with lower aberrations could help to overcome these limitations.

Low-NA GRIN lenses are currently the preferential choice for in-depth functional imaging in living animals as they permit minimal tissue damage compared to larger-diameter high-NA versions. We demonstrated the possibility to couple them with patterned illumination and temporal focusing enabling all-optical neuronal investigations in vivo. We were able to evoke calcium transients via soma illumination in cells co-expressing GCaMP6s and ReaChR in the mouse visual cortex in vivo. For single-cell activation through the GRIN lens, we found a critical distance of 18 µm, where non-target cells displayed activation probability that is 50% of that in target cells. This distance significantly increased (nearly 4 times) when multiple cells were simultaneously stimulated, as expected from the combined use of a non-somatic opsin [52,53] and a relatively low NA GRIN lens and resulted from indirect synaptic activation. Out of target activation can thus be prevented by using somatic opsins and possibly GRIN lenses with a bigger FOV or by further improving the axial resolution, e.g. by using higher NA GRIN lenses.

In the present study, we have limited the demonstration of all-optical neuronal control to a single-plane. The combination of MTF-LS with several volumetric imaging implementations as upstream divergence control [20,21] remote focusing [54] or extended depth-of-field scan [55] will enable to extend these demonstration to multiple planes. The use of chronic implantation of GRIN lenses (as shown for example in [43,46]) will also enable to extend this approach to the optical manipulation of deeper brain regions.

Methods

Animal preparations

All animal experiments were performed in accordance with the Directive 2010/63/EU of the European Parliament and of the Council of 22 September 2010. The protocols were approved by the Paris Descartes Ethics Committee for Animal Research with the registered number CEEA34.EV.118.12. Mice were anesthetized with intraperitoneal injection of a ketamine-xylazine mixture (0.1 mg ketamine and 0.01 mg xylazine/g body weight) during viral injection and with isoflurane (2% for induction and 0.5-1% for experiment) during photostimulation experiments. To express both opsin and calcium indicator in the same neuronal sub-population, stereotaxic injections of the viral vector AAV1-EF1 α -ReaChR-dTomato were performed in 4-week-old male or female mice of transgenic line GP4.3 (The Jackson Laboratory), which constitutively expresses the calcium indicator GCaMP6s 48 .Viral vectors of 1-1.5 µL were infused at either 250 µm or in combination with 500 µm to target cortical neurons in the right primary visual cortex at a speed of 80-100 nL/min. Acute experiments of holographic stimulation were performed 6-12 weeks after viral infection.

Holographic stimulation and calcium imaging through GRIN lens in vivo

The in vivo endoscope system was integrated to an existing custom-made 2P all-optical system thoroughly described in [50]. Specifically, a 0.5 NA GRIN lens was positioned by means of a custom-designed holder underneath a 10x microscope objective coupled with a SLM-based 2P patterned photostimulation and a 2P galvo-based scan imaging system. The GRIN lens holder was composed of kinematic mounts allowing X,Y,Z translation and rotation of the pitch and yaw axes of the GRIN lens, thus ensuring GRIN lens alignment to imaging and photostimulation paths. GRIN lens holder and objective were jointly connected to an axial motor allowing beam refocusing in the sample.

Initially, GRIN lens and objective were axially translated towards the head of the mouse till the image of brain surface appeared. That set the zero position of the GRIN lens, where its tip was at a distance of 250 µm (i.e., the optical system’s working distance) away from the brain surface. To perform all-optical experiments on a sub-population of cortical neurons co-expressing the opsin ReaChR and the calcium sensor GCaMP6s located up to 250 µm below the brain surface (i.e. layer 2/3), we axially refocused the GRIN lens/objective system like with an ordinary 2P objective microscope until at the brain surface.

For acute in vivo experiments, mice were anesthetized with isoflurane (as described above) and the skull was exposed after subcutaneous application of lidocaine. A custom-made head-plate was attached to the skull using dental cement (Unifast Trad, GC). A circular craniotomy of 2-3 mm diameter was made over the injection site and the dura mater was removed.

Two-photon imaging of GCaMP6s calcium signal and the fluorophore labelling of dTomato was carried out by exciting with a scan beam provided by a Ti:Sapphire laser emitting at 920 nm (Coherent Chameleon Vision II). SLM-based patterned photostimulation was provided by using high-energy fiber laser-pulses at 1030 nm (Satsuma HP, Amplitude Systemes).

Target cells were selected based on a high-resolution reference image (512 × 512 pixels) of the red channel collecting signal from ReaChR-dTomato. Through single or multiple circular holographic spots of 12-µm diameter, the target somata were simultaneously illuminated with 10 holographic light-pulses of 5 or 10 ms at 11.84 Hz. Concurrently, the neuronal population activity of GCaMP6s calcium signal in a 150 × 150 μm^2 FOV was monitored by scanning at a frame rate of 5.92 or 11.84 Hz with 128 × 128 pixel resolution.

During all-optical experiments, the photostimulation laser induced artefactal excitation of fluorophores, which appeared as consecutive lines of bright pixels. The image frames of GCaMP6s signal from regions-of-interest (ROIs) that were affected by stimulation artefacts were removed in post-processing.

Data analysis

Image analysis was performed by using ImageJ and MATLAB (Mathworks). ROIs covering individual target and non-target cell somata were manually selected in ImageJ based on both red (ReaChR-dTomato) and green (GCaMP6s) channels. The time-lapse fluorescent signal of GCaMP6s from all ROIs was exported in MATLAB. Image frames from ROIs that are affected by the photostimulation artefacts were removed in analysis. For each ROI, the relative percentage change of GCaMP6s fluorescence was computed as $\Delta F/F = (F - F0)/F0$, where F0 was the average raw fluorescence signal 3-0.2 s before photostimulation started. A cell was considered activated if the average $\Delta F/F$ 1 s after the last illumination onset was significantly larger compared to that 1 s before the first illumination onset (right-tailed paired t-test with a significance level of 0.05). The relationship between activation probability and distance-to-target was determined similarly as previously described [50]. Specifically, the threshold stimulation intensity was determined when the activation probability of target cells >=0.5. The average values of activation probability at different distance-to-target were described by fitting with an exponential function.

Acknowledgments

We thank Vincent de Sars for software developing, Coherent Inc. for the loan of the Fidelity laser, This research received support from the ‘Agence Nationale de la Recherche’ (grant ANR-15-CE19-0001-01, 3DHoloPAc), the Human Frontiers Science Program (Grant RGP0015/2016), the Fondation Bettencourt Schueller (Prix Coups d’ élan pour la recherché française), the Getty Lab, the National Institute of Health (Grant NIH 1UF1NS107574 - 01) and Axa research funding. N.A. received funding from the European Union’s Horizon 2020 research and innovation programme under the Marie Skłodowska-Curie grant agreement no. 746173. E.R. received funding from the European Research Council SYNERGY Grant scheme (HELMHOLTZ, ERC Grant Agreement # 610110). IWC received funding from the European Union's Horizon 2020 research and innovation program under the Marie Skłodowska-Curie grant agreement no. 747598.

Competing interests. The authors declare no competing interests.

Data availability. The datasets generated during and/or analysed during the current study are available from the corresponding author on reasonable request.

Author contributions

N.A., IW.C. and E.R. designed the experiments. N.A. and C.M. built the 3D holographic micro-endoscope system, performed the optical experiments and analysed the optical data. E.P. participated in the development of the optical system. IW.C. performed animal surgery. E.R and E.P built the scanning imaging and 2D stimulation microscope. C.T. designed and built the GRIN lens holders to align the endoscope both for the optical and the in vivo setups. IW.C., E.R. and N.A. performed in vivo experiments. IW.C. analysed the in vivo data. N.A., IW.C. and V.E. wrote the manuscript with the contribution of all the authors. V.E. conceived and supervised the project.

References

1. Knöpfel, T. Genetically encoded optical indicators for the analysis of neuronal circuits. Nat. Rev. Neurosci. 13, 1‑14 (2012).

2. Lin, M. Z. & Schnitzer, M. J. Genetically encoded indicators of neuronal activity. Nature Neuroscience 19, 1142‑1153 (2016).

3. Deisseroth, K. Optogenetics. Nature Methods 8, 26‑29 (2011).

4. Deisseroth, K. Optogenetics: 10 years of microbial opsins in neuroscience. Nature Neuroscience 18, 1213‑1225 (2015).

5. Emiliani, V., Cohen, A. E., Deisseroth, K. & Häusser, M. All-Optical Interrogation of Neural Circuits. J. Neurosci. 35, 13917‑13926 (2015).

6. Jennings, J. H. et al. Distinct extended amygdala circuits for divergent motivational states. Nature 496, 224‑228 (2013).

7. Zhang, F. et al. Optogenetic interrogation of neural circuits: Technology for probing mammalian brain structures. Nature Protocols 5, 439‑456 (2010).

8. Sparta, D. R. et al. Construction of implantable optical fibers for long-term optogenetic manipulation of neural circuits. Nat. Protoc. 7, 12‑23 (2012).

9. Jennings, J. H. et al. Visualizing hypothalamic network dynamics for appetitive and consummatory behaviors. Cell 160, 516‑527 (2015).

10. Adamantidis, A. R., Zhang, F., Aravanis, A. M., Deisseroth, K. & De Lecea, L. Neural substrates of awakening probed with optogenetic control of hypocretin neurons. Nature 450, 420‑424 (2007).

11. Aravanis, A. M. et al. An optical neural interface: in vivo control of rodent motor cortex with integrated fiberoptic and optogenetic technology. J. Neural Eng. 4, (2007).

12. Pisanello, F. et al. Multipoint-emitting optical fibers for spatially addressable in vivo optogenetics. Neuron 82, 1245‑1254 (2014).

13. Zorzos, A. N., Scholvin, J., Boyden, E. S. & Fonstad, C. G. Three-dimensional multiwaveguide probe array for light delivery to distributed brain circuits. Opt. Lett. 37, 4841 (2012).

14. Segev, E. et al. Patterned photostimulation via visible-wavelength photonic probes for deep brain optogenetics. Neurophotonics 4, 011002 (2016).

15. Szabo, V., Ventalon, C., De Sars, V., Bradley, J. & Emiliani, V. Spatially Selective Holographic Photoactivation and Functional Fluorescence Imaging in Freely Behaving Mice with a Fiberscope. Neuron 84, 1157‑1169 (2014).

16. Helmchen, F. & Denk, W. Deep tissue two-photon microscopy. Nature Methods 2, 932‑940 (2005).

17. Grienberger, C. & Konnerth, A. Imaging Calcium in Neurons. Neuron 73, 862‑885 (2012).

18. Packer, A. M., Russell, L. E., Dalgleish, H. W. P. & Häusser, M. Simultaneous all-optical manipulation and recording of neural circuit activity with cellular resolution in vivo. Nat. Methods 12, 140‑146 (2015).

19. Carrillo-Reid, L., Yang, W., Bando, Y., Peterka, D. S. & Yuste, R. Imprinting and recalling cortical ensembles. Science (80-.). 353, 691‑694 (2016).

20. Yang, W., Carrillo-Reid, L., Bando, Y., Peterka, D. S. & Yuste, R. Simultaneous two-photon imaging and two-photon optogenetics of cortical circuits in three dimensions. Elife 7, e32671 (2018).

21. dal Maschio, M., Donovan, J. C., Helmbrecht, T. O. & Baier, H. Linking Neurons to Network Function and Behavior by Two-Photon Holographic Optogenetics and Volumetric Imaging. Neuron 94, 774‑789.e5 (2017).

22. Ronzitti, E. et al. Sub-millisecond optogenetic control of neuronal firing with two-photon holographic photoactivation of Chronos. J. Neurosci. 37, 1246‑17 (2017).

23. Hernandez, O. et al. Three-dimensional spatiotemporal focusing of holographic patterns. Nat. Commun. 7, 11928 (2016).

24. Sun, B. et al. Four-dimensional light shaping: Manipulating ultrafast spatiotemporal foci in space and time. Light Sci. Appl. 7, 17117 (2018).

25. Pégard, N. C. et al. Three-dimensional scanless holographic optogenetics with temporal focusing (3D-SHOT). Nat. Commun. 8, 1228 (2017).

26. Mardinly, A. R. et al. Precise multimodal optical control of neural ensemble activity. Nat. Neurosci. 21, 881‑893 (2018).

27. Accanto, N. et al. Multiplexed temporally focused light shaping for high-resolution multi-cell targeting. Optica In press, Preprints @ https://doi.org/10.1101/216135 (2018).

28. Oron, D., Tal, E. & Silberberg, Y. Scanningless depth-resolved microscopy. Opt. Express 13, 1468 (2005).

29. Zhu, G., van Howe, J., Durst, M., Zipfel, W. & Xu, C. Simultaneous spatial and temporal focusing of femtosecond pulses. Opt. Express 13, 2153‑2159 (2005).

30. Papagiakoumou, E., de Sars, V., Oron, D. & Emiliani, V. Patterned two-photon illumination by spatiotemporal shaping of ultrashort pulses. Opt. Express 16, 22039‑22047 (2008).

31. Andrasfalvy, B. K., Zemelman, B. V, Tang, J. & Vaziri, A. Two-photon single-cell optogenetic control of neuronal activity by sculpted light. Proc. Natl. Acad. Sci. 107, 11981‑11986 (2010).

32. Gomez-Reino, C., Perez, M. V. (Maria V. & Bao, C. (Carmen). Gradient-Index Optics : Fundamentals and Applications. (Springer Berlin Heidelberg, 2002).

33. Jung, J. C. & Schnitzer, M. J. Multiphoton endoscopy. Opt. Lett. 28, 902‑904 (2003).

34. Levene, M. J., Dombeck, D. A., Kasischke, K. A., Molloy, R. P. & Webb, W. W. In Vivo Multiphoton Microscopy of Deep Brain Tissue. J. Neurophysiol. 91, 1908‑1912 (2004).

35. Mehta, A. D., Jung, J. C., Flusberg, B. A. & Schnitzer, M. J. Fiber optic in vivo imaging in the mammalian nervous system. Current Opinion in Neurobiology 14, 617‑628 (2004).

36. Göbel, W., Kerr, J. N. D., Nimmerjahn, A. & Helmchen, F. Miniaturized two-photon microscope based on a flexible coherent fiber bundle and a gradient-index lens objective. Opt. Lett. 29, 2521 (2004).

37. Fu, L. & Gu, M. Fibre-optic nonlinear optical microscopy and endoscopy. Journal of Microscopy 226, 195‑206 (2007).

38. Barretto, R. P. J., Messerschmidt, B. & Schnitzer, M. J. In vivo fluorescence imaging with high-resolution microlenses. Nat. Methods 6, 511‑512 (2009).

39. Murray, T. A. & Levene, M. J. Singlet gradient index lens for deep in vivo multiphoton microscopy. J. Biomed. Opt. 17, 021106 (2012).

40. Attardo, A., Fitzgerald, J. E. & Schnitzer, M. J. Impermanence of dendritic spines in live adult CA1 hippocampus. Nature 523, 592‑596 (2015).

41. Miyamoto, D. & Murayama, M. The fiber-optic imaging and manipulation of neural activity during animal behavior. Neuroscience Research 103, 1‑9 (2016).

42. Murayama, M., Pérez-Garci, E., Lüscher, H.-R. & Larkum, M. E. Fiberoptic System for Recording Dendritic Calcium Signals in Layer 5 Neocortical Pyramidal Cells in Freely Moving Rats. J. Neurophysiol. 98, 1791‑1805 (2007).

43. Moretti, C., Antonini, A., Bovetti, S., Liberale, C. & Fellin, T. Scanless functional imaging of hippocampal networks using patterned two-photon illumination through GRIN lenses. Biomed. Opt. Express 7, 3958 (2016).

44. Andermann, M. L. et al. Chronic Cellular Imaging of Entire Cortical Columns in Awake Mice Using Microprisms. Neuron 80, 900–913 (2013).

45. Sato, M. et al. Fast varifocal two-photon microendoscope for imaging neuronal activity in the deep brain. Biomed. Opt. Express 8, 4049 (2017).

46. Bocarsly, M. E. et al. Minimally invasive microendoscopy system for in vivo functional imaging of deep nuclei in the mouse brain. Biomed. Opt. Express 6, 4546 (2015).

47. Lin, J. Y., Knutsen, P. M., Muller, A., Kleinfeld, D. & Tsien, R. Y. ReaChR: A red-shifted variant of channelrhodopsin enables deep transcranial optogenetic excitation. Nat. Neurosci. 16, 1499–1508 (2013).

48. Dana, H. et al. Thy1-GCaMP6 Transgenic Mice for Neuronal Population Imaging In Vivo. PLoS One 9, e108697 (2014).

49. Chen, T. W. et al. Ultrasensitive fluorescent proteins for imaging neuronal activity. Nature 499, 295–300 (2013).

50. Chen, I.-W. et al. Parallel holographic illumination enables sub-millisecond two-photon optogenetic activation in mouse visual cortex in vivo. bioRxiv 250795 (2018). doi:10.1101/250795

51. Wang, C. & Ji, N. Characterization and improvement of three-dimensional imaging performance of GRIN-lens-based two-photon fluorescence endomicroscopes with adaptive optics. Opt. Express 21, 27142–27154 (2013).

52. Shemesh, O. et al. Supplementary of Temporally precise single-cell resolution optogenetics. Nat. Neurosci. in press, 1–16 (2017).

53. Baker, C. A., Elyada, Y. M., Parra, A. & Bolton, M. M. Cellular resolution circuit mapping with temporal-focused excitation of soma-targeted channelrhodopsin. Elife 5, (2016).

54. Botcherby, E. J. et al. Aberration-free three-dimensional multiphoton imaging of neuronal activity at kHz rates. Proc. Natl. Acad. Sci. 109, 2919–2924 (2012).

55. Lu, R. et al. Video-rate volumetric functional imaging of the brain at synaptic resolution. Nat. Neurosci. 20, 620–628 (2017).

Chapter 6: Fast sequential light patterning

In the previous chapters, we did focus the discussion on the "spatial" constraints of the photostimulation, including the single-cell resolution for 3D excitation in large volume in-depth. Nevertheless, to provide an optical technique allowing a precise study of the nervous system capable to reproduce its activity, an essential point must be addressed: "time". As mentioned in the introduction, the brain encodes the signal intensity in frequency. Therefore, complex asynchronous signals are observed within a neuronal circuit, illustrating the necessity to reach high temporal precision during neuronal photostimulation. Moreover, recent experiments highlighted the importance of the relative degree of synchronicity among optically evoked spikes (Gill et al., 2020; Robinson et al., 2020) to drive behavioral responses.

The temporal performance of a optogenetic system can be evaluated according to three criteria:

First, the temporal precision (or jitter): the spike time reproducibility among successive stimulations (Figure 42.a).

Second, synchronous temporal resolution: the minimum time delay between two consecutive action potentials (AP) of the same cell or group of cell simultaneously stimulated (Figure 42.b).

Third, the asynchronous temporal resolution: the minimum time delay between two consecutive action potentials (AP) between different cells with different degree of synchronicity (Figure 42.c).

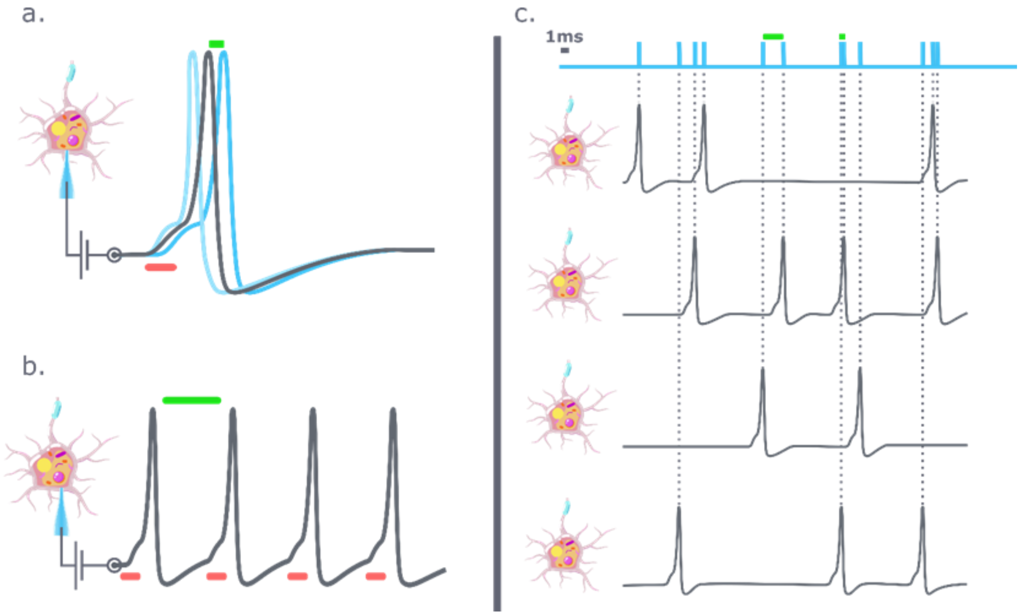

Figure 42: Illustration of temporal performance in photostimulation:

The green line represents the achievable time performance, the red one the illumination duration of the stimulation.

a. Schematic representation of the jitter. The blue trace represents the successive stimulation protocols realized on the same cell to evaluate the delta variation between.

b. synchronous temporal resolution: the highest frequence of neuronal activation

c. asynchronous temporal resolution: shortest time delay achievable between multiple neurons

The notion of temporal precision has already been introduced in (Chapter 2). As a first approximation, the shorter the stimulation protocol (illumination dwell time) to trigger an AP, the better is the temporal accuracy. Nevertheless, the illumination dwell time depends on numerous parameters: level and kind of illumination, level of viral expression, type of opsin, type of neuron, and physiological conditions.

It is important to distinguish synchronous and asynchronous temporal resolution for two reasons.

First, in terms of minimal achievable performance to reach biological performance. As presented in the introduction, the frequency of single-cell activation is limited by its refractoriness to 500-1000 Hz. Therefore, the required temporal precision to accurately reproduce the activity of a single cell or group of cells activated simultaneously shall never exceed 1-2 ms. In contrast, the time delay between the AP of different neurons with asynchronous activities is not subjected to such limitations. By this means, two neurons can trigger action potentials closer in time (Figure 42.c).

Second, in terms of photostimulation protocol. In the case of synchronous manipulation, all the targets are stimulated simultaneously for the same time dwell period. Then, to generate train of activations, we only need to repeat the stimulation process by turning on/off the illumination. In this case, the only time limitation is the dwell time and the speed at which the illumination on/off state is controlled, giving $\Delta T_{min} = T_{dwell} + T_{illum}$. Nowadays, the laser intensity output can be controlled using various devices like an AOM reaching transition speed of tens of µs. In comparison, the conventionally used T_{dwell} are around ~5ms. Then, we can neglect T_{illum} giving giving $\Delta T_{min} \approx T_{dwell}$. In brief, the maximum synchronous temporal resolution that an optogenetic system can achieve is directly related to the illumination dwell time of the protocol.

For asynchronous manipulation, all the targets are not simultaneously stimulated. Therefore, it is important to control the illumination and the target illuminated during the experiment. In this condition, the temporal resolution achievable depends of the system's switching time needed to move from one target or group of targets to another one: $\Delta T_{min} = T_{dwell} + T_{switch}$.

Therefore, we will dedicate the next part of this chapter to study the limitation introduced by the T_{switch} time for different asynchronous stimulation protocols.

6.1 High temporal resolution for neuronal photo stimulation.

To better understand the current limitation of the asynchronous resolution, we will base the explanation on the stimulation of two-cells, respectively “cell 1” and “cell 2”. (Figure 43.a). In this example, the illumination dwell time of “cell 1” is fixed at 5 ms with a power P1. For “cell 2”, the illumination time is 7 ms with a power P2. Then, we will study the protocols used to introduce asynchronous activation of those two cells with time delay of $\Delta T = 12$ and 4 ms. Those two times will present the two distinct regimes we can observe during asynchronous photostimulation protocol (Figure 43).

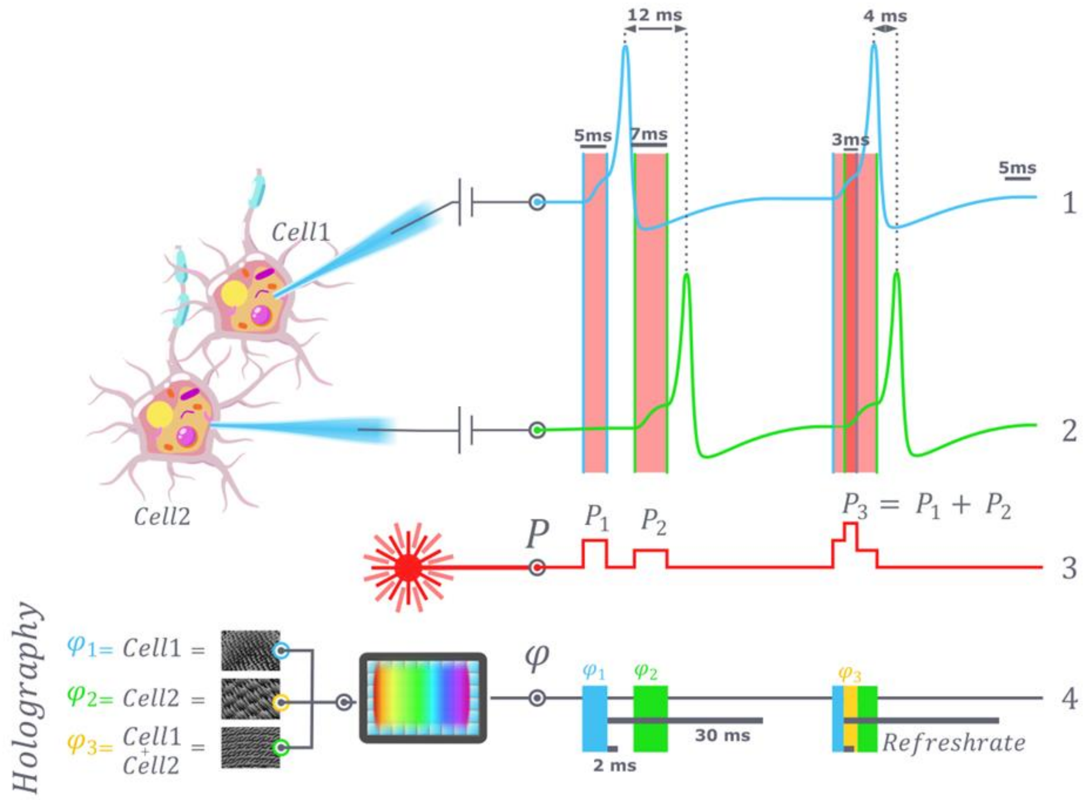

Figure 43: Photostimulation protocol to stimulate two patched-cells with holography or FLiT

1-2. Electrical signal of two patched-cells under three different photostimulation protocols, with decreasing delay between the activation introduced in the two cells across time.

3. Protocol to control the laser power of photostimulation.

4. Schema of holographic stimulation protocol, using SLM switching from one phase profile to the other with refreshing rate (bar in grey) as 20ms and 2ms.

For $\Delta T = 12\ ms$, we fall in the first regime where $\Delta T > Tdwell$. This condition express the necessity to avoid overlapping the two cells' illumination periods. In other words each target is stimulated one after the over never simultaneously. With this condition, the minimum ΔT we can reach depends on the minimum time needed for the system to switch from the target “cell 1” to “cell 2” (called T_{switch_min}) and the illumination time of “cell 2” $(called\ T_{dwell\_min})$, giving the expression $\Delta Tmin = T_{dwell\_min} + T_{switch\_min}$.

The optical generation of a single neuronal AP using powers closed to opsin saturation has been reached with illumination times below 1 ms (Bègue et al., 2013; Marshel et al., 2019b; Ronzitti et al., 2017; Yang et al., 2018). However, reaching optimal axial resolution requires choosing a shorter duration of illumination the opsin's saturation (Chen et al., 2019) which typically sets the illumination time to 5-30 ms (Chen et al., 2018). In contrast, the switching time Tsw is directly related to the system performance. For the 3D-MTF system, presented in (Chapter 4), the transition from one target to another, is done by changing the phase profile at the SLM2 . The time required for a SLM to transit from one phase to another is called “refreshing time” (i.e., the time needed for the LC molecules to rotate under a specific voltage and update the phase shift of each pixel). The current SLMs refreshing time ranges from 3 (Marshel et al., 2019b) to 16 ms(Chaigneau et al., 2016; Chen et al., 2019; Mardinly et al., 2018; Packer et al., 2012; Ronzitti et al., 2017). Faster switching time (2 ms) can be achieved using the LC-SLM in overdrive mode. However, this better performance comes at the expense of diffraction efficiency (DE) drop to 85%. In 2P excitation, this DE degradation of 15% brings a loss of nearly 30% of the achievable signal (Marshel et al., 2019b).

Thus, for asynchronous stimulation following this regime, with an SLM to change the targets the temporal resolution fall in the range of $\Delta T_{min} \sim 3 - 50\ ms$.

A possible axis of improvement would be to use another optical approach with better switching performance. Typically, the sequentially targeting strategy presented in (Chapter1) offer an optimized switching time by using galvanometric mirrors or acousto-optics deflectors to stimulate one cell after the other one. The performance of those two devices are far beyond the one obtained by an SLM, reaching typical switching time in the range of T_{switch} of ~100 µs for galvanometers and ~10 µs for AOD (Fernández-Alfonso et al., 2014). Despite a drastic improvement of T_{switch_min}, the main source of limitation remains the time of illumination T_{illum_min} which is incompressible: $\Delta T_{min} \propto T_{dwell\_min} \propto\ 1 - 49\ ms$.

With the example of $\Delta T\ =\ 4\ ms$, we fall in the second regime where $\Delta T < T_{dwell}$. In this condition, we are no longer considering T_{dwell} as a limitation, leading to: $\Delta T_{min} \propto T_{switch\_min}$. However, we observe a time interval where the two illumination periods are overlapping. This overlap corresponds to a transitory step in the protocol during which the two targets should be simultaneously illuminated with different powers (Figure 43).

An optical system capable of following such would be able to achieve asynchronous temporal resolution free from the constraint of the cell illumination time. However, to accomplish this protocol, two main criteria must be met:

- first, being able to stimulate simultaneously two targets while adapting the distribution of intensity between them.

- second, the transition between each stage of the protocol ($T_{switch\ min}$) is sufficiently fast to be considered negligible compared to the delay introduced and the opsin's kinetics ($T_{switch\_min} \ll \tau_{off}$).

This example shows the protocol for fast asynchronous stimulation of two cells. In this case, we need to perform three different patterns of excitation: Cell:1→Cell:1+2→Cell:2. But this strategy can be generalized to desynchronize n neurons (or n groups of neurons) with delays inferior to each activation dwell-time by generating excitation patterns: Cell:1→ Cell:1+2→ ⋯ →Cell:1+2+⋯+n, →Cell:2+⋯+n, →Cell:3+⋯+N→⋯,→Cell:n.

The next section will introduce the system built during this thesis to perform asynchronous stimulation.

6.2 A new optical system for fast switching rate

As introduced in (Chapter3) the, holography is a gold technique to address several targets simultaneously while controlling the intensity illumination distribution, fulfilling the first criteria for short asynchronous stimulation. However, the transition time between phases is to long to generate quick target transition and respect the second criteria. In comparison, the sequentially targeting strategy using galvo or AOM presents fast transition time respecting these last criteria but a limitation to one target.

Therefore, a solution is to develop a holographic setup where the transition between target is no longer dependent of the SLM refreshing time but rather controlled using galvo or AOM. The most straightforward combination would be to use several SLMs that are sequentially illuminated. This type of approach has been demonstrated by (Marshel et al., 2019a) using two fast LC-SLMs operating in the overdriving mode. The holographic patterns were updated every 2 ms on each SLM. The two devices were illuminated sequentially through an ultrafast optoelectronic switcher ($T_{switch} \approx 80\mu s$) and combined with a couple of galvos to enable spiral scanning and 2P optogenetics (Figure 44). Critically, this schema is incompatible with the sub-millisecond tuning of the neuronal activity of multiple neurons as proposed by the second regime protocol unless using 2H-1 or H independent SLMs, respectively. Therefore, coupling an optical switching system to several holograms allows increasing the temporal resolution. However, several SLMs are not a viable solution as it leads to a drastic increase in complexity and cost of the system.

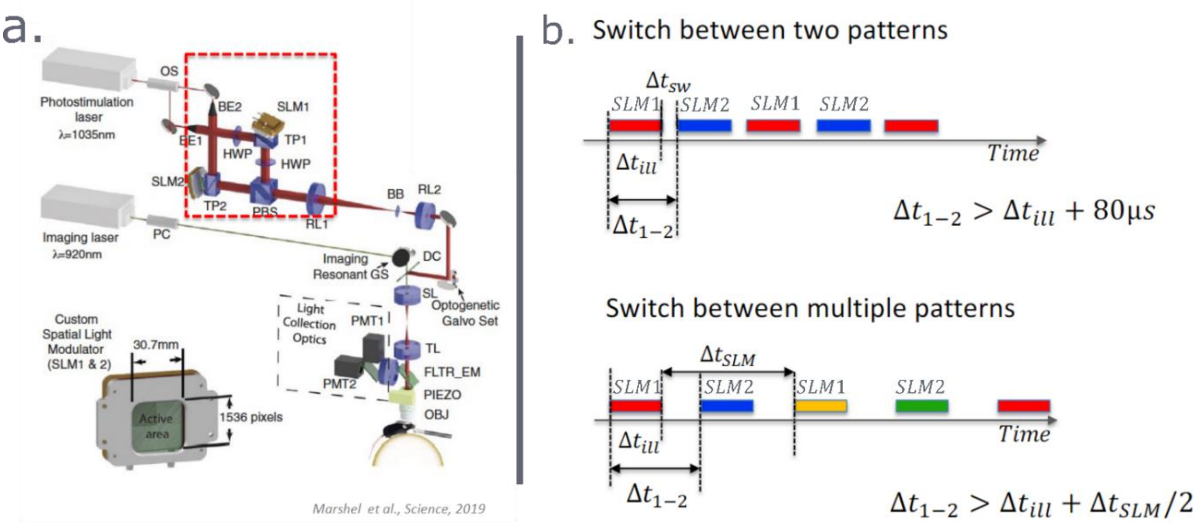

Figure 44: Use of two SLMs to improve the temporal resolution (from Marshel et al.)

a.Schema of the optical system, using two SLMs in parallel

b.Protocol of phase profile switch between two or multiple patterns

[adapted from Marshel et al Science, 2019]

This leads to the question of how simultaneously generate several independent holograms without multiplying the number of SLM?

The solution was partially introduced with the Multi-shape system presented in the (Chapter 4) publication (Figure 45). This approach was initially developed to overcome the limitation to a single 3D multiplexed shape introduced by other 3D-MTF approaches. To this end, the system takes advantage of the chirped expanded gaussian beam (“line illumination”) obtained at SLM2 when the grating is illuminated by a collimated beam (Chapter4). Therefore, multiple parallel horizontal lines illumination was generated on the SLM2 screen, aligned with an independent 3D hologram. Each line could be encoded with a different shape using amplitude modulation technique and finely displaced using CGH to hit the desired area of the SLM2 screen.

The phase profile displaced on the SLM2 was divided in multiple tiled (band) (Figure 45) according to the number of line illumination used. Each holographic band or tiled can encode for different target positions in 3D. Thus, we could consider each tiled of the phase profile as an independent SLM (Figure 45). However, in this configuration, the illumination of the different phase band (tiled) is controlled using the SLM1. Thus, the performance of this system in terms of temporal switching remains limited to that of an SLM.

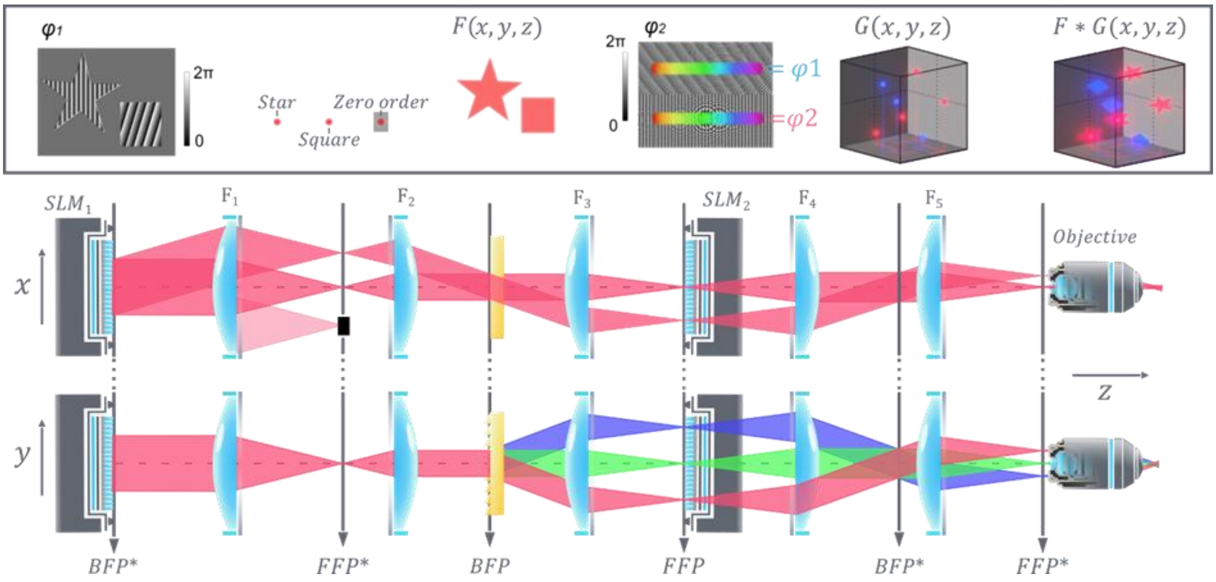

Figure 45: Multiplexed Temporally Focused Multi-Shape system (MTF-MS)

Up: Schema of observed phenomenon at different planes of the optical system

Middle: Optical system in x,z directions

Dow: Optical system in y,z directions

Those are the reasons why we proposed a new approach for ultra-fast sequential light targeting (FLiT). We coupled the multiplexing SLM2 addressed with multiple vertically tiled holograms with a galvanometric mirror (GM). The GM was incorporated upstream, replacing the SLM1 to sweep only one chirped expanded gaussian beam across the hologram tileds and generate sequential 2D or 3D illumination pattern. In this configuration, the SLM1 is completely replaced by the GM thus, the shape of the illumination can no longer be controlled. Therefore, expanded Gaussian spots are obtained at the sample plain with a diameter, function of the magnification of the system (Chapter 3).

6.2.1 Material and methods:

The system was built around a commercial upright microscope (Olympus BX51WI) placed on a XY stage for sample displacement (Luigs & Neumann, V380FM). A femtosecond pulsed beam delivered by a diode pumped, fiber amplifier system (Amplitude Systems, Goji HP; pulse width 150 fs, tunable repetition rate 10‑40 MHz, maximum pulse energy 0.5 µJ, maximum average power 5 W, wavelength λ = 1030 nm) operated at 10 MHz, was sent first through a λ/2 wave retarder (Thorlabs, 690-1200 nm, AQWP05M-980) in combination with a polarizer cube (CVI Melles Griot) for a manual control of the laser power. The beam was then demagnified with a telescope (f1 = 100 mm; AC508-100-B, Thorlabs; f2 = 50 mm, AC508-50-B, Thorlabs) and sent through an acousto-optic modulator (AOM) (AA Opto-Electronic, France) to drive fast and precise light power control. The first diffracted order was projected on a pair of XY GMs (3 mm aperture, 6215H series; Cambridge Technology) with a de-magnifying telescope (M = 0.4 magnification). Only the Y GM was used and driven by a servo driver (Cambridge Technology, MicroMax series 671). The GM plan was conjugated to a reflective dispersion grating of 800 l/mm by means of a telescope (f = 250 mm; AC508-250-B, Thorlabs; f = 500 mm, AC508-

500-B, Thorlabs). A lens (f = 500 mm, Thorlabs, AC508-500-B) transmitted the resulting spatially chirped beam on the sensitive area of a reconfigurable liquid-crystalon-silicon LC-SLM (LCOS-SLM X10468-07, Hamamatsu Photonics, resolution 800×600 pixels, 20 μm pixel size), located in the Fourier plane of the diffraction grating. The LC-SLM was finally conjugated to the back focal plane of the microscope objective (Olympus LUMPlanFL 60XW NA 0.9) via a telescope (f = 1000 mm; AC508-1000-B, Thorlabs; f = 500 mm, AC508-500-B, Thorlabs).

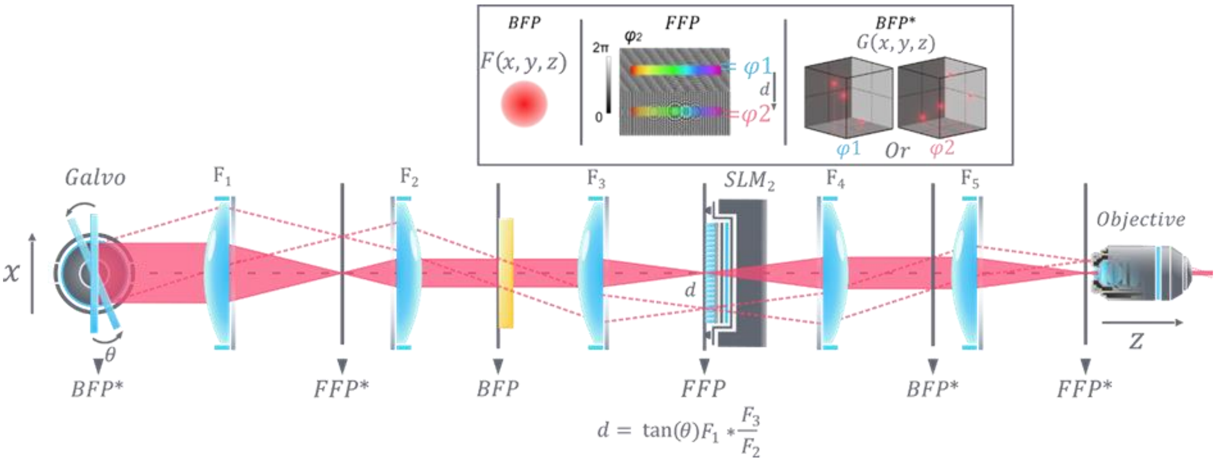

Figure 46: The fast sequential light patterning system (FLiT):

Optical setup of FLiT. A pulsed collimated beam (red line) is reflected by a galvanometric mirror (GM) onto a diffracting grating (G) via a 4f-telescope. Diffracted off the grating, the beam is collimated onto a liquid crystal spatial light modulator (LC-SLM) in the form of a horizontal (i.e., orthogonal to the orientation of the grating lines) spatially chirped strip of light. The LC-SLM is imaged onto the back aperture of an objective lens so that ad hoc phase-modulation on the LC-SLM allows multiplexing the initial beam and generating a multi-site temporally focused pattern of light in the sample. As deflection of the beam by the GM results into a translation of the illuminating bands on the LC-SLM (dark red lines), addressing the LC-SLM with H independent tiled holograms ϕi can lead to fast switch of different groups of light patterns into the sample. The top and bottom drawing represents the XY and the YZ plane views, respectively.

The LC-SLM was divided in n horizontal tiles, each independently configurable. Each tiled hologram could be encoded with different sets of 3D diffraction-limited spots enabling to multiplex the temporally focused gaussian beam in multiple targeted locations on the sample. The phase profile of each n zones was independently calculated with a weighted Gerchberg and Saxton Algorithm (Gerchberg & Saxton, 1969). The effect of the zero order in the sample when necessary was suppressed by introducing a cylindrical lens in front of the LC-SLM as detailed in (Hernandez et al., 2016) or physically blocked. Each tile of the LC-SLM was illuminated by deflecting the GM of a certain angle, corresponding to a precise driven voltage. A calibration was done in order to associate the beam position on the LC-SLM and the voltage to be applied on the GM. Additionally, fast modulation by the AOM allowed to adapt laser power accordingly with the number of spots in each hologram, their diffraction efficiency and the efficiency of each horizontal tiles.

During hybrid-FLiT experiments for sub-ms desynchronization of pairs of neurons, the AOM and GMs was driven with a Digidata 1440A interface and pClamp software (Molecular Devices). In hybrid-FLiT experiments for mimicking of random spike patterns and cyclic-FLiT experiments, the system was controlled with a digital-analog converter board (National Instrument, USB-6259). The control of the system was fully automatized through a homemade software written in Python 3 and using the open graphic library PyQt5 which allowed automatic calculation of the tiled holograms and control of the

GM rotation and AOM attenuation. The ditaile function of this software are presenter in the end of this chapter.

The use of a tiled phase profile and the introduction of an angle θ by the GM are not without consequences. In the next paragraph, we will outline those consequences on the system performances.

6.2.2 Tiled Holograms, line illumination, and performance

The dimensions of the chirped expanded gaussian beam obtained at the SLM plain depends on two effects (Figure 47)

(1) The dispersion, witch based on the laser impulsion duration and grating dispersion (related to the number of lines per mm and incident angle) will impact the line width

(2) the focalization, based on the practical numerical aperture of the lens after the grating (depending on the focal length and the Gaussian beam diameter) impact the line thickness.

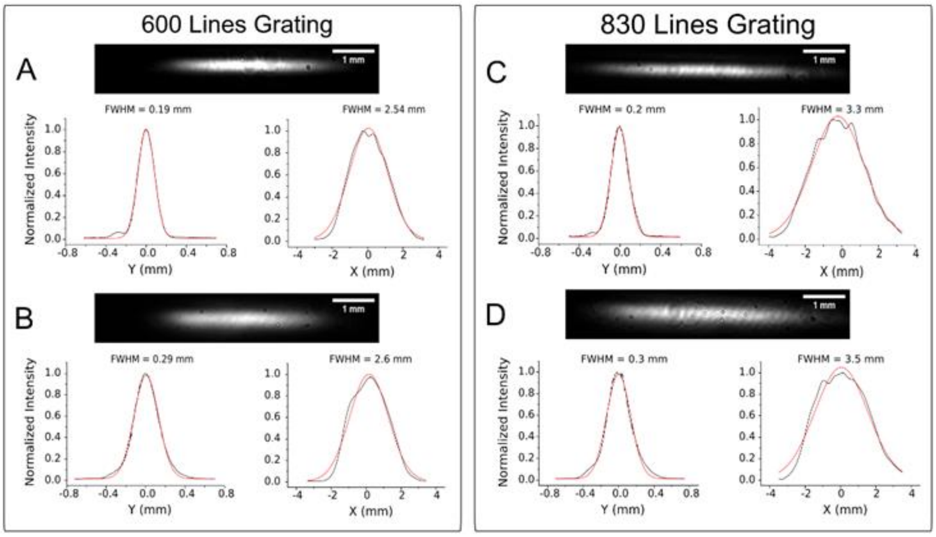

Figure 47: Degree of focusing of the illumination beam on the SLM (FLiT):

(A-D) Intensity profile of the chirped beam at the LC-SLM plane for different degree of focusing (controlled by modifying the size of the laser beam on the grating) and grating dispersion: 600line/mm grating high-focusing (A) and low-focusing (B) and 830line/mm grating high-focusing (C) and low-focusing (D). (D) corresponds to the condition used in Figure 48. For each condition is provided the image of the beam (Top) and the x- (vertical) and y- (horizontal) intensity profile of the corresponding beam (Bottom). Black line indicates the intensity profile smoothed over three pixels. Red line indicates a Gaussian fit. In the legend, the full width half maximum (FWHM) of the profile is indicated.

This line is used to illuminate one of the tield of the SLM giving rise to two scenario cases (1) the illumination line's thickness is smaller than the phase band illuminated. In this case, no notable effect is observed (Figure 48.b.1); (2) on the contrary, the thickness of the illumination line is larger than the phase band height (Figure 48.b.2). In those conditions, two effects are observed: energy loss and deformation of the spots. Indeed, a fraction of the light does not illuminate the desired phase tiled but to the adjacent, leading to energy loss. Moreover, this effect also corresponds to a low pass frequency filter resulting in the Fourier plane to a widen spot in the direction parallel to the slit’s sensor. This effect can be used to counteract the ellipticity of the spot introduced by the diffraction grating (Figure 48.e.f).

Then, for a given width of the line illumination, an optimal number of tiled divisions can be performed to minimize the energy loss and spot ellipticity. Thus, finer illumination line, allow to exploit smaller phase tiled witch correspond to a higher number of divisions for the phase profile.

However, reducing the size of the line has two effects: it reduces the surface of irradiation at the SLM and, therefore, the intensity that can be sent before inducing potential damage on the device. It also reduces the total number of pixels used per tiled and thus the complexity of the hologram that can be generated.

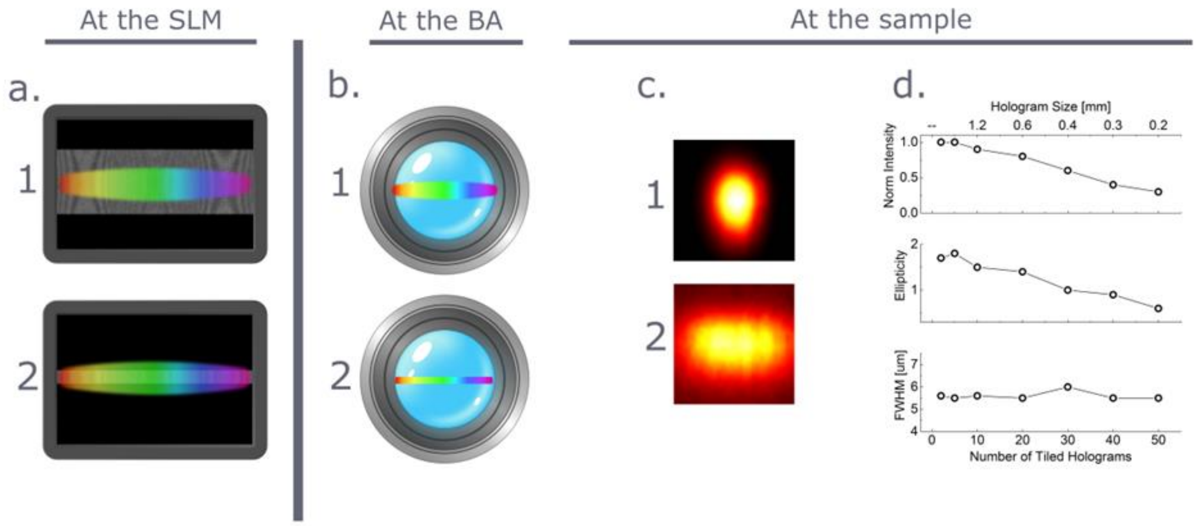

Figure 48: Evaluation of the impact of tiled Holograms and line illumination on the performance

a. Schema of a line illumination over one tiled hologram in two conditions where (1) the tiled is larger than the line (2) the tiled is smaller compared to the line

b. Line illumination obtained at the back aperture for the same case scenario presented in (b)

c. xy images of the spot encoded by using 30x800 pixels (i.e., 0.6 x 12 mm) holograms (corresponding to LC-SLM tiled in 20 regions) (Top) and 12x600 pixels (0.24 x 12 mm) holograms (corresponding to LC-SLM tiled in 50 regions) (Bottom). LC-SLM pixel size 20 µm.

d. Intensity (Top), Ellipticity (Middle) and FWHM of axial intensity distribution (Bottom) of a spot encoded by holograms of different sizes in the direction orthogonal to the grating dispersion. (B) xy images of the spot encoded by using 60x800 pixels (i.e., 1.2 x 12 mm) holograms (corresponding to LC-SLM tiled in 10 regions) (Top), 30x800 pixels (i.e., 0.6 x 12 mm) holograms (corresponding to LC-SLM tiled in 20 regions) (Middle) and 12x600 pixels (0.24 x 12 mm) holograms (corresponding to LC-SLM tiled in 50 regions) (Bottom). LC-SLM pixel size 20 µm.

6.2.3 Deflection angle and performance

With this system, the GM is used to deflect the laser beam by an angle \theta which corresponds to a displacement d of the line illumination at the SLM (or Fourier plane) (Figure 49). The introduction of this deflection has a double impact on the performance of the system:

First, the displacement d at plane of the SLM is also present in the conjugated plane at the back aperture of the objective, modulo the magnification of the intermediate telescope. Thus, as shown on the schema in (Figure 49). the lines displaced from the center are partially cut by the circular back aperture, inducing a loss of intensity (Figure 49.c right). It is possible to get rid of this effect by underfilling the objective back aperture (Chaper3). However, this will result in the deterioration of the axial confinement and change the spot size.

Second, the GM plane is conjugated to the sample plane. Thus, the laser beam coming out of the objective lens is tilted with angle \theta modulo the magnification of the system. This induces the same tilt over the spots and the FOE.

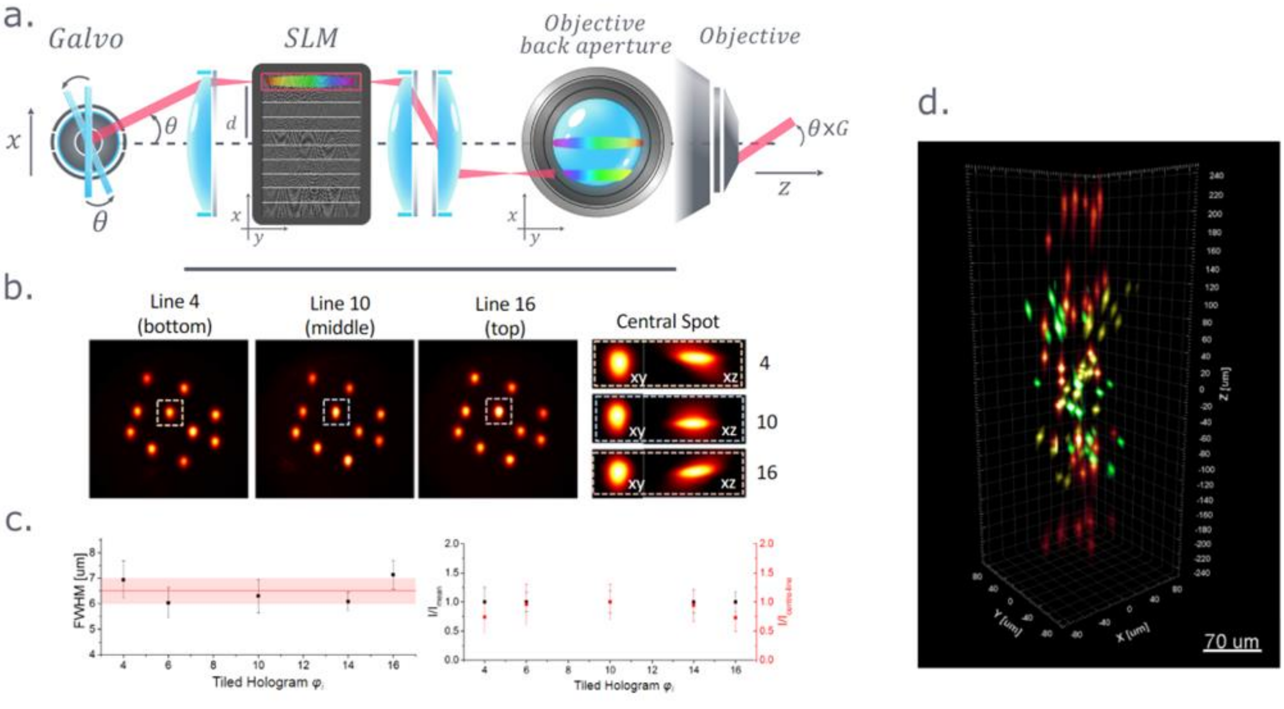

Figure 49: Evaluation of the impact of the line laser displacement on the optical performance

a. Schema of the FLiT system with combination of x,z view for the laser propagation and x,y view for the illumination over the SLM and objective back aperture

b. (Left) Representative distribution of multiple spots encoded with the central hologram (line 10) and extreme line at the objective back aperture (line 4,16) $\varphi 0$. Scale bar 10µm. (Right) xy and xz projections of the central spot in (Left) encoded by hologram $\varphi 4$ (Top), $\varphi 0$ (Middle) and $\varphi 16$ (Bottom). Scale Bar 5µm.

c. (Left) Axial intensity FWHM of individual spots distributed in a matrix as in (b) and generated by different holograms φi. Black symbols indicate Mean $\pm$ SD of FWHM per each holograms φi. Red line and reddish band indicates the global mean and SD over the different φi, respectively. (Right) Intensity distribution of 10 random spots arranged as in (b) within (black Y-axis) and between (red Y-axis) the field of view (FOV) of different holograms φi encoded on different tiles i of the LC-SLM. Black symbols indicate per each hologram φi, normalized Mean $\pm$ SD of the ratios between the intensity I of each spot and the averaged spot intensity Imean within the FoE of φi. Red symbols indicate per each hologram φi, normalized Mean $\pm$ SD of the ratios between *the intensity of each spot and the intensity of the same spot encoded by the central hologram* $\varphi 10$. *Each hologram was 30x800 pixels, i.e. the LC-SLM was tiled into 20 regions.*

d. 2PE fluorescence of different groups of spots generated by different tiled holograms φi *randomly distributed across a 120 x 120 x 300 µm3 volume. Different colors correspond to different tiled hologram (hologram* $\varphi - 6$, *yellow; hologram* $\varphi 0$, *red; and hologram* $\varphi 6$, *green). The SLM is divided in 20 tiled holograms.*

6.2.4 Switching perfomance

Next, we studied how the velocity of the scan unit defines the temporal resolution of FLiT. Specifically, we tested the minimum switching time to (i) move between two adjacent holograms (Figure 50.) and (ii) sequentially illuminate all holograms at constant rate (Figure 50). For this, we generated 20 equivalent holograms each projecting a single spot on a photodiode placed in a conjugated image plane (Figure 50).

In the first case, we measured the time needed to switch between adjacent tile i and tile i+1 of the LC-SLM subdivided in 20 holograms. For that, we generated two distinct phase masks, φi and $\varphi i + 1$, each encoding for an individual spot placed in a specific XY location of the focal plane. We positioned the photodiode (PD) in a conjugated plane of the sample, and we aligned it such that the spot illuminates the center of the detector. We displayed φi on the tile i and we recorded the light intensity on the PD, while driving the GM servo with a single-step voltage pulse (pulse width 1s) which deflect the beam across small angles between tile i to tile i+1. We repeated the same procedure by displaying $\varphi i + 1$ on tile i+1. From these two measurements, we obtained the averaged switching time to move between two consecutive tiled holograms in opposite directions, as the time taken for the signal to rise/fall between 3% and 97% of the maximum intensity. Of note, the position of PD was finely adjusted to maximize the photon counting when the GM was stationary positioned on tile i or tile i+1. We measured a switching time of $90 \pm 10\ \mu s$ (Figure 50., n = 30 measurements)

Second, we measured the minimal switching time between holograms when sequentially scanning at constant rate all holograms. We generated a hologram φi on a single tile i encoding for an individual spot detected by the PD as previously described. We then recorded the light intensity on the PD, while driving the GM servo with a staircase voltage pulse (pulse time interval 50µs) which deflects the beam across wide angles between tile 1 to tile 20. From that, we measured the beam dwell-time on hologram φi during switch between hologram $\varphi 1$ and hologram $\varphi 20$. We repeated the same procedure for all 20 holograms. From that, we measured the beam dwell-time on each tiled hologram during whole scan of all holograms at constant switch rate. Of note, scan of all holograms would be alternatively possible by driving the GM with a single-step voltage facilitating maximum speed deflection of the beam across wide angles between tile 1 to tile 20. While that can facilitate shorter dwell-time per hologram, it also gives variable dwell-time per holograms as central tiled holograms feature shorter illumination dwell-times compared to distal tiled holograms as mirror reaches maximum speed at the midpoint. We could reach a switching time of $50 \pm 10\ \mu s$ with this configuration (Figure 50, n = 30 measurements).

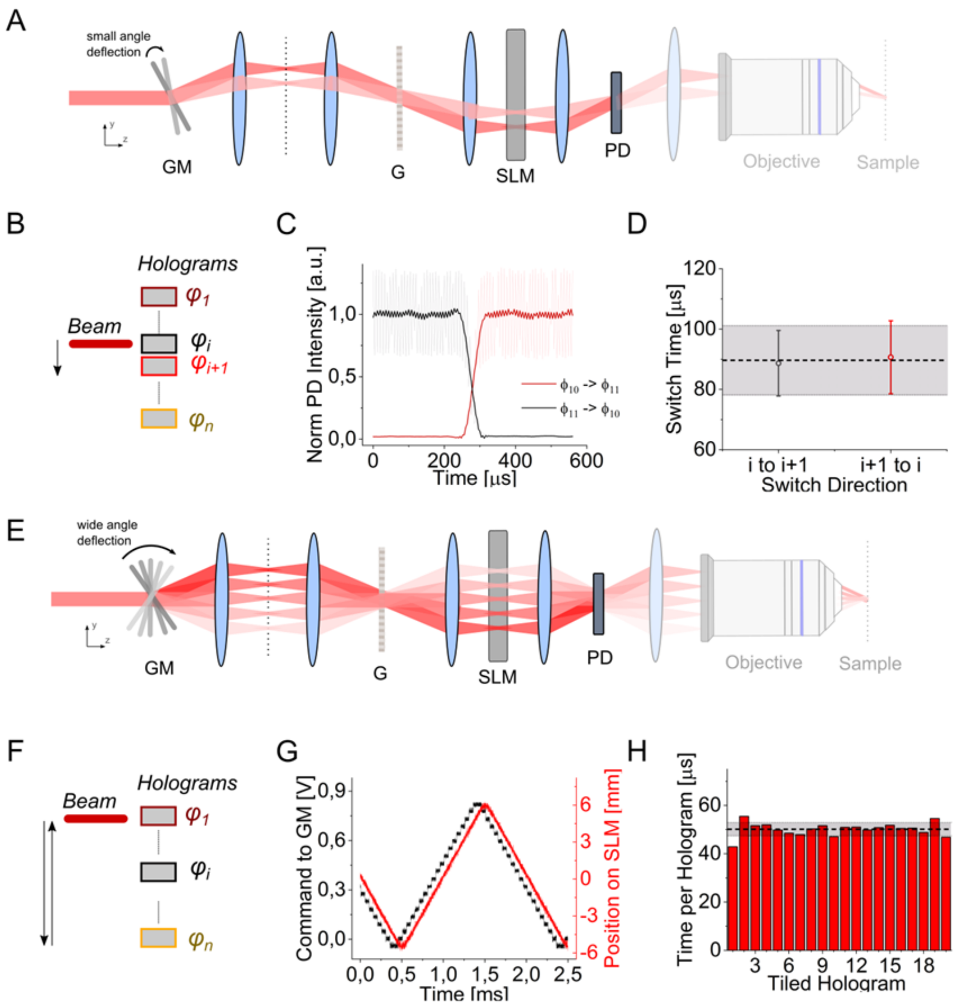

Figure 50: Evaluation of the switching speed of the system FLiT

a. Switching time between two adjacent tiled holograms (φi and $\varphi i + 1$) is measured by means of a photodiode (PD) placed in an image conjugate plane while driving the galvanometric mirror (GM) with small angles single-step voltage inputs.

b. Scheme of illumination switch between tiled hologram φi and $\varphi i + 1$ on the SLM display corresponding to sequence depicted in (A).

c. Representative intensity response of the PD when GM is switched from hologram $\varphi 11$ (encoding for an individual spot in the middle of PD) to hologram $\varphi 10$ (deviating the beam out of the PD) (black line) or, vice versa, from hologram $\varphi 10$ (encoding for an individual spot in the middle of PD) to hologram $\varphi 11$ (deviating the beam out of the PD) (red line).

d. Switch time calculated as the time taken for the signal to rise/fall between 3% and 97% of the maximum intensity, when the spot is encoded in hologram φi and GM is switched from hologram φi to $\varphi i + 1$ (black symbols) or vice versa (red symbols). Horizontal black line and grey bands indicate the global mean and SD switching time, respectively.

e. Switch time to sequentially illuminate all holograms at constant rate from $\varphi 1$ to φn is measured by driving the galvanometric mirror (GM) with a wide-angle staircase voltage input.

f. Scheme of the illumination switch to sequentially illuminate all holograms from $\varphi 1$ to φn on the SLM display corresponding to the sequence depicted in (E).

g. GM voltage input (black line) and corresponding position of the incoming beam on the LC-SLM (red line) when GM is driven as depicted in (E).

6.3 Software Development

“A picture is worth a thousand words. An interface is worth a thousand pictures.”,(Ben Shneiderman Professor for Computer Science)

During my PhD I had to develop different software elements to facilitate the handling or the study of specific systems. The work I want to present here reflects Ben Shneiderman citation: A graphical interface allowing easy and fast handling of the fast scan system and any other system controlling a SLM.

6.3.1 Fast Scan Interface

As we have seen, the fast scan system allows to achieve very short activation deltas between cells and significantly increases the maximum number of cells accessible at a given power by a better management of the illumination time. To obtain a practical and usable system for everyone, the development of dedicated software was inevitable. To fully master this system, it was necessary to control both the SLM (change the number of lines, their orientation, corrections etc), the galvos, and the AOM for power management. This represents many parameters to manage, that quickly made the use of Matlab or python scripts impractical.

SLM Control

We will review all the functionalities proposed by the software from the generation of a simple spot to the management of the fast scan protocols. We will start with the software homepage (Figure 51).

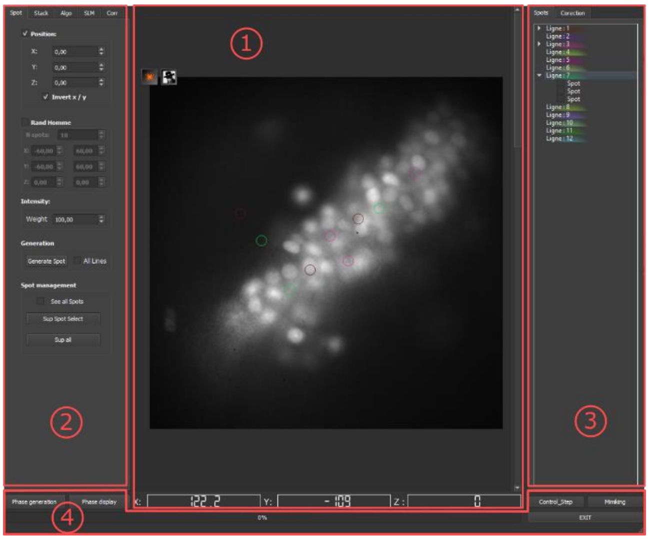

X: 0,00
Y: 0,00
Z: 0,00
Weight: 100,00
X: 122.2 Y: - 109 Z: 0

Figure 51: Software homepage divided in four sections.

This interface page is divided into 4 sections that will be detailed in the rest of this chapter (Figure 51).

- Section 1: Navigation and display of the samples and spots

- Section 2: Management of General Parameters
- Section 3: Management of lines created on the SLM
- Section 4: Phase generation and access to the protocol programming page

Section 1: Navigation and display of the samples and spots

Part 1 is a navigable area (zoom, move). The sample's background image can be obtained either directly by camera or by loading an image stack. The position of the cursor on the image is given in µm in (Figure 52.part 2). The ratio between the camera pixel size and their equivalent dimension at the sample is obtained according to the parameters entered for the imaging system (pixel size, objective, tube lens).

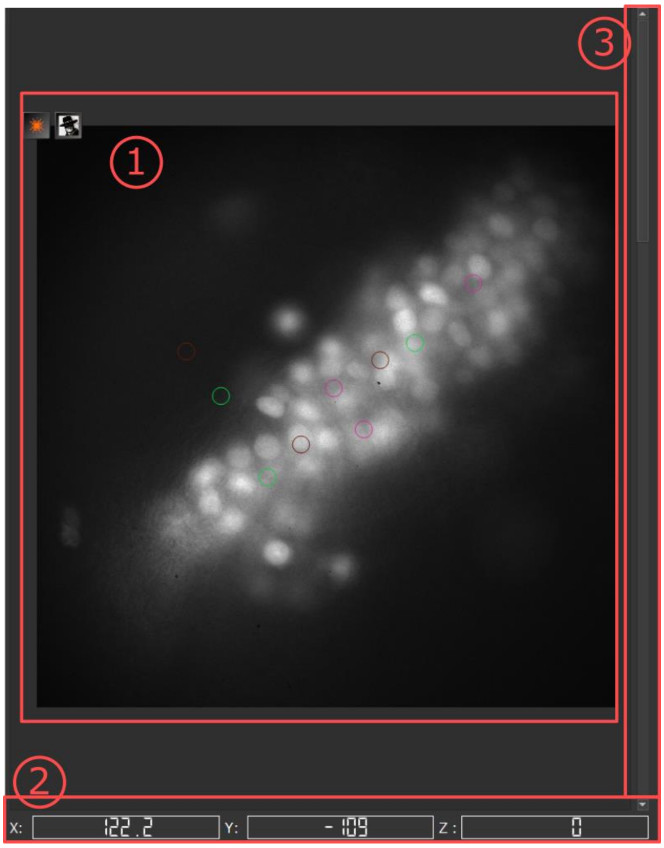

Figure 52: Navigation and display (section 1) divided in three parts.

It is possible to place the spots at the desired position by double-clicking. The spot is then assigned to the lines selected in (Figure 52.section 3). As a reminder, our SLM is divided into N number of zones or lines. They are independent of each other and therefore must be treated as a separate "SLM". Hence the need to always specify which lines we are working on. It is possible to navigate from one plane to another in z using the slider (Figure 53.part 3). If the software controls the camera, it is possible to connect the slider to control a piezo actuator.

Section 2: Management of General Parameters

The (Figure 51.section 2) consists of 5 distinct parts. Part 5 will be treated separately as it has many parameters.

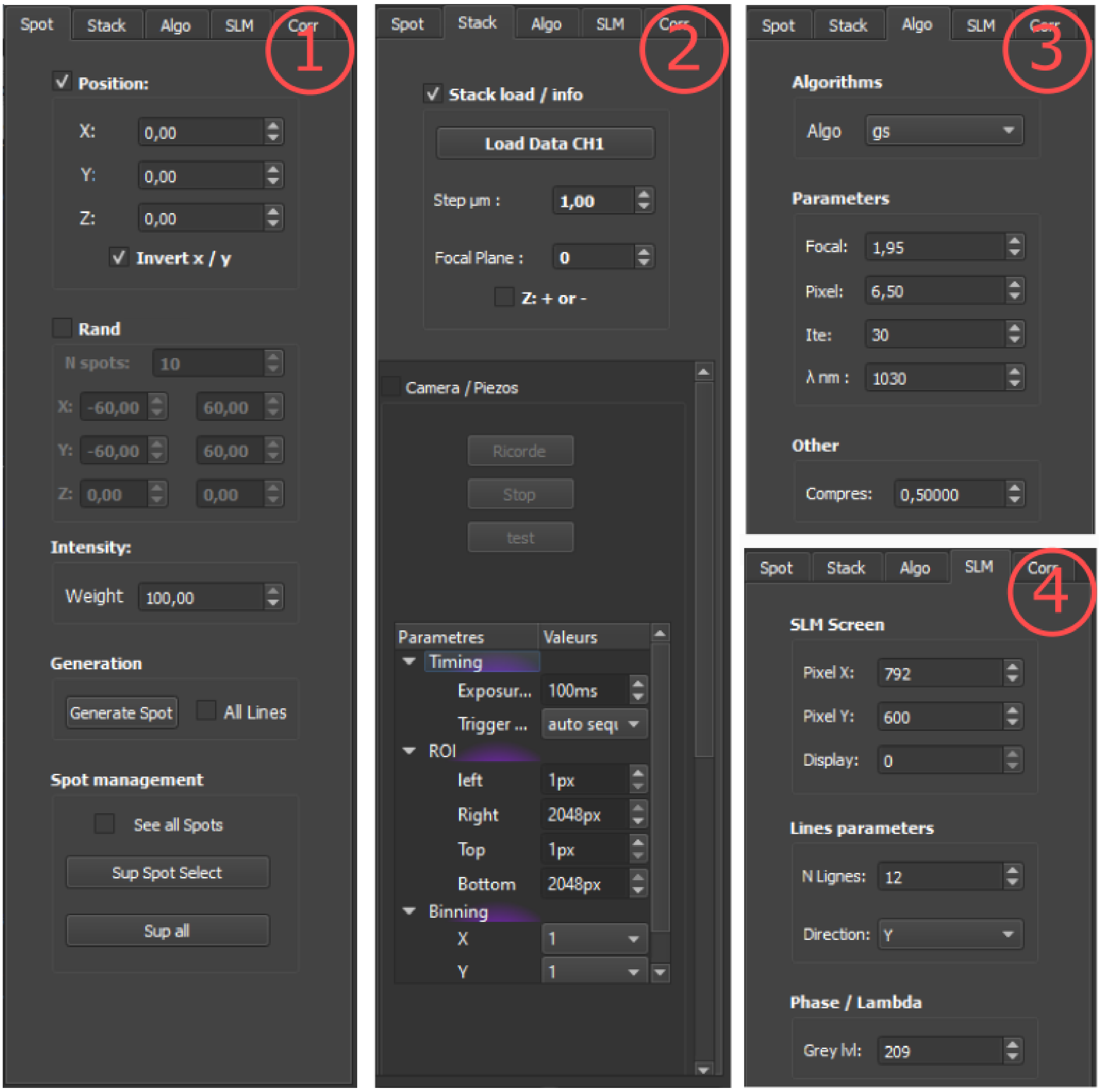

☑ Position:
X: 0,00
Y: 0,00
Z: 0,00
☑ Invert x / y

☐ Rand
N spots: 10
X: -60,00 60,00
Y: -60,00 60,00
Z: 0,00 0,00

Intensity:
Weight 100,00

Generation
☐ All Lines

Spot management
☐ See all Spots

☑ Stack load / info
Step µm : 1,00
Focal Plane : 0
☐ Z: + or -

☐ Camera / Piezos

Parametres	Valeurs
Timing	
Exposur...	100ms
Trigger ...	auto sequ
ROI	
left	1px
Right	2048px
Top	1px
Bottom	2048px
Binning	
X	1
Y	1

Algorithms
Algo gs

Parameters
Focal: 1,95
Pixel: 6,50
Ite: 30
λ nm : 1030

Other
Compres: 0,50000

SLM Screen
Pixel X: 792
Pixel Y: 600
Display: 0

Lines parameters
N Lignes: 12
Direction: Y

Phase / Lambda
Grey lvl: 209

Figure 53: Management of General Parameters (Section 2) divided in 4 parts

Part 1 Spot:

Position: allows to place a spot in X\Y\Z precisely. The “inverted x/y” box lets invert the direction of the X and Y-axis. This can be particularly useful if the camera imaging plan is rotated compared to the field of excitation.

Rand: generate N spots randomly in a volume defined by the barrier values given in XYZ.

Intensity: to change the intensity value of a spot. The sum of the respective intensity of the spots per line must be equal to 100.

Generation: simply induces the generation of the spots according to the previously selected criteria. It is possible to choose an identical generation on all the lines otherwise, the spots will be generated on the lines selected in (Figure 51.section 3).

Spot management: The “see all spot” check box displays all the spots with different z's in the same plane in (Figure 51.section 1). “Sup Spot Select” deletes the spots selected in (Figure 51.section 3) or by right-clicking on them in the “Navigation and display” (Figure 42.section 1) . “Sup all” to erase all the spots.

Part 2 Stack:

Stack load/info: Allows you to load a Stack to use in the “Navigation and display” zone (Figure 51.section 1) . “Step µm” indicates the corresponding distance in µm between each of the images in the loaded stack. “Focal plane” indicates what is the objective current focal plane in this image stack. Then the algorithm determines the z position of the spots in different planes according to the precedent parameters.

Camera / piezo: Activates the use of the camera and piezo. It is possible to change various camera parameters such as exposure, region of interest, etc. The piezo camera operation has been made for the camera used, namely a PCO.Panda 3.1 but remains valid for any PCO camera and could be generalized to cameras of other brands, especially with the help of micromanager. For the piezo, the “Slider” (Figure 52.part 3) used for z navigation is adapted to the maximum distance achievable by the device. The step represented by a slider movement is then controlled by the step value of the stack part.

Part 3 Algo:

Algo: to change the algorithm used. We used the algorithms proposed by (Pozzi et al., 2018) and a classic GS. The whole application is written in python; the algorithm is no exception. It is then possible to add any algorithm by using the same parameters.

Parameters: used by the algorithm: equivalent focal length of the system from the SLM screen to the sample, SLM pixel pitch, number of iterations, and the laser wavelength.

Part 4 SLM:

SLM screen: defines the parameters of our SLM in terms of resolution. In the case of SLM hamamatsu we can also indicate the equivalent monitor number.

Lines parameters: the number of divisions or number of lines to generate. It is possible to choose the orientation of these lines according to an axis of the SLM in the case of a possible rotation of the SLM.

Phase/Lambda: The SLM is addressed with 8-bits (value of the pixel ranging from 0 to 255) grayscale image. Each of the gray values corresponds to a certain phase delay. Normally a value of 0 should correspond to a 0-phase delay at the SLM and 255 to a 2π phase shift. However, depending on the wavelength used the gray level value corresponding to a 2π phase shift may be smaller than 255.

Part 5 Corr:

The “Part 5” deals with all the corrections that can be added either on the whole SLM without distinction of lines or mor specifically with an attribution to the selected lines only.

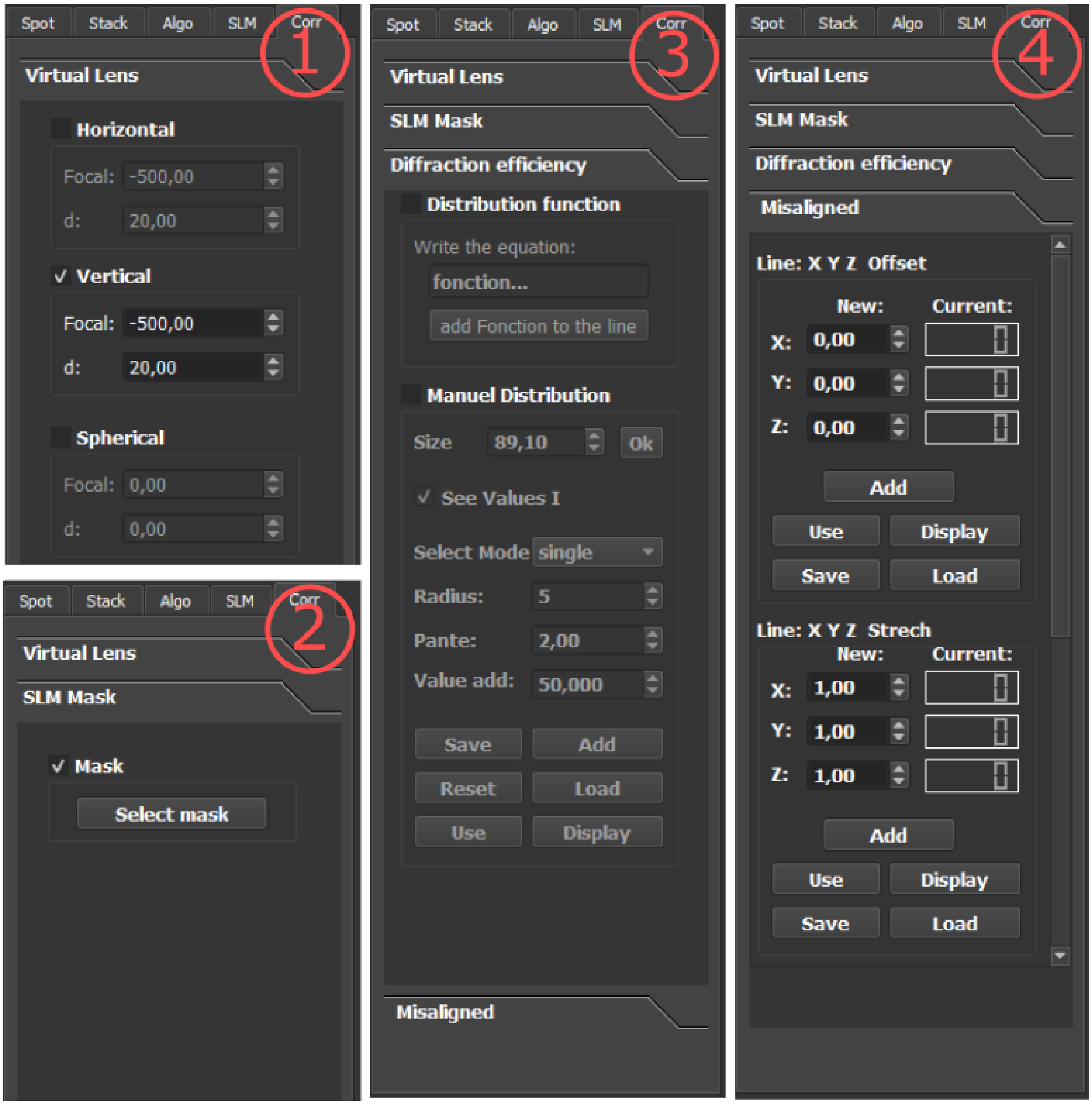

☐ Horizontal

Focal: -500,00

d: 20,00

✓ Vertical

Focal: -500,00

d: 20,00

☐ Spherical

Focal: 0,00

d: 0,00

✓ Mask

☐ Distribution function

Write the equation:

fonction...

☐ Manuel Distribution

Size 89,10

✓ See Values I

Select Mode single

Radius: 5

Pante: 2,00

Value add: 50,000

Line: X Y Z Offset

	New:	Current:
X:	0,00	
Y:	0,00	
Z:	0,00	

Line: X Y Z Strech

	New:	Current:
X:	1,00	
Y:	1,00	
Z:	1,00	

Figure 54: Management of General Parameters (Section 2) part 5

Virtual Lens: to add a Horizontal, Vertical or Spherical lens correction. It is possible to define their respective focal lengths. These corrections are applied to the entire hologram. It allows to correct for the cylindrical lens place in front of the SLM to suppress the zero-order (Chapter 3).

SLM Mask: to add the phase correction mask provided by the manufacturer. It is also possible to load any phase profile already generated by other processes.

Diffraction efficiency: corrects for the SLM diffraction efficiency (see Chapter 3). Two methods or even a combination of both can be used. The first and potentially the simplest one allows writing a mathematical formula as the one introduces in (Chapter 3). The function must be normalized to 1. The second method allows to generate a weights map for the correction, by painting directly on an interactive matrix (Figure 55).

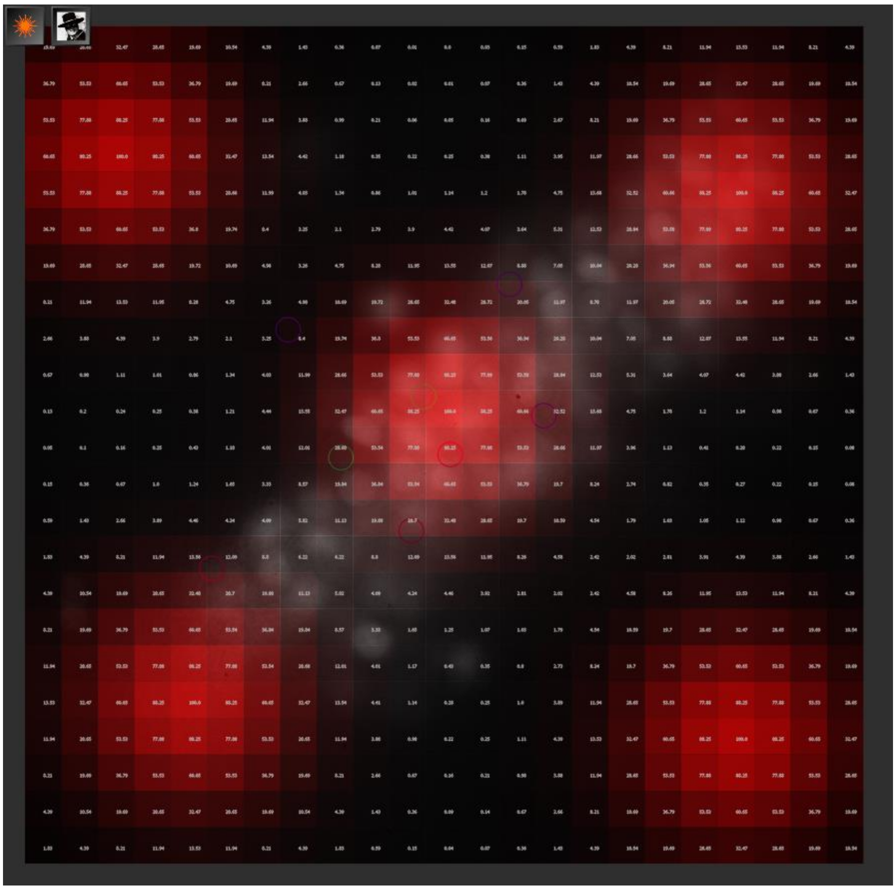

Figure 55: Diffraction efficiency Weights map

It is possible to define the size of the brush and the type of brush, either linear, Gaussian, or conical. Therefore, diffraction efficiency can be corrected, and even certain regions can be favored as shown in (Figure 55). For example, this last possibility is interesting to compensate for the non-uniformity of the opsin expression over the sample. These two corrections are generated for each line. As, each line is in a different position at the back aperture of our lens; aberrations and deformations can affect each of them differently.

Misaligned: It is possible to correct for any offset or stretch of the FOE and for each line. Here 1 represents Zero deformation. It is possible to stretch the FOE with values greater than 1 where 1.1 represents a 10% stretch and inversely for compression.

Z Correction: Is all sow an interactive matrix where the value attributed to a pixel corresponds to a z displacement in µm added to the spot placed in this area (Figure 56). It allows compensating for a potential title in z of the stimulation plane as the one introduces by the temporal focusing (Chapter 4).

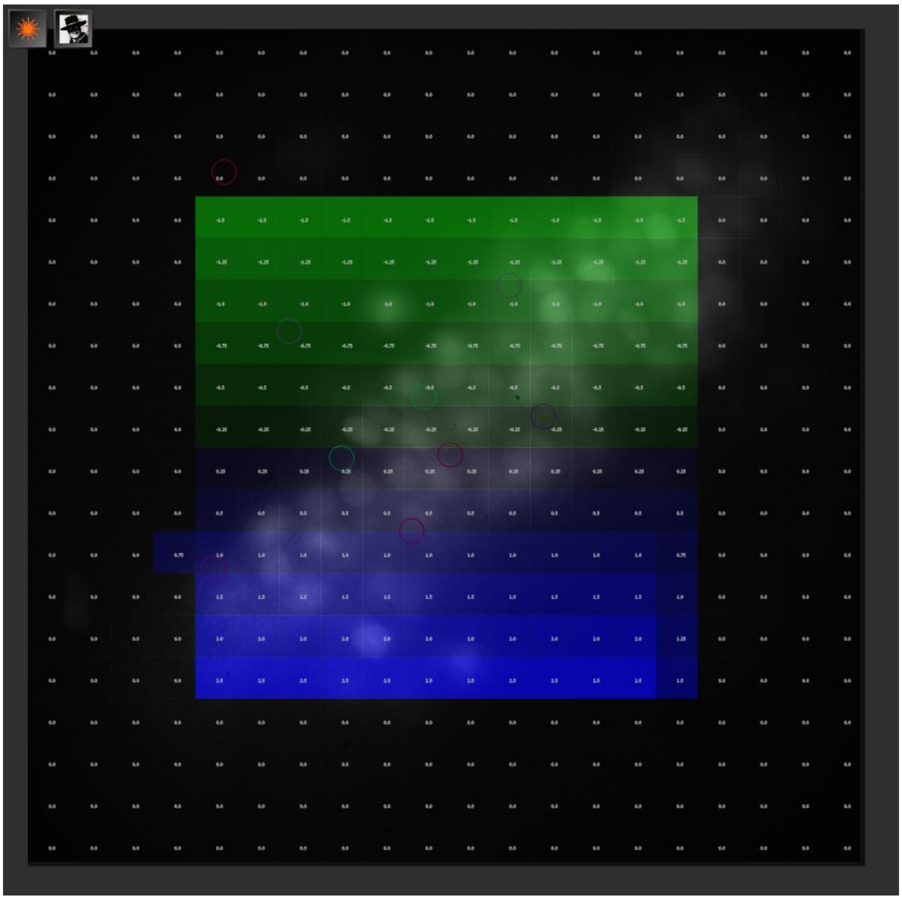

Figure 56: z displacement Weights map

It is important to note that all the corrections can be saved and reloaded later. When reloading, the correction is directly assigned to the correct line.

Section 3: Management of lines created on the SLM

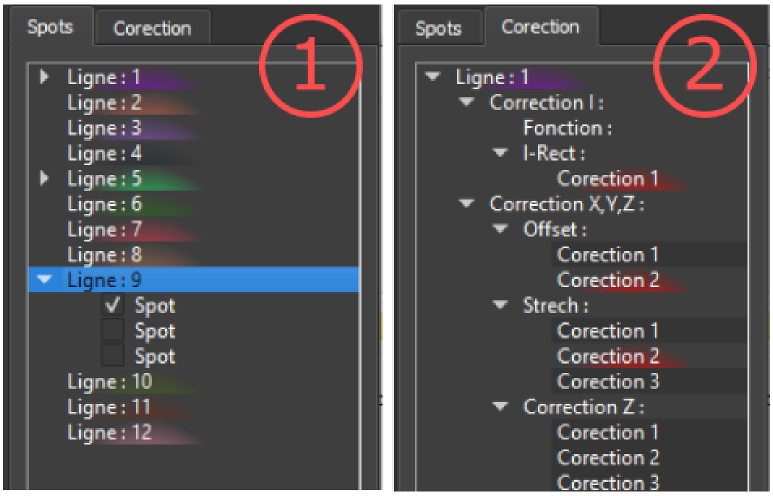

Figure 57: Management of lines created on the SLM (section 3) divided in two parts

Part 1 Spots: Each of the lines used on the SLM is represented in this tree view with an independent color, color used to display the associated spots in the: Navigation and display (section 1). All the spots assigned to the line are listed in its drop-down menu. These spots can be selected to modify their intensity or to be deleted.

Part 2 Correction: In this representation like the precedent, the scrolling menu gives access to all the different types of corrections possibly assigned to the line. For a given correction like the "Strech" in (Figure 57) it is possible to store all the different variants used during the experiment. The current version used is highlighted in red.

Section 4: Phase generation and access to the protocol programming page

Figure 58: Phase generation and access to the protocol programming page (Section 4) divided in two

Part1: "Phase generation" launches the phase calculation; "Phase display" sends this phase on the SLM screen. The distinction between these two operations will allow the management of the memory present in some SLMs. The phases of interest and the display phase are not necessarily identical. Each generation of a phase profile is saved using two files, one containing the phase image and the other keeping in memory the position of the spots for each of the lines. A progress bar can also be found underneath.

Part 2: Gives access to two control modes of the SLM galvo coupled system. The first one is a step-by-step controller and the next one control the activation of several cells to obtain the requested trace. We will see each of these modes in more detail in the following section. The control of the galvos and the AOM are done using a national instrument card.

6.3.2 Protocol Generator

Protocol 1

The control step button gives access to a new control window also divided in three parts shown below.

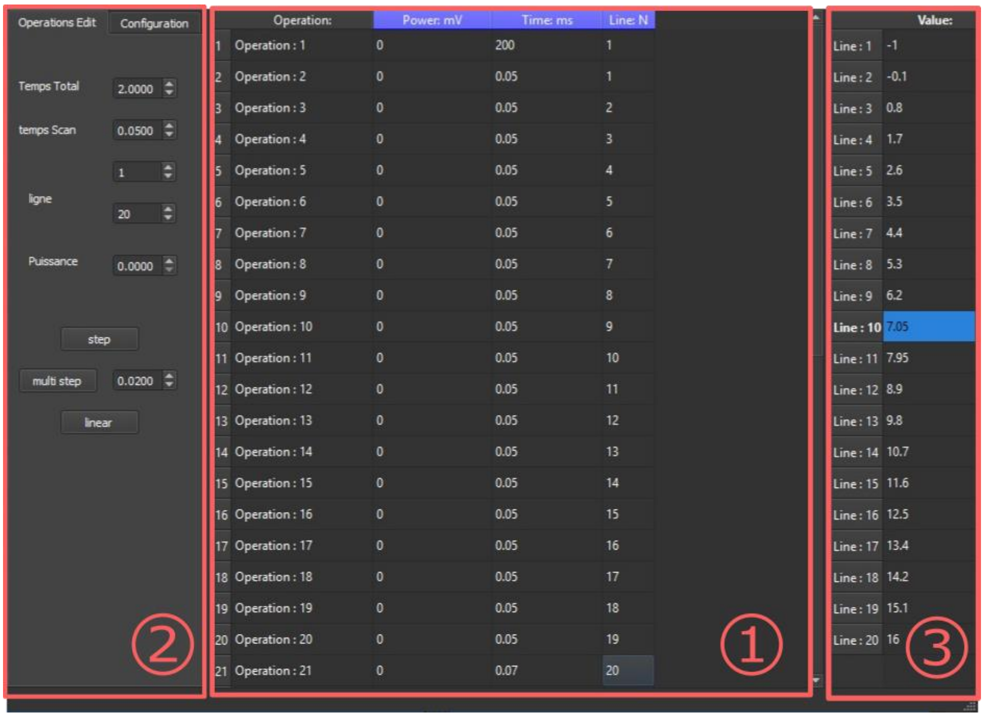

Temps Total 2.0000
temps Scan 0.0500
ligne 1
20
Puissance 0.0000
multi step 0.0200

	Operation:	Power: mV	Time: ms	Line: N
1	Operation : 1	0	200	1
2	Operation : 2	0	0.05	1
3	Operation : 3	0	0.05	2
4	Operation : 4	0	0.05	3
5	Operation : 5	0	0.05	4
6	Operation : 6	0	0.05	5
7	Operation : 7	0	0.05	6
8	Operation : 8	0	0.05	7
9	Operation : 9	0	0.05	8
10	Operation : 10	0	0.05	9
11	Operation : 11	0	0.05	10
12	Operation : 12	0	0.05	11
13	Operation : 13	0	0.05	12
14	Operation : 14	0	0.05	13
15	Operation : 15	0	0.05	14
16	Operation : 16	0	0.05	15
17	Operation : 17	0	0.05	16
18	Operation : 18	0	0.05	17
19	Operation : 19	0	0.05	18
20	Operation : 20	0	0.05	19
21	Operation : 21	0	0.07	20

	Value:
Line : 1	-1
Line : 2	-0.1
Line : 3	0.8
Line : 4	1.7
Line : 5	2.6
Line : 6	3.5
Line : 7	4.4
Line : 8	5.3
Line : 9	6.2
Line : 10	7.05
Line : 11	7.95
Line : 12	8.9
Line : 13	9.8
Line : 14	10.7
Line : 15	11.6
Line : 16	12.5
Line : 17	13.4
Line : 18	14.2
Line : 19	15.1
Line : 20	16

Figure 59: Protocol 1 fast scan control window divided in 3 sections.

Section 1: is an expandable table representing the sequence of operations created by the user. For each operation three elements must be indicated: the voltage to be sent to the AOM to control the laser power. The time duration of the operation in ms and finally the line to illuminate during this period.

Section 2:

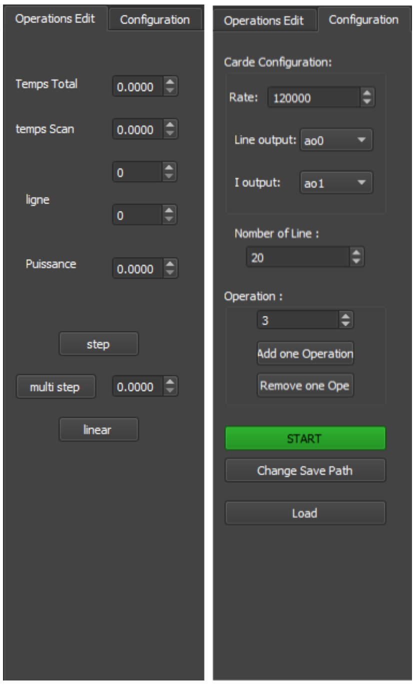

Temps Total 0.0000
temps Scan 0.0000
ligne 0
0
Puissance 0.0000
multi step 0.0000

Carde Configuration:
Rate: 120000
Line output: ao0
I output: ao1
Nomber of Line : 20
Operation : 3

Figure 60: : Protocol 1 section 2.

1) Operations Edit: This onglet automatically creates multiple operations. This part is notably used to generate the different fast scan protocols. It allows to quickly scan the whole SLM while choosing the illumination time per line. To do this, 4 parameters must be filled in:

- **Parameters:** "temps total" represents the total duration of the protocol. "temps Scan" represents the average illumination time of a line during the protocol. "Line" represent the the first and the last line to be scanned by the galvo. Finally, "puissance" the voltage for the AOM. 3 modes are then proposed:

- **Step** in this case, the galvo scans the SLM going from one extreme line to the other as fast as possible. The value given to the scan time represents the time allowed to go from one extreme line to the other. Under these conditions, a too-short time will not allow the galvos to reach the end line, it will change direction before. For a too long protocol, the excess of time will result in a longer illumination of the extreme lines. During the protocol the voltage sent to the galvos will abruptly change from one extreme line to the other, resulting in inhomogeneity of the illumination for the scanning lines due to the acceleration and deceleration of the galvos. A study of this phenomenon can be found in the supplementary of (Chapter 6).

- **Multi step** is the protocol that we ultimately used to demonstrate fast scan. It allows a better control of the illumination time for each line. Here the generated protocol is stepped. The galvo switches from one line to another, staying a short period of time on each line according to the "temps Scan" value. In front of the multi-step button, it is possible to set a correcting value, corresponding to a time supplement add to the extreme line. If the time per line is too short, a galvos delay can be observed. Without this correction, the galvos can still turn back before reaching the desired extreme line.

- **Linear** appears similar in table part 1 to the protocol generated by the Multi-step method. The difference is made during the generation of the signal that goes from a staircase to a straight line.

2) Configuration: In this panel, it is possible to modify the sampling rate of our signal thanks to "Rate". We can also change the National instrument output signals to control the galvos with "Line Output" and the AOM with" I output". It is important to indicate the number of lines used on the SLM (this parameter should be updated automatically in future versions). In the Operation section, it is possible to add or remove the operation in the protocol 1 control window divided section 1(Figure 59).

The start button launches the protocol and automatically saves it in the indicated file all the current set information. It is possible to change this file with the button below. Any saved protocol can be loaded later.

Part 3: Tables linking the galvo voltage to the corresponding line.

Protocol 2

The window obtained with the "Mimiking" button is also divided into three zones:

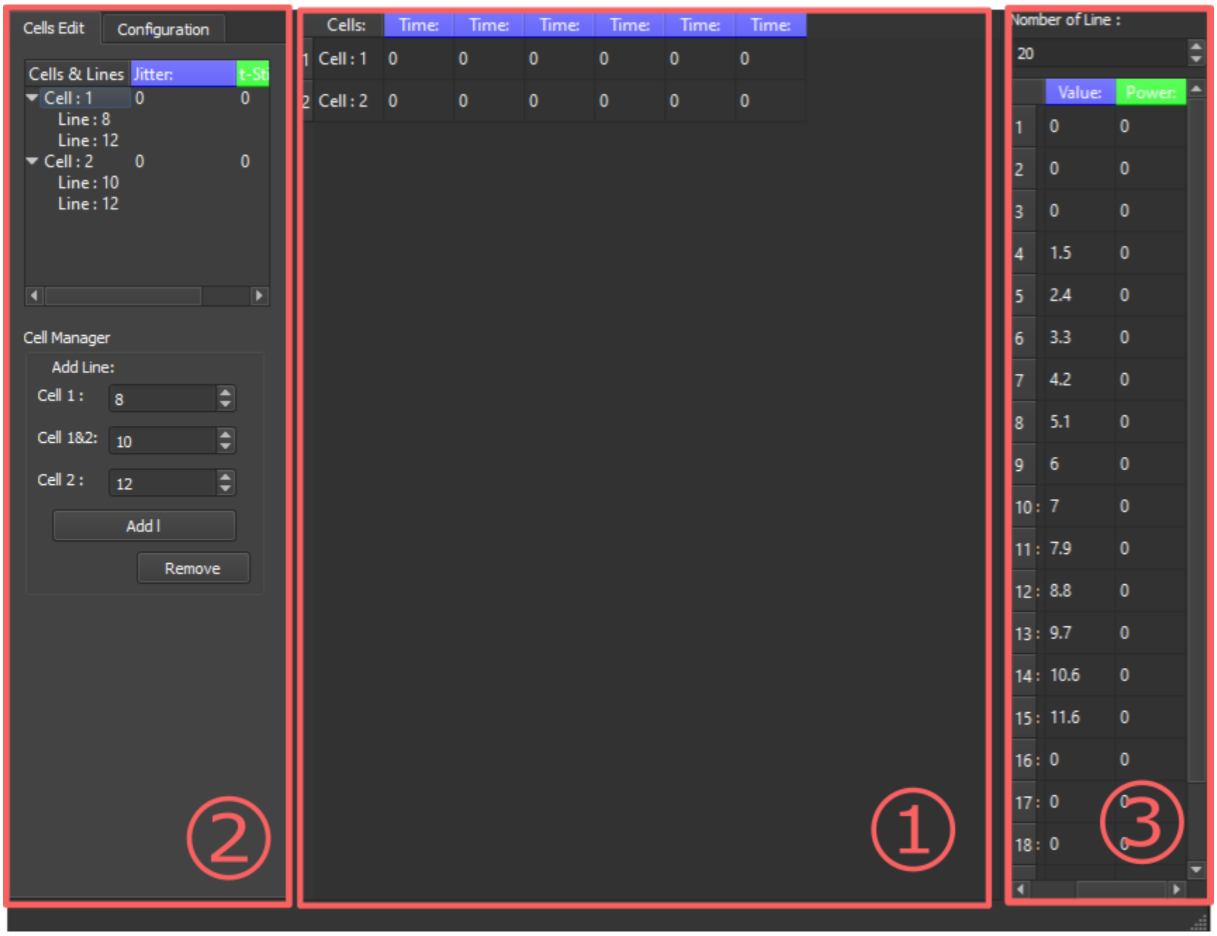

Cells & Lines	Jitter:	t-St
Cell : 1	0	0
Line : 8		
Line : 12		
Cell : 2	0	0
Line : 10		
Line : 12		

Add Line:
Cell 1 : 8
Cell 1&2: 10
Cell 2 : 12

	Cells:	Time:	Time:	Time:	Time:	Time:	Time:
1	Cell : 1	0	0	0	0	0	0
2	Cell : 2	0	0	0	0	0	0

Nomber of Line : 20

	Value:	Power:
1	0	0
2	0	0
3	0	0
4	1.5	0
5	2.4	0
6	3.3	0
7	4.2	0
8	5.1	0
9	6	0
10 :	7	0
11 :	7.9	0
12 :	8.8	0
13 :	9.7	0
14 :	10.6	0
15 :	11.6	0
16 :	0	0
17 :	0	0
18 :	0	0

Figure 61: Protocol 2 mimicking control window divided in 3 zones.

Part 1: allows to visualize the number of cells studied, (two in Figure 61). For each of the cells it is possible to indicate when to elicit an action potential by entering a time in ms in one of the "Time" columns. The number of "Time" columns and therefore of activation is not limited. Each of the cells is independent and it is not necessary to have the same number of spikes for each of them.

Part 2:

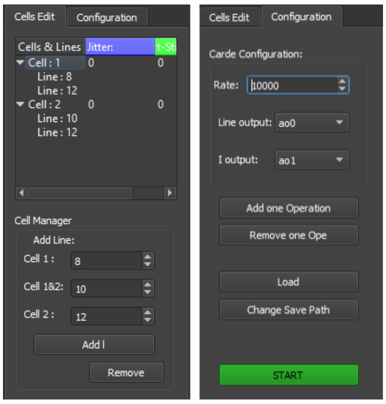

Cells & Lines	Jitter:	t-St
Cell : 1	0	0
Line : 8		
Line : 12		
Cell : 2	0	0
Line : 10		
Line : 12		

Add Line:
Cell 1 : 8
Cell 1&2: 10
Cell 2 : 12

Carde Configuration:
Rate: 10000
Line output: ao0
I output: ao1

Figure 62: Protocol 2 zone 2

Cells Edit: Starts with a table of all the cells studied. For each cell, the first two columns must be filled with the values Jitter and t-Stimulation. t-Stimulation represents the illumination time in ms used to induce cell activation. Jitter represents the delta time in ms between the end of the stimulation and the spike of the cell. Each cell has a drop-down menu. This menu lists the SLM lines at which the cell is assigned.

Configuration: as for the step control configuration section, this part controls the sampling rate and the outputs used on the national instrument card. It is also possible to add operations and launch the protocol.

Part 3: similar to the step control section with another column "power" to indicate the power to be used with the line. This element is necessary as each line may have a different number of cells to illuminate.

From all these parameters, the algorithm generates for each cell a time trace indicating the stimulation time. If several cells have overlapping stimulation periods, the algorithm looks for a line on the SLM where each of them is present. If such a line does not exist, the user is asked to add the cells on a common line. Once each stimulation has been assigned to a line on the SLM the protocol is launched.

6.4 FliT manuscript

The following manuscript demonstrates the development of the new method FLiT to write the neuronal activity with short time delays. We also demonstrate a new stimulation protocol to optimize the illumination of the target during the photo stimulation allowing a significant increase of the number of cells activable with the same laser power, compared to the methods presented in (Chapter 4). For this project, Emiliano Ronzitti assisted in the development of the optical system and analyzing the data. Giulia Faini took care of all the biological experiments and analyzed them with Emiliano Ronzitti. For my part, I realized the development of the optical system and its characterization. I also took part in the biological experiment led by Giulia Faini.

Ultrafast Light Targeting for High-Throughput Precise Control of Neuronal Networks

Giulia Faini*, Clément Molinier*, Cécile Telliez, Christophe Tourain, Benoît C. Forget, Emiliano Ronzitti ‡, and Valentina Emiliani ‡

1 Institut de la Vision, Sorbonne Université, Inserm S968, CNRS UMR7210, 17 Rue Moreau, 75012 Paris

* Equally contributing authors

‡ correspondence:

emiliano.ronzitti@inserm.fr

valentina.emiliani@inserm.fr

Understanding how specific sets of neurons fire and wire together during cognitive-relevant activity is one of the most pressing questions in neuroscience. Two-photon, single-cell resolution optogenetics based on holographic light-targeting approaches enables accurate spatio-temporal control of individual or multiple neurons. Yet, currently, the ability to drive asynchronous activity in distinct cells is critically limited to a few milliseconds and the achievable number of targets to several dozens. In order to expand the capability of single-cell optogenetics, we introduce an approach capable of ultra-fast sequential light targeting (FLiT), based on switching temporally focused beams between holograms at kHz rates. We demonstrate serial-parallel photostimulation strategies capable of multi-cell sub-millisecond temporal control and many-fold expansion of the number of activated cells. This approach will be important for experiments that require rapid and precise cell stimulation with defined spatio-temporal activity patterns and optical control of large neuronal ensembles.

INTRODUCTION

Optogenetic neuronal excitation using single-photon widefield illumination has already proven its enormous potential in neuroscience, enabling the optical manipulation of entire neuronal networks and to disentangle their role in the control of specific behaviors[1,2]. However, establishing how the activity of a single neuron or neuronal ensemble impacts a specific behavior, or how functionally identical neurons are connected and involved in a particular task, requires the precise control of single or multiple cells independently in space and time. This has imposed a transition from widefield optogenetics into a more sophisticated technology that we termed few years ago: circuit optogenetics[3]. Circuit optogenetics combines progress in opsin engineering, holographic light shaping and high-power fiber laser development. Using two-photon holographic illumination of fast-photocycle-, soma-targeted-opsins, it permits single or multi-spike generation with cellular resolution, sub-millisecond precision and high spiking rates deep in tissue[3]. Using multiplexed spiral scanning[4] or multiplexed temporally focused light shaping approaches[5–7], combined with high energy fiber lasers and soma-targeted opsins[8,9], it also enables simultaneous control of multiple targets in 3D $\sim mm^3$ volumes at cellular resolution[10–12].

The unprecedented spatiotemporal precision of circuit optogenetics has enabled high throughput connectivity mapping in living zebrafish larvae[13] and probing rod bipolar cell output across multiple layers of the mouse retina[14]. Combined with two photon Ca^{2+} imaging and behavioural assays, circuit optogenetics has been used to show that the activation of few cells can bias behavior by triggering the activity of precisely-defined ensembles in the mouse visual cortex[11,12,15]. Importantly, sequential projection of multiple holographic patterns at variable time intervals in the mouse olfactory bulb has revealed how the perceptual responses of mice not only depend on the specific group of cells and cell numbers activated but also on their relative activation latency[16].

These pioneering works suggest a number of new exciting experimental paradigms for circuit optogenetics, e.g., the investigation of the temporal bounds of functional connectivity within which neurons “fire and wire together”, or how many targets need to be activated to perturb complex behavioral responses or how large neuronal ensembles, eventually spanning across multiple cortical layers, are functionally connected. Answering these questions requires the capability to manipulate neuronal activity at fine (sub-millisecond)temporal scales and/or large cell populations, which ultimately requires overcoming the current intrinsic technological limitations of holographic light patterning, specifically the low speed of liquid crystal spatial light modulators (LC-SLMs) and the high illumination power necessary for multi-target excitation.

Multi-target optogenetics uses holographic light shaping to multiplex the excitation beam to multiple locations, combined with either spiral scanning or temporally focused light shaping approaches[17,18].

In spiral scanning approaches, a LC-SLM is used to multiplex the illumination beam into several diffraction limited spots which are scanned in spiral trajectories using a pair of galvanometric mirrors (GM), each spanning a different neuron.

Several multiplexed temporally focused light shaping (MTF-LS) approaches have been developed[5], which differ in terms of the approach used for light patterning. Generally, MTF-LS systems are comprised of three units: (1) a beam shaping unit sculpts light into particular forms, (2) a diffraction grating placed in a conjugate image plane confines photostimulation to a shallow axial region with cellular dimensions and (3) a LC-SLM multiplexes the sculpted light to multiple sample locations (Fig.1A).

This configuration admits multiple variants depending on the beam shaping unit used, which also defines the extent of the beam profile at the multiplexing LC-SLM[5]. Beam shaping units based on computer generated holography illuminate the second LC-SLM with either a single chirped hologram of the size of the LC-SLM matrix[6] or with multiple chirped holograms[19], while the use of an expanded gaussian beam[20] or of the generalized phase contrast method[6], produces a chirped horizontal line (typically ~ 2 mm high and ~ 16 mm wide) covering the horizontal dimension of the LC-SLM or a diffused chirped spot which illuminates the entire LC-SLM matrix[7] (Supplementary Fig.1).

In all described approaches, sequential generation of independent illumination patterns is achieved by projecting multiple holograms at a rate limited by the LC-SLM refresh rate (60-500 Hz) and cell illumination times (from ~1 ms to dozens of ms).

Moreover, multi-target illumination based on holography requires powerful lasers since the laser energy is divided between different targets[3,17,21]. While in principle this enables the simultaneous photostimulation of hundreds of target cells, the necessity of maintaining brain temperature within physiological thresholds[10,22,23] has thus far limited the maximum number to a few dozens.

Here, we suggest a new approach for ultra-fast sequential light targeting (FLiT) based on rapid displacement of temporally-focused sculpted light through multiple, vertically-aligned, holograms. We demonstrated that optogenetic FLiT enables tuning of distinct cells with microsecond resolution and a 20 (or more) times increase of achievable targets with minimal thermal crosstalk.

This novel capability of arbitrarily desynchronizing (or synchronizing) groups of neurons will facilitate the study of the influence of spike timing on synaptic integration, plasticity and information coding, and scaling up the number of cells activable whilst remaining safely below the threshold for thermal damage.

RESULTS

Ultra Fast Light-Targeting (FliT)

Here we introduce a new configuration of MTF-LS for ultra-fast sequential light targeting (FLiT), where the multiplexing LC-SLM is addressed with multiple vertically tiled holograms. A galvanometric mirror (GM) is incorporated upstream (Fig.1B) to sweep the chirped expanded gaussian beam across the holograms and generate sequential 2D (Fig.1C; Supplementary Movie 1) or 3D (Fig.1D) illumination patterns.

To characterize the optical properties of FliT, we first characterized the effect of the hologram tiling on the holographic spot intensity, ellipticity (i.e., ratio between vertical (y) and horizontal (x) length) and axial resolution by projecting on a thin rhodamine layer a single spot encoded by tiled holograms with different vertical extents (see Methods). We did not observe a significant deterioration of the axial resolution decreasing the tile extent to 12 lines (corresponding to 50 tiled holograms for the particular LC-SLM used), while we observed a decrease of a factor ≥ 2 in spot intensity and ellipticity by decreasing the tile extent to ≤ 20 lines (corresponding to 30 tiled holograms) (Supplementary Fig.2).

We then evaluated, for the case of 30 lines per tiled hologram (20 tiled phase holograms, φ_i), the influence of the location of the hologram on the LC-SLM on spot intensity and axial resolution by deflecting the chirped beam across 20 2D holograms (each encoding the same group of spots) using the GM. For each hologram, the intensity was homogeneously distributed among spots generated in a field of excitation (FoE) of 120 x 120 μm^2 (Fig.1C; Supplementary Fig.3). For patterns encoded in holograms located in central regions of the LC-SLM, we observed a $\geq 25\%$ higher average intensity than in patterns generated by distal holograms ($\varphi_i \leq 4$; $\varphi_i \geq 14$; Supplementary Fig.3). Although we observed a moderate axial tilt of the spots generated by using distal holograms, the axial resolution of the spots was preserved both within the FoE and while scanning across the different holograms (6.5 ± 0.5 μm; Supplementary Fig.4). Importantly, spot intensity homogeneity and axial confinement were maintained when spots were randomly distributed in 120 x 120 x 70 μm^3 volume (Supplementary Fig.5).

Next, we studied how the velocity of the scan unit defines the temporal resolution of FLiT. Specifically, we tested the minimum switching time to *(i)* move between two adjacent holograms (Fig.2A-B) and *(ii)* sequentially illuminate all holograms at constant rate (Fig.2E-F). For this, we generated 20 equivalent holograms each projecting a single spot on a photodiode placed in a conjugate image plane (Fig2A and Fig.2E) (see details in Methods). In the first case, we measured a switching time of 90 ± 10 µs (Fig.2C-D, n = 30 measurements), while in the second case, we could reach a switching time of 50 ± 10 µs (Fig.2G-H, n = 30 measurements).

Taken together these results indicate that FLiT enables sequential generation of multiple patterns with no significant deterioration of spot quality or axial resolution for up to 12 phase holograms. By scanning the chirped beam among the multiple holograms, it is possible to reach up to few tens of kHz switching rate, which is more than one order of magnitude faster than what is achievable with alternative parallel approaches using phase modulation[11].

Precisely replaying physiological patterns of activity

In order to demonstrate the capabilities of FLiT to control neuronal activity at high switching rate, we photoactivated neurons expressing the soma-restricted opsin ST-ChroME[10] while recording cellular activity via whole-cell patch clamp recordings in acute cortical brain slices (see Methods and Supplementary Fig.6A).

We initially tested the illumination conditions (excitation power, illumination time and spot size) for reliable action potential (AP) generation. Consistent with results previously obtained in standard 2P holographic configurations[9,21,24], APs could be reliably elicited with sub-ms jitter (0.25 ± 0.13 ms; n= 13 cells; Supplementary Fig.7) upon selective targeting of cell somata (spot size = 10 µm) with illumination times as short as 4-5 ms. These values and the LC-SLM refresh rate (60-500 Hz)[10,11] set the effective temporal resolution for sequential photostimulation in common holographic light patterning techniques.

Here, we demonstrate that FLiT overcomes this limit by enabling sub-millisecond temporal resolution independently of the illumination time and LC-SLM switching rate (Fig.3A). Briefly, if two groups of cells (group A and B) need to be activated with a temporal delay shorter than the necessary illumination time (dwell-time), one can use 3 phase holograms: the first one (φ_a) generating a light pattern to excite the group A, the second one (φ_b) to excite the group B and the intermediate one (φ_{ab}) to excite both groups, A and B. By steering the beam across the three holograms, each with a specific illumination time and intensity, it is possible to sequentially stimulate the two groups of cells with tightly controlled delays, only limited by the GM scanning time (i.e., in our case $\geq$ 90 µs). Notably, the same principle can be extended to *n* groups of cells by using *2n-1* tiled holograms and sequentially addressing the different groups in parallel or individually (Supplementary Fig.8). We call this configuration serial/parallel FLiT (S/P-FLiT).

We demonstrated the capability of S/P-FLiT for ultra-fast sequential light targeting by photostimulating two ST-ChroME-expressing neurons while monitoring the evoked activity by double-patch electrophysiological recordings (Fig.3B). First, we verified that amplitudes and kinetics of induced photocurrents were not affected by switching the illumination between the different holograms (Supplementary Fig.9). We then assessed the precision in controlling the relative spiking time among the two cells by photoactivating the two patched neurons with tightly controlled delays, δt, ranging from 0.2 to 3 ms, while measuring the corresponding spiking delay time $\delta t_{\mathrm{AP}}^{\mathrm{exp}}$ (Fig.3B). We found that spike delays $\delta t_{\mathrm{AP}}^{\mathrm{exp}}$ can be controlled with few hundreds µs temporal accuracy, $\left|\delta t_{\mathrm{AP}}^{\mathrm{exp}} - \delta t\right|$, (96 ± 114 µs, n = 12 pairs of cells; Fig.3C and Supplementary Fig.10). Furthermore, the photocurrent magnitude was found to be approximately independent of the vertical position of the tiled hologram (Supplementary Fig.11).

Finally, we demonstrated the capability of S/P-FLiT to precisely mimic random spiking activity in two distinct neurons. To this end, we photostimulated two neurons with distinct spiking patterns based on physiological activity (Fig.3D). Light-driven mimicking was precisely controlled with few hundreds of µs temporal accuracy, $\left|\delta t_{\mathrm{APi}}^{\exp} - \delta t_i\right|$, where *i* indicates the AP ordinal number in the train (11 ± 122 µs; n = 12 pairs of cells; Fig.3E and Supplementary Fig.12).

Taken together, these results indicate that S/P-FLiT enables precise sub-millisecond tuning of neuronal activity in distinct neurons or groups of neurons.

High-throughput activation of multiple cells by tuning Illumination to match properties of opsin photocycle

Here we demonstrated the capability of FliT to scale up the achievable number of targets for parallel multi-cell illumination.

In conventional parallel illumination approaches, the simultaneous excitation of *n* targets requires an excitation power of $n \cdot P_{std}$, where P_{std} is the excitation power which needs to be continuously applied for a time t_{std} to activate a single target (Fig.4A). Here we demonstrate that FliT approach enables targeting the same number of cells by using cyclic illumination with µs flashes of light and a factor of $\sqrt{n}$ lower power whilst maintaining identical latency and jitter. Alternatively, a factor of $\sqrt{n}$ more cells can be targeted using the same amount of power. We called this configuration serial-parallel multi-cell activation FliT (Multi-S/P FliT).

Briefly, steady illumination of a neuron for a time t_{std} shorter than the opsin rise time generates an exponential increase in photocurrent (Fig.4A) and eventually AP generation. Capitalizing on the properties of the opsin photocycle, a similar photocurrent can be generated by using cyclic illumination consisting of N_{cyc} short illumination pulses each of duration $t_{cyc} \ll t_{std}$, provided *(i)* the time interval, T_{cyc} , between two pulses is shorter than the off-time decay of the opsin (Supplementary Note 1) and *(ii)* the excitation power, P_{cyc}, generates in a time t_{cyc} a photocurrent that after a time t = $\frac{t_{std}}{N_{cyc}}$, equals the one that a steady illumination with power P_{std} would generate in the same time. It can be shown that this condition is realized for $P_{cyc} = P_{std}\sqrt{T_{cyc}/t_{cyc}}$ (Supplementary Note 1). If these conditions are satisfied, FLiT can rapidly reposition the excitation light onto $n = \frac{T_{cyc}}{t_{cyc}}$ different locations in a time $t = T_{cyc}$, thus enabling quasi-simultaneous activation of n targets with a power only $\sqrt{n}$ higher than P_{std} (Fig.4B).

In order to demonstrate this configuration, we divided the LC-SLM in *n* tiled holograms, encoding a soma-targeted illumination of a patched ST-ChroME-expressing neuron on a tiled hologram φ_i. We then recorded, using whole-cell patch clamp recordings in organotypic slices (Supplementary Fig.6B), the photoevoked neuronal activity by *(i)* continuous illumination on φ_i and *(ii)* steering the laser across the *n* holograms such that each hologram is illuminated for a duration, t_{cyc}, of 50 µs (Fig.4C; see Methods for details). We define two temporal parameters to characterize the two excitation conditions described above: the cell illumination time, t_{cell}, as the total time during which the cell is illuminated, and the experimental time, t_{exp}, as the global time needed to evoke an action potential. Under steady illumination, $t_{cell}^{std} = t_{exp}^{std} = t_{std}$, while under cyclic illumination, $t_{cell}^{cyc} = N_{cyc} \cdot t_{cyc}$ and $t_{exp}^{cyc} = n \cdot N_{cyc} \cdot t_{cyc}$, with $N_{cyc}$the number of illumination cycles (Fig.4C).

At first, we optimized the excitation power, P_{std}, to generate reliable APs under steady illumination for a given t_{std} = 5 ms. We found that for P_{std} = 20.4 ± 9.4 mW, we could generate APs with 7.7 ± 1.1 ms latency and 0.36 ± 0.30 ms jitter (n = 8 cells, data not shown). Secondly, we compared those values with the power, P_{cyc}, and the number of cycles, N_{cyc}, necessary to evoke an AP in the same cell under

Multi-S/P FliT illumination (Fig.4D) by keeping either *(i)* the same excitation power (Fig.4E) or *(ii)* the same experimental time used for steady illumination (Fig.4F), i.e. either $P_{cyc} = P_{std}$ *or* $t_{exp}^{cyc} = t_{std}$, respectively.

We found that in the first condition, Multi-S/P FliT illumination can reliably generate APs in the patched cell by using up to 20 holograms (therefore in principle 20 more excitable cells) and $N_{cyc} = \frac{t_{std}}{t_{cyc}} = 100$, which corresponds to a total experimental illumination time $t_{exp}^{cyc} = 100$ ms. Increasing the number of excitable cells up to 30 and 50 is also possible but requires increasing the excitation power P_{cyc} by a factor of ∼ 1.37 ± 0.34 and 2.48 ± 0.85, respectively (Fig.4E).

As a drawback for using t_{exp}^{cyc} *n* times longer than t_{std}, we measured large increases of AP latency and jitter (Supplementary Fig.13A). However, using $P_{cyc} \cong \sqrt{n} \cdot P_{std}$ enabled keeping $t_{exp}^{cyc} = t_{std} = 5$ ms and achieving the same spiking properties as under steady illumination (Fig.4F and Supplementary Fig.13B) in agreement with the theoretical prediction (see Supplementary Note 1).

Overall, the achieved results indicate that Multi-S/P-FLiT potentially enables increasing by $n = 20$ the number of achievable cells with no increase in illumination power with respect to that used for single cell stimulation. Maintaining ms latency and sub-ms jittering is possible by using an excitation power only $\sqrt{n}$ times higher than the one used for single cell excitation, which would have otherwise required *n* times higher power for conventional parallel illumination approaches.

Importantly, Multi-S/P FliT can be adapted to other cyclic illumination configurations. For instance, photostimulation protocols using low frequency, $1/T_P$, (10-30 Hz) photostimulation train composed of short (5-10 ms) illumination pulses, t_p[15,25,26], can be equally performed using FLiT and sequential illumination of T_P/t_P tiled holograms, each for a time t_P (in the approximation of a switching time $t \ll t_P$). This will enable to increase by T_P/t_P the number of excited cells without incrementing the illumination power or the illumination period T_P (Supplementary Fig.14).

Rise of temperature under light-driven neuronal control with FLiT

Here we demonstrated another important property of FliT illumination: the capability to minimize the light induced temperature rise for multi-target illumination.

To this end, we simulated the temperature rise under different illumination conditions using a previously validated heat diffusion model[22,23]. Firstly, we used the model to predict the temperature changes produced by 100 spots randomly distributed in a volume of 200 x 200 x 500 µm^3 (Fig.5A) under typical illumination conditions for *in vivo* 2P optogenetics, i.e., $P_{std} = 20$ mW per cell and $t_{std} = 5$ ms. To minimize thermal crosstalk, we generated the 100 spots at an average position that enabled to maximize their relative distance. This, for a 200 x 200 x 500 µm^3 FoE, corresponded to 50.7 ± 6.8 µm (Supplementary Fig.15A). The predicted temperature rise on the hottest spot was ∼ 3 times higher than the case of an isolated target (Fig.5C, Fig.5E and Supplementary Movie 2).

Next, we compared these findings with the case where the same 100 targets were illuminated through the sequential generation of *n* subsets of spots by keeping the same excitation conditions (i.e., $P_{std} = 20$ mW per target and $t_{std} = 5$ ms per subset). We considered two cases with sequential illumination of $n = 4$ and $n = 10$ holograms, each encoding for 25 or 10 spots, respectively (Fig.5B). Reducing the number of spots per hologram enables to further increase their average distance to 78.7 ± 14.6 µm and 106.0 ± 23.7 µm (Supplementary Fig.15B-C), and thus reducing of nearly 8% and 30% the corresponding maximum temperature rise in the hottest spot (Fig.5C, Fig.5F-G, Supplementary Fig.16 and Supplementary Movie 2). Delaying the sequential illumination by few milliseconds did not present significant variations in temperature rise compared to the previous conditions (Supplementary Fig.17). Whilst here, we have shown how to generate 100 spots in a 200 x 200 x 500 µm^3, the concept can be extended to arbitrarily larger FoE, and correspondingly larger numbers of spots, provided that the average distance is maintained.

Notably, here we have chosen a relative short illumination time. Longer illumination times (10-30 ms) will considerably lengthen the thermal diffusion length and the maximum temperature rise so that the gain in using FliT will be even more evident.

Similar reduction on the temperature rise, with no elongation of the total experimental time ($t_{exp} = t_{std} = 5ms$), can be reached if the same holograms are illuminated with cyclic illumination by using Multi-S/P FliT. In this case, we increased the excitation power per spot to $\sqrt{n} \cdot 20mW$ and used $t_{cyc} = 50\ \mu s$. Notably, cyclic illumination reduces the average temperature rises of nearly 40% and 50% for n=4 and n=10, respectively (Fig.5D, Fig.5H-I, Supplementary Movie 3 and Supplementary Fig.16) and also minimizes the temperature rise for single spot excitation.

These results show that using hybrid serial parallel photostimulation strategies (S/P FliT or Multi S/P FliT) for multi target illumination enable minimize temperature crosstalk among the multi-targets reaching a local temperature rise comparable to the case of an isolated target.

DISCUSSION

Optical control of multiple neurons requires holographic light multiplexing through the use of LC-SLMs either coupled with spiral scanning or with parallel illumination[3,17]. In these configurations, the temporal resolution for sequential light patterning is limited by the LC refresh rate (60-500 Hz) to 2-20 ms. Moreover, although optical generation of a single neuronal spike using powers close to opsin saturation can be reached with illumination times ≤ 1 ms[11,24,27,28], reaching optimal axial resolution requires working far from saturation[25] which typically lengthens the illumination time to 5-30 ms[3], for single spike generation, or a few seconds for the generation of multiple spikes[11] or for neuronal inhibition[10,29]. These time values impose an extra temporal delay for sequential patterned illumination.

Holographic stimulation of multiple targets divides the laser output of high powerful lasers[21] among multiple targets which are simultaneously illuminated. This requires taking into account possible thermal photodamages[22] when designing the multi-site distribution. All in all, these limitations have so far restricted the maximum achievable number of targets for multi-targets 2P-optogentics to a few dozen[10,11,28].

Here, we have presented FliT, a new scheme for multi-target excitation which overcomes all these limitations by enabling kHz projection of multiple patterns and 20 (or more) times higher number of achievable targets with respect to previously proposed holographic approaches. We have demonstrated FliT illumination in two configurations S/P-FliT and Multi-S/P-FliT where the galvanometric mirror is moved across multiple vertically aligned holograms in custom made discrete time intervals or at continuous speed, respectively.

We have shown that S/P-FliT enables to control the relative spiking time among multiple cells (or groups of cells) with a temporal delay as short as 90 µs, independently of the cell illumination dwell-time, opening the way to the investigation of synaptic integration, connectivity and neuronal coding with an unprecedented temporal precision. The ability to fast switch between multiple photostimulation patterns with sub-millisecond resolution will enable precise investigation of spatial- and time-dependent synaptic summation and integration of multiple and complex synaptic inputs[30]. Being able to stimulate multiple specific subsets of neurons, with single cell precision, either simultaneously or with sub-ms custom temporal delays will be essential to precisely probe mechanisms such as spike-time dependent plasticity (STDP), where the temporal interval between pre-and-postsynaptic spikes are necessary to strengthen or depress synaptic connections[31–34]. For instance, S/P-FliT could be used to induce STDP in adjacent spines with sub-millisecond time intervals and investigate finely the role of such processes[35]. Notably, STDP plays an important role in building specific spatiotemporal patterns involved in temporal processing, and it has been shown to be the basis for learning and memory and is known to be involved in brain pathologies[36,37].

Previous studies on mammalian neocortex have shown that optogenetic manipulation of small ($\leq$ 30 cells) groups of neurons appears sufficient to impact behavioural responses[11,12] and most importantly that this can depend on the relative degree of synchronicity among the optically evoked spikes[16,38]. S/P-FliT has the potential to refine this type of studies by mimicking with unprecedent fine temporal precision a variety of physiological firing patterns and to manipulate them with different flavors, synchronizing or de-synchronizing them at will, while observing the effect of this time-controlled manipulation at different levels, from the local response of a neuronal circuit to behavioral responses and sensory perception, in both healthy and pathological brains.

Additionally, other brain regions with sparser connectivity and activation schemes might require the control of larger neuronal ensembles. For these studies, Multi-S/P-FliT, which enables to increase many folds the number of achievable targets, could be a crucial advance.

We have shown that Multi-S/P-FliT enables increasing *n* times the achievable number of targets, using $\sim\sqrt{n}$ times less power than with conventional parallel illumination. This has two main implications: the possibility of using low power lasers and, for high energy laser, to reduce thermal photodamages as detailed below.

In vivo two photon optogenetics stimulation using mode locked Ti:Sapphire lasers (80 MHz) requires 30-50 mW/cell[29]. Considering that at the wavelengths typically used for photostimulation (i.e., 900-950 nm) these sources can provide an output of a few W (~200 mW after the objective), multi-target stimulation using those lasers remains limited to a few cells. Multi-S/P Flit thus re-opens the possibility of using conventional mode-locked lasers to reach several dozens of spots. It also enables excitation of blue shifted opsins (PsChR2[38], TsChR2[39], CoChR[39]) at their optimal photostimulation peak and to combine multi-target photostimulation of these opsins with red Ca^{2+} imaging, which drastically reduces optical crosstalk from the imaging laser[13,29].

In vivo activation of a single cell with spiral or parallel activation using low repetition (500 kHz-2 MHz) fiber lasers (~1030-1064 nm excitation wavelength) requires 2-50 mW/cell[11,16,40,41]. Considering that these lasers can deliver up to 60 W, it theoretically enables simultaneous stimulation of hundreds of cells. It must however be taken into account that minimizing thermal damages[22,23] requires reducing the thermal crosstalk among the multi targets and imposes a minimal inter-spot distance (equal to the thermal diffusion length, $l_{th} = \sqrt{6Dt}$)[22]. In cortical mice brain, this has so far limited to 50 cells the number of achievable targets within a 500 x 500 x 200 μm^3 excitation volume[10]. We have shown that this limit can be overcome by decomposing the multi-target distribution into *n* sub-groups of sparser targets (i.e., average distance between targets $\gg l_{th}$) sequentially or cyclically illuminated via S/P Flit or Multi S/P Flit. Sequential illumination via S/P Flit enables using the same excitation power per spot, P_{std}, as for the case of simultaneous illumination of the *n* sub groups but requires a *n* fold increase of the total experimental time. Cyclic illumination via Multi S/P requires increasing P_{std} by $\sqrt{n}$ times while keeping the same total experimental time. In both cases the maximum temperature rise achieved is significantly reduced.

We have demonstrated the use of FliT for fast multi-cell optical stimulation. A similar approach can also be used for fast imaging approaches. Cohen et al.[42] have used a gaussian beam focused with a cylindrical lens on an LC-SLM addressed with multiple tiled holograms each encoding for a specific x,y position thus achieving 2D ultrafast scanning of a diffraction limited spot. The FliT approach will enable the generation of single or multiple shaped temporally focused spots for fast multi-target imaging using e.g. voltage indicators, or for fast compressive multiphoton imaging[43]. Also, the possibility to rapidly switch between different holograms each introducing different defocusing effects can be exploited for fast repositioning of the imaging focus and ultrafast fast volumetric imaging[5,44].

We have shown that we can tile the LC-SLM with up to 20 independent tiled holograms without a deterioration of spot quality or axial resolution. This number can be increased by including a de-scanning unit, so that each scanned hologram is projected at the centre of the objective back aperture independently of its position on the LC-SLM. This will enable to eliminate the axial tilt and intensity losses for spots generated with distal holograms. Using a lens with a shorter focal length before the LC-SLM will reduce the vertical dimension of the chirped lines on the LC-SLM and limit the losses in intensity and ellipticity observed when using $n \geq 20$ holograms. This, eventually combined with LC-SLMs with larger pixel numbers, will enable to combine the fine temporal resolution of S/P FliT with the multi-target capability of Multi-FliT to control at fine time scale large neuronal ensembles.

In the present design, the incoming illumination has been shaped in the form of a gaussian beam. Alternatively holographic light shaping could also be used[45] with the advantage of generating spots of variable size and shape. However, in this case, a full-frame illumination is expected in the Fourier plane of the grating (i.e., on the multiplexing LC-SLM). Hence it would be necessary to introduce an additional asymmetric focusing unit (e.g., a cylindrical lens) in order to produce tiled illuminations.

The switching unit here adopted relies on a GM. Different types of scan unit, such as polygonal scanners or AODs could be incorporated to further improve the speed of the switch between light patterns.

In conclusion FLiT illumination is a new tool for the investigation of neuronal circuits with a sub-millisecond control, at single or large neuronal population scales. Combining all the aspects of FLiT presented here, together with the latest engineered fast activity sensors, will allow an all-optical interrogation and manipulation of brain activity to decipher how specific spatio-temporal patterns produced on user defined neuronal ensembles influence specific behaviors, cognitive tasks or defined pathological conditions.

Acknowledgments

We thank Florence Bui and Valeria Zampini for helping with stereotaxic injections and Imane Bendiffallah with organotypic cultures. We thank Dimitrii Tanese for helpful discussion on the modeling of opsin photocycles. We thank Ruth Sims for proof reading of the manuscript, Vincent de Sars for helpful discussion for the implementation of holographic algorithm in Python, Hillel Adesnik for providing the opsin ST-ChroME. We thank the IHU FOReSIGHT grant (Grant P-ALLOP3-IHU-000), the Fondation Bettencourt Schueller (Prix Coups d’élan pour la recherche française), the Getty Lab, the National Institute of Health (Grant NIH 1UF1NS107574 - 01), the Axa research funding and ERC advanced Grant HOLOVIS for financial support.

MATERIALS AND METHODS:

Optical Setup

The optical system was built around a commercial upright microscope (Olympus BX51WI) placed on a XY stage for sample displacement (Luigs & Neumann, V380FM). A femtosecond pulsed beam delivered by a diode pumped, fiber amplifier system (Amplitude Systèmes, Goji HP; pulse width 150 fs, tunable repetition rate 10–40 MHz, maximum pulse energy 0.5 µJ, maximum average power 5 W, wavelength λ = 1030 nm) operated at 10 MHz, was sent first through a λ/2 wave retarder (Thorlabs, 690-1200 nm, AQWP05M-980) in combination with a polarizer cube (CVI Melles Griot) for a manual control of the laser power. The beam was then demagnified with a telescope (f1 = 100 mm; AC508-100-B, Thorlabs; f2 = 50 mm, AC508-50-B, Thorlabs) and sent through an acousto-optic modulator (AOM) (Opto-Electronic, France) to drive fast and precise light power control. The first diffracted order was projected on a pair of XY GMs (3 mm aperture, 6215H series; Cambridge Technology) with a de-magnifying telescope (M=0.4 magnification). Only the Y GM was used and driven by a servo driver (Cambridge Technology, MicroMax series 671). The GM plan was conjugated to a reflective dispersion grating of 800 l/mm by means of a telescope (f = 250 mm; AC508-250-B, Thorlabs; f = 500 mm, AC508-500-B, Thorlabs). A lens (f = 500 mm, Thorlabs, AC508-500-B) transmitted the resulting spatially chirped beam on the sensitive area of a reconfigurable liquid-crystalon-silicon LC-SLM (LCOS-SLM X10468-07, Hamamatsu Photonics, resolution 800×600 pixels, 20 µm pixel size), located in the Fourier plane of the diffraction grating. The LC-SLM was finally conjugated to the back focal plane of the microscope objective (Olympus LUMPlanFL 60XW NA 0.9) via a telescope (f = 1000 mm; AC508-1000-B, Thorlabs; f = 500 mm, AC508-500-B, Thorlabs).

The LC-SLM was divided in *n* horizontal tiles, each independently configurable. Each tiled hologram could be encoded with different sets of 3D diffraction-limited spots enabling to multiplex the temporally focused gaussian beam in multiple targeted locations on the sample. The phase profile of each *n* zones was independently calculated with a weighted Gerchberg and Saxton Algorithm[46]. The effect of the zero order in the sample was suppressed by introducing a cylindrical lens in front of the LC-SLM as detailed in[47]. Each tile of the LC-SLM was illuminated by deflecting the GM of a certain angle, corresponding to a precise driven voltage. A calibration was done in order to associate the beam position on the LC-SLM and the voltage to be applied on the GM.

During S/P-FLiT experiments for sub-ms desynchronization of pairs of neurons, the AOM and GMs was driven with a Digidata 1440A interface and pClamp software (Molecular Devices). In S/P-FLiT experiments for mimicking of random spike patterns and Multi-S/P-FLiT experiments, the system was controlled with a digital-analog converter board (National Instrument, USB-6259). The control of the system was fully automatized through a homemade software written in Python 3 and using the open graphic library PyQt5 which allowed automatic calculation of the tiled holograms and control of the the GM rotation and AOM attenuation.

Optical Characterization of Two-Photon Excitation

In order to characterize system performance, 2PE holographic fluorescence patterns were collected by exciting a thin (~1 µm) spin-coated layer of rhodamine-6G in polymethyl methacrylate 2% w/v in chloroform. Holographic patterns were projected on the sample plane through an excitation objective (Olympus LUMPlanFL 60XW NA 0.9). Images were collected by an opposite imaging objective (Olympus LUMPlanFL 60XW NA 0.7) in transmission geometry and detected by a CCD camera (pco, panda 4.2 bi). A short-pass filter rejected laser light (Chroma Technology 640DCSPXR; Semrock, Brightline Multiphoton Filter 680/sp). 3D stacks were collected by maintaining the excitation objective in a fixed position and moving the imaging objective along z direction with 1µm steps by means of a piezoelectric motor (MIPOS100, Piezosystem Jena).

Axial distribution of intensity on different spots was measured by integrating the pixel intensity across circular region of observations (ROIs) around the spots in each z plane. Each axial intensity distribution was fitted with a Lorentzian model. The intensity and axial resolution for each spot was evaluated and reported as maximum intensity and Full Width Half Maximum (FWHM) of the fitted curves, respectively. Images were analyzed with ImageJ and 3D rendering was performed by Imaris. Axial resolution of in-focus spots was measured by averaging the axial resolution of individual spots distributed in a two-dimensional 5x5 spots matrix in the field of excitation of each tiled hologram (30 µm inter-spots distance) as depicted in Supplementary Fig.4. In-focus intensity homogeneity of each FoE was measured by generating two-dimensional groups of 10 spots randomly distributed in the FoE of each tiled hologram. The axial resolution of spots distributed in a 3D volume was obtained by averaging the axial resolution of groups of 8 spots randomly distributed in a 120x120x70 µm for each tiled hologram. The same groups of spots were used to measure the 3D intensity homogeneity of the different tiled holograms.

Characterization of the switching time between tiles of the LC-SLM

We characterized the switching time to reposition the beam on different tiles of the LC-SLM by means of a photodiode as schematized in Fig.2.

First, we measured the time needed to switch between adjacent tile *i* and tile *i+1* of the LC-SLM subdivided in 20 holograms. For that, we generated two distinct phase masks, φ_i and φ_{i+1}, each encoding for an individual spot placed in a specific XY location of the focal plane. We positioned the photodiode (PD) in a conjugated plane of the sample and we aligned it such that the spot illuminates the center of the detector. We displayed φ_i on the tile *i* and we recorded the light intensity on the PD, while driving the GM servo with a single-step voltage pulse (pulse width 1s) which deflect the beam across small angles between tile *i* to tile *i+1*. We repeated the same procedure by displaying φ_{i+1} on tile *i+1*. From these two measurements, we obtained the averaged switching time to move between two consecutive tiled holograms in opposite directions, as the time taken for the signal to rise/fall between 3% and 97% of the maximum intensity. Of note, the position of PD was finely adjusted to maximize the photon counting when the GM was stationary positioned on tile *i* or tile *i+1.*

Second, we measured the minimal switching time between holograms when sequentially scanning at constant rate all holograms. We generated a hologram φ_i on a single tile *i* encoding for an individual spot detected by the PD as previously described. We then recorded the light intensity on the PD, while driving the GM servo with a staircase voltage pulse (pulse time interval 50µs) which deflects the beam across wide angles between tile *1* to tile *20*. From that, we measured the beam dwell-time on hologram φ_i during switch between hologram φ_1 and hologram φ_{20}. We repeated the same procedure for all 20 holograms. From that, we measured the beam dwell-time on each tiled hologram during whole scan of all holograms at constant switch rate. Of note, scan of all holograms would be alternatively possible by driving the GM with a single-step voltage facilitating maximum speed deflection of the beam across wide angles between tile *1* to tile *20.* While that can facilitate shorter dwell-time per hologram, it also gives variable dwell-time per holograms as central tiled holograms feature shorter illumination dwell-times compared to distal tiled holograms as mirror reaches maximum speed at the midpoint.

Animals

All procedures involving animals were in accordance with national and European (2010/63/EU) guidelines and were approved by the authors' institutional review boards and national authorities (French Ministry of Research, protocol ID: 02230.02). Experiments were performed on C57BL/6J male mice (Jackson lab.) reared in a 12 hr light/dark cycle with food ad libitum. All efforts were made to minimize suffering and reduce the number of animals.

In Vivo Viral Expression

Stereotaxic injections of the fast somatic opsin ST-ChroME were performed in 3-week-old male mice. Mice were anesthetized with ketamine (80 mg/kg)–xylazine (5 mg/kg) solution and a small craniotomy (0.7 mm) was made on the skull overlying V1 cortex. Injection of 1µl of solution containing the viral vector was made with a cannula at a rate of 80-100 nl/min and 200-250 µm below the dural surface. We used a viral mixture containing the somatic opsin ST-ChroME (AAV9-hSyn-DIO-ChroME-Flag-ST-P2A-H2B-mRuby-WPRE-SV40, from the Adesnik lab, Berkeley, viral titer of 5.86×10^{13} particules/ml) and the Cre recombinase (AAV9-hSyn-Cre, from Addgene, 3.3×10^{13}p/ml), diluted at a factor 10 and 100 respectively, in fresh NaCl solution. The craniotomy and the skull were then sutured and the mouse recovered from anesthesia. After 2-3 weeks, sufficient for an adequate expression of the virus, mice were used for electrophysiological experiments. ST-ChroME expression in acute cortical slices is shown in Supplementary Fig.6A.

Preparation of Organotypic Cultures and Viral Infection

Hippocampal slices cultures were prepared from postnatal day 6-9 mice pups according to the interface culture method[48]. Briefly, hippocampi were gently detached from the brain and placed in a cold dissecting medium composed of: Gey's Balanced Salt Solution (Sigma G9779), supplemented with 25 mM D-glucose, 10 mM HEPES, 1 mM Na-Pyruvate, 0.5 mM α-tocopherol, 20 nM ascorbic acid and 0.4% penicillin/streptomycin (5000 U/mL; Fisher 11528876). Transverse slices of 300 µm tickness were cut using a McIlwain tissue chopper, maintained for at least 1h at 4°C and then transferred onto semiporous membranes inserts (47 mm diameter, 0.45 µm pore size; Millipore FHLP04700) which were placed in six well tissue culture plates containing 1.1 ml medium per well. The incubation medium consisted in: 50% Opti-MEM (Fisher 15392402), 25 % heat-inactivated horse serum (Fisher 10368902), 24% HBSS (Fisher 15266355), 1% penicillin/streptomycin (5000U/mL), and supplemented with 25 mM D-glucose, 1 mM Na-Pyruvate, 20 nM ascorbic acid and 0.5 mM α-tocopherol. Slices were maintained at 34°C in an incubator with 5% CO_2. After 3 days, the medium was replace with a fresh and warm Neurobasal culture medium composed of: 2% Neurobasal-A (Fisher 11570426), 15% heat-inactivated horse serum, 2% B27 supplement (Fisher 11530536), 1% penicillin/streptomycin (5000U/mL), and supplemented with 0.8 mM L-glutamine, 0.8 mM Na-Pyruvate, 10 nM ascorbic acid and 0.5 mM α-tocopherol. This medium was changed every 2-3 days until the experiment.

Organotypic slices were then infected with 1 µL of virus at 5-7 days in vitro (DIV). We used the same mixture as for in vivo stereotaxic injections. Slices were used for electrophysiology recordings at 12-14 DIV. See Supplementary Fig.6B for ST-ChroME expression in this preparation.

Acute Slice Preparation for Electrophysiology

Acute parasagittal slices of the visual cortex were prepared from adult mice 2-3 weeks after viral injection. Animals were decapitated after being deeply anesthetized with isoflurane (5% in air). The brain was quickly removed, immersed in an ice-cold choline solution and 300 µm-thick slices were obtained using a vibratome (Leica Biosystems VT1200S). The cutting solution contained the following (in mM): 126 choline chloride, 16 glucose, 26 $NaHCO_3$, 2.5 KCl, 1.25 NaH_2PO_4, 7 $MgSO_4$, 0.5 $CaCl_2$, pH 7.4, cooled to 4°C and equilibrated with 95% O_2/5% CO_2. Slices were maintained at 32°C for 20min in standard ACSF (sACSF) containing the following (in mM): 125 NaCl, 2.5 KCl, 26 NaHCO3, 1.25 NaH2PO4, 1 MgCl2, 1.5 CaCl2, 25 glucose, and 0.5 ascorbic acid, pH 7.4, saturated with 95% O2 and 5% CO2 and then transferred at room temperature in the same solution until recordings.

Whole-Cell Electrophysiology In Vitro

Acute slices as well as organotypic slices were placed in a recording chamber under the microscope objective, and perfused continuously with fresh sACSF saturated with 95% O2 and 5% CO2. Neurons were patched at 30-60 µm from the slice surface. Single or doubled-patched neurons were clamped at −70 mV in voltage-clamp configuration and membrane potential was kept at −70 mV with currents injections in current-clamp configuration. Patch electrodes (Borosilicate glass pipette, outer diameter 1.5 mm and inner diameter 0.86 mm, Sutter Instruments) were filled with an intracellular solution containing the following (in mM): 127 K-gluconate, 6 KCl, 10 Hepes, 1 EGTA, 2 MgCl2, 4 Mg-ATP, 0.3 Na-GTP; pH adjusted to 7.4 with KOH. The estimated reversal potential for chloride (E_{Cl}) was approximately −69 mV based on the Nernst equation. Pipettes were pulled from borosilicate glass capillaries and had a typical tip resistance of 5-6 MΩ. The averaged serie resistances were 18.5 ± 7.9 MΩ (n = 34 cells) and 17.9 ± 3.7 MΩ (n = 8 cells), for acute slices and organotypic cultures, respectively.The following receptor blockers were added to the sACSF to block any synaptic effect: DNQX and AP-V (1µM each; from Abcam). Electrophysiology data were acquired with a Multiclamp 700B amplifier and digitized with a Digidata 1322A interface and pClamp software (Molecular Devices). Signals were sampled at 20–50 kHz and filtered at 4-10 kHz.

Desynchronization of Activity of distinct neurons

In S/P-FliT experiments, we desynchronized two ST-ChroME-expressing targeted neurons, here called neuron A and neuron B (Fig.3A). The following photostimulation procedure was used in order to trigger activity in neuron A and B with a time delay shorter than the illumination dwell-times needed to evoke activity in the two neurons. We defined three tiled phase masks and we vertically piled them adjacently on the LC-SLM display such that: tile φ_A encodes for illumination of neuron A (top tile), tile φ_{AB} encodes for simultaneous illumination of neurons A and B (middle tile), and tile φ_B encodes for illumination of neurons B (bottom tile). First, we established threshold light powers P_A and $P_{B,}$ and illumination dwell-times $t_{A,}$ t_B to independently evoke an AP on neuron A and neuron B, by deflecting the GM on tile φ_A and φ_B. Threshold values were defined in current clamp mode when AP was reliably generated on 3/3 consecutive trials (40 s inter-time between trials). Photocurrents corresponding to threshold illumination conditions were also recorded in voltage-clamp. On the basis of these values, we set a sequence to drive the GM and the AOM and introduce arbitrarily defined spike delays δt between neuron A and B. Accordingly, the beam was sequentially directed by tilting the GM on tile φ_A for a time δt, on tile φ_{AB} for a time $t_A - \delta t$ and on tile φ_B for a time $t_B - (t_A - \delta t)$. The incoming power was adjusted via the AOM such that it was set to P_A when the beam was on tile φ_A, to P_B when the beam was on tile φ_B and to $P_A + P_B$ when the beam was on tile φ_{AB}. Of note, the diffraction efficiency of phase mask φ_{AB} was computationally corrected such that the ratio of intensity sent onto neuron A and B equals to ${}^{P_A}/_{P_B}$. That ensures that both neurons are constantly illuminated with the same intensity during their respective illumination dwell-time. Importantly, in voltage-clamp mode, we verified that the beam of power $P_A + P_B$ positioned on φ_{AB} for a time t_A and t_B elicited the same photocurrents previously elicited by illuminating only neuron A (with P_A power, t_A dwell-time on φ_A) and B (with P_B power, t_B dwell-time on φ_B), respectively (Supplementary Fig.18). GM deflection between the three tiles was driven with small angle single-step voltage as previously detailed. We thus recorded in current-clamp the APs driven in neuron A and B by addressing GM and AOM following the established sequence of photoactivation.

Of note, in general, for all those experiments which feature delays longer than the illumination dwell-times needed to evoke activity in the two neurons, only two tiles of the LC-SLM are necessary (tile φ_A and tile φ_B), as the beam will never be simultaneously on neuron A or B.

Importantly, this strategy can be generalized to desynchronize *n* neurons (or n groups of neurons) with delays inferior to each activation dwell-time, by dividing the LC-SLM in $2n-1$ tiled holograms and piling them on the LC-SLM such that each hologram encodes, from top to bottom: *1st* tiled hologram → *1st* neuron, *2nd* tiled hologram → *1st+2nd* neurons,..., *nth* tiled hologram → *1st+2nd+...+nth* neurons, *(N+1)th* tiled hologram → *2nd+...+nth* neurons*,* *(n+2)th* tiled hologram → *3rd+...+nth* neurons ... *(2n-1)th* tiled hologram → *nth* neuron. Power on each of the 2n-1 tiled phase masks needs to be modulated accordingly to the number of encoded targets (Supplementary Fig.8).

Mimicking of firing

In S/P FliT experiments aiming to mimic neuronal firing, reference traces originated from an individual recording under in-vivo patch-clamp. In particular, two subsections, each 2 s long and featuring characteristic firing patterns, were arbitrarily selected and delayed. The two traces were then feed to a home-made software which extracted the spike timing and automatically determined the illumination sequence (including illumination power and switch time) to be addressed on the tiled holograms of the LC-SLM to reproduce the delayed spiking patterns on two double-patched neurons.

Multi-Neuron Activation

In Multi-S/P experiments, the LC-SLM was subdivided in *n* tiled phase masks. In particular, one mask φ was encoded to illuminate one targeted ST-ChroME-positive neuron. We initially established threshold light power P_{std} and illumination dwell-time t_{std} to evoke an AP on the cell by tilting the GM to steadily illuminate φ.

The cell was then photoactivated under cyclic illumination by driving the GM with a staircase voltage input which facilitated steering the beam back and forth on all *n* holograms through discrete angle deflections and fixed dwell-time per hologram at $t_{cyc} = 50\mu s$ for N_{cyc} cycles (Supplementary Fig.19). Compared to scan the holograms by driving the GM with a single-step voltage input, staircase voltage inputs gives more homogenous dwell-time per hologram.

We tested a slow photoactivation protocol featuring a total scan time $t_{exp}^{cyc} = n \cdot N_{cyc} \cdot t_{cyc}$ and a fast photoactivation protocol featuring a total scan time $t_{exp}^{cyc} = t_{std}$. We established power to trigger an AP in both cases by varying the number of the tiled holograms (i.e., the size of each tiled hologram) between 12 and 50. Photocurrents have been recorded in voltage-clamp by displaying φ on different position of the LC-SLM, in order to verify that different tiles substantially elicit the same photocurrent (Supplementary Fig.11).

Temperature Simulation:

The spatio-temporal distribution of the temperature rise was calculated by solving the Fourier heat diffusion equation[49] considering the brain tissue as an infinite medium with isotropic and uniform thermal properties as described in [22]. The solution is obtained by convolving the Green's function for the diffusion equation by the thermal source term, which is the thermalisation of the absorbed light source intensity. This model has been experimentally validated[22]. Numerical solution was implemented in Python, taking special care in selection spatial and temporal sampling to avoid overlap due to cyclic boundary conditions induced by the use of Fourier transform based numerical convolution.

Data Analysis and Statistical Tests

We performed the analysis of the recorded stacks on Rhodamine layers with MATLAB, ImageJ, and the Imaris software (Bitplane, Oxford Instruments). The 2PE fluorescence values for each spot were obtained by integrating the intensity of all the pixels in a circular area containing the spot, in the plane where the intensity was at its maximum value (i.e., the TF plane). Axial intensity distributions were obtained by integrating the intensity of the pixels in the same area for each plane of the recorded stack, in a range of ± 20 µm around the focal plane of each spot. Reported values for the axial confinement were the fit of the axial profile of the spots with a Lorentzian model and referred to the FWHM of the curves.

All electrophysiological data were analyzed with Clampfit (Molecular Devices). For S/P-FliT experiments (Fig.3), we measured, for double patched neurons, A and B, the depolarization onset or the AP peak delay, determined as the time between the beginning of the light stimulus and membrane potential change or the AP peak, respectively. We then substracted the values of cell B to cell A and compared this temporal delay to the expected one. We evaluated the temporal accuracy as the difference between imposed $\delta\mathrm{t}$ and experimental $\delta\mathrm{t}_{\mathrm{AP}}^{\mathrm{exp}}$ delays, $\left|\delta\mathrm{t}_{\mathrm{AP}}^{\mathrm{exp}} - \delta\mathrm{t}\right|$. Global accuracy was calculated as weighted mean and SD of all imposed $\delta\mathrm{t}$. For mimicking experiments, the analysis of the results was established by pairing the closest subsequent APs in the two neurons. In particular, for each AP pair, we evaluated the temporal accuracy as the difference between driven and experimental inter-spike time. We then calculated the overall accuracy of the mimicking by weight averaging the temporal accuracy of each AP pair.

AP latencies were determined as the time between the beginning of the stimulus and the time of AP peak, and AP jitters were calculated as the standard deviation (SD) of the AP latency accros trials. All recordings were analyses and averaged across 3-5 photostimulation trials. All values are presented as mean ± SD of *n* experiments.

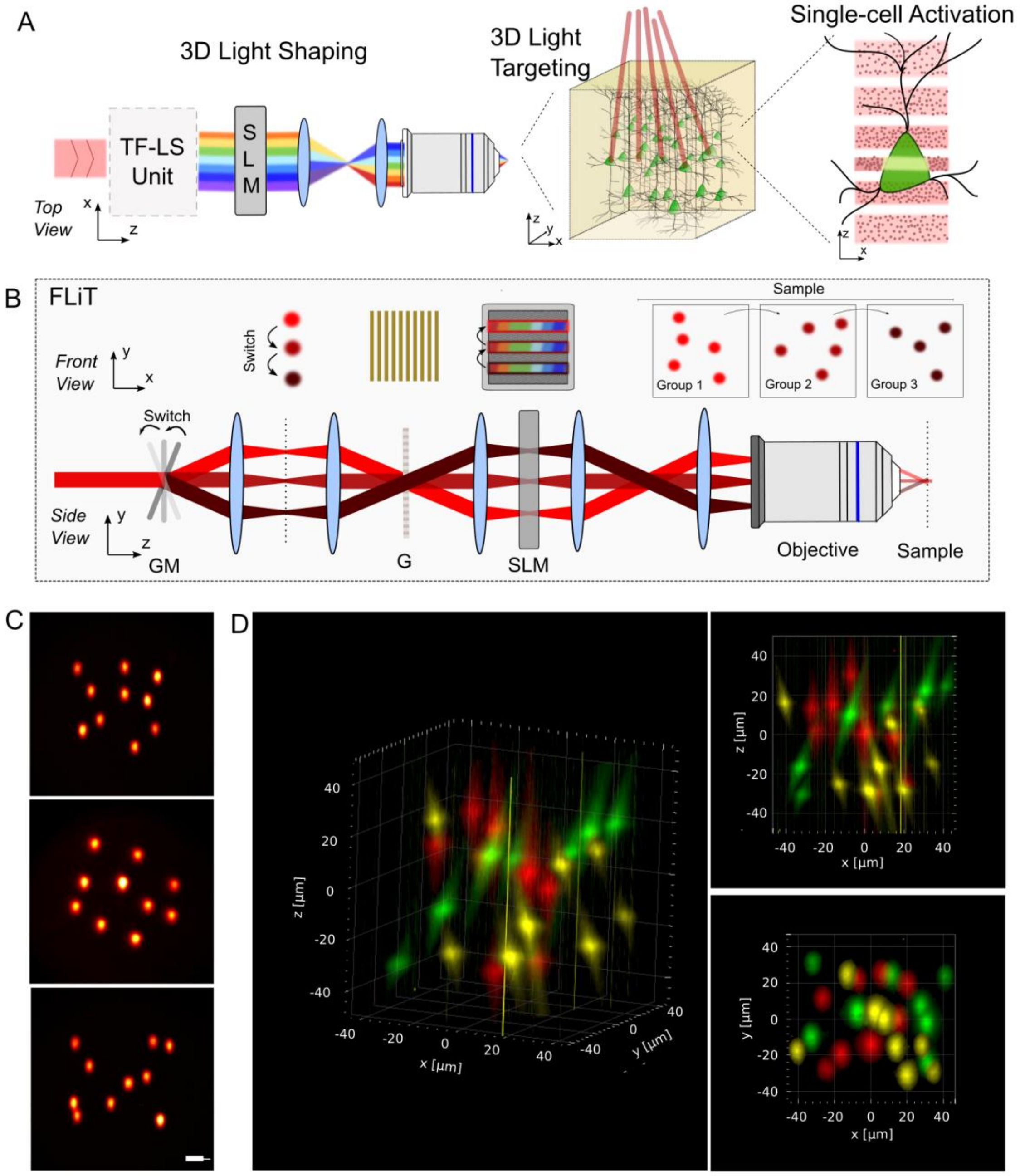

Figure 1: FLiT optical characterization. (A) General optical scheme for temporally focused light shaping. A first light-shaping temporally focusing architecture (LS-TF) allows (i) sculpting light into particular forms and (ii) temporally focusing the photons to confine photostimulation to a shallow axial region with cellular dimensions. A subsequent LC-SLM modulation allows multiplexing the sculpted light to multiple 3D sample locations. (B) Optical setup of FLiT. A pulsed collimated beam (red line) is reflected by a galvanometric mirror (GM) onto a diffracting grating (G) via a 4f-telescope. Diffracted off the grating, the beam is collimated onto a liquid crystal spatial light modulator (LC-SLM) in the form of a horizontal (i.e., orthogonal to the orientation of the grating lines) spatially chirped strip of light. The LC-SLM is imaged onto the back aperture of an objective lens so that ad hoc phase-modulation on the LC-SLM allows multiplexing the initial beam and generating a multi-site temporally focused pattern of light in the sample. As deflection of the beam by the GM results into a translation of the illuminating bands on the LC-SLM (dark red lines), addressing the LC-SLM with n independent tiled holograms φi leads to fast switch of different groups of light patterns into the sample. The top and bottom drawing represents the XY and the YZ plane views, respectively. (C) x-y 2PE fluorescence cross-sections of different groups of randomly distributed spots generated in the sample focal plane by addressing the i-th hologram φi of an LC-SLM subdivided in 20 tiled holograms: hologram φ8 (Top), hologram φ10 (Middle) and hologram φ12 (Bottom). Scale bar: 20µm. (D) 2PE fluorescence of different groups of spots generated by

different tiled holograms φi randomly distributed across a 120x120x70 μm^3 volume. Different colors correspond to different tiled hologram (hologram φ4, yellow; hologram φ10, red; and hologram φ16, green).

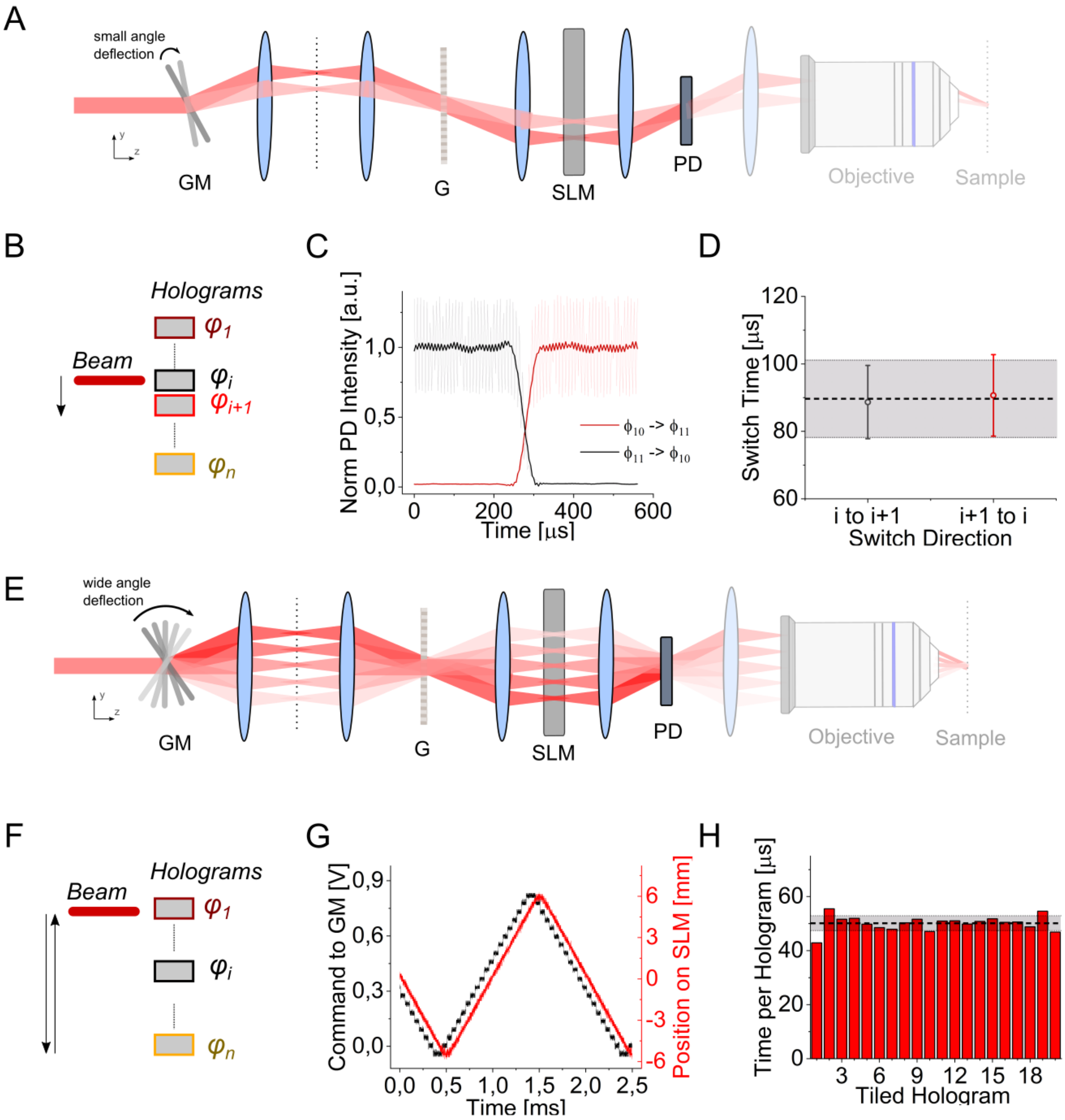

Figure 2: FLiT switching time. (A) Switching time between two adjacent tiled holograms (φi and φi+1) is measured by means of a photodiode (PD) placed in an image conjugate plane while driving the galvanometric mirror (GM) with small angles single-step voltage inputs. (B) Scheme of illumination switch between tiled hologram φi and φi+1 on the SLM display corresponding to sequence depicted in (A). (C) Representative intensity response of the PD when GM is switched from hologram φ11 (encoding for an individual spot in the middle of PD) to hologram φ10 (deviating the beam out of the PD) (black line) or, vice versa, from hologram φ10 (encoding for an individual spot in the middle of PD) to hologram φ11 (deviating the beam out of the PD) (red line). (D) Switch time calculated as the time taken for the signal to rise/fall between 3% and 97% of the maximum intensity, when the spot is encoded in hologram φi and GM is switched from hologram φi to φi+1 (black symbols) or vice versa (red symbols). Horizontal black line and grey bands indicate the global mean and SD switching time, respectively. (E) Switch time to sequentially illuminate all holograms at constant rate from φ1 to φn is measured by driving the galvanometric mirror (GM) with a wide-angle staircase voltage input. (F) Scheme of the illumination switch to sequentially illuminate all holograms from φ1 to φn on the SLM display corresponding to the sequence depicted in (E). (G) GM voltage input (black line) and corresponding position of the incoming beam on the LC-SLM (red line) when GM is driven as depicted in (E). (H) Dwell time of each hologram φi of the LC-SLM while GM is driven as depicted in (E) and φi only encodes an individual spot in the middle of the PD. Horizontal black and grey lines indicate the mean and SD dwell-time over all holograms. For all experiments the LC-SLM was dived in 20 tiled holograms.

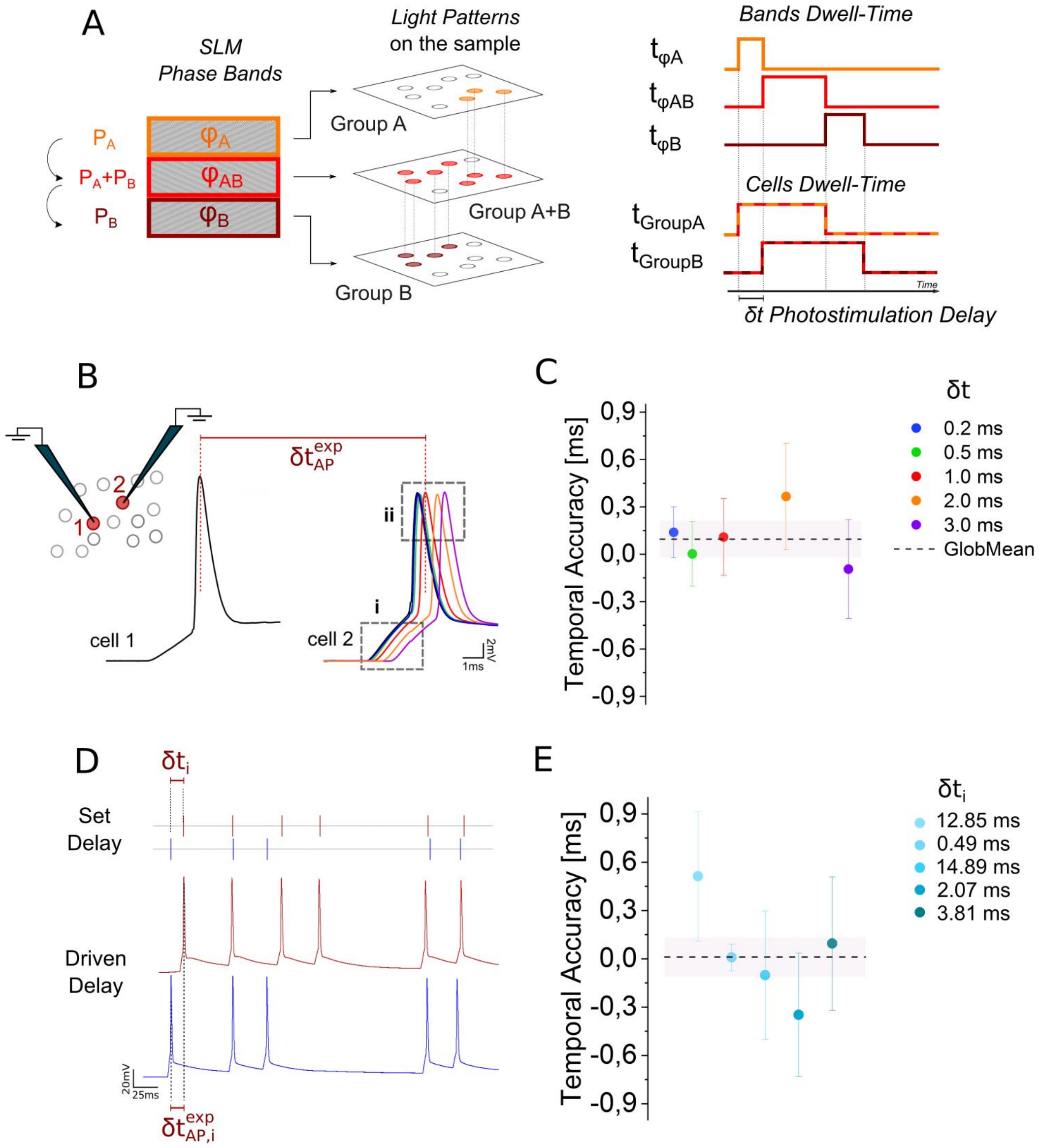

Figure 3: Tuning control of neuronal activity in targeted neurons by S/P-FLiT. (A) Conceptual scheme of S/P FliT. The LC-SLM is tiled in different regions each encoding different phase masks. In the present example, phase mask φA and φB encode for group of spots A and B, while phase mask φAB encodes for a comprehensive pattern including group A and group B. By steering the beam vertically across the phase masks with predetermined dwell-times and illumination intensities per each mask, it is possible to set arbitrary delays of activation between groups of spots. In the illustred example, the laser dwell-time is tφA, tφAB, tφB, and the illumination power is PA , PA + PB , PB on φA , φAB , φB respectively. Importantly on comprehensive phase mask φAB, the distribution of intensity must be computationally set to maintain an amount of power PA and PB on subgroup A and B, respectively. Overall, this scheme yields an activation time tφA+tφAB for group A, tφAB+tφB for group B and a delay of activation between group A and group B δt equivalent to tφA. The scheme displayed is meant to represent n groups of spots; their number is here limited to 2 for presentation purposes only. (B) Representative light-driven APs from two double-patched ST-ChroME-expressing neurons by imposing different delays δt ranging from 0.2ms to 3ms. (C) Temporal accuracy calculated as the difference between imposed δt and experimental δt_{AP}^{exp} delays, $\left|\delta t_{AP}^{exp} - \delta t\right|$. Circle symbols represent different δt delays (data are shown as mean $\pm$ SD). Horizontal dashed black line and grey bands represents global mean and SD, respectively. Error bars are SD on n = 12 pairs of cells. Mean AP accuracy is 96 ± 114 µs. (D) Representative light-driven APs from two double-patched ST-ChroME-expressing neurons (Bottom) by imposing a random spiking patterns (Top) featuring inter-spike time intervals δt_i. (E) Temporal accuracy calculated as difference between imposed δt_i and experimental δt_{APi}^{exp} delays of the i-th AP pair, $\left|\delta t_{APi}^{exp} - \delta t_i\right|$. Circles from light to dark blue indicate temporal accuracy from subsequent pairs of APs (data are shown as mean $\pm$SD). Mean temporal accuracy is 11 ± 122 µs (n = 12 pair of cells). Mean photostimulation power is 37.7 ± 21.3 mW. Illumination dwell-time ranges between and 2-5ms. 1030nm illumination has been used.

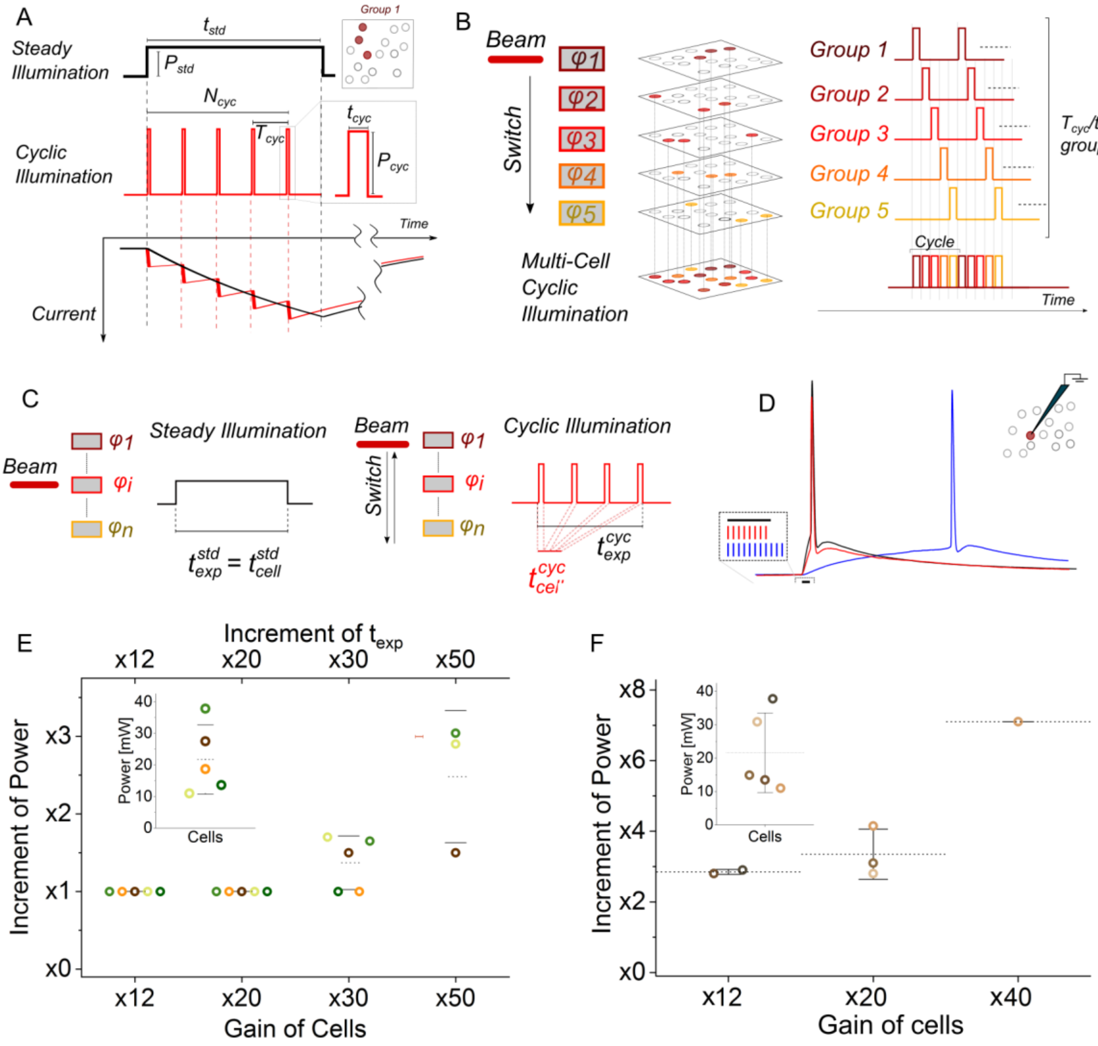

Figure 4: Multi-cell activation by S/P-MultiFLiT. (A) Photostimulation of a group of neurons under steady and cyclic illumination. A soma-targeted light pattern encoded by a single hologram can be used to photoactivate a group of neurons either under steady illumination of power P_{std} and duration t_{std} (black line, Top) or under cyclic illumination of power P_{cyc}, period T_{cyc} and pulse duration t_{cyc} over N_{cyc} cycles (red line, Middle). Corresponding simulated photocurrents in an ST-ChroME-expressing neuron are shown under steady (black) and cyclic (red) illumination when $P_{cyc} = P_{std}\sqrt{T_{cyc}/t_{cyc}}$ $(P_{std} = 0.05\, mw/\mu m^2;\ P_{cyc} = 0.05\sqrt{20}\, mw/\mu m^2;\ T_{cyc} = 20 t_{cyc};\ t_{cyc} = 50\mu s;\ 1030 nm)$ (Bottom). (B) Conceptual scheme of simultaneous photostimulation of multiple groups of neurons under Multi-S/P scheme. The LC-SLM is tiled in multiple holograms φi (here from φ1 to φ5) each encoding for different soma-targeted light-patterns illuminating different groups of cells (here from Group 1 to Group 5). The illumination beam is switched across the holograms such that each hologram is sequentially illuminated with short pulses of light t_{cyc} and the same cyclic photoactivation process is enabled sequentially on the different light patterns. The scheme displayed is meant to represent n groups of spots; their number is here limited to 5 for presentation purposes only. (C) Scheme of the experiment. The SLM is subdivided in n tiled holograms, with tiled hologram φi encoding for a spot of light targeting a ST-ChroME-expressing patched neuron. The neuron is then activated either by steadily maintaining the laser beam on φi with laser power P_{std} (steady illumination) or scanning the beam over the SLM with laser power P_{cyc} (cyclic illumination). (D) Representative light-evoked APs under steady illumination of duration t_{std}=5ms (black line) and cyclic illumination with $t_{exp}^{cyc} = t_{exp}^{std}$ (red line) or $t_{cell}^{cyc} = t_{cell}^{std}$ (blue line). Illumination last steadily 5ms (black bar) and cyclically 5ms (red bars) and 60ms (blue bars) (E) Gain of activable cells obtained in Multi-S/P for different increment of powers and $t_{cell}^{cyc} = t_{cell}^{std}$. Different colors indicate different cells. Inset represents threshold power to activate the cells under steady illumination with $t_{std} = 5ms$. (F) Gain of number of activated cells in Multi-S/P for different increment of power and $t_{exp}^{cyc} = t_{exp}^{std} = 5ms$. Different colors indicate different cells. Inset represents threshold power to activate the cells under steady illumination with $t_{std} = 5ms$.

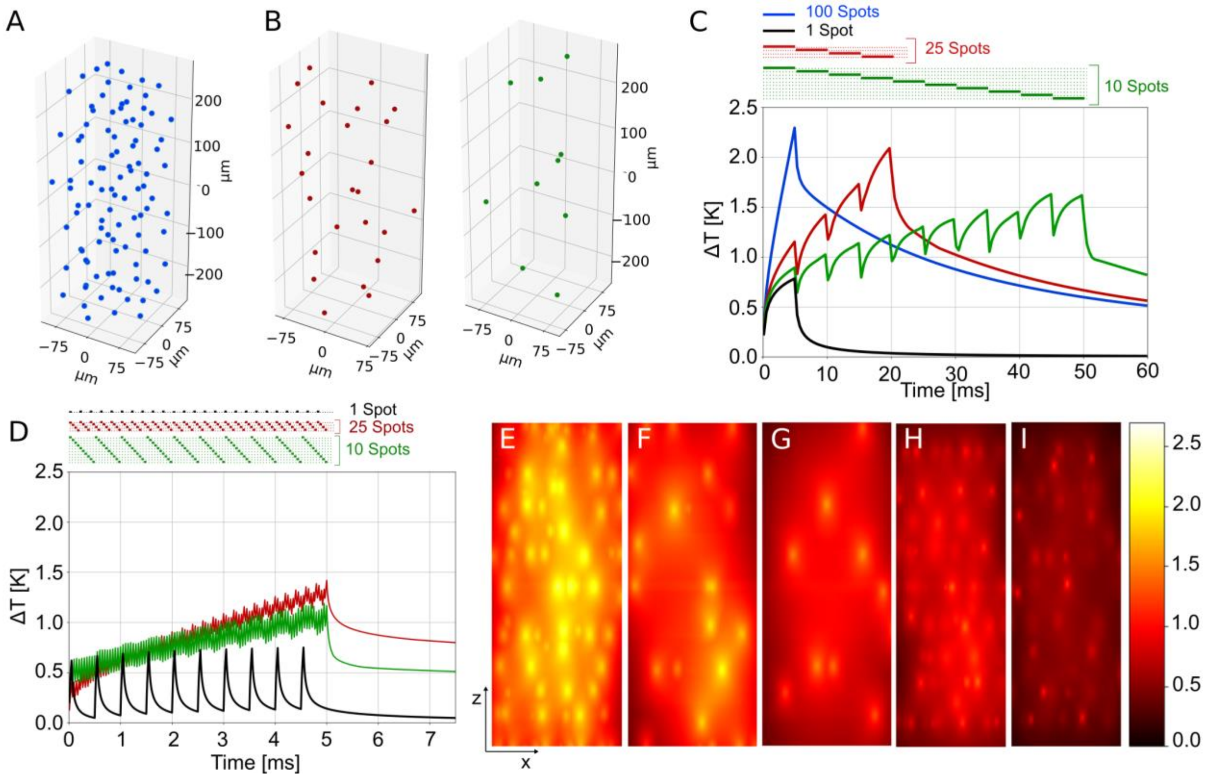

Figure 5: Simulated Temperature rise induced by FLiT activation under different S/P illumination protocols. (A) Three-dimensional view of a group of 100 spots randomly distributed in a 200x200x500µm^3 volume. Spots were distributed to maximize nearest neighboring distance (average distance between spots equals to 50.7 ± 6.8 µm) (B) Representative three-dimensional view of one subset of spots when the ensemble of spots in (A) are subdivided in n=4 subsets with 25 spots each (left) or in n=10 subsets with 10 spots each (right). Average distance between spots equal to 78.7 ± 14.6 µm and 106.0 ± 23.7 for n=4 and 10, respectively. (C) Temperature rise in the hottest location at any given time induced by steadily illuminating 100 spots as shown in (A) either in parallel with $t_{exp} = t_{std}$=5ms and global power $P = 100 \cdot P_{std}$ (with P_{std} =20mW) (blue) or sequentially with n=4 subsets of spots with t_{exp}=20ms and global power per subset $P = 25 \cdot P_{std}$ (red) or n=10 subsets of spots with t_{exp}=50ms and global power per subset $P = 10 \cdot P_{std}$ (green). The temperature rise induced by steadily illuminating one spot individually is also shown (black). The illumination timing is represented at the top of the graph with horizontal bars: different horizontal lines correspond to the timing of illumination of different subsets (illumination of one set of 100 spots (blue bar), 4 subsets of 25 spots (red bars), 10 subsets of 10 spots (green bars) and one single spot (black bar)). (D) Temperature rise in the hottest location at any given time induced by cyclically illuminating the 100 spots with n=4 subsets of spots for a t_{exp}=5ms (t_{cyc}=50µs; N_{cyc}=25) and global power per subset $P = 25\sqrt{4} \cdot P_{std}$ (red line) or n=10 subsets of spots for a t_{exp}=5ms (t_{cyc}=50µs; N_{cyc}=10) and global power per subset $P = 10\sqrt{10} \cdot P_{std}$ (green line). The temperature rise induced by illuminating one spot individually under cyclic illumination with the same conditions of n=10 subsets of spots is also shown (black line). The illumination timing is represented at the top of the graph with horizontal bars. Different horizontal lines correspond to the timing of illumination of different subsets (illumination of 4 subsets of 25 spots (red bars) and 10 subsets of 10 spots (green bars)). (E-I) xz projection of the max temperature rise produced by the 100 spots after 5 ms and simultaneous illumination of 100 spots (E); after 20 ms and sequential steady illumination with n=4 (F); after 50 ms and sequential steady illumination with n=10 (G); after 4.6 ms and cyclic illumination with n=4 (H); after 4.9 ms and cyclic illumination with n=10 (I). Color bar ranges from 0 K to 2.5 K. FoV per image 200 x 500 µm^2.

SUPPLEMENTAL INFORMATION

Supplementary Note 1

The dynamic of photocurrent can be described using a four-state model which assumes two open and two closed states[50–53] (Supplementary Fig.20A).

In this case, by denoting with O_1, O_2, C_1, and C_2 the fraction of opsin molecules in each of the four states at any given instant of time, the transition rates among the four states can be described by the following set of rate equations,

$$\begin{aligned}\dot{O}_1 &= G_{a1}(P)C_1 + G_b(P)O_2 - \left(G_{d1} + G_f(P)\right)O_1\\ \dot{O}_2 &= G_{a2}(P)C_2 + G_f(P)O_1 - \left(G_{d2} + G_b(P)\right)O_2\\ \dot{C}_1 &= G_{d1}O_1 + G_rC_2 - G_{a1}(P)C_1\\ \dot{C}_2 &= G_{d2}O_2 - \left(G_r + G_{a2}(P)\right)C_2\end{aligned} \tag{1}$$

where $O_1 + O_2 + C_1 + C_2 = 1$ and $G_{a1}(P)$, $G_{a2}(P)$, G_{d1}, G_{d2}, $G_f(P)$, $G_b(P)$ and G_r are the rate constants for transitions $C_1 \rightarrow O_1$, $C_2 \rightarrow O_2$, $O_1 \rightarrow C_1$, $O_2 \rightarrow C_2$, $O_1 \rightarrow O_2$, $O_2 \rightarrow O_1$ and $C_2 \rightarrow C_1$ respectively.

Under 2P excitation, the dependence on the excitation power, P, of the transition rates from closed to opened states, $G_{a1}(P)$ and $G_{a2}(P)$, can be expressed as[50]:

$$G_{a1}(P) = k_1 \frac{P^2}{P_m^2+P^2} \quad ; G_{a2}(P) = k_2 \frac{P^2}{P_m^2+P^2} \tag{2}$$

and between the opened states as:

$$G_f(P) = k_f \frac{P^2}{P_m^2+P^2} + G_{f0} \quad ; G_b(P) = k_b \frac{P^2}{P_m^2+P^2} + G_{b0} \tag{3}$$

Where P_m marks the transition from quadratic to saturated regime for rate constants and k_1, k_2, k_f and k_b are the transition rate at saturation of $C_1 \rightarrow O_1$, $C_2 \rightarrow O_2$, $O_1 \rightarrow O_2$, $O_2 \rightarrow O_1$, respectively.

Following the procedure described in Evans et al.[50] we fitted the photocurrent traces obtained upon targeted 2PE illumination of a ST-ChRoME-expressing neuron and determined the transition rate constants for the opsin ST-ChRoME (Supplementary Fig.20B). We then used these values to simulate the photocurrents induced in a ST-ChroME-expressing neuron by using a steady or cyclic illumination for different illumination powers and number of tiled holograms *n* (Supplementary Fig.20C). We found, that for intensities $P << P_m$ and short cyclic flashes of light, t_{cyc}, photocurrents evoked under cyclic illumination are comparable to the ones obtained under steady illumination if $P_{cyc} \cong P_{std}\sqrt{n}$ (Supplementary Fig.20D).

Interestingly, the same condition can be analytically derived by using a simplified two-state model, which only considers the O1 and C1 states. This assumption is valid when the illumination times are short compared to the decay times constants of the state O_1 (i.e., $t_{cyc} << \frac{1}{G_f(P)}$, $\frac{1}{G_{d1}}$).

In this assumption, the rate equations (1) can be simplified in:

$$\begin{aligned}\dot{O}_1 &= G_{a1}(P)C_1 - G_{d1}O_1\\ \dot{C}_1 &= G_{d1}O_1 - G_{a1}(P)C_1\end{aligned} \tag{4}$$

For a steady illumination power P_{std} and an illumination time $n \cdot t_{cyc}$ (n the number of tiled holograms and t_{cyc} = 50 µs) the fraction of opsins in O1 state during the first illumination cycle is given by

$$O_{1,std}(n \cdot t_{cyc}) = \frac{G_{a1}(P_{std})}{G_{a1}(P_{std}) + G_{d1}} \times [1 - exp(-(G_{a1}(P_{std}) + G_{d1}) \cdot n \cdot t_{cyc}\ )] \tag{5}$$

which considering short illumination time, $(G_{a1}(P_{std}) + G_{d1}) \cdot n \cdot t_{cyc} \ll 1$, becomes:

$$O_{1,std}(n \cdot t_{cyc}) \approx G_{a1}(P_{std}) \cdot n \cdot t_{cyc} \tag{6}$$

For a cyclic illumination of power P_{cyc}, and an illumination time t_{cyc}, the opsins are excited to the state O1 during t_{cyc} and decay back to C1 during $(n-1) \cdot t_{cyc}$. The fraction of opsins in O1 state is then:

$$O_{1,cyc}(n \cdot t_{cyc}) = \frac{G_{a1}(P_{cyc})}{G_{a1}(P_{cyc}) + G_{d1}} \underbrace{[1 - exp(-(G_{a1}(P_{cyc}) + G_{d1})t_{cyc}\ )]}_{excitation} \cdot \underbrace{exp(-G_{d1}(n-1)t_{cyc}\ )}_{decay} \tag{7}$$

which can be approximated to

$$O_{1,cyc}(n \cdot t_{cyc}) \approx G_{a1}(P_{cyc})t_{cyc}(1 - G_{d1}(n-1)t_{cyc}) \tag{8}$$

In order to obtain the same number of opsins in the open state under steady and cyclic illumination, i.e. $O_{1,std} = O_{1,cyc}$, two conditions need to be verified: the number of transitions from C1 to O1 are the same under steady and cyclic illuminations, i.e.:

$$G_{a1}(P_{std}) \cdot n \cdot t_{cyc} = G_{a1}(P_{cyc}) \cdot t_{cyc} \tag{9}$$

and, in the cyclic configuration, the number of transitions from O1 to C1 in the off-time $(n-1)t_{cyc}$, is negligeable:

$$G_{d1}(n-1)t_{cyc} \ll 1 \tag{10}$$

In the limit $P \ll P_m$, $G_{a1}(P)$ (equation (2)) can be approximated by:

$$G_{a1}(P) = k_1 \frac{P^2}{P_m^2 + P^2} \approx \frac{k_1}{P_m^2} P^2 \tag{11}$$

and Equation (9) can be written as:

$$\frac{k_1}{P_m^2} P_{std}^2 \cdot n \cdot t_{cyc} = \frac{k_1}{P_m^2} P_{cyc}^2 \cdot t_{cyc} \tag{12}$$

Which gives the relationship between cyclic and steady power as numerically derived using the four-states model,

$$P_{cyc} = P_{std}\sqrt{n} \tag{13}$$

SUPPLEMENTARY FIGURES:

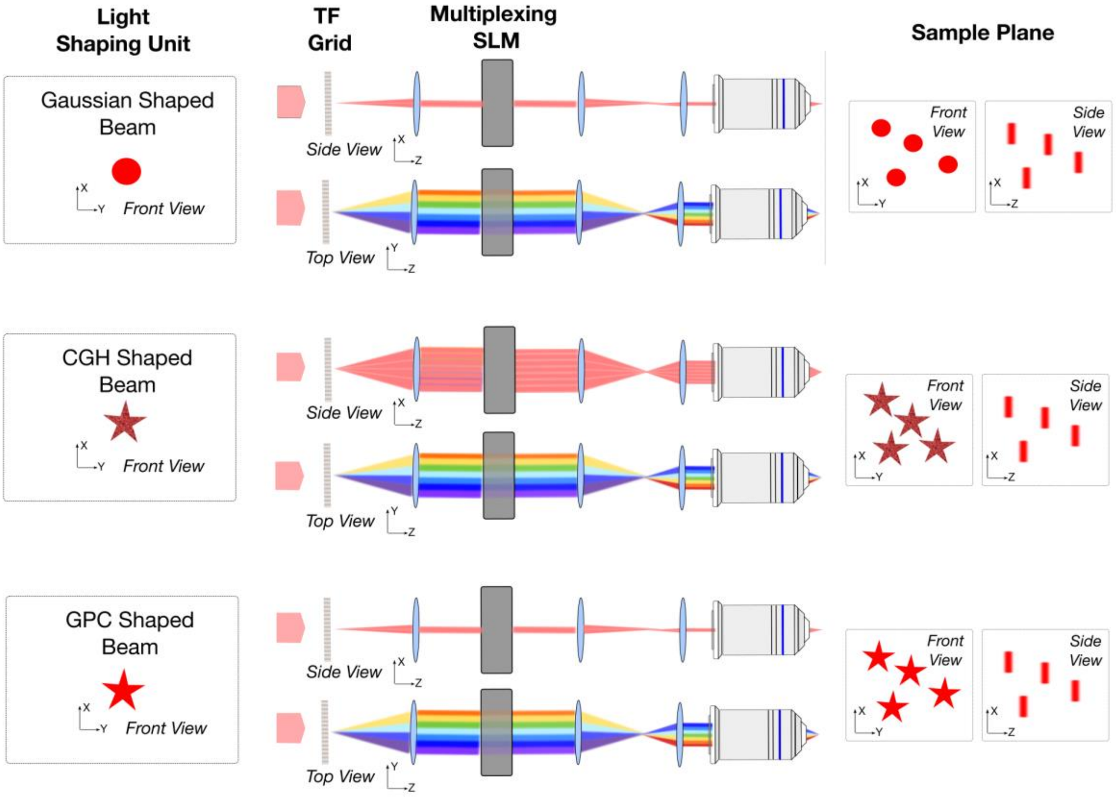

Supplementary Figure 1: Multiplexing temporally focused light patterns by using different light shaping units.Gaussian- (top), Computer Generated Holography, CGH- (middle) and Generalized Phase Contrast, GPC- (bottom) based multiplexing temporally focused systems. For each beam shape, it is here shown: XY front view of the incoming beam on the TF grating plane (left), XZ side and YZ top view of the multiplexing pathway (center), XY front and XZ side views of the XYZ multiplexed patterns on the sample plane (right).

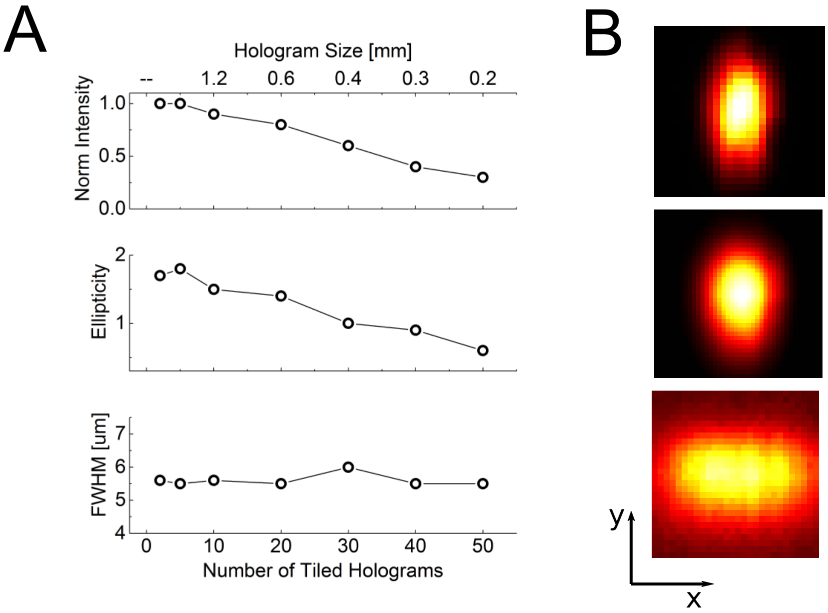

Supplementary Figure 2: Intensity, in-focus XY ellipticity and axial FWHM of the multiplexed spot vs size of tiled holograms on the LC-SLM. (A) Intensity (Top), Ellipticity (Middle) and FWHM of axial intensity distribution (Bottom) of a spot encoded by holograms of different sizes in the direction orthogonal to the grating dispersion. (B) xy images of the spot encoded by using 60pixelsx800pixels (i.e., 1.2mm x 12mm) holograms (corresponding to LC-SLM tiled in 10 regions) (Top), 30x800 pixels (i.e., 0.6mm x 12mm) holograms (corresponding to LC-SLM tiled in 20 regions) (Middle) and 12x600 pixels (0.24mm x 12mm) holograms (corresponding to LC-SLM tiled in 50 regions) (Bottom). LC-SLM pixel size 20μm.

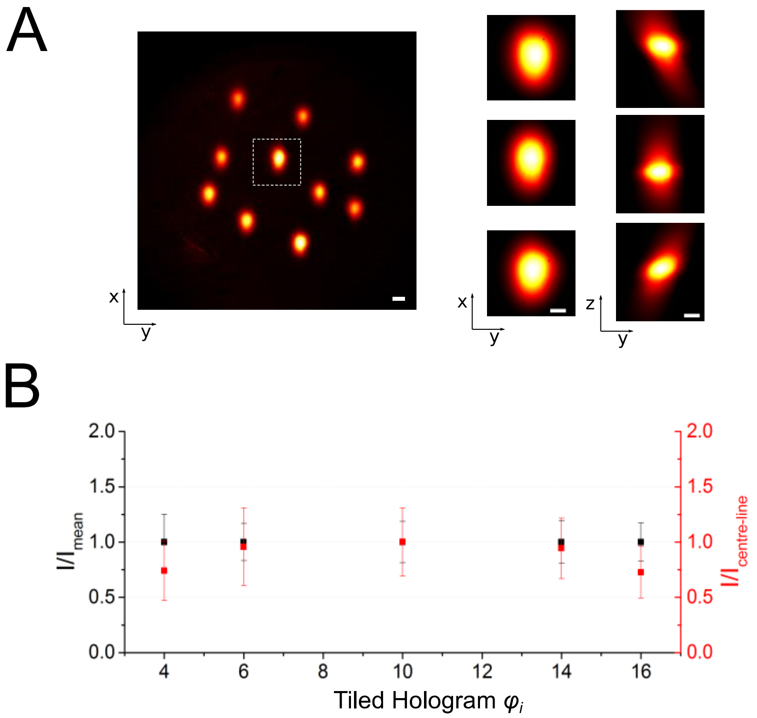

Supplementary Figure 3: Intensity distribution of groups of spots randomly distributed in the field of excitation generated by tiled holograms at different vertical position of the LC-SLM. (A) (Left) Representative distribution of multiple spots encoded with the hologram φ10. Scale bar 10μm. (Right) xy and xz projections of the central spot encoded by φ4 (Top), φ10 (Middle) and φ16 (Bottom). Scale Bar 5μm. (B) Intensity distribution of 10 random spots arranged as in (A) within (black axis) and between (red axis) the field of excitation (FoE) of different holograms φi encoded on different tiles i of the LC-SLM. Black symbols indicate per each hologram φi, normalized Mean ± SD of the ratios between the intensity I of each spot and the averaged spot intensity Imean within the FoE of φi. Red symbols indicate per each hologram φi, normalized Mean ± SD of the ratios between the intensity of each spot and the intensity of the same spot encoded by the central hologram φ10. Each hologram was 30x800 pixels, i.e. the LC-SLM was tiled into 20 regions.

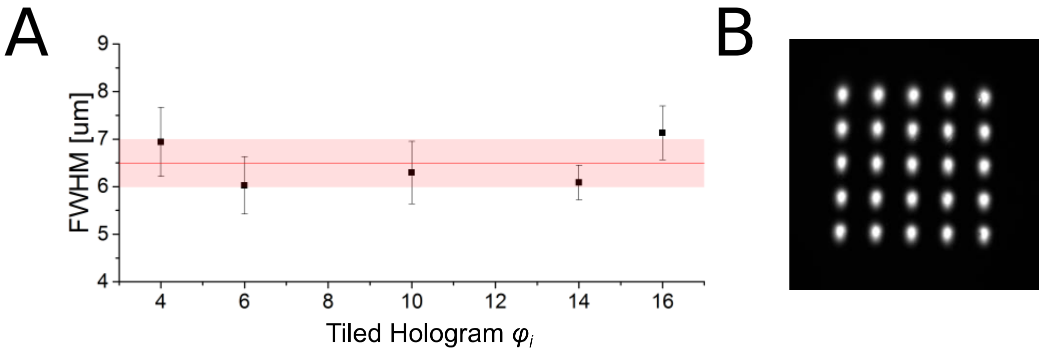

Supplementary Figure 4: Axial FWHM of multiplexed spots generated by different tiled holograms of the LC-SLM (A) Axial intensity FWHM of individual spots distributed in a matrix as in (B) and generated by different holograms φi. Black symbols indicate Mean ± SD of FWHM per each holograms φi. Red line and reddish band indicates the global mean and SD over the different φi, respectively. (B) Representative distribution of spots generated by hologram φ10.

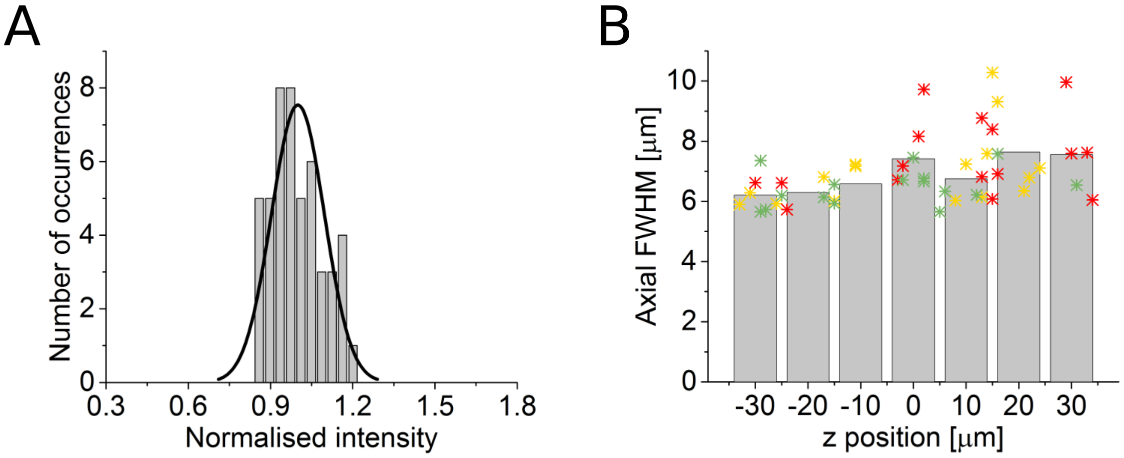

Supplementary Figure 5: Intensity distribution and axial FWHM of multiplexed spots generated by different tiled holograms of the SLM in a 3D volume. (A) Histogram of the maximal 2PE fluorescence intensity for each spot, normalized to the average intensity of all spots, after diffraction efficiency correction (48 spots randomly distributed in a 120x120x70 μm^3). (B) Axial confinement, calculated as the FWHM of the axial intensity profile of each spot (48 spots randomly distributed in 120x120x70 μm^3). Stars indicate FWHM of each spot. Different colors indicate spots encoded by different tiled holograms φi (hologram φ4, yellow; hologram φ10, red; and hologram φ16, green). Grey bars indicate the mean values in 10 μm range around the designated z position. SLM subdivided in 20 tiled holograms.

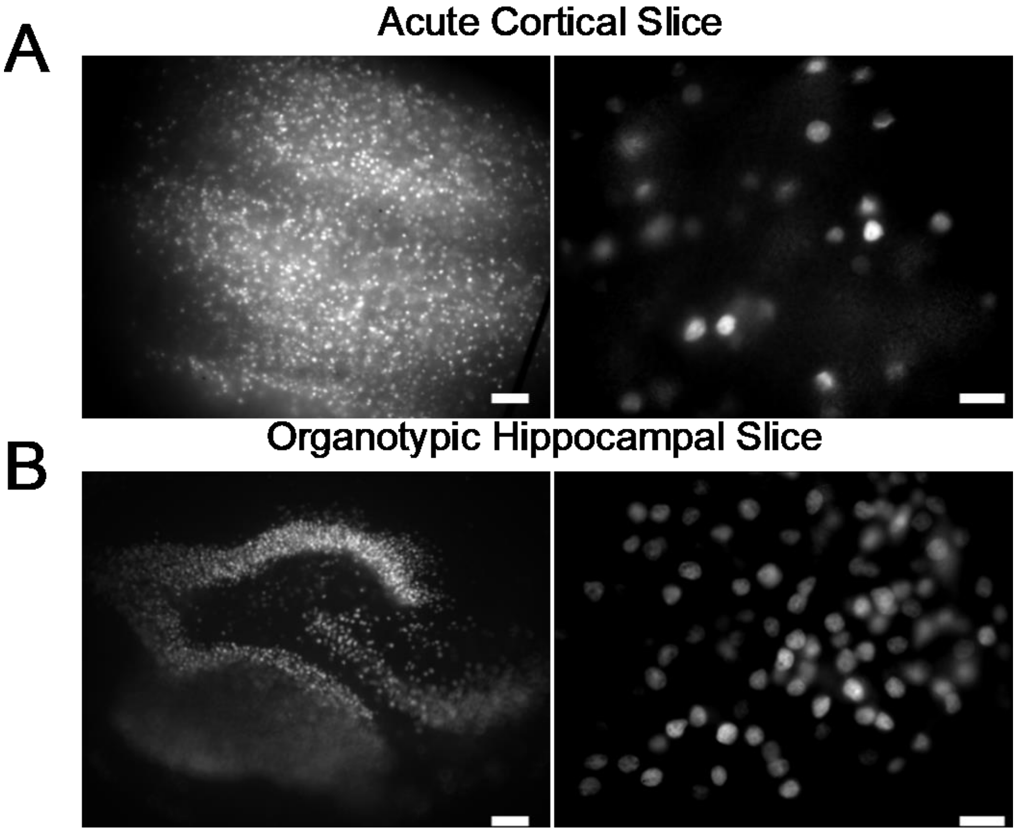

Supplementary Figure 6: ST-ChroME expression.(A) Widefield fluorescence images of ST-ChroME-positive cells in an acute cortical slice and (B) in an organotypic hippocampal slice. 300µm-thick slices. Left panels: scale bar 100µm. Right panels: scale bar 20µm.

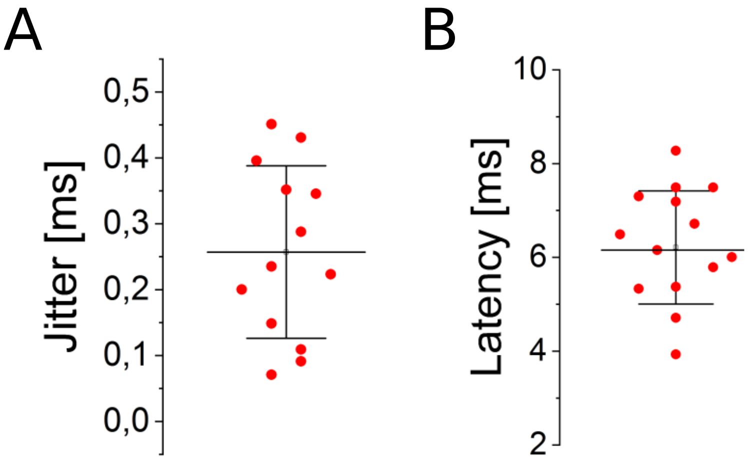

Supplementary Figure 7: Action potential jitter and latency upon soma-targeted 2PE photostimulation. (A) AP jitter and (B) latency for different ST-ChroME-expressing patched cells in acute cortical slices illuminated for 4-5ms dwell-time with a soma-targeted spot. Mean jitter is 0.25 ± 0.13 ms and mean latency is 6.2 ± 1.2 ms. Mean power 30.5 ± 13.6 mW. Different circles indicate different cells (n = 13). Data are shown as mean ± SD. 1030nm illumination has been used.

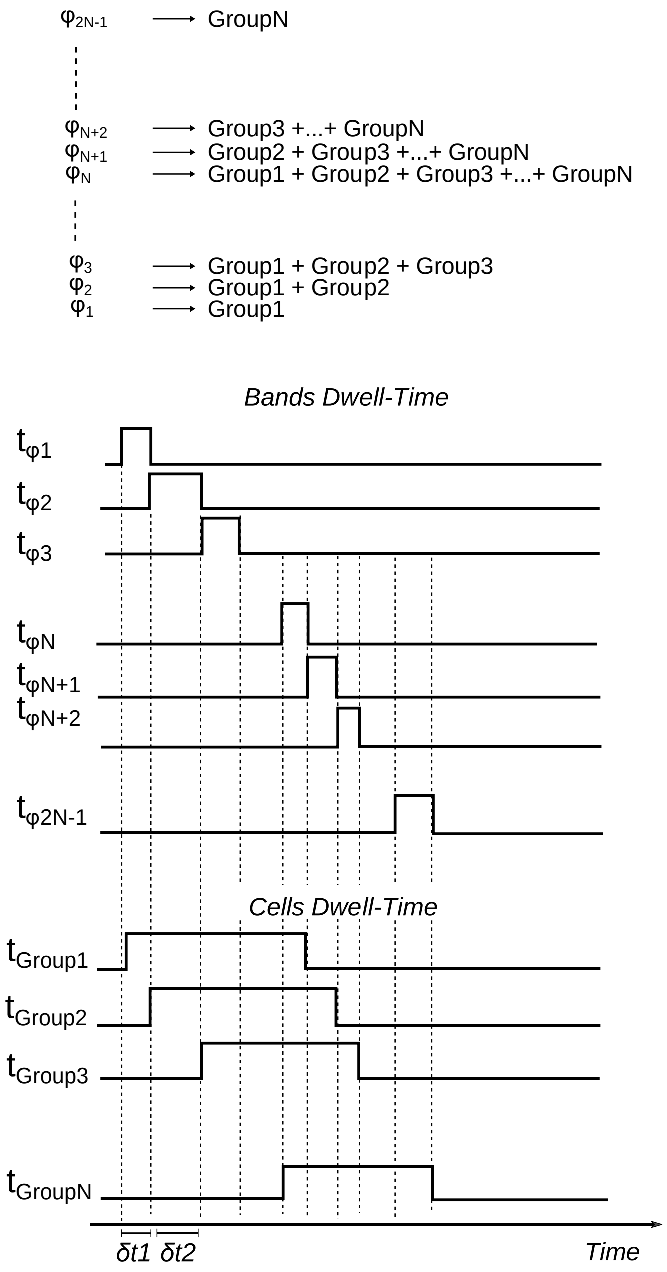

Supplementary Figure 8: FLiT configuration to desynchronize n groups of neurons with delays inferior to each activation dwell-time (A) Scheme of the disposition of the tiled holograms φi enabling to desynchronize n groups of neurons with delays δti inferior to each activation dwell time. The LC-SLM is divided in $2n-1$ *tiled holograms, each encoding to target different pools of neurons, such that the n different groups of neurons are photostimulated individually or in parallel on the basis of their activation chronological order as depicted in (B). (B) Time flow of the activation of the n different groups of neurons. Of note, power needs to be adapted on each tiled hologram such that each groups of neurons are constantly illuminated during their activation interval.*

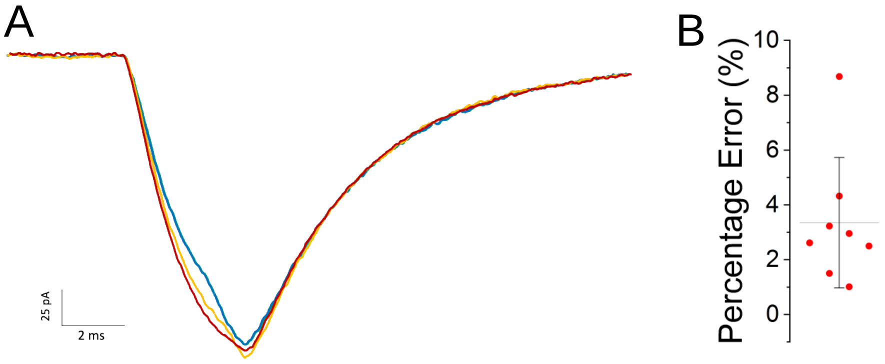

Supplementary Figure 9: Light-induced currents during switch between the different holograms. (A) Representative photocurrents from a ST-ChroME-expressing neuron when illuminated for 6ms with a single spot encoded by a single tiled hologram φi (red line) or by switching between three adjacent tiled holograms, each encoding the same spot, with different dwell time per holograms (blue line: φi=2ms + φi+1=2ms + φi+2=2ms; green line: φi=1ms + φi+1=4ms + φi+2=1ms; yellow line: φi=3ms + φi+1=2ms + φi+2=1ms). The SLM was here subdivided in 20 tiled holograms. (B) Amplitude percentage error between photocurrents induced using φi for 6ms (red in panel A) or by switching between the 3 different tiled holograms each for 2ms (i.e., φi=2ms, φi+1=2ms, φi+2=2ms, blue in panel A). Different circles represent different cells. Mean 3.35 ± 2.38 %. n = 8 cells. Incoming illumination power was maintained constant during the switches.

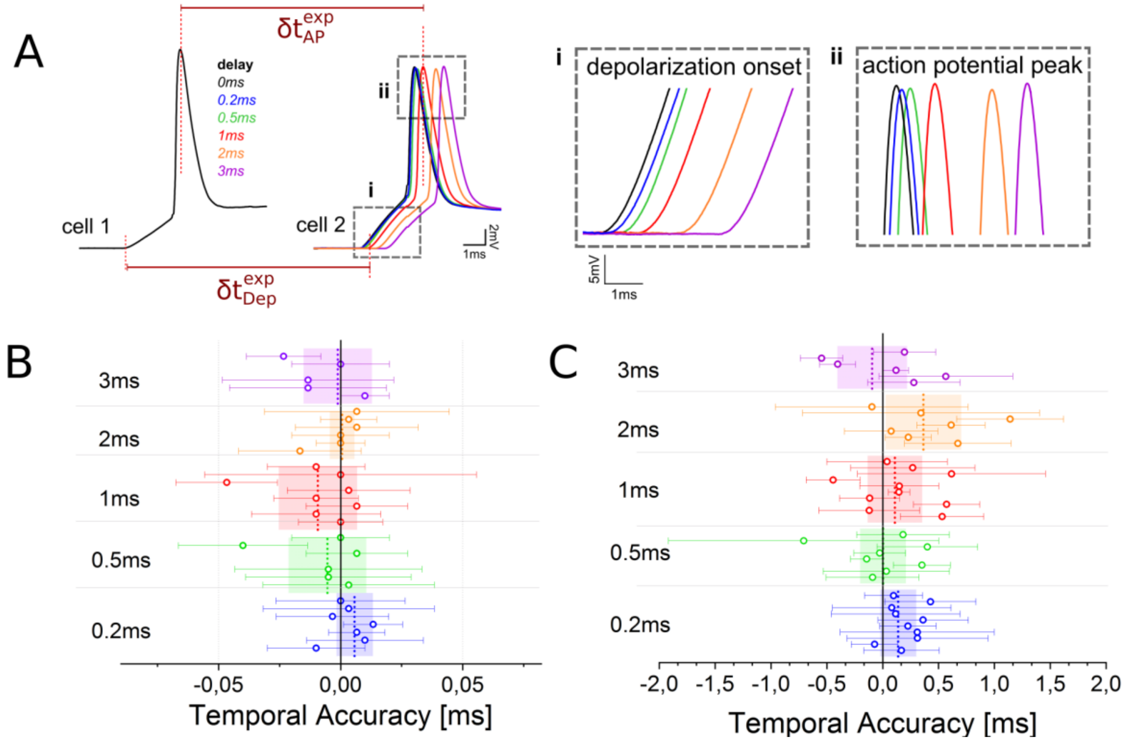

Supplementary Figure 10: Temporal accuracy of FLiT driven delays. (A) Representative traces from two ST-ChroME-expressing patched neurons illuminated with soma-targeted beams with delays δt between 0.2 and 3ms. Experimental AP peak δt_{AP}^{exp} and depolarization onset δt_{Dep}^{exp} delays are highlighted. (B-C) Temporal accuracy of depolarization (B) and AP occurrences (C) calculated for different couple of cells as $|\delta t_{AP}^{exp} - \delta t|$, and $|\delta t_{Dep}^{exp} - \delta t|$, respectively. Different circles correspond to different pairs of cells. Data are shown as mean $\pm$ SD. Different colors correspond to different delays. Vertical dashed lines and bands indicate average and SD temporal accuracy of all pairs of cells activated with the same delay time. Global mean depolarization accuracy is 1.4 ± 5.1 µs and mean AP accuracy is 96 ± 114 µs (n = 12 pair of cells). Mean photostimulation power is 36.8 ± 20.9 mW. Illumination dwell-time ranges between and 4-5ms. 1030nm illumination has been used.

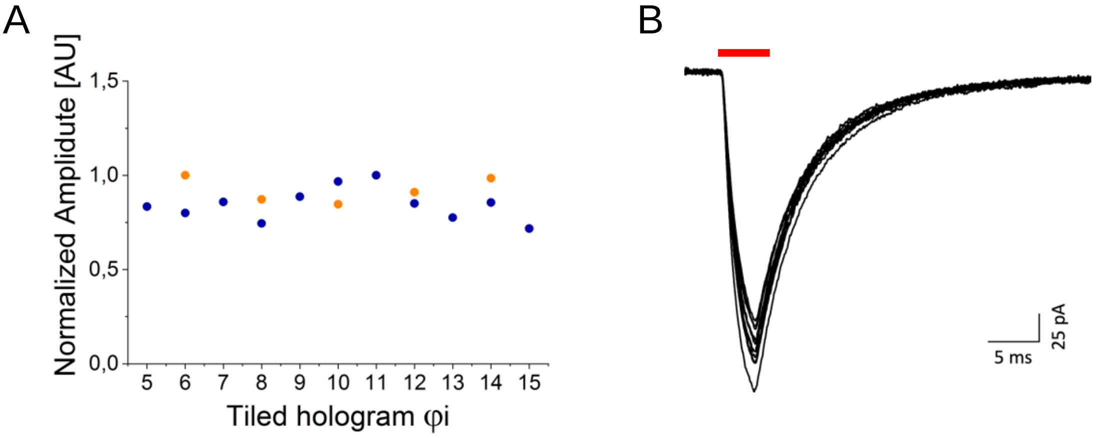

Supplementary Figure 11: Photocurrents induced by different tiled holograms. (A) Photocurrent amplitude evoked in the same ST-ChroME-expressing cell by illuminating with a spot encoded by different tiled holograms φi (n=2 cells). (B) Representative photocurrents from a ST-ChroME-expressing patched neuron when illuminated for 5ms with a spot encoded by the tiled hologram φ10. The SLM was here subdivided in 20 tiled holograms.

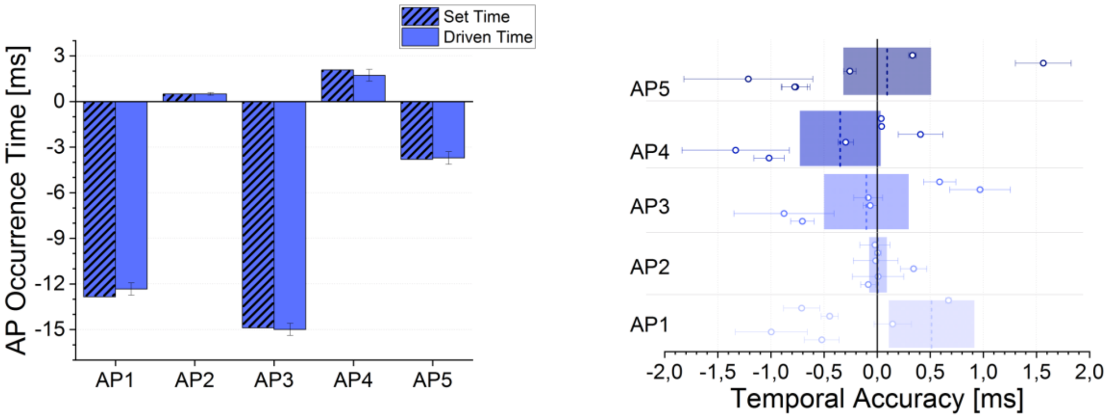

Supplementary Figure 12: Mimicking of spiking activity. AP occurrence time (left) and Temporal precision (right) between imposed and experimental delays of AP peaks for different pairs of double-patched ST-ChroME-expressing cells driven to mimic two independent random patterns of firing as depicted in Fig. 3D. Global mean temporal accuracy is 11 ± 112 µs (n = 12 pair of cells). Mean photostimulation power is 39.8 ± 21.9 mW. Illumination dwell-time ranges between and 2-5ms. 1030nm illumination has been used.

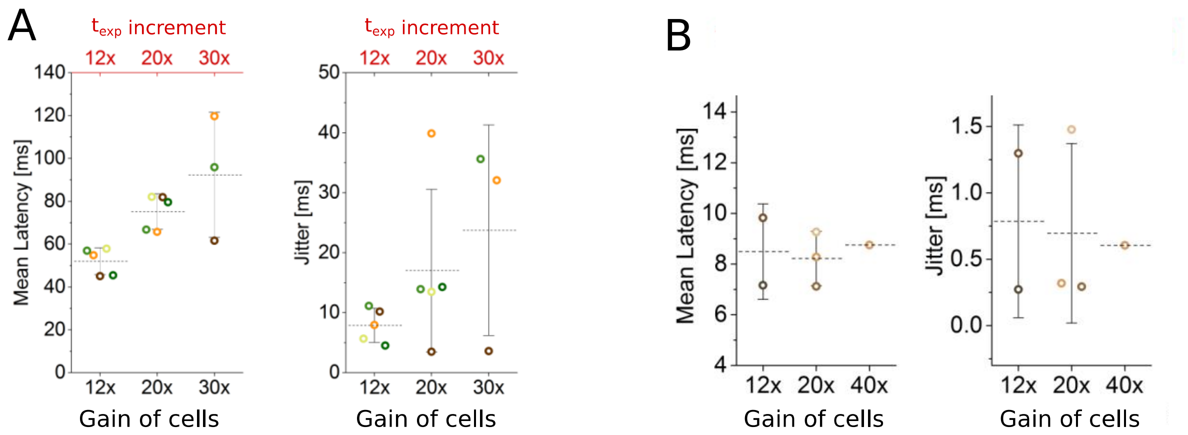

Supplementary Figure 13: Jitter and latency of light-evoked AP under Multi-S/P cyclic illumination.(A) Mean latency and jitter of the light-evoked APs obtained in Multi-S/P for different increment of power and total experimental time t_{exp} *compared to steady illumination. Different colors indicate different cells. Inset represents threshold power to activate the cells under steady illumination with* $t_{std} = 5ms$. *Global latency for gain 12x: 50.9 ± 8.6 ms; gain 20x: 76.3 ± 15.4 ms; gain 30x: 95.0 ± 33.6 ms and jitter for gain 12x: 7.9 ± 2.5 ms; gain 20x: 17 ± 12.1 ms; gain 30x: 23.8 ± 14.3 ms. (B) Mean latency and jitter of the light-evoked APs obtained in Multi-S/P for different increment of power compared to steady illumination when experimental time* $t_{exp}^{cyc} =$ *5ms. Global latency for gain 12x: 8,5 ± 1,5 ms; gain 20x: 8,2 ± 1,1 ms; gain 40x: 8,8 ± 0,5 ms and jitter for gain 12x: 0,8 ± 0,5 ms; gain 20x: 0,7 ± 0,6 ms; gain 40x: 0.6 ms. Different colors indicate different cells. Inset represents threshold power to activate the cells under steady illumination with* $t_{std} = 5ms$.

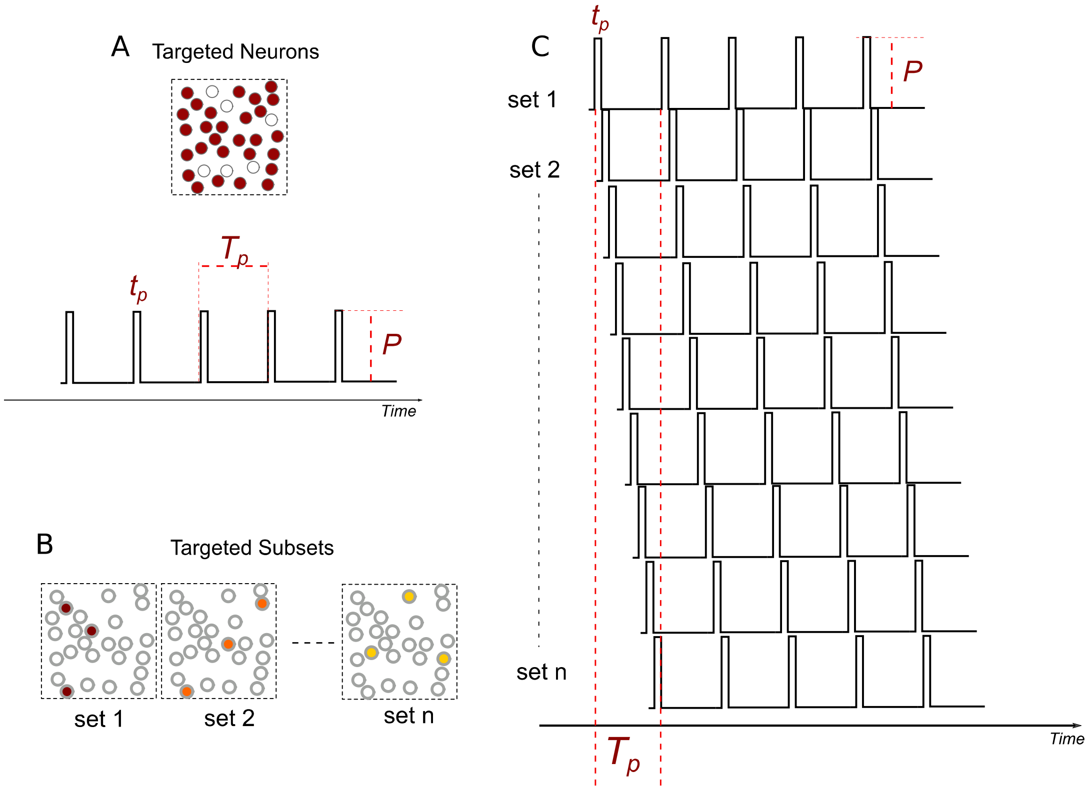

Supplementary Figure 14: Multi-S/P-FLiT applied to multi-cell activation based on train of ms-range light pulses. (A) Photostimulation protocol to activate a targeted group of neurons through a train of light pulses of duration tp and period Tp. (B) Subsets of the targeted group depicted in (A) encoded in different tiled holograms of an LC-SLM in FLiT configuration. (C) Multi-S/P-FLiT illumination protocol resulting by synchronizing the switch between different tiled holograms encoding for different subsets of neurons with the illumination duty-cycle of the pulse train in (A). Different rows correspond to the illumination cyclic occurring on different cell subsets.

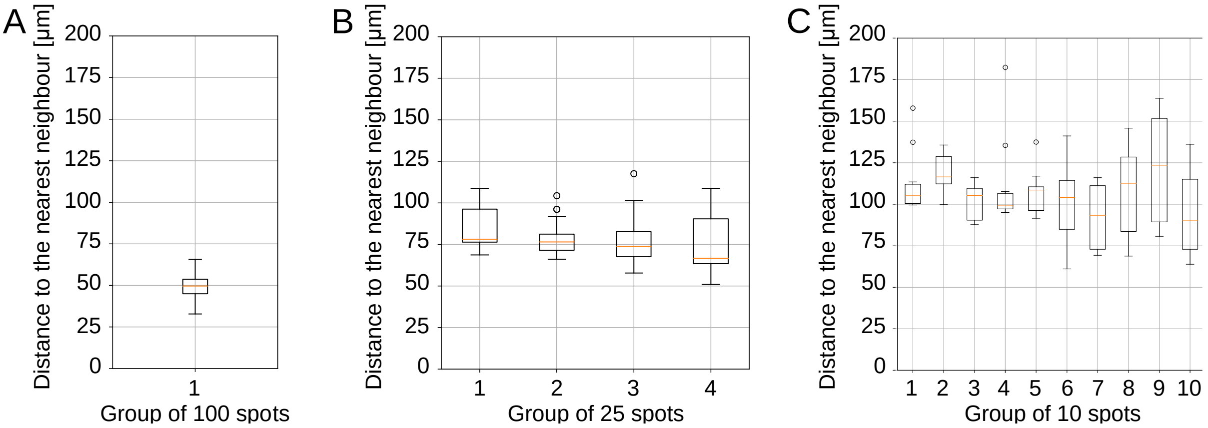

Supplementary Figure 15: Average distances of spots randomly distributed to maximize the nearest neighbors' distances. Average distance to the nearest neighbor for (A) 100 spots, (B) 10 subsets of 10 spots and (C) 4 subsets of 25 spots distributed in a 200x200x500 µm^3 volume.

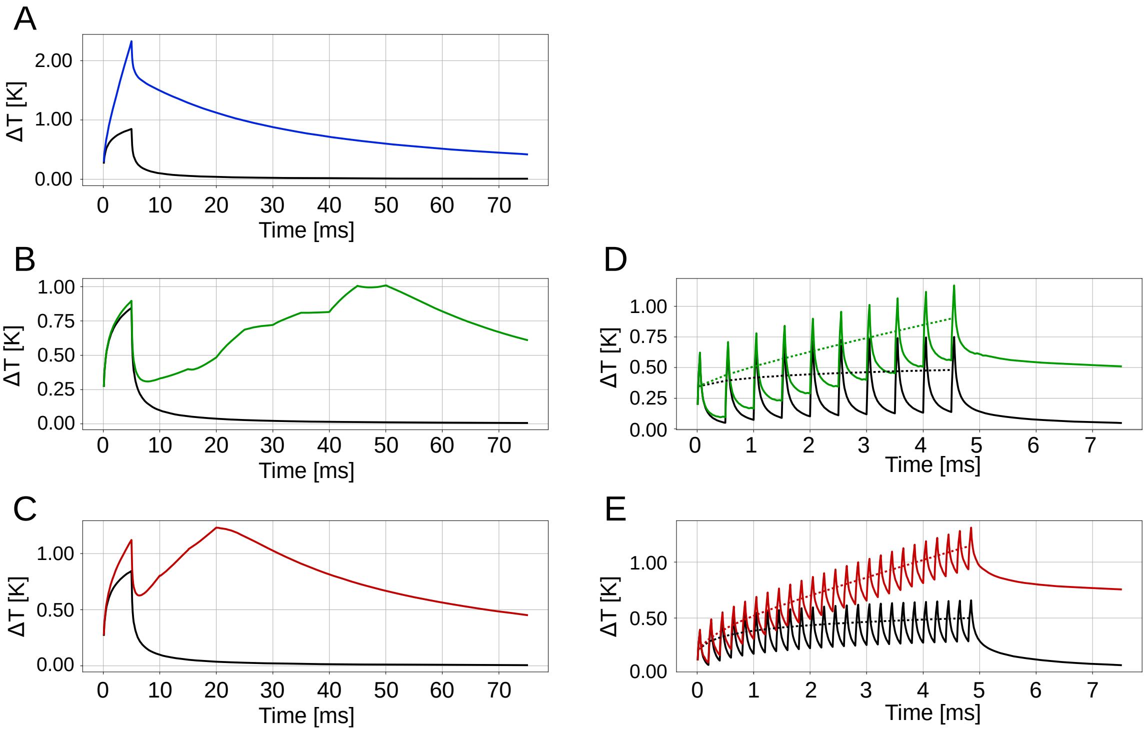

Supplementary Figure 16: Contribution of single and neighbors' spots to the rise of temperature induced by 100 spots distributed in a 200x200x500 µm^3. (A) Temperature rise averaged on a spot located at coordinate (0,0,0) when the spot in (0,0,0) is illuminated alone with $t_{std} = 5\ ms$ and $P_{std} = 20\ ms$ (black line) or together with 99 neighboring spots randomly distributed in a 200x200x500 µm^3 as described in Fig.5, with $t_{std} = 5ms$ and power per spot $P_{std} = 20\ ms$ (i.e., global power P = 2W) (blue line). (B-C) Same as A but by sequentially illuminating the 100 spots with n=10 subsets of 10 spots (green line) (B) or n=4 subsets of 25 spots (red line) (C) each illuminated for a time $t_{std} = 5\ ms$. (D-E) Same as A but by cyclically illuminating the 100 spots with n=10 subsets of spots for a t_{exp} = 5ms (t_{cyc} = 50 µs; N_{cyc} = 10) and global power per subset $P = 10\sqrt{10} \cdot P_{std}$ (green line) (D) and n=4 subsets of spots for a t_{exp} = 5ms (t_{cyc} = 50 µs; N_{cyc} = 25) and global power per subset $P = 25\sqrt{4} \cdot P_{std}$ (red line) (E). For sequential and cyclic illumination, the spot located in (0,0,0) was part of the first subset illuminated.

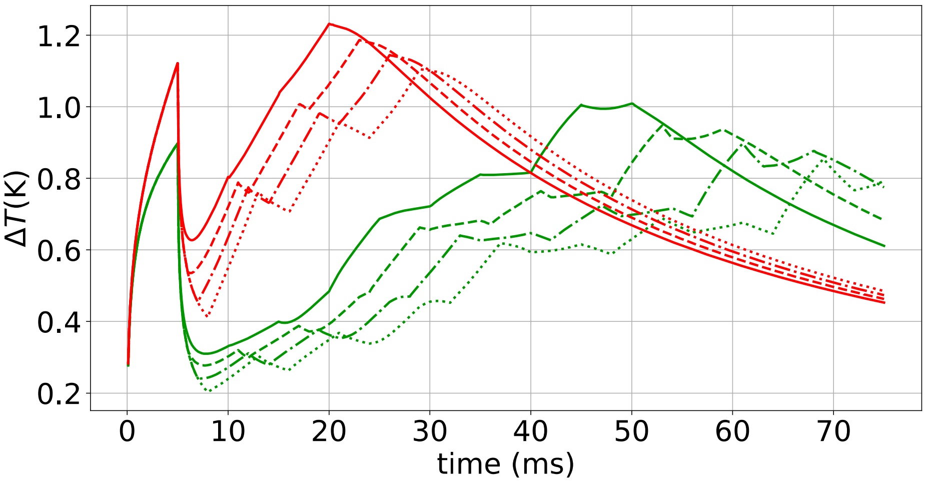

Supplementary Figure 17: Temperature rise induced by delayed sequential illumination of different subsets of spots. Temperature rise averaged on a spot located in (0,0,0) induced by sequentially illuminating 100 spots with n=4 subsets of 25 spots (red lines) or n=10 subsets of 10 spots (green lines) each illuminated for a time $t_{std} = 5\,ms$ *when a fixed delay* t_m *is introduced between the illumination of the different subsets (solid lines* $t_m = 0$*; dashed lines* $t_m = 1ms$*; dashed and dots lines* $t_m = 2$*; dots lines* $t_m = 3\,ms$*).*

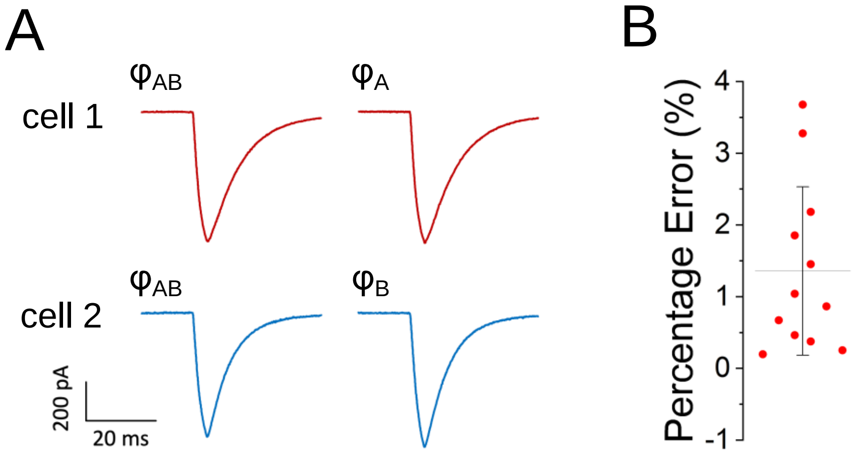

Supplementary Figure 18:Photo-evoked currents during S/P-FliT experiment. (A) Representative traces of induced photocurrents in double patched neurons (cell A, red; cell B, blue), when illuminated for 5 ms with a spot encoded by tiled hologram ϕAB (targeting both cells), ϕA (targeting cell A) and ϕB (targeting cell B) and optimizing the illumination power. (B) Percentage error of amplitude of induced photocurrents using ϕAB versus ϕA or ϕB. Different circle represents different cells. Mean 1.36 ± 1.17 % (n = 12 cells).

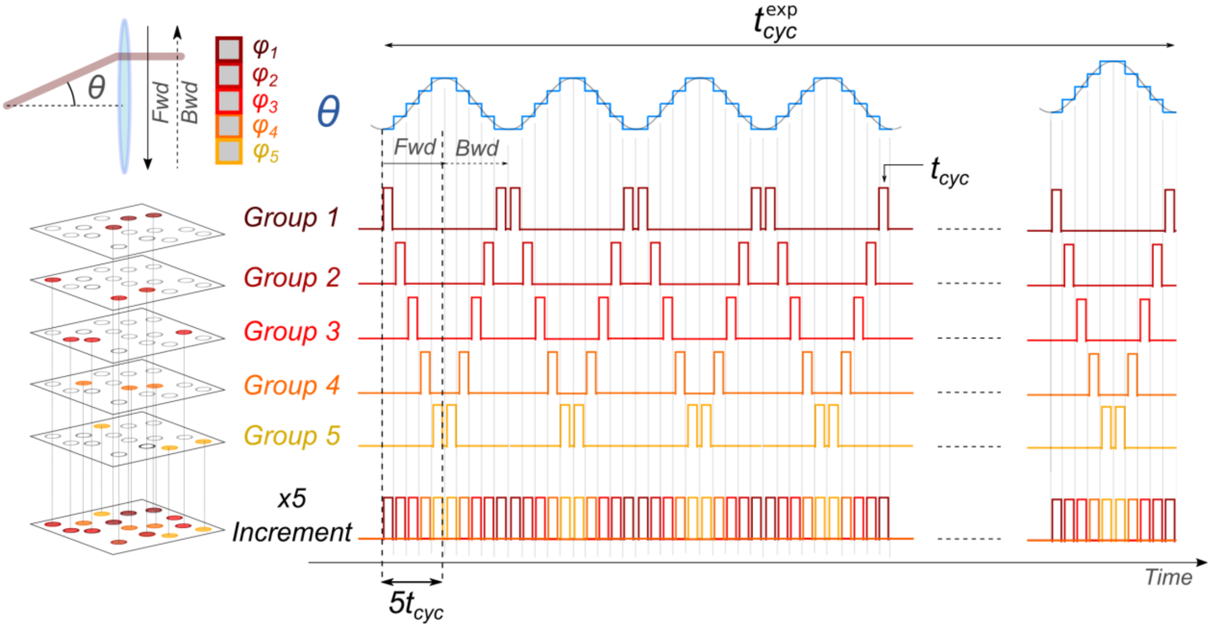

Supplementary Figure 19: Multi-S/P FLiT illumination protocol. The LC-SLM is tiled in n different tiled holograms φi, each encoding for different groups of cells (in the present scheme from 1 to 5). The laser is continuously steered back and forward across the LC-SLM by varying the deflection angle θ *of the galvanometric mirror following a staircase input voltage. Each hologram is illuminated for a dwell time tcyc over one cycle whose duration correspond to* $n \cdot t_{cyc}$ *(in the present scheme corresponding to 5tcyc) for a total duration* t_{exp}^{cyc}*. The scheme displayed is meant to represent n groups of spots; their number is here limited to 5 for presentation purposes only.*

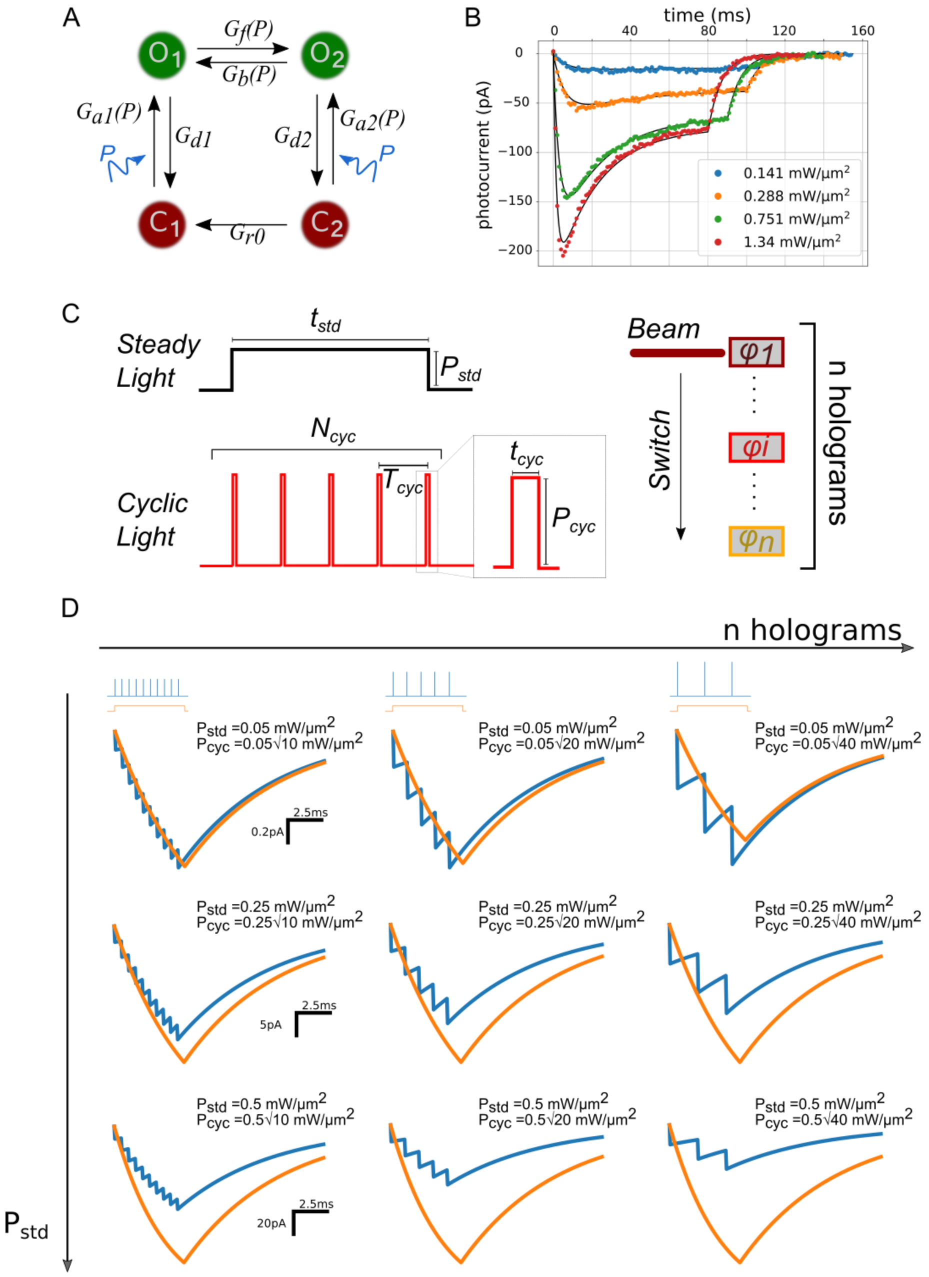

Supplementary Figure 20: Simulated photocurrents under steady and cyclic illumination. (A) Scheme of four-state model with $G_{a1}(P)$, $G_{a2}(P)$, G_{d1}, G_{d2}, $G_f(P)$, $G_b(P)$ and G_r indicating the rate constants for transitions $C_1 \rightarrow O_1$, $C_2 \rightarrow O_2$, $O_1 \rightarrow C_1$, $O_2 \rightarrow C_2$, $O_1 \rightarrow O_2$, $O_2 \rightarrow O_1$ and $C_2 \rightarrow C_1$, respectively. (B) Fitting of experimental photocurrent traces obtained by photostimulating a ST-ChroME-expressing neuron for different light intensities. (C) Scheme of photostimulation under steady illumination of power P_{std} and duration t_{std} and under cyclic illumination of power P_{cyc} and pulse duration t_{cyc} over N_{cyc} cycles. (D) Simulated photocurrents of a light-targeted neuron in the approximation of a four-state model under 2PE steady illumination (orange) or cyclic illumination with $P_{cyc} = P_{std}\sqrt{n}$ (blue) for different values of illumination power and number of holograms $n = T_{cyc}/t_{cyc}$.

SUPPLEMENTARY MOVIES:

Supplementary Movie 1: Alternation of different groups of spots in FLiT.

Different groups of spots are alternated by sequentially tilting the galvanometric mirror on different tiled holograms φ_i of the multiplexing LC-SLM, each encoding for different 2D patterns. The LC-SLM was subdivided into 10 different tiled holograms. The tiled holograms were updated after scanning the entire LC-SLM by automatically refreshing the LC-SLM with new phase masks. FoV is 150x150 µm^2. Time per frame 20 ms.

Supplementary Movie 2: Time lapse of the 3D distribution of the temperature rise during sequential illumination with *n* subsets of spots.

From left to right: Temperature rise induced by steadily illuminating one set of 100 spots in parallel as shown in Fig. 5C (blue line) with $t_{exp} = t_{std}$=5ms and global power $P = 100 \cdot P_{std}$ (with P_{std} =20mW); Temperature rise induced by steadily illuminating the 100 spots in sequence with n=4 subsets of spots as shown in Fig.5C (red line) with t_{exp}=20ms and global power per subset $P = 25 \cdot P_{std}$; Temperature rise induced by steadily illuminating the 100 spots in sequence with n=10 subsets of spots as shown in Fig. 5C (green line) with t_{exp}=50ms and global power per subset $P = 10 \cdot P_{std}$; Temperature rise induced by illuminating one spot individually under steady illumination for $t_{exp} = t_{std}$=5ms as shown in Fig.5C (black line).

Supplementary Movie 3: Time lapse of the 3D distribution of the temperature rise during cyclic illumination with *n* subsets of spots.

From left to right: Temperature rise induced by cyclically illuminating 100 spots as shown in Fig.5D (red line) with n=4 subsets of spots for a t_{exp}=5ms (t_{cyc}=50µs; N_{cyc}=25) and global power per subset $P = 25\sqrt{4} \cdot P_{std}$; Temperature rise induced by cyclically illuminating 100 spots as shown in Fig.5D (green line) with n=10 subsets of spots for a t_{exp}=5ms (t_{cyc}=50µs; N_{cyc}=10) and global power per subset $P = 10\sqrt{10} \cdot P_{std}$; Temperature rise induced by illuminating one spot individually.

REFERENCES

1. Yizhar, O., Fenno, L. E., Davidson, T. J., Mogri, M. & Deisseroth, K. Optogenetics in neural systems. *Neuron* **71**, 9–34 (2011).

2. Fenno, L., Yizhar, O. & Deisseroth, K. The Development and Application of Optogenetics. *Annu. Rev. Neurosci.* **34**, 389–412 (2011).

3. Chen, I.-W., Papagiakoumou, E. & Emiliani, V. Towards circuit optogenetics. *Curr. Opin. Neurobiol.* **50**, 179–189 (2018).

4. Rickgauer, J. P. & Tank, D. W. Two-photon excitation of channelrhodopsin-2 at saturation. *Proc. Natl. Acad. Sci. U. S. A.* **106**, 15025–30 (2009).

5. Ronzitti, E., Emiliani, V. & Papagiakoumou, E. Methods for Three-Dimensional All-Optical Manipulation of Neural Circuits. *Front. Cell. Neurosci.* **12**, 469 (2018).

6. Accanto, N. *et al.* Multiplexed temporally focused light shaping for high-resolution multi-cell targeting. *Optica* **5**, 1478 (2018).

7. Pégard, N. C. *et al.* Three-dimensional scanless holographic optogenetics with temporal focusing (3D-SHOT). *Nat. Commun.* **8**, 1228 (2017).

8. Baker, C. A., Elyada, Y. M., Parra-Martin, A. & Bolton, M. Cellular resolution circuit mapping in mouse brain with temporal-focused excitation of soma-targeted channelrhodopsin. *Elife* **5**, 1–15 (2016).

9. Shemesh, O. A. *et al.* Temporally precise single-cell-resolution optogenetics. *Nat. Neurosci.* **20**, 1796–1806 (2017).

10. Mardinly, A. R. *et al.* Precise multimodal optical control of neural ensemble activity. *Nat. Neurosci.* **21**, 881–893 (2018).

11. Marshel, J. H. *et al.* Cortical layer–specific critical dynamics triggering perception. *Science (80-.).* (2019). doi:10.1126/science.aaw5202

12. Carrillo-Reid, L., Han, S., Yang, W., Akrouh, A. & Yuste, R. Controlling Visually Guided Behavior by Holographic Recalling of Cortical Ensembles. *Cell* **178**, 447-457.e5 (2019).

13. McRaven, C. *et al.* High-throughput cellular-resolution synaptic connectivity mapping in vivo with concurrent two-photon optogenetics and volumetric Ca 2+ imaging. 1–27 (2020). doi:10.1101/2020.02.21.959650

14. Spampinato, G. *et al.* All-optical interrogation of a direction selective retinal circuit by holographic wave front shaping. *bioRxiv* 1–36 (2019). doi:10.1101/513192

15. Chettih, S. N. & Harvey, C. D. Single-neuron perturbations reveal feature-specific competition in V1. *Nature* (2019). doi:10.1038/s41586-019-0997-6

16. Gill, J. V. *et al.* Precise Holographic Manipulation of Olfactory Circuits Reveals Coding Features Determining Perceptual Detection. *Neuron* **108**, 382–393 (2020).

17. Ronzitti, E. *et al.* Recent advances in patterned photostimulation for optogenetics. *Journal of Optics* (2017).

18. Papagiakoumou, E., Ronzitti, E. & Emiliani, V. Scanless two-photon excitation with temporal focusing. *Nat. Methods* **17**, 571–581 (2020).

19. Hernandez, O. *et al.* Three-dimensional spatiotemporal focusing of holographic patterns. *Nat. Commun.* **7**, 11928 (2016).

20. Sun, B. *et al.* Four-dimensional light shaping : manipulating ultrafast spatio-temporal foci in space and time. *ArXiv* 1–14 (2017).

21. Chaigneau, E. *et al.* Two-Photon Holographic Stimulation of ReaChR. *Front. Cell. Neurosci.* **10**, 234 (2016).

22. Picot, A. *et al.* Temperature Rise under Two-Photon Optogenetic Brain Stimulation. *Cell Rep.* **24**, 1243-1253.e5 (2018).

23. Liu, C. & et al. ,. -*In Prep.*

24. Ronzitti, E. *et al.* Submillisecond Optogenetic Control of Neuronal Firing with Two-Photon Holographic Photoactivation of Chronos. *J. Neurosci.* **37**, 10679–10689 (2017).

25. Chen, I.-W. *et al.* In vivo sub-millisecond two-photon optogenetics with temporally focused patterned light . *J. Neurosci.* **39**, 1785–18 (2019).

26. Rickgauer, J. P., Deisseroth, K. & Tank, D. W. Simultaneous cellular-resolution optical perturbation and imaging of place cell firing fields. *Nature neuroscience* **17**, 1816–24 (2014).

27. Begue, A. *et al.* Two-photon excitation in scattering media by spatiotemporally shaped beams and their application in optogenetic stimulation. *Biomed Opt Express* **4**, 2869–2879 (2013).

28. Yang, W., Carrillo-Reid, L., Bando, Y., Peterka, D. S. & and Yuste, R. Simultaneous two-photon optogenetics and imaging of cortical circuits in three dimensions. *Elife* **7**, e32671 (2018).

29. Forli, A. *et al.* Two-Photon Bidirectional Control and Imaging of Neuronal Excitability with High Spatial Resolution In Vivo. *Cell Rep.* **22**, 3087–3098 (2018).

30. Lyall, E. H., Mossing, D. P., Pluta, S. R., Dudai, A. & Adesnik. Synthesis of higher order feature 1 codes through stimulus-specific supra-linear summation. *bioRxiv* 1–42 (2020).

31. Dan, Y. & Poo, M. Spike Timing-Dependent Plasticity of Neural Circuits. *Neuron* **44**, 23–30 (2004).

32. Froemke, R. C. & Dan, Y. Spike-timing-dependent synaptic modification induced by natural spike trains. *Nature* (2002). doi:10.1038/416433a

33. Markram, H., Lu, J., Frotscher, M. & Sakmann, B. Regulation of Synaptic Efficacy by Coincidence of Postsynaptic APs and EPSPs. *Science (80-.).* **275**, 213–215 (1997).

34. Udakis, M., Pedrosa, V., Chamberlain, S. E. L., Clopath, C. & Mellor, J. R. Interneuron-specific plasticity at parvalbumin and somatostatin inhibitory synapses onto CA1 pyramidal neurons shapes hippocampal output. *Nat. Commun.* **11**, (2020).

35. Tazerart, S., Mitchell, D. E., Miranda-Rottmann, S. & Araya, R. A spike-timing-dependent plasticity rule for dendritic spines. *Nat. Commun.* (2020). doi:10.1038/s41467-020-17861-7

36. Di Lorenzo, F. *et al.* Impaired Spike Timing Dependent Cortico-Cortical Plasticity in Alzheimer's Disease Patients. *J. Alzheimer's Dis.* (2018). doi:10.3233/JAD-180503

37. Feldman, D. E. The Spike-Timing Dependence of Plasticity. *Neuron* **75**, 556–571 (2012).

38. Chong, E. *et al.* Manipulating synthetic optogenetic odors reveals the coding logic of olfactory perception. *Science (80-.).* **368**, (2020).

39. Klapoetke, N. C. *et al.* Independent optical excitation of distinct neural populations. *Nat. Methods* **11**, 338–46 (2014).

40. Yang, W., Carrillo-Reid, L., Bando, Y., Peterka, D. S. & Yuste, R. Simultaneous two-photon imaging and two-photon optogenetics of cortical circuits in three dimensions. *Elife* **7**, e32671 (2018).

41. Chen, I.-W. *et al.* Parallel holographic illumination enables sub-millisecond two-photon optogenetic

activation in mouse visual cortex in vivo. *BioArxiv* (2018). doi:10.1101/250795

42. Parot, V. J., Nichols, S., Testa-Silva, G. & Cohen, A. E. Microsecond Timescale Selective Access Two-photon Targeting for Functional Measurements in Tissue. in *Biophotonics Congress: Biomedical Optics 2020(Translational, Microscopy, OCT, OTS, BRAIN)* (2020).

43. Wijesinghe, P., Escobet-Montalbán, A., Chen, M., Munro, P. R. T. & Dholakia, K. Optimal compressive multiphoton imaging at depth using single-pixel detection. *Opt. Lett.* **44**, 4981 (2019).

44. Ji, N., Freeman, J. & Smith, S. L. Technologies for imaging neural activity in large volumes. *Nature Neuroscience* **19**, 1154–1164 (2016).

45. Lutz, C. *et al.* Holographic photolysis of caged neurotransmitters. *Nat. Methods* **5**, 821–7 (2008).

46. Gerchberg, R. W. & Saxton, W. O. A pratical algorithm for the determination of the phase from image and diffraction pictures. *Optik (Stuttg).* **35**, 237–246 (1972).

47. Hernandez, O. *et al.* Three-dimensional spatiotemporal focusing of holographic patterns. *Nat. Commun.* **7**, 11928 (2016).

48. Gähwiler, B. H., Capogna, M., Debanne, D., McKinney, R. A. & Thompson, S. M. Organotypic slice cultures: A technique has come of age. *Trends Neurosci.* **20**, 471–477 (1997).

49. Fourier, J. B. J. *Theorie Analytique de la Chaleur*. (1822).

50. Evans, B. D., Jarvis, S., Schultz, S. R. & Nikolic, K. PyRhO: A Multiscale Optogenetics Simulation Platform. *Front. Neuroinform.* **10**, 8 (2016).

51. Bansal, H., Gupta, N. & Roy, S. Theoretical Analysis of Low-power Bidirectional Optogenetic Control of High-frequency Neural Codes with Single Spike Resolution. *Neuroscience* **449**, 165–188 (2020).

52. Grossman, N. *et al.* The spatial pattern of light determines the kinetics and modulates backpropagation of optogenetic action potentials. *J. Comput. Neurosci.* **34**, 477–488 (2013).

53. Nikolic, K. *et al.* Photocycles of channelrhodopsin-2. *Photochem. Photobiol.* **85**, 400–411 (2009).

Chapter 7: Conclusions

This doctoral work aimed to develop new advance optical systems for optogenetics application.

Three new approaches were presented in this work, each solving different limitations for light delivery in Neurobiology experiments:

(1) Multiplexed temporally focused light shaping for multiple target excitation with single-cell resolution in a three-dimensional volume.

(2) Multiplexed temporally focused endoscopy for structured photostimulation of deep brain regions

(3) Ultra-fast sequential light targeting for fast sequential light shaping.

Understanding how the brain works involves the manipulation of neuronal circuits in 3D. Towards this objective, a previous system with temporal focusing approach was developed in the lab (Hernandez et al., 2016) Nevertheless, the number of z plans accessible at the same time was limited (~ 6 plans). Therefore, I have developed a new system combining 3D light shaping with temporal focusing. This new configuration is flexible and allows to easily change the optical configurations to use different light shaping approaches. Using computer-generated holography (CGH) and generated phase contrast (GPC) as a light patterning method, we demonstrated this flexibility. Nevertheless, those approaches (CGH/GPC+TF) were limited to replicating the same pattern in 3D. Therefore, we proposed a third configuration capable of generating different patterns simultaneously (~ 6 different patterns) by tiling the SLM2. We established our system's precision and 3D capability *in vivo* in drosophila larva and zebrafish by photoconverting targeted neuronal cells in densely packed ensembles. This optical system coupled with actuators and/or calcium/voltage sensors has a great potential for investigating 3D neural circuits. We could apply the multishape strategy to study different region of the brain were the cell morphology may vary, for instance, in the visual cortex (L1-L6).

Temporal focusing technique presents numerous advantages, notably reducing the scattering effect in tissue, enabling access to deeper regions ~500 µm. Unfortunately, this performance is not sufficient to reach deep brain regions in the mouse. For that reason, we developed a new microendoscope system where the previous configurations were coupled with a GRIN lens. By these means, we were able to generate multiple excitation spots in FOV of 150x150x400 μm^3. We confirm the potential of this approach with *in vivo experiments* in mouse primary visual cortex. By implanting the GRIN lens inside the brain, this new technique would permit to manipulate deeper brain regions, for instance, the study of memory in the hippocampus and mechanisms involved in locomotion from the cerebellum neural code in the mouse. In the current conditions of the imaging and photostimulation of neurons, the animal was head-restrained. Then, an interesting future development would be to add flexibility to the microendoscope using a fiber, allowing experiment with naturally behaved animals or freely-moving.

In the brain all neurons do not activate in synchronized hubs. In neuronal ensembles, one can observe a very short time delay between the activation of 2 single neurons. To replicate this delay activation between 2 targets, the holography approach was originally limited by the refreshing rate of the SLM. Standard SLM has a 30ms refreshing rate. However, new development ones can reach 1ms but it comes with an expensive budget. Hence, we proposed an alternative by introducing galvanometric mirrors to scan a line illumination over a tiling SLM. We used two patched cells to demonstrate our capacity to delay the activation up to sub milliseconds with fast sequential light shaping. During this work, we also demonstrated the possibility of optimizing the light illumination on multiple targets. Compared to the conventional holographic method, we could photo stimulate more neurons with the same laser power. This performance gain would permit all-optical investigation with less powerful lasers. Therefore, the possibility to realize an optogenetics experiment targeting several neurons in 3D would be accessible to a larger community. Ultrafast sequential light shaping is a promising tool for decrypting the temporal code of neural mechanisms.

References:

A Berndt, SY Lee, C Ramakrishnan, & K Deisseroth. (2014). Structure-guided transformation of channelrhodopsin into a light-activated chloride channel. *Science (New York, N.Y.)*, *344*(6182), 420–424. https://doi.org/10.1126/SCIENCE.1252367

A Matsuno-Yagi, & Y Mukohata. (1977). Two possible roles of bacteriorhodopsin; a comparative study of strains of Halobacterium halobium differing in pigmentation. *Biochemical and Biophysical Research Communications*, *78*(1), 237–243. https://doi.org/10.1016/0006-291X(77)91245-1

Aharoni, D., & Hoogland, T. M. (2019). Circuit Investigations With Open-Source Miniaturized Microscopes: Past, Present and Future. *Frontiers in Cellular Neuroscience*, *0*, 141. https://doi.org/10.3389/FNCEL.2019.00141

AM Packer, DS Peterka, JJ Hirtz, R Prakash, K Deisseroth, & R Yuste. (2012). Two-photon optogenetics of dendritic spines and neural circuits. *Nature Methods*, *9*(12), 1202–1205. https://doi.org/10.1038/NMETH.2249

Andrasfalvy, B. K., Zemelman, B. v, Tang, J., & Vaziri, A. (2010). Two-photon single-cell optogenetic control of neuronal activity by sculpted light. *Proceedings of the National Academy of Sciences of the United States of America*, *107*(26), 11981–11986. http://www.ncbi.nlm.nih.gov/entrez/query.fcgi?cmd=Retrieve&db=PubMed&dopt=Citation&list_uids=20543137

Aristotle. (1955). Aristotle: Parva Naturalia. *Aristotle: Parva Naturalia*. https://doi.org/10.1093/ACTRADE/9780198141082.BOOK.1

Bègue, A., Leshem, B., Oron, D., Papagiakoumou, E., Enke, L., Conti, R., & Emiliani, V. (2013). Two-photon excitation in scattering media by spatiotemporally shaped beams and their application in optogenetic stimulation. *Biomedical Optics Express, Vol. 4, Issue 12, Pp. 2869-2879*, *4*(12), 2869–2879. https://doi.org/10.1364/BOE.4.002869

Bègue, A., Papagiakoumou, E., Leshem, B., Conti, R., Enke, L., Oron, D., & Emiliani, V. (2013). Two-photon excitation in scattering media by spatiotemporally shaped beams and their application in optogenetic stimulation. *Biomedical Optics Express*, *4*(12), 2869–2879. http://www.osapublishing.org/viewmedia.cfm?uri=boe-4-12-2869&seq=0&html=true

Bommel, B., Konietzny, A., Kobler, O., Bär, J., & Mikhaylova, M. (2019). F-actin patches associated with glutamatergic synapses control positioning of dendritic lysosomes. *The EMBO Journal*, *38*(15). https://doi.org/10.15252/embj.2018101183

Booth, M. J. (2007). Adaptive optics in microscopy. In *Philosophical Transactions of the Royal Society A: Mathematical, Physical and Engineering Sciences* (Vol. 365, Issue 1861, pp. 2829–2843). Royal Society. https://doi.org/10.1098/rsta.2007.0013

Borzsonyi, A., Kovacs, A. P., & Osvay, K. (2013). What we can learn about ultrashort pulses by linear optical methods. In *Applied Sciences (Switzerland)* (Vol. 3, Issue 2, pp. 515–544). MDPI AG. https://doi.org/10.3390/app3020515

Bowman, R., D'Ambrosio, V., Rubino, E., Jedrkiewicz, O., di Trapani, P., & Padgett, M. J. (2011). Optimisation of a low cost SLM for diffraction efficiency and ghost order suppression. *The*

European Physical Journal Special Topics 2011 199:1, *199*(1), 149–158. https://doi.org/10.1140/EPJST/E2011-01510-4

BR Rost, F Schneider-Warme, D Schmitz, & P Hegemann. (2017). Optogenetic Tools for Subcellular Applications in Neuroscience. *Neuron*, *96*(3), 572–603. https://doi.org/10.1016/J.NEURON.2017.09.047

Chang, C., Xia, J., Yang, L., Lei, W., Yang, Z., & Chen, J. (2015). Speckle-suppressed phase-only holographic three-dimensional display based on double-constraint Gerchberg–Saxton algorithm. *Applied Optics*, *54*(23), 6994. https://doi.org/10.1364/ao.54.006994

Crick Francis. (1979). Thinking about the brain. *Scientific American*, *241*(3), 219–232. https://doi.org/10.1038/SCIENTIFICAMERICAN0979-219

Crick Francis, & Frs O M. (1999). *The impact of molecular biology on neuroscience*.

Curtis, J. E., Koss, B. A., & Grier, D. G. (2002). Dynamic holographic optical tweezers. *Optics Communications*, *207*(1–6), 169–175. https://doi.org/10.1016/S0030-4018(02)01524-9

Curtis, J. E., Schmitz, C. H. J., & Spatz, J. P. (2005a). Symmetry dependence of holograms for optical trapping. In *OPTICS LETTERS* (Vol. 30, Issue 16).

Curtis, J. E., Schmitz, C. H. J., & Spatz, J. P. (2005b). Symmetry dependence of holograms for optical trapping. *Opt. Lett.*, *30*(16), 2086–2088. https://doi.org/10.1364/OL.30.002086

D Oesterhelt, & W Stoeckenius. (1971). Rhodopsin-like protein from the purple membrane of Halobacterium halobium. *Nature: New Biology*, *233*(39), 149–152. https://doi.org/10.1038/NEWBIO233149A0

Dana, H., & Shoham, S. (2011). Numerical evaluation of temporal focusing characteristics in transparent and scattering media. *Optics Express, Vol. 19, Issue 6, Pp. 4937-4948*, *19*(6), 4937–4948. https://doi.org/10.1364/OE.19.004937

Dana, H., & Shoham, S. (2012). Numerical evaluation of temporal focusing characteristics in transparent and scattering media: erratum. *Optics Express, Vol. 20, Issue 27, Pp. 28281-28281*, *20*(27), 28281–28281. https://doi.org/10.1364/OE.20.028281

Das, B. B., Liu, F., & Alfano, R. R. (1997). Time-resolved fluorescence and photon migration studies in biomedical and model random media. In *Rep. Prog. Phys* (Vol. 60).

Denk, W., Strickler, J., & Webb, W. (1990). Two-photon laser scanning fluorescence microscopy. *Science*, *248*(4951), 73–76. https://doi.org/10.1126/SCIENCE.2321027

di Leonardo, R., Ianni, F., & Ruocco, G. (2007). Computer generation of optimal holograms for optical trap arrays. *Optics Express*, *15*(4), 1913. https://doi.org/10.1364/OE.15.001913

di Leonardo, R., Ianni, F., Ruocco, G., Leach, J., Sinclair, G., Jordan, P., Courtial, J., Cooper, J., & Laczik, Z. (2001). Dynamic holographic optical tweezers. In *Opt. Commun* (Vol. 72).

E Neher, & B Sakmann. (1992). The patch clamp technique. *Scientific American*, *266*(3), 44–51. https://doi.org/10.1038/SCIENTIFICAMERICAN0392-44

E Ronzitti, M Guillon, v de Sars, & v Emiliani. (2012a). LCoS nematic SLM characterization and modeling for diffraction efficiency optimization, zero and ghost orders suppression. *Optics Express*, *20*(16), 17843. https://doi.org/10.1364/OE.20.017843

E Ronzitti, M Guillon, v de Sars, & v Emiliani. (2012b). LCoS nematic SLM characterization and modeling for diffraction efficiency optimization, zero and ghost orders suppression. *Optics Express*, *20*(16), 17843. https://doi.org/10.1364/OE.20.017843

E Ronzitti, R Conti, v Zampini, D Tanese, AJ Foust, N Klapoetke, ES Boyden, E Papagiakoumou, & v Emiliani. (2017). Submillisecond Optogenetic Control of Neuronal Firing with Two-Photon Holographic Photoactivation of Chronos. *The Journal of Neuroscience : The Official Journal of the Society for Neuroscience*, *37*(44), 10679–10689. https://doi.org/10.1523/JNEUROSCI.1246-17.2017

EG Govorunova, OA Sineshchekov, R Janz, X Liu, & JL Spudich. (2015). NEUROSCIENCE. Natural light-gated anion channels: A family of microbial rhodopsins for advanced optogenetics. *Science (New York, N.Y.)*, *349*(6248), 647–650. https://doi.org/10.1126/SCIENCE.AAA7484

Feldbauer, K., Zimmermann, D., Pintschovius, V., Spitz, J., Bamann, C., & Bamberg, E. (2009). Channelrhodopsin-2 is a leaky proton pump. *Proceedings of the National Academy of Sciences*, *106*(30), 12317–12322. https://doi.org/10.1073/PNAS.0905852106

Forli, A., Vecchia, D., Binini, N., Succol, F., Bovetti, S., Moretti, C., Nespoli, F., Mahn, M., Baker, C. A., Bolton, M. M., Yizhar, O., & Fellin, T. (2018). Two-Photon Bidirectional Control and Imaging of Neuronal Excitability with High Spatial Resolution In Vivo. *Cell Reports*, *22*(11), 3087. https://doi.org/10.1016/J.CELREP.2018.02.063

G Buzsáki. (2004). Large-scale recording of neuronal ensembles. *Nature Neuroscience*, *7*(5), 446–451. https://doi.org/10.1038/NN1233

G Nagel, D Ollig, M Fuhrmann, S Kateriya, AM Musti, E Bamberg, & P Hegemann. (2002). Channelrhodopsin-1: a light-gated proton channel in green algae. *Science (New York, N.Y.)*, *296*(5577), 2395–2398. https://doi.org/10.1126/SCIENCE.1072068

G Nagel, T Szellas, W Huhn, S Kateriya, N Adeishvili, P Berthold, D Ollig, P Hegemann, & E Bamberg. (2003). Channelrhodopsin-2, a directly light-gated cation-selective membrane channel. *Proceedings of the National Academy of Sciences of the United States of America*, *100*(24), 13940–13945. https://doi.org/10.1073/PNAS.1936192100

Gabor, D. (1948). A new microscopic principle. *Nature*, *161*(4098), 777–778. https://doi.org/10.1038/161777A0

Gaunt, A. L., & Hadzibabic, Z. (2012). Robust Digital Holography For Ultracold Atom Trapping. *Scientific Reports 2012 2:1*, *2*(1), 1–5. https://doi.org/10.1038/srep00721

Georgiou, A., Christmas, J., Moore, J., Jeziorska-Chapman, A., Davey, A., Collings, N., & Crossland, W. A. (2008). Liquid crystal over silicon device characteristics for holographic projection of high-definition television images. *Applied Optics*, *47*(26), 4793–4803. https://doi.org/10.1364/AO.47.004793

Gerchberg, R. W., & Saxton, W. O. (1972). *A Practical Algorithm for the Determination of Phase from Image and Diffraction Plane Pictures*.

Glü, J., & Mogensen, P. C. (2001). *Optimal phase contrast in common-path interferometry*.

Glückstad, J. (1996). Phase contrast image synthesis. *Optics Communications*, *130*(4), 225–230. https://doi.org/https://doi.org/10.1016/0030-4018(96)00339-2

Glückstad, J., & Mogensen, P. C. (2001). Optimal phase contrast in common-path interferometry. *Appl. Opt.*, *40*(2), 268–282. https://doi.org/10.1364/AO.40.000268

Golan, L., Reutsky, I., Farah, N., & Shoham, S. (2009). Design and characteristics of holographic neural photo-stimulation systems. *Journal of Neural Engineering*, *6*(6). https://doi.org/10.1088/1741-2560/6/6/066004

Gupta, M., & Ballato, J. (2007). The Handbook of Photonics: Second Edition. *The Handbook of Photonics: Second Edition. Edited by Mool C. Gupta and John Ballato. ISBN 978-0-8493-3095-7 (HB). Published by CRC Press, Taylor & Francis Group, Boca Raton, FL, USA, 2007.*

Haist, T., Schönleber, M., & Tiziani, H. J. (1997). Computer-generated holograms from 3D-objects written on twisted-nematic liquid crystal displays. *Optics Communications*, *140*(4–6), 299–308. https://doi.org/10.1016/S0030-4018(97)00192-2

Helmchen, F., & Denk, W. (2005). Deep tissue two-photon microscopy. *Nature Methods*, *2*(12), 932–940. https://doi.org/10.1038/nmeth818

Hermerschmidt, A., Hesseling, C., Denz, C., & Woerdemann, M. (2011). Controlling ghost traps in holographic optical tweezers. *Optics Letters, Vol. 36, Issue 18, Pp. 3657-3659*, *36*(18), 3657–3659. https://doi.org/10.1364/OL.36.003657

Hernandez, O., Guillon, M., Papagiakoumou, E., & Emiliani, V. (2014). *Zero-order suppression for two-photon holographic excitation*. https://doi.org/10.1364/ol.39.005953ï

Hernandez, O., Papagiakoumou, E., Tanese, D., Fidelin, K., Wyart, C., & Emiliani, V. (2016). Three-dimensional spatiotemporal focusing of holographic patterns. *Nature Communications 2016 7:1*, *7*(1), 1–11. https://doi.org/10.1038/ncomms11928

Horton, N. G., Wang, K., Kobat, D., Clark, C. G., Wise, F. W., Schaffer, C. B., & Xu, C. (2013). In vivo three-photon microscopy of subcortical structures within an intact mouse brain. *Nature Photonics*, *7*(3), 205. https://doi.org/10.1038/NPHOTON.2012.336

J Duebel, K Marazova, & JA Sahel. (2015). Optogenetics. *Current Opinion in Ophthalmology*, *26*(3), 226–232. https://doi.org/10.1097/ICU.0000000000000140

Jennings, J. H., Sparta, D. R., Stamatakis, A. M., Ung, R. L., Pleil, K. E., Kash, T. L., & Stuber, G. D. (2013). Distinct extended amygdala circuits for divergent motivational states. *Nature*, *496*(7444), 224. https://doi.org/10.1038/NATURE12041

Jennings, J. H., Ung, R. L., Resendez, S. L., Stamatakis, A. M., Taylor, J. G., Huang, J., Veleta, K., Kantak, P. A., Aita, M., Shilling-Scrivo, K., Ramakrishnan, C., Deisseroth, K., Otte, S., & Stuber, G. D. (2015). Visualizing hypothalamic network dynamics for appetitive and consummatory behaviors. *Cell*, *160*(3), 516. https://doi.org/10.1016/J.CELL.2014.12.026

John Graham White, E Southgate, JN Thomson, & S Brenner. (1976). The structure of the ventral nerve cord of Caenorhabditis elegans. *Philosophical Transactions of the Royal Society of London. Series B, Biological Sciences*, *275*(938), 327–348. https://doi.org/10.1098/RSTB.1976.0086

JP Rickgauer, & DW Tank. (2009). Two-photon excitation of channelrhodopsin-2 at saturation. *Proceedings of the National Academy of Sciences of the United States of America*, *106*(35), 15025–15030. https://doi.org/10.1073/PNAS.0907084106

JP Rickgauer, K Deisseroth, & DW Tank. (2014). Simultaneous cellular-resolution optical perturbation and imaging of place cell firing fields. *Nature Neuroscience*, *17*(12), 1816–1824. https://doi.org/10.1038/NN.3866

Karl Deisseroth. (2011). Optogenetics. *Nature Methods*, *8*(1), 26. https://doi.org/10.1038/NMETH.F.324

Karl Deisseroth. (2015). Optogenetics: 10 years of microbial opsins in neuroscience. *Nature Neuroscience*, *18*(9), 1213. https://doi.org/10.1038/NN.4091

Katz, O., Small, E., Bromberg, Y., & Silberberg, Y. (2011). Focusing and compression of ultrashort pulses through scattering media. *Nature Photonics 2011 5:6*, *5*(6), 372–377. https://doi.org/10.1038/nphoton.2011.72

Keller, D., Erö, C., & Markram, H. (2018). Cell Densities in the Mouse Brain: A Systematic Review. *Frontiers in Neuroanatomy*, *12*. https://doi.org/10.3389/FNANA.2018.00083

Kobat, D., Horton, N. G., & Xu, C. (2011). In vivo two-photon microscopy to 1.6-mm depth in mouse cortex. *Journal of Biomedical Optics*, *16*(10), 106014. https://doi.org/10.1117/1.3646209

Leshem, B., Oron, D., Papagiakoumou, E., Hernandez, O., & Emiliani, V. (2014). When can temporally focused excitation be axially shifted by dispersion? *Optics Express, Vol. 22, Issue 6, Pp. 7087-7098*, *22*(6), 7087–7098. https://doi.org/10.1364/OE.22.007087

Lin, D., Boyle, M. P., Dollar, P., Lee, H., Perona, P., Lein, E. S., & Anderson, D. J. (2011). Functional identification of an aggression locus in the mouse hypothalamus. *Nature*, *470*(7333), 221. https://doi.org/10.1038/NATURE09736

Lohmann, A. W., & Paris, D. P. (1967). Binary Fraunhofer Holograms, Generated by Computer. *Applied Optics, Vol. 6, Issue 10, Pp. 1739-1748*, *6*(10), 1739–1748. https://doi.org/10.1364/AO.6.001739

Lutz, C., Otis, T. S., DeSars, V., Charpak, S., DiGregorio, D. A., & Emiliani, V. (2008a). Holographic photolysis of caged neurotransmitters. *Nature Methods*, *5*(9), 821. https://doi.org/10.1038/NMETH.1241

Lutz, C., Otis, T. S., DeSars, V., Charpak, S., DiGregorio, D. A., & Emiliani, V. (2008b). Holographic photolysis of caged neurotransmitters. *Nature Methods 2008 5:9*, *5*(9), 821–827. https://doi.org/10.1038/nmeth.1241

M Oheim, E Beaurepaire, E Chaigneau, J Mertz, & S Charpak. (2001). Two-photon microscopy in brain tissue: parameters influencing the imaging depth. *Journal of Neuroscience Methods*, *111*(1), 29–37. https://doi.org/10.1016/S0165-0270(01)00438-1

M Scanziani, & M Häusser. (2009). Electrophysiology in the age of light. *Nature*, *461*(7266), 930–939. https://doi.org/10.1038/NATURE08540

Marshel, J. H., Kim, Y. S., Machado, T. A., Quirin, S., Benson, B., Kadmon, J., Raja, C., Chibukhchyan, A., Ramakrishnan, C., Inoue, M., Shane, J. C., McKnight, D. J., Yoshizawa, S., Kato, H. E., Ganguli, S., & Deisseroth, K. (2019). Cortical layer–specific critical dynamics triggering perception. *Science*, *365*(6453). https://doi.org/10.1126/SCIENCE.AAW5202

Martial, F. P., & Hartell, N. A. (2012). Programmable illumination and high-speed, multi-wavelength, confocal microscopy using a digital micromirror. *PLoS ONE*, *7*(8). https://doi.org/10.1371/journal.pone.0043942

Martinez, O. (1987). Design of high-power ultrashort pulse amplifiers by expansion and recompression. *IEEE Journal of Quantum Electronics*, *23*(8), 1385–1387. https://doi.org/10.1109/JQE.1987.1073518

Martinez, O. E. (1986). PULSE DISTORTIONS IN TILTED PULSE SCHEMES FOR ULTRASHORT PULSES. In *OPTICS COMMUNICATIONS* (Vol. 59, Issue 3).

Mattis, J., Tye, K. M., Ferenczi, E. A., Ramakrishnan, C., O'Shea, D. J., Prakash, R., Gunaydin, L. A., Hyun, M., Fenno, L. E., Gradinaru, V., Yizhar, O., & Deisseroth, K. (2011). Principles for applying optogenetic tools derived from direct comparative analysis of microbial opsins. *Nature Methods 2011 9:2*, *9*(2), 159–172. https://doi.org/10.1038/nmeth.1808

Nägerl, U. V., & Bonhoeffer, T. (2010). *Imaging Living Synapses at the Nanoscale by STED Microscopy*. https://doi.org/10.1523/JNEUROSCI.0990-10.2010

O Yizhar, le Fenno, M Prigge, F Schneider, TJ Davidson, DJ O'Shea, VS Sohal, I Goshen, J Finkelstein, JT Paz, K Stehfest, R Fudim, C Ramakrishnan, JR Huguenard, P Hegemann, & K Deisseroth. (2011). Neocortical excitation/inhibition balance in information processing and social dysfunction. *Nature*, *477*(7363), 171–178. https://doi.org/10.1038/NATURE10360

Oron, D., Tal, E., & Silberberg, Y. (2005a). Scanningless depth-resolved microscopy. *Optics Express*, *13*(5), 1468–1476.

Oron, D., Tal, E., & Silberberg, Y. (2005b). *Scanningless depth-resolved microscopy*.

Óscar R. Hernández Cubero. (2016). *Méthodes optiques innovantes pour le contrôle rapide et tridimensionnel de l'activité neuronale Advanced optical methods for fast and three-dimensional control of neural activity Pour obtenir le grade de*.

Osten, W. (2006). *Holography in New Shoes: A Digital-Analogue Interface*.

Ozbay, B. N., Futia, G. L., Ma, M., Bright, V. M., Gopinath, J. T., Hughes, E. G., Restrepo, D., & Gibson, E. A. (2018). Three dimensional two-photon brain imaging in freely moving mice using a miniature fiber coupled microscope with active axial-scanning. *Scientific Reports 2018 8:1*, *8*(1), 1–14. https://doi.org/10.1038/s41598-018-26326-3

Packer, A. M., Russell, L. E., Dalgleish, H. W. P., & Häusser, M. (2014). Simultaneous all-optical manipulation and recording of neural circuit activity with cellular resolution in vivo. *Nature Methods*, *12*(december), 140–146. https://doi.org/10.1038/nmeth.3217

Papagiakoumou, E., Anselmi, F., Begue, A., Sars, V. de, Glückstad, J., Isacoff, E., & Emiliani, V. (2010). Scanless two-photon excitation of channelrhodopsin-2. *Nature Methods*, *7*(10), 848. https://doi.org/10.1038/NMETH.1505

Papagiakoumou, E., Bègue, A., Leshem, B., Schwartz, O., Stell, B. M., Bradley, J., Oron, D., & Emiliani, V. (2013a). Functional patterned multiphoton excitation deep inside scattering tissue. *Nature Photonics*, *7*(4), 274–278. https://doi.org/10.1038/nphoton.2013.9

Papagiakoumou, E., Bègue, A., Leshem, B., Schwartz, O., Stell, B. M., Bradley, J., Oron, D., & Emiliani, V. (2013b). Functional patterned multiphoton excitation deep inside scattering tissue. *Nature Photonics*, *7*(4), 274–278. https://doi.org/10.1038/NPHOTON.2013.9

Papagiakoumou, E., de Sars, V., Oron, D., & Emiliani, V. (2008). Patterned two-photon illumination by spatiotemporal shaping of ultrashort pulses. *Optics Express*, *16*(26), 22039–22047. https://doi.org/10.1364/OE.16.022039

Papagiakoumou, E., Oron, D., Emiliani, V., & Sars, V. de. (2008). Patterned two-photon illumination by spatiotemporal shaping of ultrashort pulses. *Optics Express, Vol. 16, Issue 26, Pp. 22039-22047*, *16*(26), 22039–22047. https://doi.org/10.1364/OE.16.022039

Papagiakoumou, E., Ronzitti, E., & Emiliani, V. (2020a). Scanless two-photon excitation with temporal focusing. In *Nature Methods* (Vol. 17, Issue 6, pp. 571–581). Nature Research. https://doi.org/10.1038/s41592-020-0795-y

Papagiakoumou, E., Ronzitti, E., & Emiliani, V. (2020b). Scanless two-photon excitation with temporal focusing. In *Nature Methods* (Vol. 17, Issue 6, pp. 571–581). Nature Research. https://doi.org/10.1038/s41592-020-0795-y

Persson, M., Engström, D., & Goksör, M. (2012). Reducing the effect of pixel crosstalk in phase only spatial light modulators. *Opt. Express*, *20*(20), 22334–22343. https://doi.org/10.1364/OE.20.022334

Pozzi, P., Maddalena, L., Ceffa, N., Soloviev, O., Vdovin, G., Carroll, E., & Verhaegen, M. (2018). Fast Calculation of Computer Generated Holograms for 3D Photostimulation through Compressive-Sensing Gerchberg–Saxton Algorithm. *Methods and Protocols 2019, Vol. 2, Page 2*, *2*(1), 2. https://doi.org/10.3390/MPS2010002

Prakash, R., Yizhar, O., Grewe, B., Ramakrishnan, C., Wang, N., Goshen, I., Packer, A. M., Peterka, D. S., Yuste, R., Schnitzer, M. J., & Deisseroth, K. (2012). Two-photon optogenetic toolbox for fast inhibition, excitation and bistable modulation. *Nature Methods 2012 9:12*, *9*(12), 1171–1179. https://doi.org/10.1038/nmeth.2215

RD Proville, M Spolidoro, N Guyon, GP Dugué, F Selimi, P Isope, D Popa, & C Léna. (2014). Cerebellum involvement in cortical sensorimotor circuits for the control of voluntary movements. *Nature Neuroscience*, *17*(9), 1233–1239. https://doi.org/10.1038/NN.3773

Rickgauer, J. P., & Tank, D. W. (2009). Two-photon excitation of channelrhodopsin-2 at saturation. *Proceedings of the National Academy of Sciences*, *106*(35), 15025–15030. https://doi.org/10.1073/PNAS.0907084106

Ronzitti, E., Ventalon, C., Canepari, M., Forget, B. C., Papagiakoumou, E., & Emiliani, V. (2017). Recent advances in patterned photostimulation for optogenetics. In *Journal of Optics (United Kingdom)* (Vol. 19, Issue 11). IOP Publishing Ltd. https://doi.org/10.1088/2040-8986/aa8299

Saleh, B., & Teich, M. (2019). *Fundamentals of Photonics, 3rd Edition*.

SC Barnett, BAL Perry, JC Dalrymple-Alford, & LC Parr-Brownlie. (2018). Optogenetic stimulation: Understanding memory and treating deficits. *Hippocampus*, *28*(7), 457–470. https://doi.org/10.1002/HIPO.22960

Shemesh, O. A., Tanese, D., Zampini, V., Linghu, C., Piatkevich, K., Ronzitti, E., Papagiakoumou, E., Boyden, E. S., & Emiliani, V. (2017). Temporally precise single-cell-resolution optogenetics. *Nature Neuroscience 2017 20:12*, *20*(12), 1796–1806. https://doi.org/10.1038/s41593-017-0018-8

Theer, P., & Denk, W. (2006). On the fundamental imaging-depth limit in two-photon microscopy. *JOSA A, Vol. 23, Issue 12, Pp. 3139-3149*, *23*(12), 3139–3149. https://doi.org/10.1364/JOSAA.23.003139

Upputuri, P. K., & Pramanik, M. (2019). Photoacoustic imaging in the second near-infrared window: a review. *Journal of Biomedical Optics*, *24*(04), 1. https://doi.org/10.1117/1.JBO.24.4.040901

v Nikolenko, BO Watson, R Araya, A Woodruff, DS Peterka, & R Yuste. (2008). SLM Microscopy: Scanless Two-Photon Imaging and Photostimulation with Spatial Light Modulators. *Frontiers in Neural Circuits*, *2*(DEC). https://doi.org/10.3389/NEURO.04.005.2008

Vaziri, A., & Emiliani, V. (2012). Reshaping the optical dimension in optogenetics. *Current Opinion in Neurobiology*, *22*(1), 128–137. https://doi.org/10.1016/J.CONB.2011.11.011

Vogel, A., & Venugopalan, V. (2003). Mechanisms of pulsed laser ablation of biological tissues. In *Chemical Reviews* (Vol. 103, Issue 2, pp. 577–644). https://doi.org/10.1021/cr010379n

Xu Chris. (2002). Cross-Sections of Fluorescence Molecules in Multiphoton Microscopy. *John Wiley & Sons*.

Yang, W., Carrillo-Reid, L., Bando, Y., Peterka, D. S., & Yuste, R. (2018). Simultaneous two-photon imaging and two-photon optogenetics of cortical circuits in three dimensions. *ELife*, *7*. https://doi.org/10.7554/ELIFE.32671

Z Zalevsky, D Mendlovic, & RG Dorsch. (1996). Gerchberg-Saxton algorithm applied in the fractional Fourier or the Fresnel domain. *Optics Letters*, *21*(12), 842. https://doi.org/10.1364/OL.21.000842

Zhang, F., Wang, L.-P., Brauner, M., Liewald, J. F., Kay, K., Watzke, N., Wood, P. G., Bamberg, E., Nagel, G., Gottschalk, A., & Deisseroth, K. (2007). Multimodal fast optical interrogation of neural circuitry. *Nature 2007 446:7136*, *446*(7136), 633–639. https://doi.org/10.1038/nature05744

Zheng, J.-Y., Boustany, N. N., & Pasternack, R. M. (2009). Optical Scatter Imaging with a digital micromirror device. *Optics Express, Vol. 17, Issue 22, Pp. 20401-20414*, *17*(22), 20401–20414. https://doi.org/10.1364/OE.17.020401

Zhu, G., van Howe, J., Durst, M., Zipfel, W., Xu, C., Denk, W., Delaney, K. R., Gelperin, A., Kleinfeld, D., Strawbridge, B. W., Tank, D. W., Yuste, R., Squirrell, J. M., Wokosin, D. L., White, J. G., Bavister, B. D., Zipfel, W. R., Williams, R. M., Christie, R., … Webb, W. W. (2005). Simultaneous spatial and temporal focusing of femtosecond pulses References and links "Anatomical and functional imaging of neurons using 2-photon laser microscopy "Long-term two-photon fluorescence imaging of mammalian embryos without compromising viability. In *J. Neuroscience Methods* (Vol. 54). http://www.opticsexpress.org/abstract.cfm?URI=OPEX-13-5-1468.

Zong, W., Wu, R., Li, M., Hu, Y., Li, Y., Li, J., Rong, H., Wu, H., Xu, Y., Lu, Y., Jia, H., Fan, M., Zhou, Z., Zhang, Y., Wang, A., Chen, L., & Cheng, H. (2017). Fast high-resolution miniature two-photon microscopy for brain imaging in freely behaving mice. *Nature Methods 2017 14:7*, *14*(7), 713–719. https://doi.org/10.1038/nmeth.4305

Publications:

Nicolò Accanto, Clément Molinier, Dimitrii Tanese, Emiliano Ronzitti, Zachary L. Newman, Claire Wyart, Ehud Isacoff, Eirini Papagiakoumou, and Valentina Emiliani, "Multiplexed temporally focused light shaping for high-resolution multi-cell targeting," Optica 5, 1478-1491 (2018)

Nicolò Accanto, I-wen Chen, Emiliano Ronzitti, Clément Molinier, Christophe Tourain, Eirini Papagiakoumou, Valentina Emiliani. "Multiplexed temporally focused light shaping through a gradient index lens for precise in-depth optogenetic photostimulation. " Sci Rep. 2019 May 20;9(1):7603.

Giulia Faini, Clément Molinier, Cécile Telliez, Christophe Tourain, BenoîtC.Forget, Emiliano Ronzitti, and Valentina Emiliani, “Ultrafast Light Targeting for High-Throughput Precise Control of Neuronal Network ” (under review)

Développement de systèmes optiques avancés pour la manipulation des neurones avec une haute résolution spatiale et temporelle

Résumé :

Avec la découverte de l'optogénétique, l'utilisation de la lumière est devenue essentielle pour étudier et contrôler l'activité et la connectivité neuronales. Cependant, la complexité des circuits cérébraux exige d'employer des méthodes optiques avancées pour toute investigation approfondie de son fonctionement. C'est pourquoi, l'un des plus grands défis optiques est d'atteindre des cibles multiples avec une résolution cellulaire et une bonne précision temporelle dans les régions les plus profondes du cerveau. Au cours de cette thèse, j'ai travaillé sur trois nouveaux systèmes optiques afin d'apporter une réponse possible à certains de ces défis techniques.

Premièrement, nous avons développé un nouveau système de génération de formes lumineuses focalisées dans le temps (MTF-LS) pour la photostimulation précise en 3D des neurones. Grâce à la flexibilité de cette nouvelle approche, différentes méthodes de modelage de la lumière ont put être utilisées: l'holographie générée par ordinateur (CGH) ou le contraste de phase généralisé. Avec ces deux approches, le système était limité à la multiplication en 3D d'une seule forme à la fois. Pour résoudre ce problème, nous avons proposé une technique innovante de modulation amplitude/phase, pour générer différentes formes en 3D.

En raison de l'absorption et de la diffusion, il est difficile de stimuler des cellules au-delà de ~ 600 µm de tissu cérébral avec une methode de stimulation à deux photons (2P). Face à des limitations similaires en matière d'imagerie, d'autres laboratoires ont utilisé des lentilles à gradient d'indice (GRIN) implantées dans le cerveau pour accéder à des régions profondes. Nous avons donc développé une nouvelle méthode de photostimulation en profondeur, en couplant une lentille GRIN avec le MTF-LS précédemment démontré. Ce système représente le premier microendoscope capable de générer des dizaines de sites d'excitation 2P, confinés axialement et correspondant aux dimensions du soma d'un neurone cible dans un volume 3D .

Troisièmement, pour manipuler l'activité neuronale à des échelles temporelles inférieures à la milliseconde et/ou de grandes populations de cellules, nous avons construit un nouveau système utilisant le ciblage lumineux séquentiel ultra-rapide (FLiT). Nous sommes parvenus à contrôler le retard d'activation entre deux cellules avec une résolution temporelle de l'ordre de la microseconde. Nous avons également démontré un nouveau protocole de stimulation où l'optimisation du temps d'illumination permet de stimuler cinq fois plus de cellules que l'illumination statique conventionnelle pour la même puissance laser.

Mots-clefs: optogénétique, excitation à deux photons, photostimulation, modulation de phase, modulation d'amplitude, holographie générée par ordinateur, contraste de phase généralisé, focalisation temporelle, tridimensionnelle, gradient d'indice, microendoscope, profondeur, précision temporelle, milliseconde, ultra-rapide, ciblage séquentiel de la lumière.

Development of advanced optical systems for spatially and temporally precise brain interrogation

Abstract :

With the discovery of optogenetics, using light becomes essential to study and control neural activity and connectivity. However, the complexity of the brain circuits demands advanced optical methods for detailed investigation. One of the most significant optical challenges is to address multiple targets with cellular resolution and high temporal precision in deep brain regions. During this thesis, I worked on three new optical systems to provide a possible answer to some of these technical challenges.

First, we developed a new system to multiplex temporally focused light shapes (MTF-LS) for precise 3D photostimulation of neurons. Thanks to the flexibility of this new approach, different light-shaping methods can be applied: either computer-generated holography (CGH) or speckle-free generalized phase contrast. With these two approaches, the system was limited to multiplex only one shape at the time. To solve this issue we demonstrate an innovative amplitude/phase modulation technique, to multiplex different shapes in 3D.

Due to the absorption and scattering, it is difficult to stimulate cells beyond ~ 600 µm of brain tissue with two-photon (2P) stimulation technique. Facing similar limitations in imaging, other laboratories used gradient index (GRIN) lenses implanted in the brain to access deep regions. Thus we develop a new in-depth photostimulation method, by coupling a GRIN lens with the MTF-LS previously demonstrated. This system represented the first microendoscope capable of generating tens of axially confined 2P excitation patterns matching target neuronal soma in a 3D volume for in-depth experiments.

Third, to manipulate neuronal activity at sub-millisecond temporal scales and large cell populations, we built a new system using ultra-fast sequential light targeting (FLiT). We managed to control the spike delay among two cells with µs temporal resolution. We also demonstrate a new stimulation protocol where the illumination time optimization allows to stimulate five times more cells than conventional static illumination for the same laser power.

Keywords : optogenetics, two-photon excitation, photostimulation, light-shaping, wave-front shaping, computer generated holography, generalized phase contrast, temporal focusing, three-dimensional, gradient index, microendoscope, in-depth, temporal precision, sub-millisecond, ultra-fast, sequential light targeting.